EPA under Grant #U-914726-01-0

Predicting Particle Critical Supersaturation From Hygroscopic Growth Measurements In The Humidified Tandem Differential Mobility Analyzer

by Fredrick J. Brechtel

Sonia M. Kreidenweis, P.I.

Colorado State University

DEPARTMENT OF ATMOSPHERIC SCIENCE

PAPER NO. 662

Predicting Particle Critical Supersaturation From Hygroscopic Growth Measurements in the Humidified Tandem Differential Mobility Analyzer

by

Fredrick J. Brechtel

Department of Atmospheric Science

Colorado State University

Fort Collins, CO 80523

Environmental Protection Agency

under Graduate Student Fellowship number #U-914726-01-0.

September 25, 1998

Atmospheric Science Paper Number 662

Abstract

Predicting Particle Critical Supersaturation From Hygroscopic Growth Measurements in the Humidified Tandem Differential Mobility Analyzer

A new method is described to estimate the critical supersaturation of a quasi-monodisperse, dry particle population composed of pure salts using measurements of hygroscopic growth at several relative humidities below 100%. We describe how Köhler theory may be used to derive two chemical composition dependent parameters, with appropriate accounting for solution effects through a simplified model of the osmotic coefficient. Using a regression routine, the two unknown chemical parameters are derived by fitting the Köhler model to the results from hygroscopic growth experiments. The derived parameters are then used in the Köhler model to calculate critical supersaturations for given dry particle size. From these studies, it is possible to derive the cloud condensation nucleus spectrum if simultaneous measurements of the total number size distribution are made and a sufficient number of critical supersaturations for different particle sizes are determined to characterize the cloud condensation nucleus sub-population of the total particle population. This work represents one of the first, detailed studies on the relationships between particle hygroscopicity and CCN activity using simultaneous measurements of droplet growth and particle critical supersaturation on particles composed of pure salts. In this work we present the theory and methodology that allow the critical supersaturation to be derived from hygroscopic growth measurements, and perform numerical sensitivity studies with respect to assumptions made and anticipated uncertainties in key input parameters to the Köhler model. Laboratory studies are conducted on

particles composed of NaCl, $(NH_4)_2SO_4$, NH_4HSO_4, internally and externally mixed NaCl-$(NH_4)_2SO_4$ to validate the technique. Studies on ambient particles are also conducted to test if the technique can predict accurate values of S_{crit} for particles of unknown chemical composition.

Results from numerical studies show that for particle diameters of 40 and 100 nm, the maximum errors in critical supersaturations derived using the proposed method are between ±15%. This error is similar to the observed average experimental uncertainty in estimates of the critical supersaturation of -0.6%±11% determined from CCN studies on particles of known composition.

Laboratory studies demonstrate that the critical supersaturation can be derived from hygroscopic growth measurements within experimental uncertainties for the particles of known chemical composition examined in this work. The largest observed differences (-3% to -62%) between HTDMA and CCN derived values of S_{crit} occured for ambient particle samples where the chemical composition was unknown and most likely contained a significant amount of hydrophobic material. The numerical and laboratory studies indicate that the proposed technique can establish quantitative relationships between particle size and hygroscopic growth and cloud condensation nucleus activity. The method should help reduce uncertainties in estimates of the indirect effect of particles on climate by allowing more commonly measured aerosol properties, for example particle size and hygroscopic growth, to be directly related to the particle critical supersaturation.

Acknowledgements

Over the last five years, so many people have helped me in some way that to list them all here individually would take several pages, to anyone who finds their name missing from this page: I apologize. First and foremost in my mind is the support I received from my wife, Lauren, who was unlucky enough to marry me right at the beginning of my Ph.D. She stood by me when things didn't seem to work, supported our family financially, put-up with my long days and work on the weekends, and unselfishly gave her love. Without her, I would not have finished this work.

My advisor, Sonia Kreidenweis, allowed me the freedom to explore my research in my own sometimes inefficient ways, always keeping me in-check at the right time with a sage comment. My other committee members: Jeffrey Collet Jr., William Cotton, William Massman and John Ogren, all made themselves available to me and provided the feedback necessary to greatly improve the quality of this research. The invaluable assistance of Richard Leaitch through the loan of and assistance with the CCN counter used in this work is greatly appreciated.

Finally, this research would not have been possible without the generous support of several funding agencies. Over the last five years, my work has been supported by the Office of Naval Research under grant #N00014-93-1-0420, and, between 1995 and 1998, by EPA STAR Fellowship #U-914726-01-0.

Contents

List of Tables

List of Figures

List of Symbols Used in This Work.

Symbol	Definition
a	temperature coefficient for surface tension ($1.53x10^{-4}$ N m^{-1} K^{-1})
a	fit parameter in sigmoidal function fit to the ratio $\frac{N_{CCN}}{N_{UCPC}}$
a_w	water activity
a_s	activity of solute
a_i	calibration coefficient for RH calibration equation
α	Pitzer osmotic coefficiennt fit parameter
A_ϕ	Debye-Huckel coefficient for Φ
b_{pit}	Pitzer osmotic coefficient fit parameter
b_i	calibration coefficient for thermistor calibration equation
b	solution molality coefficient for surface tension (N m^{-1} kg^{-1} mole)
b, D_1, D_2	fit parameters in sigmoidal function fit to the ratio $\frac{N_{CCN}}{N_{UCPC}}$
β_0, β_1	Pitzer osmotic coefficient fit parameters
$\beta_{0,f}$	osmotic coefficient fit parameter derived from HTDMA fit routine
C_ϕ	Pitzer osmotic coefficient fit parameter
C_c	Cunningham Slip Correction Factor
D	diffusion coefficient ()
D_{drop}	droplet diameter (m)
D_{crit}	droplet diameter at S_{crit} (m)
D_p	dry particle diameter (m)
$D_{p,insol}$	diameter of insoluble inclusion, if present (m)
$D_{p,sol}$	dry particle diameter of soluble material (m)
e	unit electric charge ($1.619*10^{-19}$ coulomb)
E_r	radial electric field in DMA column (V m^{-1})
η_{cpc}	detection efficiency of Model 3010 CPC
η_{ucpc}	detection efficiency of Model 3025 CPC
f	Degrees of freedom (unitless)
f_i	mole fraction of species 'i'
G	Gibbs Free Energy (Joules)
γ_w	activity coefficient of water in solution droplet (unitless)
γ_s	activity coefficient of solute in solution droplet (unitless)
I	ionic strength of solution (moles kg^{-1})
Φ_s	practical osmotic coefficient for droplet containing a single water soluble substance (unitless)
$\Phi_{s,mix}$	practical osmotic coefficient for droplet solution with more than one than one water soluble substance (unitless)
Φ_f	simplified form of osmotic coefficient
$\Phi_{s,i}$	practical osmotic coefficient for solute 'i'
Φ_{crit}	value of osmotic coefficient at S_{crit}
k	Boltzmann's constant ($1.38x10^{-23}$ $kg\ m^2\ s^{-2}\ K^{-1}$)
λ	mean free path of air (m)
L	distance from DMA column inlet to monodisperse sampling slit (m)
M_w	molecular weight of water ($\frac{kg}{kmol}$)

List of Symbols Used in This Work (cont.).

Symbol	Definition
$m_{s,t}$	total solute mass in solution (kg)
m_s	solute mass in dry particle (kg)
m_w	water mass in solution (kg)
m_i	molality of species 'i', i $\neq$'s' or 'w' (moles$_i$ kg$_w^{-1}$)
$\bar{M}_s$	average molecular weight of mixture of solutes ($\frac{kg}{kmol}$)
$\bar{M}_{drop}$	average molecular weight of water droplet ($\frac{kg}{kmol}$)
M_s	molecular weight of solute for a single solute solution ($\frac{kg}{kmol}$)
μ_i	chemical potential of species 'i' (Joules/mole)
N	number concentration (cm^{-3})
N_{av}	Avogadro's Number ($6.0224x10^{23}$ mol^{-1})
N_{CCN}	coincidence and loss corrected droplet concentration from CCN counter (cm^{-3})
N_{true}	coincidence corrected droplet concentration from CCN counter (cm^{-3})
N_{UCPC}	loss corrected particle concentration from UCPC (cm^{-3})
N_{act}	uncorrected droplet concentration from CCN counter (cm^{-3})
n_i	number of moles of species 'i'
$\bar{\nu}_l$	partial molar volume of water (m^3 mole^{-1})
ν_i	moles of cations or anions produces upon dissociation (ions)
ν_{air}	kinematic viscosity of air (kg m^{-2} s^{-1})
$\bar{\nu}_s$	mean number of ions dissociated in solution per solute molecule (ions)
P, p	ambient pressure (Pascals)
p_w	partial pressure of water vapor in sample air stream (Pa)
p_w^o	saturation pressure of pure water vapor at sample temperature (Pa)
$p_{w,sol}^o$	saturation pressure of water vapor over solution droplet at sample temperature (Pa)
P_{ucpc}	penetration efficiency of sample line of Model 3025 CPC
P_{ccn}	penetration efficiency of sample line of Model DH-1 CCN Counter
q_{sh}	sheath air flow rate (m^3 s^{-1})
q_s	DMA outlet sample air flow rate (m^3 s^{-1})
q_a	DMA inlet sample air flow rate (m^3 s^{-1})
q_e	DMA excess outlet air flow rate (m^3 s^{-1})
r_o	outside radius of DMA center rod (m)
r_i	inside radius of DMA outer cylinder (m)
r	arbitrary radial position within DMA column (m)
r_{in}	radial position where particle enters DMA column (m)
ρ_w	density of pure water ($\frac{kg}{m^3}$)
ρ_s	density of dry solute ($\frac{kg}{m^3}$)
ρ_d	density of droplet solution ($\frac{kg}{m^3}$)
ρ_l	density of droplet solution from Tang's data ($\frac{kg}{m^3}$)
RH	relative humidity (%)
R, R_v	gas constant for water vapor ($8.3144 \frac{kJ}{kgkmolK}$)

List of Symbols Used in This Work (cont.).

Symbol	Definition
R	thermistor resistance (ohms)
R_{ref}	reference resistance value used in voltage divider (ohms)
$\bar{\rho}_{drop}$	droplet density corrected for composition and temperature ($\frac{kg}{m^3}$)
σ_j^i	surface tension with respect to phase 'j', where j=liquid, solid, vapor and interface 'i' (N m^{-2})
σ_o	surface tension of pure water at 273.15 K (0.0756 N m^{-2})
σ_w	surface tension of pure water (N m^{-2})
$\bar{\sigma}_{drop}$	droplet surface tension corrected for composition and temperature ($\frac{N}{m}$)
S	Entropy (Joules/Kelvin)
S_{crit}	critical supersaturation (%)
S_{max}	maximum supersaturation within CCN chamber (%)
T	Temperature (Kelvin)
T_t	CCN top plate Temperature (Kelvin)
T_b	CCN bottom plate Temperature (Kelvin)
t	transport time through DMA column (s)
V	volume (m^3) or DMA voltage (v)
V_o	reference voltage (10 v) used in voltage divider (v)
x_a	mass fraction of solute 'a' in solution (kg_s kg_{soln})
x_b	mass fraction of solute 'b' in solution (kg_s kg_{soln})
x_s	solute mass fraction in solution (kg_s kg_{soln})
x_w	mass fraction of water in solution (kg_w kg_{soln})
Y	$\frac{\nu \rho_s}{M_s}$
Y_f	osmotic coefficient fit parameter derived from HTDMA fit routine
z_i	electrical charge on ion 'i'
Z_p	particle electrical mobility (m V s^{-1})

Chapter 1

INTRODUCTION

Atmospheric particulate matter is derived from a variety of sources. Species such as dust, sea salt, and soot are directly emitted to the atmosphere, whereas other components are derived from gas-to-particle conversion processes. Semi-volatile organic compounds, nitrates, and sulfates are examples of the latter category. These species are created in the atmosphere via nonlinear chemical pathways and generally are oxidation products of gaseous emissions. For example, sulfates are created from gas-phase precursors, such as sulfur dioxide (SO_2), and are oxidized in both the gas and aqueous phases to sulfuric acid, which has a low vapor pressure and remains partitioned to the particle phase. Particulate organic material may also form by condensation directly onto pre-existing particles without chemical reaction.

Acidic and other ionic species readily absorb water, so that particles containing these species grow when exposed to increasing relative humidity (RH). This property is termed particle hygroscopicity. Another property of particles is their ability to effectively scatter and absorb solar radiation; particles with increased cross-sectional areas due to uptake of water have increased extinction. Hygroscopicity and extinction properties influence visibility, cloud formation, and the earth's radiation budget.

Unfortunately, what renders a particle hygroscopic is not a well-known quantity. It is clear that ionic species, such as ammonium sulfate, that have well-known deliquescence and water growth behavior, serve as effective light scatterers under high

RH conditions, and as effective cloud condensation nuclei (CCN). However, particles in the atmosphere are rarely composed of a single species [*Murphy et al.,* 1998; *Svenningson et al.,* 1992]. It may be that a hygroscopic coating on an insoluble particle causes it to become hygroscopic to some extent; conversely, an organic coating on a sulfate containing particle may cause it to become nonhygroscopic [*Cruz and Pandis,* 1997]. The relationships between total ambient particle number concentration and the subset of particles that act as CCN must be understood in order to quantify the so-called 'indirect effect', or the ability of particulate matter to alter climate by acting as CCN and thereby altering cloud radiative properties.

A recent report by the Intergovernmental Panel on Climate Change indicates that current estimates of the uncertainty in predictions of the indirect effect are at least twice as large as the uncertainty in the total direct effect of CO_2 [*IPCC,* 1995]. There are at least two major reasons why the predictions of the potential climate forcing associated with the indirect effect have large uncertainties. First, climatological datasets of CCN concentrations, total particle concentrations, and particle chemical composition are not available. Such datasets are necessary to elucidate the relationships between particle properties and CCN concentrations. One exception is the 20 year record of condensation nuclei (CN) and CCN concentrations at the Cape Grim Baseline Station in Tasmania [*Gras,* 1995], however, this unique record is only available at one location. The lack of data means that parameterizations relating changes in particle characteristics to CCN concentrations are very tentative. Second, there are no validated experimental techniques for reliably determining CCN concentrations from measurements of particle physical and chemical properties. This is primarily due to the fact that the molecular composition of ambient particles in the 30 to 200 nm diameter size range cannot be reliably determined over the generally short timescales of variability in ambient CCN concentrations. The 30 to 200 nm size range is important relative to CCN activity, since a large fraction of the CCN num-

ber concentration at typical cloud supersaturations (0.05 to 1%) occurs in this size range [*Covert et al.*, 1998; Hallberg et al.,1994]. For example, CCN measurements by *Hudson et al.* [1998] indicate that approximately 50% of the CCN number concentration was accounted for by particles that formed cloud droplets at supersaturations between 0.3% and 1% over the remote Southern Ocean. Particles composed of pure salts and having diameters smaller than 100 nm serve as CCN at supersaturations between 0.3% and 1%.

In order to better understand the roles played by various sources of ambient particles in determining the CCN population, experimental techniques are needed that can separate the effects of particle size from particle chemical composition in determining CCN concentrations at different water supersaturations. Without such techniques, the relationships between sources of particles, particle size, chemical composition, number concentration, and cloud droplet nucleating ability will be difficult to elucidate. A key parameter in these relationships is the critical supersaturation, S_{crit}, the water supersaturation necessary to activate a cloud condensation nucleus and form a cloud droplet. A particle is said to be activated when it experiences a supersaturation defined by the peak of the Köhler curve, such that, if the droplet formed on the particle grows slightly, the droplet will continue to grow rapidly by condensation. At any given size, particles having different chemical compositions can exhibit different values of S_{crit}. Knowledge of how the critical supersaturation varies among similar sized particles and across the size spectrum can reveal which particle sub-populations would act as cloud condensation nuclei in different cloud-forming regimes. This effect cannot be discerned using conventional CCN spectrometers that provide the integral number of particles of all sizes that act as CCN at a given supersaturation.

In this work, a technique for directly relating particle size and chemical composition to its critical supersaturation is proposed. The technique uses hygroscopic growth measurements from a Humidified Tandem Differential Mobility Analyzer [*HTDMA;*

Rader and McMurry, 1986] at relative humidities below 100%. Although such measurements are not yet routine, they have been made in many locations and yield more detailed information on particle characteristics than traditional CCN measurements. Briefly, in the HTDMA, dry (RH<10%), quasi-monodisperse particles are selected from a polydisperse size distribution using a differential mobility analyzer (DMA). The monodisperse particles are exposed to a controlled humidity environment prior to entering a second DMA. If the particles take up water, they will grow in size and exhibit a lower electrical mobility (larger size) in the second DMA. A condensation particle counter (CPC) is used to count the particles exiting the second DMA. By observing the electrical mobility where the CPC measures the maximum number of particles, the size of the wetted particles can be determined, and the water content derived from the difference between the wet and dry sizes. By controlling the second DMA humidity at several different values, the growth as a function of relative humidity may be determined for each input, dry monodisperse particle population.

In the proposed method for deriving S_{crit}, the results from HTDMA measurements are used in a simplified version of the Köhler equation recast into a form with two unknown parameters that depend upon the dry particle chemical composition. The unknown parameters are solved for using results from hygroscopic growth measurements performed on the same monodisperse particles at different RHs. Essentially, we use hygroscopic growth as a surrogate for chemical composition and derive parameters that depend on the dry particle chemical composition. Using the derived parameters in the simplified Köhler theory, the critical supersaturation may be determined for a given monodisperse dry particle size by finding the maximum supersaturation for assumed values of droplet size. In laboratory studies, the derived value of S_{crit} is compared to an experimentally determined value from simultaneous measurements of S_{crit} using a thermal gradient diffusion cloud chamber (TGDCC) sampling the same particles as the HTDMA.

This work is organized as follows. In chapter 2, a review of previous work on bulk and monodisperse particle hygroscopicity and CCN activity is presented. The first studies involving concurrent measurements of hygroscopic growth and CCN activity were performed in 1995 [*Covert et al.*, 1998]. Results from numerous HTDMA studies reveal the complex chemical composition of ambient particles and therefore the distinct advantage of a technique for determining S_{crit} that does not rely on simultaneous chemical composition measurements.

The scientific questions addressed by this research are presented in chapter 3. Various hypotheses are outlined, and experiments are presented to prove or disprove the hypotheses. The fundamental question addressed by this work is: 'Can the S_{crit} of monodisperse particles be predicted within experimental uncertainty using measurements of particle growth at RH's between 80 and 92%?' The value of 92% was chosen as this is the highest value that can be accurately controlled in our HTDMA system. The methodology outlined here extends previous work in two major ways. First, it allows S_{crit} to be derived for quasi-monodisperse particle populations composed of pure salts without simultaneous chemical composition measurements. Second, it allows the determination of hygroscopic growth of the sampled dry particles at RH's above 92% by using a thermodynamic model of the osmotic coefficient with correct limiting behavior.

This work has two major components: one involves numerical sensitivity studies, while the other focuses on laboratory experiments. In order to perform the numerical studies, a 'reference' Köhler model of particle growth as a function of RH is required. This model is developed from first principles in chapter 4.

In chapter 5, we explore three simplifications to the reference model: volume additivity of solute and solvent, setting the surface tension of the droplet solution equal to that for pure water, and assuming a simplified version of Pitzer's model of the osmotic coefficient for electrolyte solutions [*Pitzer*, 1973]. A simplified form of Köhler theory

is required that results in as few unknown chemical composition dependent unknowns as possible and still accurately models droplet growth. Minimizing the number of unknown parameters is necessary to insure that the fitting procedure will be successful. We test the sensitivity of predicted values of equilibrium RH to each of the three assumptions. In chapter 5 we show how S_{crit} may be derived from HTDMA study results used in the simplified Köhler model and explore numerically the sensitivity of derived values of S_{crit} to experimental uncertainties in a variety of measureands. We apply the least-squares fitting procedure to perturbed HTDMA data to test the sensitivity of predicted S_{crit} to random measurement uncertainties.

Before presenting results from the laboratory studies, a detailed discussion of the theories of operation of the HTDMA, TGDCC and the various other instruments used in the laboratory studies is given in chapter 6. The experimental uncertainties in each measurement are quantified, and an error analysis is used to determine uncertainties in droplet size and RH. Calibration procedures for the DMA, CPC, RH sensors, and temperature sensors are described. Quality control checks that were performed on the various datasets are also outlined.

In chapter 7, results from the laboratory studies of the hygroscopic growth and CCN activity of particles composed of pure salts, mixed salts and on ambient particles are discussed. The droplet growth results for particles of known composition are used to validate HTDMA operation.

A summary of the disseration work is presented in the final chapter, as well as suggestions for future work.

Chapter 2

Review of Previous Studies of Particle Hygroscopicity and CCN Activity

In this chapter a review of previous studies of particle hygroscopicity and CCN activity is provided. Until the First Aerosol Characterization Experiment (ACE 1) in 1995, there were no hygroscopicity studies that included simultaneous CCN observations. Therefore, except for the results from ACE 1, HTDMA results cannot be quantitatively related to simultaneous CCN observations. The results from previous studies are summarized and shortcomings in present understanding of the factors controlling particle hygroscopicity are discussed. The unavoidable ambiguities in the interpretation of results from previous studies are discussed and serve to help define the scientific questions addressed by this study.

2.1 *Previous Bulk Particle Hygroscopicity Studies*

Some of the first, and most geographically and temporally extensive, measurements of particle hygroscopicity were carried out by *Winkler and Junge* [1972], *Winkler* [1973], and *Hänel* [1976, 1981]. Other similar studies include those by *Sloane et al.* [1986], where impactors were used to examine the hygroscopicity of particles in different size ranges. Our study differs from these investigations in that monodisperse, and

not bulk, particle populations are studied, *in-situ*, and we extend our results beyond determining particle hygroscopic growth to also evaluating CCN activity. However, in some respects, the research presented here is similar to that performed in the aforementioned studies, therefore it is worth reviewing the methods in some detail.

Winkler and Junge [1972], *Winkler* [1973], and *Hänel* [1976, 1981] used impactors to segregate particles smaller than 2 μm from larger particles. The hygroscopic growth of the fine and coarse particle fractions was determined by placing the filter samples inside a weighing chamber equipped with precise humidity control so that the increase in mass attributable to the addition of water to the filter deposit could be measured as a function of RH. Insoluble mass was determined by washing the filter after the growth measurements had been completed to remove all the soluble mass and then re-weighing the filter. Due to the extremely small collected sample mass, the results depended critically on the ability to resolve very small changes in the weight of the filter. Furthermore, during the long collection times employed, it is likely that particles of various chemical compositions were impacted onto the same filter. Since the equilibrium water uptake of an aerosol particle depends upon its chemical composition (dissolved and undissolved), mixing several different solutes from different particles together while exposing them to an environment subsaturated with respect to water is not the same as the *in-situ* equilibrium water uptake of individual ambient particles at the same RH. *Tang* [1997] and *Sangster and Lenzi* [1974] have shown that errors in estimated water uptake between 1 and 6% can occur if it is assumed that the water mass associated with individual solutes in mixed solute solutions may simply be added. Over one hour was typically required at each RH for the weight of the filter to stabilize, indicating that 'burial' of particles under each other on the filter may have inhibited the establishment of an equilibrium between the controlled ambient humidity and the deposited particles. Such long equilibration times required long weighing times (order one day) for each filter for several RH's, and volatilization

of particle mass could have been a problem during collection and weighing.

Table 2.1 contains a summary of the results from several bulk aerosol hygroscopicity studies. Results, in general, agree fairly well with theoretical calculations for the assumed or measured chemical composition. However, a monotonic, smooth increase in hygroscopic growth with increasing RH was typically observed for particle diameters (D_p) less than 2 μm, not the step function type response that would be associated with a pure, externally mixed ammonium salt exhibiting a well defined deliquescence RH. This last result was assumed to demonstrate that the gathered particles were internally mixed with respect to their chemical composition, that is, the individual particles consisted of mixtures of different chemical species. Particles with D_p>2 μm were found to grow to a greater degree than smaller particles, and the observed growth was consistent with a seasalt composition.

Given the bulk collection methods employed, it is not possible to unambiguously extrapolate the single particle chemical mixing state, for example, the distribution of soluble and insoluble material within individual particles, from the observed hygroscopic growth as a function of RH. This is important, since the presence of insoluble material preferentially in larger particles compared to smaller particles would have a much smaller influence on the supersaturation required to activate the particles relative to the supersaturations typically encountered in clouds. As an example, a 40 nm NaCl particle consisting of 100% NaCl will activate and become a cloud droplet at a RH of 100.41%, whereas the same size particle containing only 40% NaCl by mass will activate at 100.8% RH. The 100.1% to 101% RH range is typical of that found in stratus clouds around the globe [*Rogers and Yau,* 1989]. In contrast, a 100 nm NaCl particle with the same volume fractions of NaCl will activate at RH's of 100.1% and 100.3%, respectively, a much smaller range compared to the range of supersaturations found in stratus clouds. Therefore, the ability of a 100 nm NaCl particle to act as a CCN is much less influenced by an insoluble inclusion compared to a 40 nm particle.

In other words, if insoluble material was preferentially found in 40 nm particles, it is more likely that the supersaturation required for activation of these particles would be raised above values typically found in nature; whereas the presence of a similar volume fraction of insoluble material in 100 nm particles would most likely not alter their ability to act as CCN in the same way.

Also listed in Table 2.1 are results from other 'bulk' measurements of particle hygroscopicity, including simple microscope examination [*Meszaros,* 1971], ambient impactors with compositional analysis [*Sloane et al.,* 1986], parallel impactors with one impactor sampling at low RH and the other at high RH [*Heintzenberg and Covert,* 1987; *Covert and Heintzenberg,* 1984], thermal gradient diffusion cloud chambers [*Fitzgerald et al.,* 1982; *Harrison,* 1985], and nephelometer measurements conducted at controlled values of sample temperature and RH [*Rood et al.,* 1987; *Shaw and Rood,* 1990]. Except for the study by *Fitzgerald et al.* [1985], which involved sampling a monodisperse aerosol from a differential mobility analyzer (DMA) into a TGDCC, all of the aforementioned studies were 'bulk' in nature, since they involved observations of integral parameters of the sampled particle population as a function of RH (e.g. light scattering coefficient or hygroscopic mass increase over finite size intervals collected in an impactor).

Results from the aforementioned impactor studies by *Heintzenberg and Covert* and *Covert and Heintzenberg* are different from the findings from the electrobalance/filter studies. The submicrometer aerosol was sampled onto different stages in different impactors at different controlled RHs that allowed the composition of various size ranges and their relative hygroscopicity to be determined. These impactor studies indicated that submicrometer particles were externally mixed with respect to hygroscopic growth and not internally mixed as suggested by *Winkler* [1973] and others. The difference may be due to the different location and time of the impactor and electrobalance studies. The impactor study results are more consistent with HTDMA

study results than with those from bulk studies.

Results from the TGDCC study by *Harrison* [1985] indicate an externally mixed submicrometer particle population with respect to hygroscopic growth, consistent with the impactor studies. Both types of studies were performed predominantly in anthropogenically perturbed conditions. *Harrison* [1985] studied the chemical composition differences between CCN and non-CCN by segregating the populations using a thermal gradient diffusion cloud chamber to grow the CCN and then deposited the droplets, and not the interstitial aerosol, on to a filter. He found that the mean non-CCN mass fraction in Seattle, WA was greater than 50% at a CCN chamber supersaturation of 0.64%, and that both non-CCN and CCN mass fractions contained soot. The TGDCC results are consistent with impactor studies performed in urban locations, and those from remote sites during anthropogenically perturbed periods. These results are also in qualitative agreement with previous HTDMA study results in anthropogenic settings [*Svenningsson et al.,* 1992; *Zhang et al.,* 1993], where insoluble volume fractions on the order of 40-50% were required to reconcile the observed hygroscopic growth with measured water soluble chemical composition.

Results from temperature and humidity controlled nephelometry studies also indicate that, in general, an external mixture of sub-micrometer particles exists with respect to hygroscopic growth. The mixing state of ambient particles with respect to hygroscopic growth, and therefore presumably with respect to chemical composition, is important toward understanding the visibility reducing and cloud nucleating properties of the total particle population.

2.2 *Previous HTDMA Studies*

The first use of the HTDMA to measure particle hygroscopic growth was by *Liu et al.* [1978]. They took advantage of the greater hygroscopic growth of sulfuric acid particles compared to most other particle chemical species in the atmosphere and

constructed a HTDMA system specifically to test for the presence of H_2SO_4 particles in the atmosphere. In the HTDMA a relatively monodisperse aerosol sample is selected from the ambient particle size distribution using one DMA, the sample is exposed to a controlled RH environment, and the RH conditioned size is measured by a second DMA positioned after the RH conditioner. Since this first study by *Liu et al.* [1978], several other HTDMA studies have been performed. The results from all published HTDMA studies, performed at various locations around the globe, are listed in Table 2.2. The major conclusions which can be drawn from these studies are listed below.

For the types of ionic species generally present in the atmosphere (e.g. the various ammonium and sodium salts and sulfuric acid), the range of theoretical growth factors for a pure particle at 85% RH is 1.51 to 1.94, and 1.75 to 2.25 for 90% RH [*Tang,* 1995]. According to Table 2.2, except for the study by *Sekigawa* [1983], almost none of the HTDMA studies report growth factors that could be attributable to particles consisting of pure salts. The lower growth factors observed in the HTDMA studies cannot be attributed to internal mixtures of different soluble salts within individual particles, as particles consisting of such mixtures also would have demonstrated larger growth factors than those observed [*Tang et al.,* 1997]. Errors associated with the HTDMA technique can be discounted based on the observed good agreement (within 5%) between predicted and actual growth when particles of known chemical composition were sampled by the HTDMA. There are at least two possible explanations for the observed, lower growth factors. First, it is possible that the particles consisted of a mixture of soluble salts and insoluble material within the bulk solid phase. This has been the preferred interpretation by previous investigators. Second, it is possible that surface coatings on the particles either enhanced or inhibited the hygroscopic growth of different particles in different ways. A third possibility that must be considered is that some particles consisted of a mixture of insoluble and

soluble material in the bulk phase and other particles may have had hygroscopic or hygrophobic coatings and a uniform bulk composition. These conclusions are significant: they point out that, assuming the sources of insoluble, soluble, and coating materials are distinct, processes in the atmosphere during transport of the particles (e.g. gas-to-particle conversion inside and outside of cloud, coagulation of particles, air mass mixing) and the distribution of different chemical species within individual particles determine their hygroscopic growth. Previous studies have generally done a good job demonstrating that the presence of both soluble and insoluble material within individual particles is needed in order to explain the observed low hygroscopic growth factors. This research avoids the difficulties in explaining the variability of observed hygroscopic growth and CCN activity inherent in methods that rely on measurements of particle chemical composition by inferring the chemical properties from several hygroscopicity measurements.

For almost all HTDMA studies, particularly those in strongly anthropogenically perturbed and in background continental air mass conditions, the sampled particles appear to be externally mixed with respect to hygroscopic growth (e.g. 'less' and 'more' hygroscopic modes are observed). Furthermore, based on the low observed hygroscopic growth factors compared to pure salts, the more hygroscopic mode is assumed to be internally mixed with both soluble and insoluble material. The results from anthropogenically perturbed HTDMA studies are generally consistent with modeling studies performed by *Tang et al.* [1981] that showed an external chemical mixture of the urban aerosol better reproduced the observed variability of the extinction coefficient as a function of RH in Los Angeles. Most previous investigators have assumed that the presence of two hygroscopic modes indicated the particles were externally mixed with respect to chemical composition (Po Valley, Italy; *Svenningsson et al.* [1992]). However, *Svenningsson et al.* [1992] point out that only a very small water soluble volume fraction, for example <7%, or only about a molecular mono-

layer on a 40 nm diameter particle, results in a growth factor for the 'less' hygroscopic mode significantly different from 1.0 at elevated RHs. Although technically externally mixed, particles exhibiting very different amounts of hygroscopic growth, and possibly CCN activity, may have only subtle differences in their chemical compositions that would not be revealed by ion chromatography on filter and impactor samples or electron microscopy chemical analysis techniques.

During severely anthropogenically influenced conditions, smaller (D_p<0.1 μm) particles appear to be relatively less hygroscopic than larger particles (e.g. Los Angeles, Kleiner Feldberg, Japan, Lithuania). This behavior may be primarily due to the proximity of particle sources to sampling sites during polluted conditions and the influence of transformation processes such as heterogeneous condensation and coagulation in determining the observed size and chemical composition dependent hygroscopic response. Recent HTDMA studies by *McMurry et al.* [1996] in Minneapolis, MN showed that the less hygroscopic mode did not grow when humidified to 90% RH, and that the particles in this mode consisted mainly of chain agglomerates, irregular shapes, spheres and flakes, and contained mostly carbon. More hygroscopic particles were liquid droplets that contained sulfur and sometimes carbon or some other ionic species.

In contrast to the above results, preliminary results from ACE 1 HTDMA studies suggest that only a 'more' hygroscopic mode, that does not grow as much as pure salts of ammonium sulfate or sodium chloride, is present during clean marine conditions [*Covert et al.*, 1998; *Berg et al.*, 1998]. Furthermore, during studies conducted in more remote conditions (Grand Canyon, Arctic, Southern Ocean), a variation of hygroscopic growth with particle size is often not observed. Interestingly, observations by *Murphy et al.* [1998] of chemical composition at Cape Grim during ACE 1 indicate that almost all particles larger than 130 nm were mixtures of sea salt, sulfate and calcium or magnesium. They also found that a significant number fraction of the

sampled particles contained organic material.

The role of organics toward determining the hygroscopic nature of a particle, either as a surfactant, coating, or in the bulk particle solid or liquid phases remains a completely open question. *Gill and Graedel* [1983] inferred from bulk studies of water droplets and electron microscope analyses of individual particles that organics can be present as films on these aerosols, and that these films are relatively common. They concluded that such films would generally impede mass transfer across the aerosol surface and increase the lifetime of aerosols in the atmosphere by inhibiting wet deposition and evaporation processes. Organic material in the troposphere was studied by *Duce et al.* [1983], and they found that anthropogenic sources often dominate the atmospheric chemistry of organic material near urban sources, but that better understanding of the biogenically-produced organic aerosol was required in order to understand the global cycle of aerosol organic material. Organics were believed to have played a role in determining the hygroscopic growth in the Po Valley study, which was dominated by anthropogenically-influenced conditions [*Svenningsson et al.*, 1992]. In that study no significant functional dependence of growth on dry particle size was observed, in contrast to results from other studies conducted during polluted conditions. *Hansson et al.* [1990] studied the change in hygroscopic growth of NaCl particles coated with three different organics. They found that the deliquescence RH did not change but that the growth of coated particles was 20% to 60% less than that observed for pure NaCl. They concluded that the organic coating may not have been uniform around the NaCl core, or was permeable to water vapor molecules, to explain why the coated particles were not more hydrophobic. The authors also speculated that the solution surface tension and osmotic coefficient parameters may have been changed for the coated particles and that these changes may have been responsible for the observed change in droplet growth with RH. *Hämeri et al.* [1992] examined the hygroscopic growth of NaCl particles coated with different carboxylic

acids. As in the above study, they found no change in the deliquescence humidity but a slightly decreased (10%) hygroscopic growth for the coated particles. Interestingly, the recrystallization RH was found to be much lower for the coated compared to pure particles. Droplets formed on coated NaCl particles remained as metastable droplets at humidities as low as 35% compared to the 45% recrystallization humidity of pure NaCl. Another observation provides insight to the explanation for this phenomenon. *Hämeri et al.* found that after coating, for RH's between 50 and 70%, the coated particles actually *decreased* in size with increasing RH, a process not observed with pure NaCl particles. These studies show that results of laboratory simulations of coated particles are difficult to interpret and similar behavior should be looked for in ambient particles. New analyses of previous HTDMA results by *Saxena et al.* [1995] indicate that organics substantially alter the hygroscopic properties of inorganic particles, and can either increase or decrease the observed hygroscopicity. A general finding from their study was that organics tended to increase the hygroscopicity of inorganic particles in the nonurban location examined, while organics tended to diminish the hygroscopicity in urban settings.

The growth factors for both the less and more hygroscopic modes, as evidenced in Table 2.2, are surprisingly constant for the various studies despite having been conducted at widely spaced geographic locations around the globe. On the other hand, the relative number abundance in the two modes did vary considerably from site to site. The relative consistency of the growth factors from site to site might simply be due to the fact that almost all studies have been performed in anthropogenically influenced settings with similar particle sources and transformation processes.

Observations made during ACE 1 at Cape Grim, Tasmania between Nov. 19 and Dec. 15, 1995 [*Covert et al.*, 1998] represent the first comprehensive simultaneous CCN-HTDMA dataset. Results suggest that significant differences exist between the hygroscopic response and CCN activity of clean marine and anthropogenically per-

turbed particles, supporting the assumption that hygroscopic response can be used to differentiate CCN activity. The prediction of the CCN concentration from simultaneous chemical composition data and size distributions generally agreed with the actual CCN concentration to within 10-20% during clean marine conditions when the chemical composition was dominated by a few identifiable compounds [*Covert et al.*, 1998]. However, the chemical samples were obtained over much longer time periods (several hours) compared to the time resolution of the HTDMA studies for a given size. Large differences (e.g. factor 2) were found between predicted and actual CCN concentrations during anthropogenically perturbed situations when the particle chemical composition was much more complex and also during clean marine conditions that had been weakly influenced by continental sources [*Covert et al.*, 1998]. The poorer agreement between predicted and observed CCN concentrations for particles having more heterogeneous chemical composition illustrates one potential advantage of our new approach that does not rely upon simultaneous chemical composition measurements.

Besides the study by *Covert et al.*, there have been a few studies [*Svenningsson et al.*, 1992; *Weingartner et al.*, 1997] where S_{crit} was derived using HTDMA measurements. A major limitation of the studies by *Covert et al.* and *Svenningsson et al.* was that knowledge of the chemical composition of the monodisperse particles was required in order to derive S_{crit}. In all of the studies, the osmotic coefficient was assumed to be constant with RH. The osmotic coefficient, Φ, is a thermodynamic parameter used to model non-ideal solution behavior and is important for the concentrated droplet solutions encountered in HTDMA measurements. Assuming $\Phi = 1$ or that it is constant with RH may not be valid, even at the critical supersaturation, for particle sizes and chemical compositions of atmospheric relevance. In the study by *Covert et al.*, the composition of the 50 nm particles sampled by the HTDMA was estimated by assuming the chemical composition was either sulfuric acid or ammonium

bisulfate based on chemical data for the 100-to-200 nm size range. An accounting for internally mixed insoluble material was made by comparing the observed growth with that for pure sulfuric acid and ammonium bisulfate particles and attributing any observed lower growth to an insoluble fraction. The effect of the osmotic coefficient value not equaling unity was unavoidably lumped together with the estimate of the insoluble fraction. *Svenningsson et al.* made basically the same assumptions in analyzing HTDMA results from the Kleiner Feldberg experiment. The major difference was that a mixture of $(NH_4)_2SO_4$ and NH_4NO_3 was assumed, based on simultaneous chemical composition data. *Weingartner et al.* [1997] used a dilute limit form of the Köhler theory, and extrapolated the observed growth to estimate S_{crit} values between 0.8 and 2.7% for combustion particles with diameters between 50 and 110 nm. Simultaneous CCN measurements were not made by *Weingartner et al.* [1997].

2.3 *Previous CCN Activity Studies*

The focus of this review of historical studies of CCN activity will be on work where the CCN observations were associated with simultaneous chemical measurements.

It could be argued that deriving S_{crit} from a simplified version of the Köhler equation is invalid since the CCN measurements themselves assume the validity of the Köhler equation. This argument stems from the use of Köhler theory by investigators to calibrate the CCN counter thermal gradient diffusion chamber supersaturation against a calculated critical supersaturation corresponding to a dry particle of given chemical composition. In this work, the supersaturation in the CCN chamber is calculated independently of the droplet activation process using the chamber surface temperatures alone. Furthermore, previous work by *Gerber et al.* [1977] showed that dry particles of known size and chemical composition did activate to cloud droplets at threshold supersaturations in their CCN instrument that agreed well with Köhler theory, providing experimental verification of Köhler theory.

Hoppel [1979] studied the size distribution and CCN activity spectrum of particles during a transit across the Atlantic ocean and through the Mediterranean sea. Using a thermal gradient diffusion cloud chamber, he measured the critical supersaturation required to nucleate ambient monodisperse particles selected by a DMA. In general, ambient particles had larger dry nuclei sizes for a given critical supersaturation compared to laboratory particles composed of pure inorganic salts, implying that insoluble material or a hygrophobic coating was present on the ambient particles. Similar to the method proposed here, *Hoppel* [1979] used the CCN measurements on monodisperse particle populations to infer unknown chemical composition dependent properties of the dry nuclei. However, he used supersaturated conditions to do so, whereas we use subsaturated conditions. Furthermore, only one monodisperse particle size was studied for the entire parent population, even though it is probable that the particle chemical composition varied over the size range of particles contributing to the CCN activity spectrum. Therefore, the CCN activity spectrum resulting from the entire size distribution was characterized by the CCN activity of a relatively narrow size range of particles at the peak of the number distribution. Uncertainties in the CCN activity spectrum predicted from the ambient size distribution observations were on the order of 20%.

A recent study by *Cruz and Pandis* [1997] investigated the ability of monodisperse, single component particles composed of carboxylic acids and dioctylphthalate (DOP) in the 50 to 150 nm size range to act as CCN in a TGDCC. Carboxylic acids have been observed by *Rogge et al.* [1993] to constitute a significant fraction of the organic component of the ambient aerosol in the Los Angeles area. *Cruz and Pandis* found that particles composed of the two hygroscopic organics they studied, glutaric acid and adipic acid, were able to act as CCN at supersaturations between 0.3 and 1.0%, while DOP particles showed no CCN activity at supersaturations up to 1.2%. This is the first known study of the CCN activity of pure organic particles, and the most

striking conclusion is that some secondary organic particles are as effective at acting as CCN as inorganic salts, supporting the finding of *Novakov and Penner* [1993] that organic particles contributed significantly to observed ambient CCN concentrations. Results from *Cruz and Pandis* also suggest that organics with characteristics similar to DOP may not be effective CCN.

Leaitch et al. [in press] studied the CCN activity of ambient particles believed to have been influenced by oxidation of pinene vapors emitted by vegetation. Simultaneous gas-phase terpene and particle size distribution measurements in the 6 to 200 nm size range allowed the authors to infer that particle production and growth from organic vapor precursors had occured. They observed that the particles were active as CCN at supersaturations of 0.3%, a value commonly found in ambient clouds.

Podzimek et al. [1991] doped 425 nm NaCl particles with 60 nm carbon particles containing 0.8% sulfur by weight and investigated the supersaturation required to activate the doped compared to undoped salt particles. They found critical supersaturations for the 60 nm carbon particles between 0.7% and 1%, about twice the value expected for similarly sized, inorganic salt particles. The undoped NaCl exhibited a critical supersaturation around 0.012%, while the doped NaCl had a critical supersaturation only 3% lower. It was not clear from the study whether such a small observed change in critical supersaturation was greater than the uncertainty in S_{crit}. Intuitively one might expect that the addition of the carbon particles (insoluble carbon) would result in a larger decrease in the critical supersaturation required to activate the doped NaCl particles. The effect was reduced due to the large particle sizes studied and the addition of a small amount of soluble mass associated with the carbon particles themselves. *Podzimek et al.* [1991] state that the influence of insoluble material on the equilibrium RH would be greater for smaller haze droplets at subsaturated conditions and for smaller soluble nuclei. Interestingly, microscope studies of deposited droplets from the experiments revealed that the carbon parti-

cles existed both at the droplet surface and within the droplet, similar to findings of deposited natural cloud and haze droplets [*Podzimek et al.*, 1991].

Hagen et al. [1986] have looked at the condensation coefficient for water droplets growing in a cloud simulation chamber. They found that repeated, simulated cloud cycles on the same nuclei in their chamber resulted in lower condensation coefficients during the initial activation period in later cycles compared to the first cloud cycle. That is, once the nuclei had participated in one expansion and experienced one condensation cycle, in subsequent expansions the effectiveness of water condensation on the same nuclei was reduced. They speculated that contamination could have played some role in the observed behaviour. Another explanation is that the condensation process during the first expansion 'rearranged' the chemical constituents in the nuclei. If hygrophobic material was present, after the first condensation process it may have been located preferentially at the particle surface where it could more effectively inhibit subsequent water condensation.

Hallett et al. [1986] studied the ice and cloud nucleation properties of several carbonaceous particles derived from the combustion of fossil fuels. They found the highest critical supersaturations were required for paraffin wax particles, while acetylene combusted with excess oxygen and sooty acetylene smoke each had similar CCN activity spectra. In aging studies, they found that over time (e.g. 2 days) the ratio of CCN to the total particle concentration increased for all fuel types, presumably due to coagulation producing more viable CCN through the mixing of hygroscopic and hygrophobic material. In general, these investigators found that a significant fraction of the combustion aerosol were active as CCN, even at supersaturations as low as 0.05%.

2.4 *Summary*

Studies of the hygroscopic growth of bulk particle samples reported in the literature tend to show a smooth increase of particle water uptake with RH, suggesting that the sampled particles are either internally mixed, or consist of species that do not deliquesce (for example, acids). However, bulk sampling techniques mix particles of different chemical compositions together so that the effects of changes in chemical composition with particle size on hygroscopic growth and CCN activity cannot be discerned using bulk hygroscopicity measurements. Furthermore, the CCN concentration at any given water supersaturation is often very sensitive to the size distribution shape and size-dependent chemical properties over a relatively narrow size range of particles. Therefore, methods for exploring the relationships between the total particle and CCN populations must independently examine several narrow size ranges of the total particle population.

Numerous HTDMA studies have been performed over the last two decades. During extremely clean air mass conditions a single hygroscopic mode is often observed, but even this single mode is found to grow less than particles composed of pure salts studied in the laboratory. This suggests that even in clean marine air masses, particles are likely to be composed of mixtures of materials, possibly including biogenic organics, some of which are less hygroscopic than inorganic salts. Alternatively, particles may be composed only of organic material with lower hygroscopicity than pure salts.

Most HTDMA hygroscopicity studies have been conducted during anthropogenically perturbed conditions and two growth modes, 'less' and 'more' hygroscopic, are almost always observed at each of the sub-500 nm sizes examined. It has been inferred from these results that the chemical composition of the sampled monodisperse particle populations may be divided into externally mixed sub-populations, and the more hygroscopic sub-population is also almost always found (assumed) to be an internal

mixture including some inactive, or insoluble, material. This complicated hygroscopic response reveals the complex nature of the chemical composition of ambient particles with respect to hygroscopic growth and points to the difficulty of quantifying the particle composition so that the hygroscopic growth results may be extrapolated outside of the RH range of the measurements. These findings suggest that in order to understand the processes controlling the water nucleating properties and CCN activity of ambient particles, the distribution of water soluble and insoluble chemical species within individual particles must be measured. Current measurement techniques are not capable of revealing such a complex chemical composition for the submicrometer size range of interest. Therefore, obtaining sufficient chemical and morphological information for a population of particles to reliably determine S_{crit} would, in general, be an extremely difficult undertaking.

Previous CCN studies relevant to this work have involved TGDCC measurements on particles of known composition, on particles composed of mixtures of salts and carbonaceous material, and on ambient particles. Results suggest that adding carbonaceous material to salt particles, may, or may not, significantly influence the particle's S_{crit}. The magnitude of the effect most likely depends upon the soluble content of the carbonaceous material, its molecular properties, and whether the added material can form a relatively impervious hygrophobic coating around the salt particle. Particles produced by biomass burning, composed of certain carboxylic acids, and influenced by condensation of biogenic organic vapors, appear to have S_{crit} values similar to supersaturations found in ambient clouds. This is consistent with several HTDMA studies [*Pitchford and McMurry*, 1994; *McMurry et al.*, 1996; *Covert and Heintzenberg*, 1993] that found carbon in both the less and more hygroscopic growth modes.

The next chapter describes the specific scientific questions, hypotheses and experiments that are undertaken to validate the proposed method for determining S_{crit}.

Table 2.1: Summary of previous particle hygroscopicity studies using various methods in both clean and influenced maritime (CM & IM) and continental conditions (CC & IC). EB = Electrobalance, TGDCC = Thermal gradient diffusion cloud chamber, Mic = Microscope ($D_p$larger than 1 μm), Imp = Parallel impactor samplers, one at 35% and the other at 90% RH, and Humido = Temperature and humidity controlled nephelometer. '-' implies not observed. 'I' = internally mixed, 'E' = externally mixed chemical composition. 'All' = all conditions or RH range 0 to 95 %. 'Var' = function of location, chemical composition, and D_p. A less hygroscopic particle subpopulation, if observed, is designated as 'Less Hygro', while a more hygroscopic population is designated as 'More Hygro'. Simultaneous chemical measurements designated by 'Y' in 'Chem Meas.' column. Size range of all studies except EB studies was between 100 and 1000 nm.

Study	Method	Location (cond.)	Study RH (%)	Less Hygro	More Hygro	Inferred Mixture	Chem. Meas.
1	EB	?	All	-	f(chem)	E,I	N
2	EB	?	All	-	f(chem)	E,I	N
3	EB	All	All	Var	Var	E,I	N
4	EB	All	All	Var	Var	E,I	N
5	Mic	IC	All	-	Var	?	N
6	Imp	Arctic	35-90	Carbon	Sulfur	E	Y
7	Imp	IC	35-90	Carbon	Sulfur	E	Y
8	TGDCC	IC	-	?	f(D_p)	?	N
9	TGDCC	IC	-	Var	Var	E	Y
10	Imp	IC	All	Var	Var	E	Y
11	Humido	IC	All	-	-	E	Y
12	Humido	IC,CC	All	-	-	E	Y

1. *Winkler and Junge* [1972]

2. *Winkler* [1973]; Hygroscopicity variable; concluded particles greater than 2 microns μm externally mixed; smaller internally mixed.

3. *Hänel* [1976]; Extended findings of *Winkler* [1973].

4. *Hänel and Lehmann* [1981]; Hygroscopicity variable; evidence for hysteresis; $D_p > 2$ μm hygro. different than $D_p < 2$ μm .

5. *Meszaros* [1971]; Hygroscopicity results dependent upon $D_p$and season.

6. *Heintzenberg and Covert* [1987]; AGASP I; particles retain hygroscopic, mass mode, chemical properties after 5000 km transport from Europe.

7. *Covert and Heintzenberg* [1984]; Stockholm; results correlate with AGASP I; Sulfur and Metals in more hygro. fraction.

8. *Fitzgerald et al.* [1982]; smaller $D_p$more hygroscopic, opposite most other studies.

9. *Harrison* [1985]; 57% of CN mass not CCN; Hygroscopicity results dependent upon $D_p$and chemical composition; equal soot in both fractions.

10. *Sloane et al.* [1986]

11. *Rood et al.* [1987]

12. *Shaw and Rood* [1990]; Riverside, Grand Canyon, Mojave Desert; observed crystallization RH 30% of time.

Table 2.2: Summary of previous HTDMA studies in both clean and influenced maritime (CM & IM) and continental conditions (CC & IC). Other acronyms are the same as in Table 2.1. The size ranges of particle samples depends on the individual study, but the 30 to 200 nm size range is representative of the sizes sampled.

Study	Location (cond.)	Study RH (%)	$\frac{D_{drop}}{D_{p,sol}}$ Less Hygro	$\frac{D_{drop}}{D_{p,sol}}$ More Hygro	Inferred Mixture	Chem. Meas.
a	IC	80	-	1.2-1.8	I	N
b	IC	90	1.0	1.12-1.49	E	Y
c	IC	90	1.07	1.38-1.44	E	Y
d	CC,IC	85	1.15	1.36-1.51	E,I	Y
e	CC,IC	90	1.05	1.44-1.48	E	Y
f	IC	-	-	-	E	N
g	IC	85	1.1	1.44	E	Y
h	IC,CC	85	1.02-1.11	1.34-1.37	E,I	Y
i	CC,IC	85	1.15	1.43	E,I	Y
j	IC	79	1.02	1.3	E,I	N
k	CM,IM	50,85	1.1	1.4	E,I	Y
l	All	90	1.1	1.5	E,I	Y
m	IC	90	1.0	1.4	E	Y
n	Lab	80-97	1.0	0.94	I	Y

a. *Sekigawa* [1983]; Insoluble fraction varies with D_p.

b. *McMurry and Stolzenburg* [1989]; Los Angeles (SCAQS); larger $D_p$more hygroscopic (1.33x)

c. *Covert et al.* [1991]; Carbon in less hygroscopic fraction.

d. *Zhang et al.* [1993]; Grand Canyon winter 1990 (NGS and SCAQS); insoluble inclusions; hygroscopicity was a function of [Ions]/[Carbon].

e. *Covert et al.* [1993]; Sulfur and Carbon in more hygroscopic fraction.

f. *Juozaitis et al.* [1993]; high soot; observed hydrophobic size distribution
60% hydrophobic fraction at 0.02 μm , 15% at 0.05 μm , 4% at 0.45 μm .

g. *Svenningsson et al.* [1992]; potential large organic influence; hygroscopic growth not f(D_p) significant insoluble fraction in both modes.

h. *Svenningsson et al.* [1994]; 50% of CN concentration non-hygroscopic.

i. *Pitchford and McMurry* [1994]; NGS and SCAQS; 85% of CN volume in non-hygroscopic fraction non-soluble.

j. *Liu et al.* [1978]; Minneapolis, MN; focused on H_2SO_4.

k. *Berg et al.* [1998]; ACE-1 study; *Discoverer*

l. *Covert et al.* [1998]; ACE-1 study; Cape Grim

m. *McMurry et al.* [1996]; less hygroscopic = C chains, more hygroscopic = liquid drops with S and some C.

n. *Weingartner et al.* [1997]; Combustion particles; Particles shrink with increasing RH.

Chapter 3

Proposed Questions, Hypotheses & Experiments

3.1 *Introduction*

The scientific questions addressed by this research are presented in this chapter. Hypotheses are outlined and specific experiments, both numerical and in the laboratory, are described to prove or disprove each hypothesis.

3.2 *Scientific Questions*

The fundamental question addressed by this research is this: 'Can the critical supersaturation of particles of known size be determined from chemical composition-dependent parameters derived from fitting a simplified Köhler theory model to numerically simulated and measured hygroscopic growth?' The goal of answering this question is to demonstrate the feasibility of a new technique for quantifying the cloud droplet nucleating potential of particles using their hygroscopic growth at relative humidities between 80 and 92%. If feasible, the technique will allow the contribution of monodisperse particle sizes to the CCN activation to be determined without simultaneous chemical composition measurements. Relating specific particle sizes to the CCN spectrum is an important step towards determining how different sources of particles, anthropogenic and natural, contribute to CCN and reducing uncertainties

in estimates of the indirect effect of particles on climate.

3.3 *Hypotheses & Experiments*

Our hypothesis that S_{crit} can be accurately predicted from hygroscopic growth data for particles composed of single, internally mixed, and externally mixed pure salts is tested in several ways and on several different types of particles.

3.3.1 Single Solutes

First, numerical tests are performed to examine the feasibility of the proposed idea. Our initial hypothesis is that S_{crit} can be predicted within experimental uncertainties for NaCl, NH_4HSO_4, $(NH_4)_2SO_4$, NH_4NO_3, and H_2SO_4 particles with diameters of 40 and 100 nm using numerically generated HTDMA data with assumed uncertainties equal to those encountered during laboratory HTDMA measurements. The feasibility of the proposed method for deriving S_{crit} from HTDMA data must be tested numerically before actual laboratory HTDMA experiments. These studies are also necessary to evaluate the accuracy and precision in RH and D_{drop} measurements required for the laboratory measurements relative to deriving accurate values of S_{crit}. Calculations are performed using the full Köhler model first to accurately compute the hygroscopic growth of particles with the aforementioned compositions. The growth factors are used as input to the regression code to derive 'theoretically' predicted values of S_{crit}. Values of S_{crit}-derived from numerically modeled hygroscopic growth with assumed uncertainties in the input data are compared to the theoretically perfect values from the full Köhler model. Agreement between the values of S_{crit} from the two calculations within experimental uncertainty in S_{crit} constitutes proof of our hypothesis that the proposed regression technique can predict S_{crit} using numerically simulated HTDMA results for known compcsitions.

After demonstrating that the technique works for the pure salts listed above, vari-

ous other chemical compositions, listed in Table 3.1, are studied in the same manner. The limits of applicability of the regression model are determined by comparing theoretical and modeled values of S_{crit}.

To test our hypothesis that S_{crit} can be determined from chemical composition dependent parameters derived from the fit technique using measured hygroscopic growth in the laboratory, combined measurements of droplet growth and CCN activity are undertaken. A HTDMA system is assembled in the laboratory for testing. Proper RH and temperature control are verified. Studies with no humidification are conducted to test the TDMA data inversion routine and to quantify the experimental precision of particle size measurements. Droplet growth is measured at various humidities with NaCl and $(NH_4)_2SO_4$ particles, and observed growth compared to theoretical predictions. A CCN instrument is used to measure S_{crit} for the same particles sampled in the HTDMA system. Tests of particle losses and the diffusion chamber top and bottom plate temperature difference in the CCN instrument are performed. The operation of the CCN instrument is verified by sampling various monodisperse aerosol of known chemical composition while the device is operated at constant chamber supersaturation and observing the dry particle size ($D_{act,50}$) where 50% of the input particles are activated to droplets. For the observed value of $D_{act,50}$ and the known particle chemical composition, the value of S_{crit} is calculated. The instrument supersaturation compared to the value of S_{crit} predicted by Köhler theory for each composition. A second technique is also used to evaluate an experimental value for S_{crit}. In this technique, a constant, monodisperse particle size of known composition is sampled by the CCN instrument and the chamber supersaturation varied to determine the supersaturation where 50% of the sampled particles are activated to droplets. Measured values of S_{crit} are compared to values derived from the fit technique and droplet growth measurements in the laboratory, and to theoretical values for the known particle size and chemical composition.

Results from the sensitivity studies above are used to refine the experimental methods where necessary. Once the HTDMA system operation has been validated, the hygroscopic growth of the particle types listed in Table 3.1 is measured. The monodisperse size from DMA1 is kept constant during each HTDMA/CCN study. Hygroscopic growth is measured at several RH's between 78 and 92% on the monodisperse particles from DMA1. The input size to the CCN instrument is held constant and the chamber supersaturation varied from a value where the fraction of the input particles active as CCN is greater than 0.75 to a value where fewer than 20% of the input particles are activated to droplets. The chamber supersaturation where 50% of the input particles are activated to droplets is defined as the experimentally measured value of S_{crit}. The D_{drop} and RH values from the HTDMA measurements are then used in the fit routine to derive a value of S_{crit} for the particles under study. Agreement between the values of S_{crit} determined from the CCN runs, those from the full Köhler theory, and those from the fit routine using HTDMA experimental results within experimental uncertainties in S_{crit} constitutes proof of our hypothesis for the chemical compositions examined.

3.3.2 Externally and Internally Mixed Solutes

As discussed in chapter 2, ambient particles are often combinations of external and internal mixtures of a variety of chemical species. Our hypothesis is that accurate values of S_{crit} can be derived using the proposed regression technique for the externally and internally mixed particles involving the solutes listed in Table 3.1. As discussed above, the feasibility of the method will be examined both numerically and in the laboratory through measurements on externally and internally mixed particle chemical compositions.

Laboratory studies are conducted in a manner similar to those outlined above, except that two atomizers are operated in parallel and their output flows mixed

together to create externally mixed particle populations. One atomizer is used to generate NaCl and the other to generate $(NH_4)_2SO_4$. The CCN counter is unable to differentiate between droplets formed on NaCl and $(NH_4)_2SO_4$ particles, therefore, simultaneous CCN measurements are not expected to reveal the values of S_{crit} associated with each individual composition. However, simultaneous CCN measurements are conducted to evaluate an experimental value of S_{crit}. This limitation to the CCN measurements points out one of the advantages of using hygroscopic growth to derive individual values of S_{crit} for mixed particle populations, something that cannot be accomplished using the CCN counter. The hygroscopic growth of the externally mixed, monodisperse particles is measured at several RH's between 80 and 92%. Due to the difference in growth of NaCl and $(NH_4)_2SO_4$ particles, different S_{crit} values are derived for the two populations of particles. The derived values of S_{crit} are compared to the previously measured S_{crit} values for NaCl and $(NH_4)_2SO_4$ from the CCN runs. Agreement between values of S_{crit} from the CCN runs, those from theory, and those derived from HTDMA measurements on the externally mixed particles constitutes proof of our hypothesis that the proposed technique can differentiate between particles of different chemical composition that are externally mixed, and that accurate values of S_{crit} can be derived independently for each particle sub-population.

Simultaneous HTDMA growth and CCN measurements are conducted on internally mixed NaCl and $(NH_4)_2SO_4$ particles atomized from an equimolar solution containing both salts. Numerical and laboratory studies are conducted as outlined above for particles containing single salts.

3.3.3 Ambient Particle Samples

Having tested the proposed method in the laboratory on the various particle types discussed above, the final application is to ambient particles of unknown chemical composition to evaluate the feasibility of deriving S_{crit} for these particles. As with the

laboratory studies discussed above, simultaneous CCN measurements are conducted. If the sampled particles are externally mixed with respect to hygroscopic growth, and one of the growth modes is essentially non-hygroscopic, then all of the droplets observed in the CCN device may be attributed to the more hygroscopic mode. In this case, the value of S_{crit} derived from the CCN observations should be directly comparable to that derived from HTDMA measurements. If the ambient particles are externally mixed and the observed growth modes are both hygroscopic, as in the case with the external mixture of NaCl and $(NH_4)_2SO_4$, then it will be impossible to partition the observed CCN droplet number to the two different hygroscopic modes. Furthermore, defining the CCN-derived value of S_{crit} by when the ratio of CCN-to-input particles is 0.5 may be inaccurate. In this case, the value of S_{crit} derived from CCN measurements is more difficult to compare to that from HTDMA measurements.

There is an important difference between the laboratory studies described above and those using ambient particles: the chemical composition is truly unknown and must be assumed to vary with particle size and time for the ambient particle samples. Furthermore, monodisperse particle number concentrations will be between one and two orders of magnitude lower during ambient samples compared to experiments where laboratory particles are generated. The low concentrations will be an important consideration for the CCN measurements, as the sample volume of this instrument is only 0.006 cm^{-3}. The lower number concentrations increase the amount of time required to count a significant number of droplets in the CCN counter. The longer the period of time required to complete the CCN study, the greater the likelihood that changes have occured in the ambient particle characteristics.

3.4 *Summary*

The scientific question addressed by this work, whether values of S_{crit} may be derived from hygroscopic growth measurements, will be examined for particles composed of

various pure salts, external and internal mixtures of salts and for ambient particles of unknown chemical composition. The experiments to test our hypotheses have been outlined and are discussed in greater detail in chapter 6. In the next chapter, the theory required to calculate droplet growth for given particle size and chemical composition is presented.

Table 3.1: Particle chemical compositions examined in this work.

Compositions Studied Numerically
NaCl
$(NH_4)_2SO_4$
NH_4HSO_4
NH_4NO_3
H_2SO_4
Internally mixed NaCl-$(NH_4)_2SO_4$
Internally mixed NaCl-NH_4NO_3
Internally mixed NaCl-Na_2SO_4
Internally mixed $(NH_4)_2SO_4$-NH_4NO_3
Compositions Studied in Laboratory
NaCl
$(NH_4)_2SO_4$
NH_4HSO_4
Internally mixed NaCl-$(NH_4)_2SO_4$
Externally mixed NaCl-$(NH_4)_2SO_4$
Ambient Aerosols

Chapter 4

Development of the Theory Describing the Equilibrium Between A Particle and Its Humid Environment

4.1 *Introduction*

In this chapter we derive the relation describing the equilibrium between the water vapor phase and liquid water droplet containing a single, completely dissolved chemical species. Partially-dissolved salts are not treated in the present work. The goal is to derive a form of the Köhler equation applicable to the particle types studied in this work that have been listed in Table 3.1. Once the generalized Köhler equation is derived for a particle composed of a single salt, the relations are derived that allow internally mixed compositions to be treated. Although we focus here on the nucleation of water droplets, the equations are applicable to any compound undergoing a vapor-to-liquid phase change process. The Köhler equation describes the equilibrium between a particle that has taken up water and its humid environment, and is the focus of this work. First we derive the equation describing the change in Gibbs free energy (G) from basic principles for the general case of a particle containing one soluble compound. The general expression for G demonstrates how the droplet surface tension, molar volume and solution osmotic coefficient enter into the final form of the

Köhler equation used in HTDMA studies.

4.2 *Nucleation of Water Droplets: the Gibbs Free Energy Change*

We require an equation to compute the vapor pressure of pure water over the curved surface of a droplet containing one soluble salt. We assume that the salt species in the droplet are not present in the vapor phase. However, we note that, given the volatile nature of some soluble materials, particularly organic compounds, the possibility of their presence in the vapor phase should be kept in mind. Our system, defined as a droplet solution and the surrounding vapor, constitutes two 'bulk' phases. We assume that the salt is completely dissolved within the droplet.

According the Gibbs phase rule [*Pruppacher and Klett,* 1997; *hereafter referred to as 'PK97'*], the number of free parameters, f, that completely specify the thermodynamic equilibrium of a water droplet formed on a salt particle in equilibrium with humid air is defined as

$$f = 1 + Number\ of\ Component\ Substances\ in\ System \tag{4.1}$$

which, for the system studied here, may be written as

$$f = 1 + \ Salt \ + \ Air \ + \ Water. \tag{4.2}$$

For example, in a droplet containing one or more salts, the degree of freedom of the system is four. However, the total amount of solute in the droplet is assumed to be constant since the solute is non-volatile and completely dissolved. Therefore, the mole fraction of water in solution can be determined from the drop radius and known amount of solute, constituting another constraint on the system and reducing the degrees of freedom so that $f = 3$.

For this work, we will assume that the largest degree of freedom encountered will be three. The total gas pressure (atmospheric pressure) and temperature are

held constant, leaving one intensive variable free to define the droplet equilibrium. Therefore, we can vary the relative humidity and examine the dependence of the droplet size on RH. This is precisely the sort of experiment that will be the focus of the empirical studies conducted for this research.

4.2.1 The Gibbs Free Energy, G

In this section we review some fundamental thermodynamic principles related to the Gibbs free energy [*PK97*]. The Köhler equation is derived by evaluating the maximum change in Gibbs free energy for the adsorption of water vapor by an initially water-free particle. Therefore, we must find an expression for ΔG and minimize its derivative with respect to the moles of water in the droplet. We relate G to the 'i' components of our system via the definition of the chemical potential

$$\mu_i = \left(\frac{\partial G}{\partial n_i}\right)_{p,T,n_{j,j\neq i}}. \tag{4.3}$$

The total Gibbs free energy for a hypothetical, binary mixture may be written

$$G = \mu_i n_i + \mu_j n_j. \tag{4.4}$$

This expression may be extended to as many components as are present in the system. Differentiating the above relation, we find

$$dG = n_i d\mu_i + n_j d\mu_j + \mu_i dn_i + \mu_j dn_j. \tag{4.5}$$

From the first law of thermodynamics, an alternative definition of the Gibbs free energy is

$$dG = -SdT + Vdp + \mu_i dn_i + \mu_j dn_j. \tag{4.6}$$

For the system we are considering here, temperature and pressure are assumed to be constant, so that

$$dG = \mu_i dn_i + \mu_j dn_j \tag{4.7}$$

Since G is a state function, and therefore does not depend on the thermodynamic path between the initial and final states of the system, the two different relations for dG derived above must be equal

$$\mu_i dn_i + \mu_j dn_j = n_i d\mu_i + n_j d\mu_j + \mu_i dn_i + \mu_j dn_j \tag{4.8}$$

which reduces to

$$n_i d\mu_i + n_j d\mu_j = 0 \tag{4.9}$$

which is a special case of the Gibbs-Duhem relation for a two component (i.e. water and one solute) system at constant temperature and pressure. The purpose in deriving this last relation is to explicitly demonstrate that the chemical potentials (and other partial molar properties) of a mixture cannot change independently. If one decreases, then the other must increase. In other words, component properties in mixtures interact and influence each other. In the following sections we use the above relations for G to define the Gibbs free energy of the initial and final states of our system. We then combine these relations to derive a generalized Köhler equation.

4.2.2 Derivation of the Change in Gibbs Free Energy, ΔG

We desire an expression describing the change in G as a dry particle surrounded by water vapor and air in the initial state becomes a droplet solution surrounded by water vapor and air in the final state. Contributions to ΔG must be accounted for from water in the vapor phase as well as the soluble substances in the liquid phase. Although air is also a component of the system, we assume that it does not participate in the change in Gibbs free energy since neither the chemical potential nor the number of moles of air change during the condensation process. The Henry's Law constant for O_2 is small enough that dissolution of oxygen can be neglected [*Seinfeld,* 1986]. G for the initial state may be written:

$$G_i = n_w^v \mu_w^v + n_s^s \mu_s^s + \sigma_s^{sv} A_s^{sv} \tag{4.10}$$

where G is the Gibbs free energy per mole. Superscripts refer to phase, 'v' denotes the vapor phase, 's' denotes the solid phase, and 'sv' denotes the solid/vapor interface. Subscripts denote components, 'w' denotes water, and 's' denotes soluble salt material. n_w^v and μ_w^v are the number of moles and chemical potential of water in the vapor phase, respectively. n_s^s is the number of moles of soluble material in the solid phase. μ_s^s is the chemical potential of the soluble material in the solid phase. σ_s^{sv} is the interfacial surface tension of the soluble material in the solid phase. A_s^{sv} is the solid/vapor interfacial area of the soluble compounds. In general, the above relation for the Gibbs free energy can be written for a particle containing several different salts. In this case, each term with a superscript 's' and 'sv' would require a summation over all of the individual components for each of the solutes.

The final state consists of a droplet solution surrounded by water vapor and air. We assume that the salt is fully dissociated in solution, and explicitly account for the vapor/solution interface between the drop and surrounding air/water vapor mixture. G for the final state may be written

$$G_f = n_w^l \mu_w^l + n_s^l \mu_s^l + \sigma_d^{lv} A_d^{lv} + (n_w^v - n_w^l)\mu_w^v. \tag{4.11}$$

In the above relation, the number of moles of liquid water in the droplet embryo is n_w^l, and the number of moles of soluble material in solution is n_s^l. Again, superscripts refer to phase, with 'l' denoting the solution. 'lv' designates the liquid/vapor interface and should not be interpreted as a separate phase. Subscripts refer to components as described above, 'd' refers to the droplet liquid solution. μ_w^l is the chemical potential of water in the solution, and μ_s^l is the chemical potential of the salt in the solution.

The overall change in the Gibbs free energy associated with the formation of a droplet embryo including all of the phases discussed above may be determined by subtracting G_i from G_f:

$$\Delta G = G_f - G_i = n_w^l(\mu_w^l - \mu_w^v) + n_s^l(\mu_s^l - \mu_s^s) + \sigma_d^{lv} A_d^{lv} - \sigma_s^{sv} A_s^{sv}. \tag{4.12}$$

To simplify the above relation for ΔG the interfacial terms may be written

$$\Delta G = n_w^l(\mu_w^l - \mu_w^v) + n_s^l(\mu_s^l - \mu_s^s) + \pi D_{drop}^2 \sigma_d^{lv} - \pi D_{p,sol}^2 \sigma_s^{sv} \tag{4.13}$$

where D_{drop} is the droplet diameter and $D_{p,sol}$ is the dry particle diameter. In the above relation is is assumed that the dry particle is spherical. The actual particle surface area may be larger than the sphere-equivalent diameter due to surface irregularities. In the following sections, the contributions to ΔG by each component are determined.

4.2.3 Contribution by Water Substance to ΔG

In order to express the above equation for ΔG in terms of known and measurable quantities, the differences in the various chemical potentials must be known. For water substance, we can derive an equation expressing the difference in potentials in terms of vapor pressures using the equilibrium relation for the derivative of the chemical potential with respect to pressure at constant temperature:

$$\left(\frac{\partial \mu}{\partial p}\right)_T = \nu_l \tag{4.14}$$

where ν_l is the molar volume of water and we assume the condensation process occurs at constant temperature. The difference in chemical potentials μ_w^l and μ_w^v of pure water in the liquid and vapor phases, respectively, may be written

$$\frac{\partial}{\partial p}(\mu_w^l - \mu_w^v) = \nu_w^l - \nu_w^v \approx -\nu_w^v = -\frac{RT}{p} \tag{4.15}$$

under the assumption that $\nu^v \gg \nu^l$ [*PK97*] and that the vapor behaves ideally. R is the universal gas constant and T is the droplet temperature. *PK97* have studied the validity of the assumption of ideality for temperatures between -30°C and 30°C and pressures between 1100 and 300 mb, and found that the deviation was less than 0.2%. We consider an isothermal condensation process between an initial state, $p_i = p_s$, the saturation vapor pressure of water over a flat surface of pure water, and a final state,

$p_f = p_w^g$, the partial pressure of water vapor over a droplet of pure water. In the initial state $\mu_w^l = \mu_w^v$ [*Wallace and Hobbs*, 1977], so that the relation above may be integrated to give

$$\int_{0\ (\mu_w^l=\mu_w^v)}^{\mu_w^l-\mu_w^v} d\mu = \mu_w^l - \mu_w^v = -RT \int_{p_s}^{p_w^g} \frac{1}{p} dp = -RT ln \left[\frac{p_w^g}{p_s}\right]. \tag{4.16}$$

The above relation has been derived for pure water, whereas the droplet consists of an electrolyte solution. The water vapor pressure over a droplet containing dissolved solute may be written [*Seinfeld*, 1986]

$$p_w^l = \gamma_w x_w p_w^g \tag{4.17}$$

where γ_w is the activity coefficient of water in the solution and x_w is the mole fraction of water. Substituting the above relation into Eqn. 4.16,

$$\mu_w^l - \mu_w^v = -RT ln \left[\frac{p_w^l}{p_s} \frac{1}{\gamma_w x_w}\right] = -RT ln \left[\frac{RH}{a_w}\right] \tag{4.18}$$

where RH is the relative humidity ($\frac{p_w^l}{p_s}$, taken on the 0 to 1 scale here), and a_w is the water activity of the solution ($\gamma_w x_w$).

For solutions containing ionic species, another definition of the water activity is [*Seinfeld*, 1986] :

$$a_w = \gamma_w x_w = exp\left[\frac{-\nu m M_w \Phi_s}{1000}\right] \tag{4.19}$$

where ν is the number of ions produced by the dissociation of one mole of solute, M_w is the molecular weight of water, m is the molality of the droplet solution, and Φ_s is the practical osmotic coefficient, which accounts for ion-ion interactions that can be important for the high solute concentrations in droplets for RH's below 100%. The practical osmotic coefficient is related directly to the osmotic pressure effect, which is the pressure that must be applied to the solution in order to stop the influx of solvent through a hypothetical, semi-permeable membrane separating the solution and pure solvent. For known particle compositions, the parameters in the above definition of

a_w may be determined. We will return to the above definition of a_w when we examine how the method outlined in *Pitzer* [1973] may be used to calculate Φ_s for the droplet solutions studied here.

Using the difference in chemical potentials derived in Eqn. 4.18, the first term on the right side of Eqn. 4.13 may be written

$$n_w^l(\mu_w^l - \mu_w^v) = n_w^l RT(ln[a_w] - ln[RH]). \tag{4.20}$$

4.2.4 Contribution by Soluble Material to ΔG

Following the above analysis for water substance, the chemical potential of a solute in solution is related to its activity, a_s, [*Konopka*, 1996] by

$$\mu_s^l = \mu_s^s + RTln[a_s] \tag{4.21}$$

where μ_s^s refers to the pure soluble substance. The activity is generally expressed as

$$a_s = \gamma_s x_s \tag{4.22}$$

where x_s is the mole fraction of solute in solution, and γ_s is the activity coefficient of the solute in solution and depends upon the solution composition and temperature. The above expression will be used in the relation for ΔG to account for contributions by the salt to the Gibbs free energy of the droplet solution.

4.3 *Generalized Köhler Equation*

Using the above relations for the various chemical potentials and activities, the change in Gibbs free energy may be written as

$$\Delta G = -RTn_w^l ln[RH] + RTn_w^l ln[a_w] + RTn_s^l ln[a_s] + \pi D_{drop}^2 \sigma_d^{lv} - \pi D_{p,sol}^2 \sigma_s^{sv}. \tag{4.23}$$

For spontaneous absorption (desorption) of water by (from) the droplet, ΔG must be negative as the droplet passes from the initial to final state. The equilibrium RH over

a droplet solution is determined by the balance between the positive contribution to ΔG by the work required to sustain the droplet surface and the negative contribution to ΔG attributable to the solute in solution through the Raoult effect.

The final equilibrium state will be defined by the number of moles of liquid water that minimize ΔG. We therefore evaluate the derivative of the above relation with respect to n_w^l and set the resulting equation equal to zero

$$\begin{aligned}\frac{d(\Delta G)}{dn_w^l} = \quad & -RTln[RH] - RTn_w^l \frac{\partial ln[RH]}{\partial n_w^l} + RTln[a_w] \\ & + RTn_w^l \frac{\partial ln[a_w]}{\partial n_w^l} + RTln[a_s]\frac{\partial n_s^l}{\partial n_w^l} + RTn_s^l \frac{\partial ln[a_s]}{\partial n_w^l} \\ & + 2\pi\sigma_d^{lv} D_{drop} \frac{\partial D_{drop}}{\partial n_w^l} + \pi D_{drop}^2 \frac{\partial \sigma_d^{lv}}{\partial n_w^l} - \pi D_{p,sol}^2 \frac{\partial \sigma_s^{sv}}{\partial n_w^l}. \end{aligned} \tag{4.24}$$

The RH of the system is specified, therefore the second term is zero. The number of moles of salt, n_s^l, is constant, so $\frac{\partial n_s^l}{\partial n_w^l}$ is zero. Furthermore, the last two terms on the right hand side cancel each other [*Wilemski*, 1984]. We now examine the fourth and sixth terms on the right hand side of the above relation more closely. Recall the form of the Gibbs-Duhem relation for a two component system at constant pressure and temperature

$$n_i d\mu_i + n_j d\mu_j = 0 \text{ or } n_w^l d\mu_w^l + n_s^l d\mu_s^l = 0. \tag{4.25}$$

The chemical potentials can be expressed as

$$\mu_w^l = \mu_w^o + RTln[a_w] \tag{4.26}$$

$$\mu_s^l = \mu_s^o + RTln[a_s]. \tag{4.27}$$

Using these equations for the chemical potentials, the Gibbs-Duhem relation may be written

$$n_w^l RTd(ln[a_w]) + n_s^l d(ln[a_s]) = 0. \tag{4.28}$$

Taking the partial derivative of the above relation with respect to n_w^l, we find

$$n_w^l RT \frac{\partial ln[a_w]}{\partial n_w^l} + n_s^l \frac{\partial ln[a_s]}{\partial n_w^l} = 0. \tag{4.29}$$

This last equation reveals that the fourth and sixth terms of the equation for $\frac{d(\Delta G)}{dn_w^l}$ cancel each other. The simplified relation for the derivative of ΔG becomes

$$\frac{d(\Delta G)}{dn_w^l} = -RTln[RH] + RTln[a_w] + 2\pi\sigma_d^{lv} D_{drop} \frac{\partial D_{drop}}{\partial n_w^l}. \tag{4.30}$$

To simplify this equation, the partial derivative of D_{drop} with respect to the number of moles of water in the droplet must be known. D_{drop} satisfies the mass conservation relation

$$\frac{\pi \rho_d D_{drop}^3}{6} = n_w^l M_w + n_s^l M_s \tag{4.31}$$

where ρ_d is the density of the droplet solution and M_s is the molecular weight of the salt in solution. Differentiating this expression with respect to n_w^l

$$\frac{3\pi \rho_d D_{drop}^2}{6} \frac{\partial D_{drop}}{\partial n_w^l} + \frac{\pi D_{drop}^3}{6} \frac{\partial \rho_d}{\partial n_w^l} = M_w. \tag{4.32}$$

Simplifying, one obtains

$$\frac{\partial D_{drop}}{\partial n_w^l} = \frac{2}{\pi \rho_d D_{drop}^2} \left[M_w - \frac{\pi D_{drop}^3}{6} \frac{\partial \rho_d}{\partial n_w^l} \right]. \tag{4.33}$$

Following *Konopka* [1996], the partial derivative of ρ_d can be expressed in terms of the corresponding total derivative with respect to solute mass fraction x_s

$$\frac{\partial \rho_d}{\partial n_w^l} = \frac{\partial x_s}{\partial n_w^l} \frac{d\rho_d}{dx_s}. \tag{4.34}$$

The mass fraction can be written as

$$x_s = \frac{M_s n_s^l}{M_w n_w^l + M_s n_s^l}. \tag{4.35}$$

Differentiating the relation for x_s with respect to n_w^l one obtains

$$\frac{\partial x_s}{\partial n_w^l} = -\frac{M_w x_s}{M_w n_w^l + M_s n_s^l} \tag{4.36}$$

which can be written

$$\frac{\partial x_s}{\partial n_w^l} = -\frac{6 M_w x_s}{\pi \rho_d D_{drop}^3}. \tag{4.37}$$

Substituting the above relation into that for the partial derivative of D_{drop} with respect to n_w^l one finds

$$\frac{\partial D_{drop}}{\partial n_w^l} = \frac{2M_w}{\pi \rho_d D_{drop}^2}\left[1 + \frac{x_s}{\rho_d}\frac{d\rho_d}{dx_s}\right]. \tag{4.38}$$

Substituting the above relation into the equation for the derivative of ΔG with respect to the number of moles of water, and setting this equal to zero one obtains

$$RTln[RH] = RTln[a_w] + \frac{4M_w\sigma_d^{lv}}{\rho_d D_{drop}}\left[1 + \frac{x_s}{\rho_d}\frac{d\rho_d}{dx_s}\right] \tag{4.39}$$

which may be rewritten

$$RH = exp\left[\frac{4M_w\sigma_d^{lv}}{RT\rho_d D_{drop}}\left(1 + \frac{x_s}{\rho_d}\frac{d\rho_d}{dx_s}\right)\right] a_w. \tag{4.40}$$

We note that the definition of the partial molar volume of water in the droplet solution is

$$\bar{\nu}_l = \frac{M_w}{\rho_d}\left(1 + \frac{x_s}{\rho_d}\frac{d\rho_d}{dx_s}\right). \tag{4.41}$$

Values of $\bar{\nu}_l$ as a function of solute mass fraction are shown in Figure 4.1 for most of the solutes investigated in this work. In the figure, solid lines designate the molar volume of pure water and the plus symbols represent the partial molar volume of water in solution. The definition of $\bar{\nu}_l$ can be substituted into Eqn. 4.40

$$\begin{aligned} RH = &\quad exp\left[\tfrac{4\sigma_d^{lv}\bar{\nu}_l}{RTD_{drop}}\right] exp\left[\tfrac{-\nu m M_w \Phi_s}{1000}\right] \qquad (a) \\ RH = &\quad exp\left[\tfrac{4\sigma_d^{lv}\bar{\nu}_l}{RTD_{drop}}\right] a_w \qquad (b). \end{aligned} \tag{4.42}$$

This is the generalized form of the Köhler equation describing the RH in equilibrium with a droplet of size D_{drop} nucleated on a particle containing a fully dissolved, soluble salt. The first exponential term on the right hand side of Eqn. 4.42(a) is commonly referred to as the Kelvin, or curvature term, by virtue of its $\frac{1}{D_{drop}}$ dependence. The second exponential term is referred to as the Raoult, or solute term, and describes the vapor pressure lowering over a solution containing dissolved solute. Eqn. 4.42(b)

is the form used for calculating equilibrium RH's using the polynomial fits of a_w as a function of solute weight percent in solution given by

$$a_w = 1.0 + \Sigma C_i x_s^i \tag{4.43}$$

where x_s is the solute weight percent and C_i are polynomial coefficients tabulated by from *Tang and Munkelwitz* [1994]. The treatment of appropriate parameters for mixtures of salts is discussed below.

To simplify the above general form of the Köhler equation we apply the relationship proposed by *Hänel* [1976] to correct droplet surface tension for temperature and chemical composition effects:

$$\bar{\sigma}_{drop} = \sigma_o(T_o) + a(T_o - T) + bm \tag{4.44}$$

where $\sigma_o(T_o)$ is the surface tension of pure water at T_o=273.15 K (0.0756 N/m), a is a coefficient to account for the temperature dependence of the droplet surface tension (a=1.53x10^{-4} N/m K), b is a composition dependent factor tabulated in Table 4.1, and m is the solution molality. Values of $\bar{\sigma}_{drop}$ as a function of solute mass fraction are shown in Figure 4.1 for most of the solutes investigated in this work. In the figure, solid lines designate σ for pure water and the plus symbols represent solution surface tension ($\bar{\sigma}_{drop}$).

The molality, m, is defined as the number of moles of solute per kilogram of water, and may be written for the droplet solution as

$$m = \frac{1000 m_s}{M_s m_w} = \frac{1000 x_s}{M_s(1 - x_s)} \tag{4.45}$$

where m_s and m_w are the masses of solute and water in the droplet. The mass fraction of solute in solution may be written

$$x_s = \frac{m_s}{m_s + m_w} = \frac{\rho_s D_{p,sol}^3}{\rho_d D_{drop}^3} \tag{4.46}$$

where ρ_s and ρ_d are the densities of the solute and solution, respectively.

In the expression for the partial molar volume of water in the droplet solution (Eqn. 4.41), $\frac{d\rho_d}{dx_s}$ is the change in solution density with mass fraction of solute. ρ_d and $\frac{d\rho_d}{dx_s}$ may be calculated for droplet solutions containing the solutes studied here using the polynomial fits of ρ_d as a function of x_s from *Tang and Munkelwitz* [1994].

4.3.1 The Osmotic Coefficient, Φ_s

For HTDMA measurement conditions at RHs between 80 and 92%, application of the Köhler equation to the droplet solution molalities encountered in this work requires either data for a_w as a function of x_s or an accurate model of the osmotic coefficient.

Water activities and densities have been reported by *Tang and Munkelwitz* [1994], *Tang et al.* [1981], and *Tang* [1997] for the solutes examined here. Values of a_w and ρ_d are reported as polynomial fits to results of droplet growth experiments using the single-particle levitation technique. The polynomials are written as functions of the solute weight percent in solution. In this work, the results from Tang's polynomials are used to validate the results of from the reference Köhler model derived in chapter 4. Comparisons of RHs calculated using both techniques are provided in chapter 5.

Values of Φ_s are determined using the model of *Pitzer and Mayorga* [1973], which is capable of reproducing the variation of Φ_s with solution molality for over two hundred 1:1, 1:2 and 2:1 solutes. They found the following functional form for Φ_s:

$$\Phi_s = 1 - \mid z_1 z_2 \mid \left[A_\phi \frac{\sqrt{I}}{1 + b_{pit}\sqrt{I}} \right] + m \frac{2\nu_1\nu_2}{\nu} \left[\beta_0 + \beta_1 e^{-\alpha\sqrt{I}} \right] + m^2 \frac{2(\nu_1\nu_2)^{\frac{3}{2}}}{\nu} C_\phi. \quad (4.47)$$

In the above equation, α and b_{pit} were 2 and 1.2, respectively, for all of the solutes examined, z_1 and z_2 are the respective charges on the ions in electronic units, ν_1 and ν_2 are the number of moles of ions of species 1 and 2, respectively, produced when one mole of solute dissociates, ν is defined as $\nu_1 + \nu_2$, I is the ionic strength of the solution, $1/2 \sum m_i z_i^2$, β_0 and β_1 are coefficients that depend on the chemical composition of the solute and are tabulated by *Pitzer and Mayorga* [1973]. A_ϕ is the Debye-Hückel

coefficient for the osmotic function, and is defined as

$$A_\phi = \frac{1}{3}\sqrt{\frac{2\pi N_{av}\rho_w}{1000}}\left[\frac{e^2}{DkT}\right]^{\frac{3}{2}}. \tag{4.48}$$

A_ϕ has the value 0.394 for water at 29.5°C, the average temperature observed during laboratory HTDMA studies and assumed in this work. N_{av} is Avogadro's number, e is the unit electric charge, D is the dielectric constant of water, and k is Boltzmann's constant. In the above equation for Φ_s, the term involving A_ϕ models the long range forces through which ions in solution interact, and determines the value of Φ_s when the solution becomes very dilute and the molality, m, approaches zero. As m approaches zero, Φ_s approaches unity, the thermodynamic limit, as the ionic strength of the solution also approaches zero. The terms involving m model the interaction forces between ions and are important in more concentrated solutions when ions are close enough to each other that the radial electric field distributions associated with the ions are capable of altering the osmotic pressure, and therefore the osmotic coefficient, of the solution.

4.3.2 Reference Köhler Model

In this section we present the full Köhler equation in terms of parameters to be determined from HTDMA studies. Substituting the above relations for $\bar{\sigma}_{drop}$ and m into the Köhler equation we find

$$RH = 100exp\left[\frac{4\bar{\nu}_l\left[\sigma_o + b\frac{1000x_s}{M_s(1-x_s)}\right]}{RTD_{drop}}\right]exp\left[\frac{-M_w x_s \nu \Phi_s(x_s)}{M_s(1-x_s)}\right] \tag{4.49}$$

where the temperature dependence of the surface tension has been absorbed into the σ_o term, Φ_s is given by Pitzer's model described above, and x_s is given by Eqn. 4.45.

It is important to understand which terms in the above equation are known and which are unknown. For example, RH is the relative humidity inside the DMA during the HTDMA study, and is measured at both the inlet and outlet flows of DMA2. R and M_w are constants, and are known. ν_l depends upon x_s and is unknown

for unknown particle chemical composition. D_{drop} is the wet size measured by the HTDMA system, which is known. $D_{p,sol}$ is, for pure salt particles, the dry particle size selected by the first DMA in the HTDMA system, and is known. T_o is a constant reference temperature (273.15 K). T is the temperature of the droplet, and is assumed to be equal to the temperature inside DMA2, which is measured. The unknowns in the above equation depend upon the chemical composition of the dry particle nucleus, and are ν_l, b, x_s, M_s, ν and Φ_s.

4.3.3 Evaluation of Mixture Properties

The form of the Köhler equation given above is explicitly written for a single solute. In order to study the hygroscopic growth of particles containing two salts, expressions are required to calculate the chemical composition dependent parameters for internally mixed solutes. For two solutes, the mole fractions of solute 'a' and solute 'b' in the dry particle are designated as f_a and f_b, respectively. The molecular weight of the mixed solute particle can be calculated

$$M_s = f_a M_{s,a} + f_b M_{s,b} \tag{4.50}$$

where $M_{s,a}$ is the molecular weight of solute 'a' and $M_{s,b}$ is the molecular weight of solute 'b'. The mass fractions of the two solutes can then be determined from

$$x_a = \frac{f_a M_{s,a}}{M_s} \tag{4.51}$$

similarly

$$x_b = \frac{f_b M_{s,b}}{M_s}. \tag{4.52}$$

Using the calculated mass fractions, the solute density ρ_s may be determined from

$$\rho_s = \frac{1}{\frac{x_a}{\rho_{s,a}} + \frac{x_b}{\rho_{s,b}}} \tag{4.53}$$

where $\rho_{s,a}$ is the density of solute 'a' and $\rho_{s,b}$ is the density of solute 'b'. Furthermore, the mole fraction weighted number of ions produced when one mole of the mixed solute

dissolves in solution may be calculated from

$$\nu = f_a(\nu_{1,a} + \nu_{2,a}) + f_b(\nu_{1,b} + \nu_{2,b}) \tag{4.54}$$

where $\nu_{1,a}$ and $\nu_{2,a}$ are the number of anions and cations, respectively, resulting from the dissociation of one mole of solute 'a' and $\nu_{1,b}$ and $\nu_{2,b}$ are the respective values for solute 'b'. Assuming volume additivity for the ternary solution, the droplet solution density may be calculated using the expression from *Tang* [1997]

$$\rho_d = \frac{1}{\frac{x_a}{\rho_{d,a}} + \frac{x_b}{\rho_{d,b}}} \tag{4.55}$$

where $\rho_{d,a}$ and $\rho_{d,b}$ are the corresponding solution densities of the binary solutions evaluated at the total solute mass fraction in the ternary solution. The solution densities of the binary mixtures of solute 'a' and water and solute 'b' and water are calculated for assumed droplet size, dry particle size, and mass fractions of solutes 'a' and 'b' in the dry particle using a mass conservation relation described in chapter 5. Therefore, it is assumed that solutes 'a' and 'b' do not interact with each other in the ternary solution. In the calculations using Eqn. 4.42 for internally mixed composition solutes, the term involving $\bar{v}_l$ contains the derivative of ρ_d with respect to the solute mass fraction. The derivative is evaluated by differentiating Eqn. 4.54 with respect to x_s, where $\rho_{d,a}$ and $\rho_{d,b}$ in Eqn. 4.54 depend on x_s. The surface tension of the mixed salt solution is determined from *Chen* [1994]

$$\sigma = \sigma_o + f_a b_a m + f_b b_b m \tag{4.56}$$

where b_a and b_b are listed in Table 4.1 and m is the molality of the ternary solution. Following *Pruppacher and Klett* 1997, we use a molality weighting approach to evaluate the osmotic coefficient of the solution containing two solutes

$$\Phi_{s,mix} = \frac{m_a(\nu_{1,a} + \nu_{2,a})\Phi_{s,a} + m_b(\nu_{1,b} + \nu_{2,b})\Phi_{s,b}}{m_a(\nu_{1,a} + \nu_{2,a}) + m_b(\nu_{1,b} + \nu_{2,b})} \tag{4.57}$$

where m_a and m_b are the molalities of solutes 'a' and 'b' in the ternary solution, respectively. The above expressions were used to calculate the equilibrium RH over

droplets consisting of ternary solutions involving a variety of solutes. The results are compared against the ZSR relation [*Zdanovskii,* 1936; *Stokes and Robinson,* 1966] using data reported by *Tang* [1997] in chapter 5. A more detailed discussion of the results from our studies on mixtures is provided in chapter 5.

4.4 *Summary*

A general form of the Köhler equation applicable to particles containing one or more salts has been derived from first principles using a Gibbs free energy minimization approach. Contributions to ΔG from the various components were determined and then combined, along with a form of the Gibbs-Duhem relation, to derive the generalized Köhler equation. Using a mass conservation relation, terms involving derivatives of solution density and D_{drop} with respect to the number of moles of water in the droplet were recast in terms of quantities that could be calculated from data of the variation of ρ_d with x_s from the literature. Models for the solution surface tension and osmotic coefficient were chosen for use in the generalized Köhler equation. The next chapter includes sensitivity studies to examine which terms, if any, may be simplified in order to derive a version of the Köhler equation that can be fit to D_{drop}, RH data pairs to derive a particle's critical supersaturation.

Table 4.1: Values of ρ_s, M_s, β_o, surface tension 'b' parameter, deliquescence RH's and crystallization RH's for solute chemical compositions examined in this work. Values for mixed composition solutes assume an equimolar mixture of the two salts.

Solute	Ratio $\frac{Cation}{Anion}$	ρ_s^a $\frac{kg}{m^3}$	M_s^a $\frac{g}{mol}$	β_0^b	b^c $\frac{Nmol_w}{m.kg_{sol}} x10^{-3}$	RHdel[d] %	RHcrys[d] %
NaCl	1:1	2165	58.44	0.1082	1.64	75.3	45-48
$(NH_4)_2SO_4$	2:1	1769	132.1	0.04763	2.17	80	37-40
NH_4HSO_4	1:1	1780	115.1	0.04494	2.3	40	0.05-22
H_2SO_4	2:1	1841	98.01	-0.0933	0.67	-	-
NH_4NO_3	1:1	1725	80.04	-0.0154	2.2	62	
$(NH_4)_3H(SO_4)_2$	4:2	1830	247.0	0.0463	2.2	69	35-44
$(NH_4)_2SO_4$-NaCl	3:2	1874	95.30	0.078	1.91		
$(NH_4)_2SO_4$-NH_4NO_3	3:2	1752	106.1	0.016	2.185		
NaCl-NH_4NO_3	2:2	1887	69.24	0.0464	1.6		
NaCl-Na_2SO_4	3:2	2506	100.2	0.048	2.05	84[e]	53[e]

a. Weast [1988]

b. Pitzer and Mayorga [1973]

c. Chen [1994]

d. Tang and Munkelwitz [1994]

e. Tang [1997]

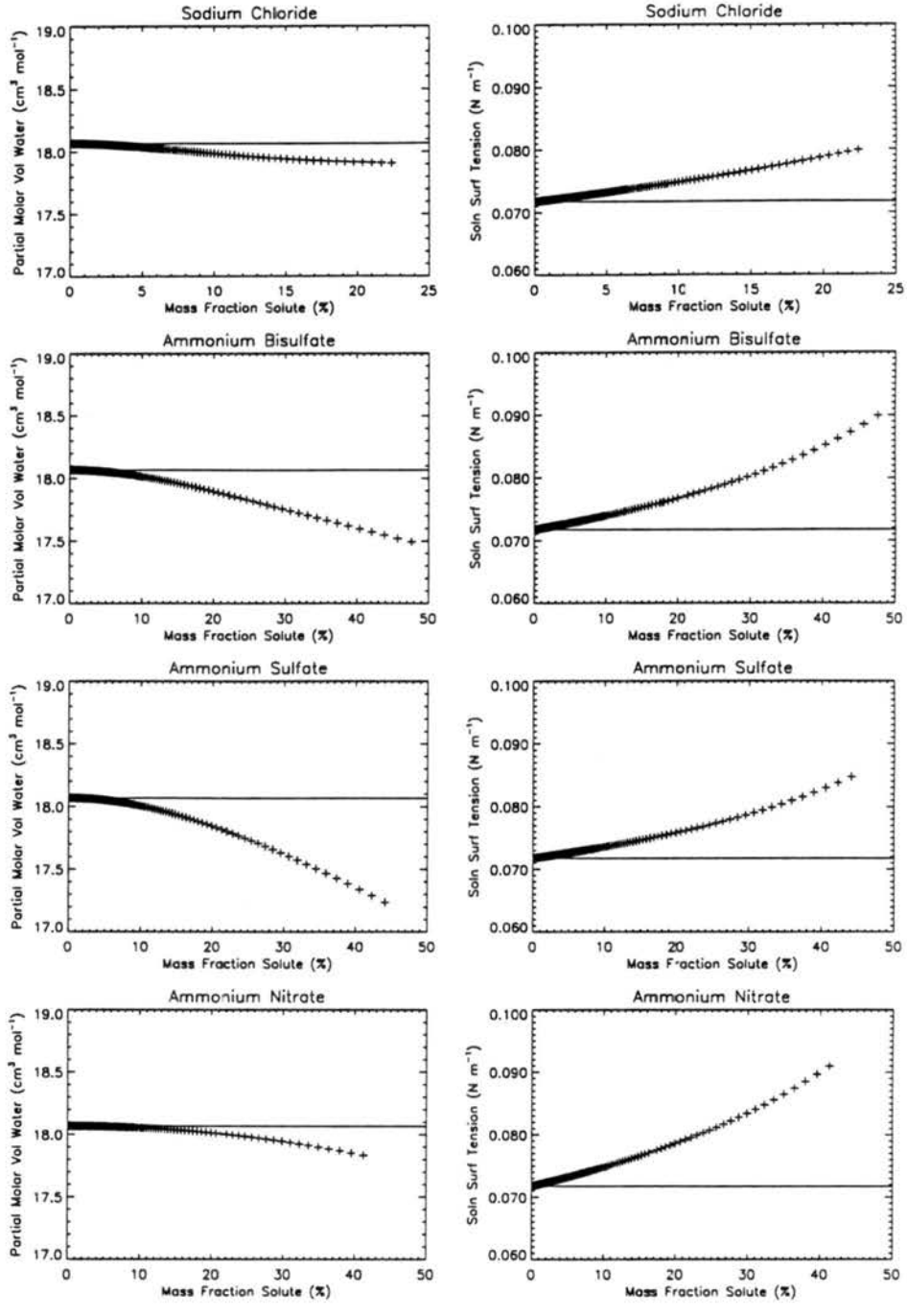

Figure 4.1: Molar volume and surface tension of solutions examined in this work. Solid lines designate the property value for pure water, 'plus' symbols represent the partial molar volume of water in solution and solution surface tension.

Chapter 5

Numerical Sensitivity Studies of Assumptions and of Proposed Technique for Predicting S_{crit} from HTDMA Results

5.1 *Introduction*

The results from numerical sensitivity studies on the reference Köhler model derived in chapter 4 are presented in this chapter. The sensitivity to three specific assumptions: volume additivity, surface tension of solution equal to that for pure water, and the use of a simplified model for the osmotic coefficient, are studied. A simplified version of the Köhler equation is derived using these assumptions, and the ability of this form of the equation to fit simulated HTDMA study results and derive S_{crit} is tested.

5.2 *Reference Model Calculations*

Reference values of RH corresponding to a given mass fraction of solute in solution are required to compare subsequent values of RH predicted from simplified versions of the Köhler equation. The mass fraction, x_s, of solute in a drop of diameter D_{drop} formed on a dry particle of size $D_{p,sol}$ was found by iteratively solving

$$\rho_d(x_s)x_s D_{drop}^3 - \rho_s D_{p,sol}^3 = 0 \tag{5.1}$$

where x_s is given by Eqn. 4.46. The solution density and molality corresponding to this mass fraction were used to compute $\bar{\sigma}_{drop}$ and Φ. The equilibrium RH for the particular $D_{p,sol}$ and D_{drop} was then determined using the reference Köhler model (Eqn. 4.49). The same value of x_s used in the reference Köhler model was also used in Tang's polynomials to calculate a_w (Eqn. 4.43). The RH corresponding to x_s was then calculated using Eqn. 4.42(b). Values of the various material properties for the solutes examined were listed in Table 4.1. Values of D_{crit}, S_{crit}, and Φ at S_{crit} are shown in Table 5.1 for various dry particle sizes and compositions. Uncertainties between $\pm 0.1\%$ and $\pm 0.4\%$ in the fit of Pitzer's model of Φ to experimental data are reported by *Pitzer and Mayorga* [1973]. Values of RH calculated using the reference Köhler model are compared with values determined using the results of *Tang and Munkeltwitz* [1994] in Figure 5.1(a) for binary solutions in order to validate the results from the reference model. The reference model results are shown as solid lines and results calculated from *Tang and Munkeltwitz* [1994] as dotted lines. Also shown is the percent error between the values of RH predicted by the two methods. Results in Fig. 5.1(a) demonstrate agreement between the two different methods for determining RH within 0.5% for NaCl and $(NH_4)_2SO_4$ (ammonium sulfate) over the range of RH's experienced during HTDMA studies. The agreement for NH_4HSO_4 (ammonium bisulfate) and NH_4NO_3 (ammonium nitrate) is not as good as for the other solutes, but still between 0% and 2.5%. Uncertainties in the values of a_w and RH determined from the reference model are estimated between $\pm 1\%$ and $=2.5\%$, based on errors in Pitzer's model of Φ, and errors in the polynomial fits to solution density data.

The RH values predicted by the reference Köhler model for internally mixed solutes were compared with results from the ZSR relation [*Zdanovskii,* 1936; *Stokes and Robinson,* 1966]. First, the dry particle density, ρ_s, was calculated using Eqn. 4.53 assuming volume additivity for assumed values of mass fractions x_a and x_b in the dry particle. Next, the total mass fraction of solute in solution (x_s) was determined

for the assumed mass fractions of solutes 'a' and 'b' in the dry particle and for a given drop diameter by iteratively solving the equation

$$x_s \rho_d D_{drop}^3 - \rho_s D_{p,sol}^3 = 0 \tag{5.2}$$

where ρ_d is the solution density determined using Eqn. 4.55. The value of x_s solving the above equation was determined as follows. First, the mass fractions of solutes 'a' and 'b' in the dry particle were fixed. Using Eqn. 4.53, ρ_s was calculated. The total mass of solute could then be determined for the assumed dry particle size and the calculated value of ρ_s assuming the particle was spherical in shape. Next, for an assumed value of D_{drop}, an initial guess for x_s could be calculated. The value of ρ_d in Eqn. 5.2 corresponding to x_s could then be determined using Eqn. 4.55 and the polynomials from Tang. The Newton-Raphson technique was used to iteratively solve for the value of x_s in Eqn. 5.2 so that the difference between the two terms on the left side of Eqn. 5.2 was less than 10^{-6}. The value of x_s determined from the iteration was then used to calculate the solution molality, m, and the solution density. Using the polynomials of molality as a function of water activity from *Tang and Munkelwitz* [1994] in the ZSR relation, the water activity solving the ZSR relation was determined using the following form

$$\frac{f_a m}{m_{a,0}} + \frac{f_b m}{m_{b,0}} = 1 \tag{5.3}$$

where $m_{a,0}$ and $m_{b,0}$ are the molalities of the binary solutions of solutes 'a' and 'b' calculated using Tang's polynomials as a function of a_w for the given water activity. Eqn. 5.3 was solved iteratively using a procedure similar to that outlined above for the value of a_w corresponding to x_s. Once the correct water activity was determined from the ZSR relation, the RH was calculated by applying the Kelvin correction as shown in Eqn. 4.42(b). According to *Tang* [1997], the assumption that the solutes in ternary solutions do not interact can lead to errors in predicted values of a_w using the ZSR relation between 1% and 6% for solution molalities greater than 1 molal. *Tang*

[1997] presents results for an extended ZSR relation that better fits experimental data of a_w as a function of m for a variety of mixed solutes in ternary solutions where the two solutes have one common ion. Below we compare values of RH from the extended ZSR relation proposed by *Tang* [1997] for the system NaCl-Na_2SO_4-Water, and for the simpler ZSR relation (Eqn. 5.3) for three other ternary solutions.

RH values were also calculated using the reference Köhler model with solution density, osmotic coefficient, and other parameters calculated as outlined in chapter 4 for mixed solutes. Values of RH determined from the ZSR relation using Tang's density and water activity polynomials are compared with those from the reference model for ternary solutions in Figure 5.1(b). In the figure, the ZSR results are shown as dotted lines and the reference model results are shown as solid lines. The percent difference between the RH values calculated using the two different techniques is shown in the plots in the right column. The agreement between the ZSR and reference model predicted RH's is not as good as for the single solutes examined. For the internal mixtures of NaCl-$(NH_4)_2SO_4$, NaCl-NH_4NO_3, and $(NH_4)_2SO_4$-NH_4NO_3, the percent error in RH is less than 3.3% for the RH range 80% to 92%. Better agreement is found at higher RH, corresponding to more dilute solutions where the assumption that the osmotic coefficient of the ternary solution can be determined by the molality weighting approach is more valid. For the one case where the extended version of the ZSR relation was used (NaCl-Na_2SO_4-Water), the agreement is between 1% and 7%, but is better than 2% for RH's greater than 89%. This demonstrates that interactions between solutes in solution can be important for ternary solutions. Parameters for the extended ZSR relation are not available for any of the other ternary solutions examined.

5.3 *Simplifications*

In this section we describe the simplifying assumptions made to the reference Köhler model, and our methodology for testing their validity. The assumptions include volume additivity of solute and solvent within the drop, substitution of the surface tension of pure water for the solution surface tension, and the use of a simplified, parameterized form of the osmotic coefficient in the Raoult term. The validity of the assumptions is checked over the range of RH's of HTDMA studies (80 to 92%) to ensure that the final, simplified Köhler model can accurately describe the hygroscopic growth of particles over this range.

5.3.1 Assumption of Volume Additivity

To assess the validity of assuming that the solute and solvent volumes may be added to determine solution density, we have performed calculations of the partial molar volume of water for a variety of solution compositions and compared these results to the molar volume of pure water. The values were shown in Figure 4.1. The difference between the partial molar volume of water and the molar volume of pure water increases with increasing mass fraction due to the association of ions in solution. The largest difference is found for $(NH_4)_2SO_4$ and amounts to -4% for $x_s = 40\%$. Assuming the volumes of solute and solvent may be added to determine the solution total volume is equivalent to assuming the partial molar volume of water in solution is equal to the molar volume of pure water. If volume additivity is assumed, the mass fraction may be determined as follows:

$$x_s = \frac{\rho_s D_{p,sol}^3}{\rho_w (D_{drop}^3 - D_{p,sol}^3) + \rho_s D_{p,sol}^3}. \tag{5.4}$$

We tested the sensitivity of values of x_s, Φ, a_w, the natural log of the Kelvin term, and equilibrium RH predicted by Eqn. 4.49 using the Pitzer model for Φ to the assumption of volume additivity. Results are presented in Figure 5.2. Each

chemical composition is represented by a different point style in the figure. Results are reported as percent error relative to the values from the reference model for the same dry and wet particles sizes. A dry particle size of 40 nm was assumed for all calculations as this is the nominal size selected during HTDMA laboratory studies. Furthermore, the Kelvin effect is larger for the smaller droplets formed on this size dry particle compared to droplets formed on larger dry particles. Differences in x_s when volume additivity is assumed lead to maximum errors in Φ of about 1%, with similar errors propagating to a_w. The Kelvin term depends on x_s through $\bar{\sigma}_{drop}$ and exhibits relatively larger error than a_w. However, as shown in Figure 4.1, for RH's below 95% the Kelvin term has a relatively smaller effect on the predicted equilibrium RH than the Raoult term, so the influence of the error in the Kelvin term on RH is very small. The errors in equilibrium RH's in Figure 5.2 are between 0.6 and -0.9%, smaller than uncertainties in the reference model RH values. The differences between the reference RH's and RH's predicted by the simplified models decrease as RH increases, consistent with the fact that as the solution becomes more dilute, the assumption that the volumes may be added becomes more valid. Based on the results of this analysis, the assumption of volume additivity is made in this work, therefore, the molar volume of pure water is used in place of $\bar{\nu}_l$.

5.3.2 Assumption of $\bar{\sigma}_{drop} = \sigma_w$

We tested whether $\bar{\sigma}_{drop}$ in the reference Köhler model could be replaced by σ_w. As shown in Fig. 4.1, for the solute mass fraction range encountered in HTDMA studies, the difference between $\bar{\sigma}_{drop}$ and σ_w can be as high as 28% for NH_4NO_3. Assuming $\bar{\sigma}_{drop} = \sigma_w$ only affects the Kelvin term and equilibrium RH. We compare the natural log of the Kelvin term and equilibrium RH values calculated assuming $\bar{\sigma}_{drop} = \sigma_w$ to values from the reference Köhler model in Figure 5.3. Although the error in the Kelvin term is relatively large, the associated error in RH is small for the same reason

given above. As the solution becomes more dilute, the assumption that $\bar{\sigma}_{drop} = \sigma_w$ becomes more valid. The maximum error in RH is less than the maximum uncertainty in the reference model RH values, therefore we assume that $\bar{\sigma}_{drop} = \sigma_w$, equivalent to setting $b = 0$ in the reference Köhler model.

5.3.3 Parameterization of Φ

The full model for Φ proposed by *Pitzer and Mayorga* [1973], is too complex to be easily applied to determining S_{crit} from HTDMA study results. They suggest that for most solutes and solution ionic strengths below 6 molal, approximately the maximum molality encountered in solutions studied here, the term involving m^2 is very small and may be neglected; therefore we do so. Furthermore, our investigations show that for the values of solution ionic strengths in our studies, the β_1 term is very small compared to the β_0 term, therefore, we choose to set $\beta_1 = 0$. With the above simplifications, the original expression for Φ (Eqn. 4.47) becomes

$$\Phi = 1 - \mid z_1 z_2 \mid \left[A_\phi \frac{\sqrt{I}}{1 + b_{pit}\sqrt{I}} \right] + m \frac{2\nu_1\nu_2\beta_0}{\nu}. \tag{5.5}$$

In Figure 5.4 we compare values of Φ from the full Pitzer model to values calculated under the assumption that the m^2 and β_1 terms in Pitzer's model may be neglected. Calculations were performed for RH values between 80% and slightly over 100% for all of the compositions investigated in this work. Values of solution molalities are listed along the x-axis. The 80% to 95% RH range is typical for HTDMA studies. The solid line in each plot designates values from the full Pitzer model of Φ, with the mole weighting approach outlined in chapter 4 being applied to calculate Φ for the equimolar internal mixtures shown. The dashed line in each plot represents the values of Φ calculated under the assumption that the m^2 and β_1 terms in Pitzer's model could be neglected. For H_2SO_4, the m^2 term in Pitzer's model is very important, and neglecting it results in poor agreement between the full and simplified version of Φ at RH's below 99%. Therefore, the proposed simplified version of Φ cannot cannot

accurately reproduce the true variation of Φ with solution molality for droplets formed on particles composed of H_2SO_4. Given the poorer agreement between actual and parameterized values of Φ for H_2SO_4, we do not include this compound in our tests of the various assumptions made in formulating the simplified Köhler model. However, we do examine the ability of the simplified Köhler model to predict accurate values of S_{crit} for H_2SO_4 in the sensitivity studies discussed below.

For NaCl, NH_4HSO_4, $(NH_4)_2SO_4$, and NH_4NO_3, the proposed simplified version of Φ does a good job reproducing the values of Φ from the full Pitzer model. The worst agreement is for NH_4HSO_4, where Φ is overpredicted by as much as 19% at a RH of 80%. The full Pitzer model is less accurate for this compound compared to $(NH_4)_2SO_4$, NaCl, and NH_4NO_3[*Kim et al.*, 1993]. We note that for the binary solutions examined, the simplified model for Φ tends to overpredict Φ for RH's between 80% and 93%, the range observed during laboratory HTDMA studies in this work. Overpredictions of Φ will result in underpredictions of S_{crit}, since the larger values of Φ will effectively increase the solute effect, resulting in a lower predicted equilibrium RH for a given solution composition. The situation for mixtures is slightly different. In Fig. 5.4 for NaCl-Na_2SO_4 there is a tendency for the simplified form for Φ to underpredict Φ. The same behavior, with much better agreement, is seen for internally mixed NaCl-NH_4NO_3. For internally mixed NaCl-Na_2SO_4 we expect values of S_{crit} to be overpredicted by the simplified Köhler model since the solute effect will be lowered for lower predicted values of Φ.

We next examine the ability of the reference Köhler model to predict correct values of a_w for $(NH_4)_2SO_4$, NaCl, NH_4NO_3, and NH_4HSO_4using Eqn. 5.5 for Φ. x_s and the Kelvin term are unaffected by using the definition of Φ given in Eqn. 5.5. This comparison allows us to test the assumptions neglecting the m^2 and β_1 terms in Pitzer's full model of Φ on values of a_w and RH predicted by the reference Köhler model.

The comparison between the reference model values of Φ, a_w and RH and the simplified model of Φ is shown in Figure 5.5. Maximum errors in Φ near 12% are evident for NH_4HSO_4 and $(NH_4)_2SO_4$. However, these large errors in Φ correspond to smaller errors, within 2.75%, in a_w. The proposed parameterization does a very good job of predicting the values of a_w as a function of solute mass fraction, particularly for a_w greater than about 0.85. The poorer agreement for NH_4HSO_4 and $(NH_4)_2SO_4$ is due to the relatively larger contribution of the term involving m^2 in the expression for Φ.

We wish to derive a simpler parameterization for Φ that depends on as few unknowns and measured quantities as possible. We note that the molality, m, may be written

$$m = \frac{1000\rho_s D_{p,sol}^3}{M_s \rho_w (D_{drop}^3 - D_{p,sol}^3)}. \tag{5.6}$$

We can define a coefficient c as

$$c = \frac{1000 D_{p,sol}^3}{\rho_w (D_{drop}^3 - D_{p,sol}^3)} \tag{5.7}$$

which can be calculated for each HTDMA (D_{wet}, RH) data pair for known $D_{p,sol}$. The molality may be rewritten in terms of c

$$m = \frac{\rho_s c}{M_s} \tag{5.8}$$

and the ionic strength of the solution may be written

$$I = \frac{1}{2}\left[z_1^2\nu_1 + z_2^2\nu_2\right]\frac{\rho_s c}{M_s}. \tag{5.9}$$

Substituting the above expressions for m and I into Eqn. 5.5 we find

$$\Phi = 1 - \mid z_1 z_2 \mid \left[\frac{A_\phi \sqrt{\frac{1}{2}\left[z_1^2\nu_1 + z_2^2\nu_2\right]\frac{\rho_s c}{M_s}}}{1 + b_{pit}\sqrt{\frac{1}{2}\left[z_1^2\nu_1 + z_2^2\nu_2\right]\frac{\rho_s c}{M_s}}}\right] + \frac{2\nu_1\nu_2\beta_0}{\nu}\frac{\rho_s c}{M_s}. \tag{5.10}$$

In an effort to further simplify the form for Φ given by Eqn. 5.10, we define different parameters, Y_i, and substitute them into Eqn. 5.10. In the numerator of

the Debye-Hückel term, a parameter Y_a can be defined for a solute molecule that dissociates into two ions

$$Y_a = \mid z_1 z_2 \mid^2 \left[\nu_1 z_1^2 + \nu_2 z_2^2\right] \frac{\rho_s}{M_s} \tag{5.11}$$

while in the denominator a parameter Y_b can be defined as

$$Y_b = \left[\nu_1 z_1^2 + \nu_2 z_2^2\right] \frac{\rho_s}{M_s}. \tag{5.12}$$

In the β_0 term, a parameter Y_c can be defined as follows

$$Y_c = \frac{\nu_1 \nu_2}{\nu} \frac{\rho_s}{M_s}. \tag{5.13}$$

The theoretically correct values of Y_a, Y_b and Y_c are shown in Table 5.2. Substituting the above definitions for each of the Y_i into Eqn. 5.10, we find Eqn. 5.14, equivalent to Eqn. 5.5:

$$\Phi = 1 - \frac{A_\phi \sqrt{Y_a c}}{\sqrt{2} + b_{pit}\sqrt{Y_b c}} + 2 Y_c c \beta_0. \tag{5.14}$$

The above definitions of Y_a, Y_b, and Y_c have the common factor $\frac{\rho_s}{M_s}$ and prefactors involving ν_i and z_i that depend upon the chemical composition of the solute. Furthermore, the common factor also appears in the coefficient of Φ in the Köhler model (Eqn. 4.49). We define the following variable unknown

$$Y = \frac{\nu \rho_s}{M_s}. \tag{5.15}$$

Values of Y, Y_a, Y_b, and Y_c are listed in Table 5.2. The various Y_i differ from Y by a constant that depends on the ratio of cations to anions for a given solute. Although a single definition of the combination of ν_i, z_i and $\frac{\rho_s}{M_s}$ cannot be substituted into Eqn. 5.14 for Φ for the different Y_i, we substitute a single unknown Y_f for each of the Y_i, and assume that the retained functional dependence on $\frac{\rho_s}{M_s}$ of the resulting parameterization is sufficient to accurately model the variation of Φ with RH for HTDMA conditions and to predict S_{crit}. This assumption is tested in our numerical simulations of the derivation of S_{crit}. In the simplified form of the Köhler equation,

the product $\Phi_f Y_f c = m\Phi_f$ will be substituted for the product of molality and Φ. With all of the aforementioned assumptions, and accepting that Y, Y_a, Y_b and Y_c can be modeled as a single parameter Y_f, the parameterized form for Φ becomes

$$\Phi_f = 1 - \frac{A_\phi c^{\frac{1}{2}} Y_f^{\frac{1}{2}}}{\sqrt{2} + b_{pit} c^{\frac{1}{2}} Y_f^{\frac{1}{2}}} + 2c\beta_{0,f} Y_f \tag{5.16}$$

where Φ_f denotes the proposed simplified form for Φ, Y_f and $\beta_{0,f}$ are the only unknowns and depend only on the dry particle chemical composition. Note that in the above equation for Φ_f, the parameter $\beta_{0,f}$ no longer has the same value as Pitzer's β_0 coefficient if the single definition of Y_f is used. Although b_{pit}, another adjustable parameter in Pitzer's model, would also be different in Φ_f, we assume the same value of 1.2 used by Pitzer.

To test the validity of assuming $Y_f = Y_a = Y_b = Y_c$ in Eqn. 5.16, we fit the product $Y_f\Phi_f$ to data of $\frac{\nu\rho_s}{M_s}\Phi$ as a function of x_s and determined best fit values of Y_f and $\beta_{0,f}$. All terms are retained in the osmotic coefficient expression used to calculate the product $Y\Phi$. $D_{p,sol}$, D_{drop} pairs were chosen for a given solute chemical composition and Φ calculated as a function of molality using the full Pitzer model. The product $Y_f\Phi_f$ was fit since it is this product that appears in the relation for a_w. The product $Y_f\Phi_f$ must be able to fit actual values of $Y\Phi$, where $Y = \frac{\nu\rho_s}{M_s}$ calculated with the correct values of ν, ρ_s and M_s, in order for accurate values of RH to be predicted from the simplified Köhler model. The fits were performed for molality ranges expected during HTDMA conditions, between 1 and 8 molal. Best fit values of Y_f and $\beta_{0,f}$ have been tabulated in Table 5.2 for each solute. For the solutes listed in Table 5.2, the agreement between values of Y_f and values of Y is between -28% and 8%, suggesting that some information about the chemical composition of the particle nuclei can be inferred from the fit of $Y_f\Phi_f$ to $Y\Phi$ data.

In Figure 5.6 we examine the differences between values of a_w and RH predicted using the full model for $Y\Phi$ and those calculated using the best fit parameters in

$Y_f\Phi_f$ as shown in Table 5.2. The best fit values of Y_f and $\beta_{0,f}$ shown in Table 5.2 were used in equation 5.16 to calculate Φ_f and the product of c, Y_f and Φ_f were then used in place of the product of m and Φ to calculate a_w. The value of a_w was substituted in Eqn. 4.42(b) to examine how errors in a_w propagated to errors in RH. The proposed parameterization for Φ with values of Y_f and $\beta_{0,f}$ from the fit produces smaller errors in $Y\Phi$ than the errors in Φ shown in Figure 5.5. The corresponding maximum errors in a_w and RH are also lower and generally less than the uncertainties in the reference model values for these parameters. Based on the results shown in Figure 5.6, we accept the proposed parameterization of Φ_f, Eqn. 5.16, for use in the simplified Köhler model.

Eqn. 5.16 was also tested on particles composed of H_2SO_4. As mentioned above, due to the relatively greater importance of the term involving m^2 in the full Pitzer model of Φ for this compound, the proposed parameterization for Φ cannot accurately reproduce the variation of Φ with m. In fact, the full Pitzer model for Φ cannot accurately reproduce measurements of Φ for sulfuric acid solutions for solution molalities greater than approximately 2 molal, corresponding the RH's less than approximately 98% [*Kim et al.*, 1993]. The poorer approximation of the model of Φ for H_2SO_4 is indicated in Table 5.2 by the large differences between values of Y_f and $\beta_{0,f}$ derived by fitting the product of $Y_f\Phi_f$ to calculated values of the product $Y\Phi$ for H_2SO_4. A more complex relation for the osmotic coefficient is necessary to properly model aqueous solutions containing H_2SO_4.

5.3.4 Combined Assumptions of $\bar{\nu}_l = \nu_w$, $\bar{\sigma}_{drop} = \sigma_w$ and $\Phi = \Phi_f$

In Figure 5.7 we explore errors in the various parameters when all of the aforementioned assumptions are made simultaneously. The errors in a_w and RH are between $\pm 1\%$ and $\pm 0.4\%$, respectively, for all compounds except $NH_4HSO_4$and H_2SO_4 (not shown). The errors for NH_4HSO_4 are relatively larger due to the relatively poorer

approximation made when the m^2 term is neglected as discussed above. Based on the results shown in Figure 5.7, the simplified Köhler model is shown to correctly predict RH and a_w within reference model uncertainties ($\pm 1\%$ to $\pm 2.5\%$) and experimental uncertainties in RH ($\pm 1\%$) during HTDMA studies for all of the compounds examined, except NH_4HSO_4 and H_2SO_4.

5.3.5 Simplified Form of Köhler Equation

Substituting the above relation for Φ_f (Eqn. 5.16) and incorporating the simplifications discussed in the previous section, the Köhler equation for a droplet containing a single solute that completely dissociates may be written

$$RH = 100exp\left[\frac{4\sigma_w M_w}{\rho_w RT D_{drop}}\right] exp\left[\frac{-M_w c}{1000}\left(Y_f - \frac{A_\phi c^{\frac{1}{2}} Y_f^{\frac{3}{2}}}{\sqrt{2} + b_{pit} c^{\frac{1}{2}} Y_f^{\frac{1}{2}}} + 2c\beta_{0,f} Y_f^2\right)\right] \tag{5.17}$$

where c is defined as

$$c = \frac{1000 D_{p,sol}^3}{\rho_w (D_{drop}^3 - D_{p,sol}^3)}. \tag{5.18}$$

In the above equations, M_w, R, and b_{pit} are constants, $D_{p,sol}$, D_{drop}, RH and T are measured during HTDMA studies, σ_w, ρ_w and A_ϕ are known given T, and c is known if $D_{p,sol}$, ρ_w and D_{drop} are known. This leaves Y_f and $\beta_{c,f}$ as the two, chemical composition dependent unknowns that remain to be determined. By fitting the above, simplified form of the Köhler equation to (D_{drop},RH) data pairs determined from HTDMA studies performed on the same monodisperse dry particle size at different RH's, the two unknowns, Y_f and $\beta_{0,f}$, may be determined. Once known, the values of Y_f and $\beta_{0,f}$ may be used in the simplified Köhler model to calculate the equilibrium RH at any assumed droplet size and the maximum equilibrium RH set equal to S_{crit}.

5.3.6 Köhler Model of *Weingartner et al.*

Another, simpler Köhler model was proposed by *Weingartner et al.* [1997] that could be fit to HTDMA study results in order to derive S_{crit}. It is of interest to compare the

results from their model with those from the model proposed in this work to examine possible differences in predicted values of S_{crit} for different chemical compositions. The model took the form

$$RH = 100exp\left[\frac{\alpha}{D_{drop}}\right] exp\left[\frac{-\beta N_i}{D^3_{drop} - D^3_{p,sol}}\right] \tag{5.19}$$

where α was taken equal to 2.155 nm, β was set equal to $5.712\text{x}10^{-2}$ nm^3, and the droplet and particle sizes were in nanometers [*Weingartner et al.*, 1997]. N_i denoted the number of dissociated molecules in the water layer of the droplet, and was the one unknown in the model. In Eqn. 5.19, the one unknown, N_i, is defined as

$$N_i = Y N_{av} \frac{\pi}{6} D^3_{p,sol} \tag{5.20}$$

where N_{av} is Avogadro's number and Y is defined by Eqn. 5.15. Implicit in the form of Eqn. 5.19 is the assumption that Φ is constant and does not vary with RH. The variation of Φ with RH is built into the simplified Köhler model proposed in this work (Eqn. 5.17). One disadvantage of the model proposed by *Weingartner et al.* [1997] is that the unknown, N_i, depends on both the particle diameter and chemical composition, making it difficult to separate the effects of particle size from composition on hygroscopic growth and S_{crit}. More discussion of this model and the results of *Weingartner et al.* [1997] is provided in chapter 7, when we fit experimental HTDMA data from this work with their model and compare derived values of S_{crit} to those from the model of this work. Below, we compare the values of S_{crit} derived by fitting Eqns. 5.17 and 5.19 to (D_{drop},RH) pairs to the theoretical values predicted by the reference Köhler model.

5.4 *Estimating S_{crit} Using Simulated HTDMA Data*

For the numerical sensitivity studies, a dry particle size and composition were chosen. The reference Köhler model was used to calculate the theoretical equilibrium RH for assumed droplet sizes. The (D_{drop}, RH) data pairs, and the assumed dry particle

size were used in a non-linear, least-squares fit routine to derive values of Y_f and $\beta_{0,f}$ in Eqn. 5.17 and N_i in Eqn. 5.19. The values of Y_f and $\beta_{0,f}$ derived from sensitivity studies are different than those shown in Table 5.2 because when the simplified Köhler model is fit to (D_{drop}, RH) data pairs, the fit routine finds values of Y_f and $\beta_{0,f}$ that minimize the square of the differences between the fit-predicted RH values and the RH values input to the fit routine. The values of Y_f and $\beta_{0,f}$ in Table 5.2 were determined by fitting the product $Y_f\Phi_f$ to values of $Y\Phi$. Two input data pairs were insufficient to capture the curvature of the Köhler curve. Ten pairs were used for each of the sensitivity studies described below. Trial and error sensitivity studies on the minimum number of input data pairs required to maintain acceptable error in derived values of S_{crit} from Eqn. 5.17 showed that three input data pairs equally spaced between 80 and 95% RH produced the same error in S_{crit} as ten data pairs over the same RH range.

Four different cases were investigated. First, we determined Y_f and $\beta_{0,f}$ from a fit to Eqn. 5.17 using perfect values for $D_{p,sol}$, D_{drop} and RH. Second, we verified that the results from the fit routine were not sensitive to the initial guess for Y_f and $\beta_{0,f}$. Third, we determined the sensitivities of the derived values for Y_f and $\beta_{0,f}$ to assumed $\pm 0.5\%$ random errors in RH, D_{drop} and $D_{p,sol}$. Fourth, we examined the sensitivity of derived values of the unknowns to $\pm 1\%$ random error in RH, dry particle size, and droplet size. The random errors in the three input parameters were applied simultaneously. The experimental uncertainty in RH during HTDMA studies was $0.7\% \pm 0.2\%$, therefore, the 0.5% to 1% range of applied random RH error is relevant for investigating the influence of RH uncertainties on fit routine results. *Rader and McMurry* [1986] have studied the sizing errors in the TDMA. They determined that errors in the measured midpoint diameter in the second DMA were $0.11\% \pm 0.06\%$ for particle diameters less than 200 nm. For flow uncertainties in the HTDMA measurement system, the estimated experimental uncertainty in particle

sizing is between 0.2% and 1%. Standard deviations of less than 1% have been reported for controlled, elevated RH studies in a HTDMA system [*Svenningsson et al.*, 1994]. Our results indicate that standard deviations of less than 0.5% RH were common during HTDMA droplet growth measurements. Laboratory studies on the accuracy and precision of RH measurements made in this study revealed values of $\pm$ 1% and $\pm$0.03% (1σ, n=8), respectively. RH control could be maintained within $\pm$0.7% RH (95% CL). Details of the experimental uncertainties in RH are described in chapter 6. We assume $\pm$1% error in RH as a typical RH uncertainty in our sensitivity studies. The model of *Weingartner et al.* [1997] and that proposed in this work were run simultaneously only for the fourth case, and dry particle sizes of 40 nm and 100 nm were examined. For studies on internally mixed particles, only the cases described above with perfect input and with assumed 1% random uncertainties applied to all input data were investigated.

The cases including errors in the input parameters were performed as follows. For each case, randomly distributed errors between $\pm$0.5% or $\pm$1% were applied to the values of RH, $D_{p,sol}$, and D_{drop}. A single case study of the effect that a single set of applied random errors has on values of Y_f, $\beta_{0,f}$, and S_{crit} from the fit procedure would be less representative of the average influence of experimental uncertainties than averaging the results from several cases of assumed random errors. Therefore, one hundred cases were run on the same input $D_{p,sol}$, D_{drop} and RH data for each assumed range of random errors in order to obtain a statistically significant estimate of the influence of uncertainties on the derived values of Y_f and $\beta_{0,f}$.

Results from our numerical simulations are shown in Table 5.3 for dry diameters of 40 and 100 nm. The values of Y_f and $\beta_{0,f}$ in Table 5.3 for the cases of perfect input, are close to, but not exactly the same as values in Table 5.2. The reason for this is that the values in Table 5.2 were determined by fitting the product of $Y_f\Phi_f$ to values of $Y\Phi$ as described above, whereas the values in Table 5.3 were determined by fitting

the simplified Köhler model to (RH, D_{drop}) data pairs calculated using the reference model. The values of Y_f and $\beta_{0,f}$ shown in the table for cases where errors were applied are obtained by averaging the results from the 100 different cases of applied error. Ratios of the standard deviation computed from the 100 different cases to the average values of Y_f, $\beta_{0,f}$ and S_{crit} were always less than 0.2, 1.30 and 0.16, respectively. The small standard deviations for Y_f and S_{crit} indicate that the fit routine is quite stable. The relatively larger value for $\beta_{0,f}$ is due to the lower sensitivity of the goodness of fit to the value of this parameter compared to Y_f. Tests of the sensitivity of the fit routine to assumed initial conditions showed it to be insensitive, therefore, we report results from these cases for NaCl only. For the laboratory studies, dry particle sizes near 40 nm were chosen since the CCN counter could not reliably maintain the low supersaturations required to activate 100 nm diameter particles.

The percent errors in derived values of S_{crit} are listed in Table 5.3 for the four different pure solute compositions examined and in Table 5.4 for the mixed solutes examined. Only results from cases where $\pm 1\%$ random errors were applied to the input data are reported for the mixed solutes. Results of the fit routine using the Köhler model in this work have been plotted as the solid dots in Figure 5.8, with the solid line designating the 1:1 line. The results from the model of *Weingartner et al.* [1997] are shown as squares in the figure and are discussed below. The plus symbols in the figure represent results when no uncertainties were applied to the input data to the fit routine. As can be seen from the figure, the agreement between theoretical and predicted values of S_{crit} is very good. The errors are between -20% and +15%, similar to the uncertainties in experimental estimates of S_{crit} determined from CCN studies on known particles (-0.6%, 1σ=11%, n=16). The average agreement between predicted and theoretical values of S_{crit} for all compounds listed in Tables 5.3 and 5.4 is -7.5% (1σ=10%, n=8). Also shown in Tables 5.3 through 5.6 are the χ^2 convergence values of the fit for each compound. The small values of χ^2

indicate that the fit routine does a good job fitting the simplified Köhler model to the input data. The χ^2 values are calculated as the sum of the squares of the differences between fit routine-derived RH values and input RH values. Values of S_{crit} from the reference Köhler model are listed in Table 5.1 for the various dry particle sizes and chemical compositions examined. The largest errors in predicted values of S_{crit} are found for NH_4HSO_4 and internally mixed NaCl-Na_2SO_4. This is not surprising for at least three reasons. First, it is possible that the simplified Köhler model is less capable of capturing the hygroscopic behavior of certain particle chemical compositions compared to others. Second, the full Pitzer model of Φ is less accurate for NH_4HSO_4 [*Kim et al.*, 1993]. Third, other than H_2SO_4, NH_4HSO_4 and internally mixed NaCl-Na_2SO_4 compositions exhibited the poorest agreement between values of Φ from the full Pitzer model and values calculated using the simplified model of Φ. The overprediction of Φ by the simpler model for NH_4HSO_4 results in an underpredition of S_{crit} for this compound. In contrast, the underprediction of Φ by the simpler model for internally mixed NaCl-Na_2SO_4 results in an overprediction of S_{crit} . A surprising result in Table 5.3 is the relatively good agreement between predicted and theoretical values of S_{crit} for H_2SO_4, especially given the poor agreement between values of Φ from the full Pitzer model and values calculated using the simplified model of Φ. The values of Y_f and $\beta_{0,f}$ in Table 5.3 are significantly different from the values of Y and β_0 and the values of Y_f and $\beta_{0,f}$ in Table 5.2. Even though the parameterization for Φ does not accurately reproduce the actual behavior of Φ for H_2SO_4, for this compound fit parameters could be derived that allowed the simplified Köhler model to accurately reproduce the droplet growth with increasing RH as well as values of S_{crit}.

In Table 5.3, for some cases where random errors were applied to the input data, S_{crit} values were predicted that agreed slightly better with theory than when no errors were applied. The better agreement is most likely due to limitations in the

model of Φ. The results from cases where errors were applied represent averages of 100 runs of the fit routine. Therefore, in some cases, the applied errors happen to allow the simplified Köhler model to compensate for its shortcomings and produce better values of S_{crit}. The agreement between the predicted values of S_{crit} in Tables 5.3 and 5.4 and the reference values listed in Table 5.1 is better than $\pm 12\%$, indicating that the proposed method is capable of accurately determining S_{crit} for the particle compositions studied.

5.4.1 Comparison of Results from Different Köhler Models

A comparison of the results of numerical sensitivity studies on the model proposed here and that proposed by *Weingartner et al.* [1997] is presented in Table 5.5 for 40 nm diameter particles, and in Table 5.6 for 100 nm diameter particles. The first row of results for each compound is from the case with no applied random error to the input data. The second row lists the average of the results where 100 cases were performed of fitting each model to input data with applied errors. The maximum coefficient of variation, defined as the ratio of the standard deviation to the mean value, for predicted values of Y_f was 0.2 and for predicted values of S_{crit} was 0.16. Therefore, the standard deviations in predicted values of Y_f and S_{crit} from the fit routine with perturbed input data were small. Results have been plotted in Figure 5.8. For the results of studies on 40 nm particles, the average agreement between predicted values of S_{crit} and theoretical values is -2.6% (16%, n=9) for the model of *Weingartner et al.* and -1.1% (10%, n=9) for the model from this work. The values listed in Table 5.6 for 100 nm particles are similar. The poorer performance of the model proposed in this work for NH_4HSO_4 and internally mixed NaCl-Na_2SO_4 is evident in both tables. For NH_4HSO_4, the predicted values of $\beta_{0,f}$ in Table 5.3 are close to zero, consistent with the better agreement found between fit-derived values of S_{crit} using the model of *Weingartner et al.* and theoretical values of S_{crit}. The

good agreement between the predicted values of S_{crit} from the simpler Köhler model proposed by *Weingartner et al.* and theoretical values is surprising, particularly since this model assumes that the osmotic coefficient does not vary with RH over the range of RH's experienced during HTDMA studies. Except for NH_4NO_3, both models tend to underpredict S_{crit} for particles composed of single solutes. Underpredictions of S_{crit} by the model of this work are associated with underpredictions of the Kelvin term and overpredictions of values of Φ by the parameterized form for Φ used in the simplified Köhler model. The larger χ^2 values in Table 5.5 for the model of *Weingartner et al.* compared to those in Tables 5.3 and 5.4 for the model of this work indicate that the model of *Weingartner et al.* does not capture the hygroscopic behavior as well as the two parameter model. The underprediction of S_{crit} by the model of *Weingartner et al.* could be due to the assumption that Φ is constant, a bias in the derived fit values of N_i associated with the relatively larger values of χ^2, or a combination of these factors. The larger errors in predicted values of S_{crit} from the *Weingartner et al.* model for NH_4NO_3 and H_2SO_4 suggest that the assumption on Φ and the goodness of fit are both important. NH_4NO_3 and H_2SO_4 exhibit values of Φ that change significantly with RH over the range of RH's during HTDMA studies, and the χ^2 values in Table 5.5 for NH_4NO_3 are approximately one order of magnitude larger than those for other compounds.

The results in Tables 5.5 and 5.6 indicate that the model of *Weingartner et al.* does not do as well for solution droplets formed on particles composed of NH_4NO_3, H_2SO_4, and internally mixed $(NH_4)_2SO_4$-NH_4NO_3. From the plots of osmotic coefficient values for these compounds (Fig. 5.4), it is evident that the osmotic coefficient varies with RH (NH_4NO_3 & H_2SO_4) and exhibits a value far from unity (NH_4NO_3, H_2SO_4 and $(NH_4)_2SO_4$-NH_4NO_3) for the RH range typical of HTDMA experiments. The other compounds studied here exhibit osmotic coefficient values that are closer to unity and do not vary as much as for NH_4NO_3, H_2SO_4 and $(NH_4)_2SO_4$-NH_4NO_3 so-

lutions. Therefore, the simpler model of *Weingartner et al.* is a reasonable approach for solutions with osmotic coefficients that do not vary significantly over the range of RH's for HTDMA studies and that are not significantly different from unity, the approximate value of Φ for solution droplets at their critical size (at S_{crit}). Although the current model for Φ, and therefore the simplified Köhler model, has its limitations, it may be applied more generally to particles composed of pure salts since a thermodynamically based model for Φ with correct limiting behavior has been integrated into the simplified Köhler model.

Values of Y were derived from the values of N_i reported in Tables 5.5 and 5.6 using Eqn. 5.20. For particles composed of single solutes, the agreement between values of Y reported in Table 5.2 and values derived from the N_i values for all compounds was between -4% (H_2SO_4) and -43% (NH_4NO_3). For comparison, the agreement between values of Y_f reported in Table 5.3 and values of Y in Table 5.2 was 6% for NaCl, -33% for $(NH_4)_2SO_4$, 15% for NH_4HSO_4, -41% for H_2SO_4 and 3% for NH_4NO_3. The agreement between values of Y in Table 5.2 and values derived from N_i values was poorer for the internally mixed compositions examined: between -52% (NaCl-NH_4NO_3) and -69% ($(NH_4)_2SO_4$-NH_4NO_3). In comparison, agreement between values of Y_f reported in Table 5.4 and values of Y in Table 5.2 was between -18% and -29%. The values of Y derived from the N_i values were always less than the values reported in Table 5.2. Results for 40 nm and 100 nm diameter particles were similar.

5.5 *Summary*

A simplified Köhler model was derived including a parameterization for the solution osmotic coefficient that approaches the correct thermodynamic limit as the solution becomes more dilute. The method involves fitting the proposed Köhler model to (D_{drop}, RH) data pairs obtained from HTDMA studies on a single dry particle size. Chemical composition dependent unknowns, Y_f and $\beta_{0,f}$, derived from the fit pro-

cedure are used to calculated S_{crit}. The various assumptions made in the simplified model, volume additivity, setting the surface tension of the droplet solution set equal to that for pure water, and a simplified parameterization for Φ, were independently tested for the range of RH values experienced in the HTDMA by comparing values of x_s, Φ, a_w, the Kelvin term, and RH from the simplified and reference models. These comparisons showed that the errors in RH values calculated from the simplified model were similar to uncertainties in the reference model values themselves and to typical errors in experimental RH for NaCl, NH_4NO_3, $(NH_4)_2SO_4$, and several internally mixed particle compositions. For NH_4HSO_4, the RH values from the reference and simplified models did not agree as well because the term involving m^2 in Φ is important for this compound and the full Pitzer model itself does not accurately reproduce the behavior of Φ for NH_4HSO_4 [*Kim et al.*, 1993]. The proposed technique was also tested on particles composed of H_2SO_4. The parameterization for Φ cannot accurately reproduce the variation of Φ with m.

The technique for using hygroscopic growth measurements at RHs<100% to derive the critical supersaturation required to activate a particle to a cloud droplet was studied numerically in order to validate that S_{crit} could be derived within experimental uncertainties in this parameter. The sensitivity of the predicted values of S_{crit} to assumed uncertainties in the input parameters was investigated as a function of dry particle chemical composition and size. The method is effective at predicting values of S_{crit} for 40 and 100 nm diameter particles composed of NaCl, $(NH_4)_2SO_4$, NH_4HSO_4, H_2SO_4, NH_4NO_3, and for the interally mixed compositions examined. The good agreement for H_2SO_4 was surprising, given the limitations of the parameterization of Φ. The good agreement is most likely due to the ability of the simplified Köhler model to capture the hygroscopic behavior of particles composed of H_2SO_4 through the fit routine-derived values of Y_f and $\beta_{0,f}$. Comparisons between values of S_{crit} predicted by the Köhler model proposed in this work and the model

proposed by *Weingartner et al.* [1997] indicated that both models produced results that agreed well with theoretical values of S_{crit}. However, for compounds where the osmotic coefficient varies significantly from its value at S_{crit}, the model proposed by *Weingartner et al.* will not predict accurate values of S_{crit}. Both models tend to underpredict values of S_{crit} compared to theory. This is due, in part, to the assumption that the solution surface tension can be replaced by the surface tension for pure water in the Kelvin term, resulting in an underprediction of the Kelvin term. Furthermore, the proposed parameterized form for Φ tends to overpredict Φ for most of the single solutes examined. Numerical sensitivity studies results on the Köhler model proposed here indicate that values of S_{crit} can be predicted within -7.5%±10% using the proposed technique, similar to estimated experimental uncertainties in S_{crit} in thermal gradient diffusion chambers.

Table 5.1: Values of critical diameters (nm), supersaturations (%) and osmotic coefficients at the critical supersaturation for chemical compositions studied in this work. Results are reported for indicated dry particle sizes and assumed temperature of 29.5°C .

	$D_{p,sol}$ (nm)			
	40	70	100	200
	Sodium Chloride NaCl			
D_{crit}	321	748	1285	3668
S_{crit}	0.475	0.203	0.119	0.042
Φ_{crit}	0.937	0.951	0.960	0.974
	Amm. Bisulf. NH_4HSO_4			
D_{crit}	210	484	829	2364
S_{crit}	0.730	0.314	0.184	0.064
Φ_{crit}	0.925	0.942	0.952	0.968
	Amm. Sulf. $(NH_4)_2SO_4$			
D_{crit}	210	504	879	2575
S_{crit}	0.705	0.295	0.170	0.058
Φ_{crit}	0.778	0.832	0.863	0.911
	Sulfuric Acid H_2SO_4			
D_{crit}	239	590	1039	1818
S_{crit}	0.603	0.249	0.143	0.012
Φ_{crit}	0.752	0.826	0.863	0.840
	Amm. Nitrate NH_4NO_3			
D_{crit}	255	598	1029	2944
S_{crit}	0.534	0.228	0.133	0.046
Φ_{crit}	0.922	0.943	0.954	0.971
	Sodium Chloride - Sodium Sulf. NaCl-Na_2SO_4			
D_{crit}	278	685	1185	3407
S_{crit}	0.447	0.190	0.110	0.038
Φ_{crit}	0.858	0.895	0.914	0.943
	Sodium Chloride - Amm. Sulf. NaCl-$(NH_4)_2SO_4$			
D_{crit}	166	421	730	2109
S_{crit}	0.709	0.304	0.176	0.061
Φ_{crit}	0.823	0.869	0.891	0.928
	Sodium Chloride - Amm. Nit. NaCl-NH_4NO_3			
D_{crit}	187	467	804	2288
S_{crit}	0.644	0.278	0.162	0.057
Φ_{crit}	0.916	0.939	0.950	0.968
	Amm. Sulf. - Amm. Nit. $(NH_4)_2SO_4$-NH_4NO_3			
D_{crit}	147	380	662	1915
S_{crit}	0.780	0.334	0.193	0.066
Φ_{crit}	0.799	0.855	0.881	0.922

Table 5.2: Values of $Y = \frac{\nu\rho_s}{M_s}$, β_0, Y_a, Y_b, Y_c, Y_f and $\beta_{0,f}$ for solute chemical compositions examined in this work. The units of all Y parameters are $10^{-3}\ m^{-3}$ and β_0 is dimensionless. Values of Y_f and $\beta_{0,f}$ were determined by fitting the product $Y_f\Phi_f$ to calculated values of the product $Y\Phi$.

Solute	Y	β_0	Y_a	Y_b	Y_c	Y_f	$\beta_{0,f}$
NaCl	74.09	0.1082	74.1	74.1	18.52	77.4	0.018
$(NH_4)_2SO_4$	40.16	0.04763	321.3	80.3	8.93	29.1	0.008
NH_4HSO_4	30.93	0.04494	30.93	30.93	7.73	33.3	0.006
H_2SO_4	56.35	-0.0933	450.8	112.7	12.5	2.0	21.8
NH_4NO_3	43.10	-0.0154	43.1	43.1	10.78	44.1	-0.004
NaCl-$(NH_4)_2SO_4$	49.2	0.078	197.7	77.2	13.7	43.1	0.013
$(NH_4)_2SO_4$-NH_4NO_3	41.3	0.016	182.2	61.7	9.9	36.3	-0.002
NaCl-NH_4NO_3	54.5	0.046	58.6	58.6	14.6	57.6	0.006
NaCl-Na_2SO_4	62.5	0.064	263.5	93.7	15.6	45.9	0.03

Table 5.3: Sensitivity of fit routine results as a function of particle composition, initial guess and assumed $D_{p,sol}$, RH and D_{drop} errors for 40 and 100 nm dry particle diameters and indicated compositions. Ratios of the standard deviation computed from the 100 different cases of applied error to the average values of Y_f, $\beta_{0,f}$ and S_{crit} were always less than 0.2, 1.3 and 0.16, respectively. Input RH's were calculated using the reference model. The simplified Köhler model was run with initial conditions equal to five times the perfect initial conditions for the cases including assumed uncertainties.

Case	$D_{p,sol}$ (nm)	Y_f	$\beta_{0,f}$	S_{crit} (%)	Error (%)	D_{crit} (nm)	Error (%)	χ^2
Sodium Chloride								
Perfect Input	40	81.653	0.01488	0.43	-10	315	-1	5.22e-01
5xICs	40	81.653	0.01488	0.43	-10	315	-1	5.22e-01
0.5% Error	40	80.944	0.01532	0.43	-10	316	-1	3.67e-02
1% Error	40	78.504	0.01754	0.43	-9	313	-2	3.90e-01
Perfect Input	100	80.098	0.01598	0.11	-9	1265	-1	7.14e-01
1% Error	100	78.349	0.01838	0.11	-8	1251	-2	3.63e-01
Ammonium Sulfate								
Perfect Input	40	28.723	0.01023	0.65	-8	208	0	2.84e-01
0.5% Error	40	28.549	0.01059	0.65	-7	208	0	4.02e-02
1% Error	40	28.367	0.01086	0.65	-7	206	-1	4.88e-01
Perfect Input	100	28.295	0.01093	0.16	-5	839	-4	2.66e-01
1% Error	100	26.889	0.01374	0.17	-2	816	-7	3.62e-01
Ammonium Bisulfate								
Perfect Input	40	35.801	0.00064	0.58	-20	232	10	7.48e-03
0.5% Error	40	35.653	0.00068	0.58	-20	231	10	3.70e-02
1% Error	40	34.939	0.00099	0.59	-19	229	9	3.75e-01
Perfect Input	100	34.784	0.00158	0.15	-20	929	12	1.09e-03
1% Error	100	32.987	0.00307	0.15	-19	918	10	3.84e-01
Sulfuric Acid								
Perfect Input	40	37.340	0.05529	0.56	-7	243	1	8.14e-01
0.5% Error	40	36.843	0.05864	0.56	-6	241	0	9.18e-02
1% Error	40	33.323	0.08634	0.59	-1	232	-2	3.82e-01
Perfect Input	100	35.986	0.06038	0.14	0	951	-8	1.46e+00
1% Error	100	34.050	0.08118	0.15	1	934	-10	3.80e-01
Ammonium Nitrate								
Perfect Input	40	44.386	-0.00418	0.52	-2	258	1	4.25e+00
0.5% Error	40	44.201	-0.00419	0.52	-2	258	1	1.91e-02
1% Error	40	42.899	-0.00415	0.53	0	252	0	3.31e-01
Perfect Input	100	44.073	-0.00388	0.13	-2	1047	1	1.44e+00
1% Error	100	42.812	-0.00377	0.13	-2	1045	1	3.36e-01

Table 5.4: Sensitivity of fit routine results as a function of particle composition, and assumed $D_{p,sol}$, RH and D_{drop} errors for 40 and 100 nm dry particle diameters and indicated equimolar mixtures of solutes. Ratios of the standard deviation computed from the 100 different cases of applied error to the average values of Y_f, $\beta_{0,f}$ and S_{crit} were always less than 0.2, 1.3 and 0.16, respectively. The input RH's used in the fit routine were calculated using the reference model. The simplified Köhler model was run with initial conditions equal to the perfect initial conditions for the cases including assumed uncertainties.

Case	$D_{p,sol}$ (nm)	Y_f	$\beta_{0,f}$	S_{crit} (%)	Error (%)	D_{crit} (nm)	Error (%)	χ^2
Sodium Chloride - Ammonium Sulfate								
Perfect Input	40	43.140	0.01317	0.74	4	183	10	5.89e-01
With 1% Error	40	40.835	0.01727	0.76	7	177	6	3.76e-01
Perfect Input	100	42.096	0.01456	0.19	5	728	0	6.91e-01
With 1% Error	100	40.336	0.01719	0.19	6	718	-1	3.37e-01
Ammonium Sulfate - Ammonium Nitrate								
Perfect Input	40	36.247	-0.00233	0.81	3	166	12	1.48e-01
With 1% Error	40	34.850	-0.00169	0.83	6	162	10	3.01e-01
Perfect Input	100	35.611	-0.00183	0.20	4	670	1	1.19e-01
With 1% Error	100	33.536	-0.00043	0.21	6	654	-1	2.79e-01
Sodium Chloride - Ammonium Nitrate								
Perfect Input	40	57.578	0.00625	0.64	0	210	12	1.07e-01
With 1% Error	40	55.991	0.00734	0.64	0	210	12	3.36e-01
Perfect Input	100	56.508	0.00717	0.16	-1	848	5	1.71e-01
With 1% Error	100	54.910	0.00823	0.16	-1	845	5	3.02e-01
Sodium Chloride - Sodium Sulfate								
Perfect Input	40	45.869	0.03092	0.71	13	190	0	1.52e+00
With 1% Error	40	45.040	0.03302	0.72	15	188	-1	3.79e-01
Perfect Input	100	46.140	0.02974	0.18	13	766	-8	1.01e+00
With 1% Error	100	44.288	0.03403	0.18	15	758	-9	4.32e-01

Table 5.5: Comparison of results from fit routine using the model proposed in this work and that from *Weingartner et al.* [1997]. Results are shown as a function of particle composition, and assumed $D_{p,sol}$, RH and D_{drop} errors for a 40 nm dry particle diameter and indicated equimolar mixtures of solutes for internally mixed particles. First row for each compound lists results for no applied error, second row lists results for assumed 1% error in each input parameter. The ratio of the standard deviation of predicted values of S_{crit} to the average of the predicted values of S_{crit} for the 100 cases with applied error was always less than 0.16. The simplified Köhler model was run with initial conditions equal to the perfect initial conditions for the cases including assumed uncertainties. N_i denotes the number of ions formed upon dissociation of the solute, and is the one unknown in the model of *Weingartner et al.* [1997]. $S_{crit,w}$ and $S_{crit,tw}$ are the predicted critical supersaturations from the model of *Weingartner et al.* and this work, respectively.

Compound	N_i (ions)	$S_{crit,w}$ (%)	$S_{crit,tw}$ (%)	Error,w (%)	Error,tw (%)	χ^2
NaCl	1.38e+06	0.40	0.43	-15.7	-10.1	5.22e-01
	1.37e+06	0.40	0.43	-15.3	-9.5	9.50e-01
$(NH_4)_2SO_4$	5.64e+05	0.63	0.65	-11.3	-8.5	2.84e-01
	5.56e+05	0.63	0.65	-10.7	-7.4	6.28e-01
NH_4HSO_4	5.55e+05	0.63	0.58	-13.7	-20.8	7.48e-03
	5.49e+05	0.63	0.59	-13.2	-19.7	2.76e-01
H_2SO_4	1.10e+06	0.45	0.56	-25.7	-7.1	8.14e-01
	1.09e+06	0.45	0.59	-25.3	-1.0	1.84e+00
NH_4NO_3	5.04e+05	0.66	0.52	23.9	-2.8	4.25e+00
	4.96e+05	0.67	0.53	24.8	-0.6	3.80e+00
NaCl-$(NH_4)_2SO_4$	4.56e+05	0.70	0.74	-1.8	4.1	5.89e-01
	4.50e+05	0.70	0.76	-1.1	7.3	8.14e-01
$(NH_4)_2SO_4$-NH_4NO_3	2.63e+05	0.92	0.81	17.6	3.9	1.48e-01
	2.59e+05	0.92	0.83	18.5	6.6	3.57e-01
NaCl-NH_4NO_3	5.29e+05	0.65	0.64	0.4	-0.9	1.07e-01
	5.23e+05	0.65	0.64	1.0	-0.7	3.66e-01
NaCl-Na_2SO_4	6.00e+05	0.61	0.71	-2.9	13.7	1.52e+00
	5.91e+05	0.61	0.72	-2.2	15.2	1.55e+00
Avg. Err.				-2.6	-1.1	
Std. Dev.				16	10	

Table 5.6: Comparison of results from fit routine using the model proposed in this work and that from *Weingartner et al.* [1997]. Results are shown as a function of particle composition, and assumed $D_{p,sol}$, RH and D_{drop} errors for a 100 nm dry particle diameter and indicated equimolar mixtures of solutes for internally mixed particles. First row for each compound lists results for no applied error, second row lists results for assumed 1% error in each input parameter. The ratio of the standard deviation of predicted values of S_{crit} to the average of the predicted values of S_{crit} for the 100 cases with applied error was always less than 0.16. The simplified Köhler model was run with initial conditions equal to the perfect initial conditions for the cases including assumed uncertainties. Column headings as in Table 5.5.

Compound	N_i (ions)	$S_{crit,w}$ (%)	$S_{crit,tw}$ (%)	Error,w (%)	Error,tw (%)	χ^2
NaCl	2.17e+07	0.10	0.11	-15.1	-9.9	7.14e-01
	2.15e+07	0.10	0.11	-14.8	-8.8	7.48e-01
$(NH_4)_2SO_4$	8.64e+06	0.16	0.16	-6.0	-5.1	2.66e-01
	8.54e+06	0.16	0.17	-5.4	-2.3	9.59e-01
NH_4HSO_4	8.71e+06	0.16	0.15	-13.5	-20.9	1.09e-03
	8.64e+06	0.16	0.15	-13.1	-20.0	5.71e-01
H_2SO_4	1.71e+07	0.11	0.14	-20.3	0.1	1.46e+00
	1.70e+07	0.11	0.15	-19.9	1.9	2.19e+00
NH_4NO_3	8.30e+06	0.16	0.13	22.6	-2.9	1.44e+00
	8.22e+06	0.16	0.13	23.2	-2.8	2.16e+00
NaCl-$(NH_4)_2SO_4$	7.03e+06	0.18	0.19	0.6	5.2	6.91e-01
	6.98e+06	0.18	0.19	1.0	6.7	1.14e+00
$(NH_4)_2SO_4$-NH_4NO_3	4.13e+06	0.23	0.20	19.8	4.5	1.19e-01
	4.07e+06	0.23	0.21	20.6	6.6	2.13e-01
NaCl-NH_4NO_3	8.26e+06	0.16	0.16	0.9	-1.4	1.71e-01
	8.17e+06	0.16	0.16	1.5	-1.4	6.49e-01
NaCl-Na_2SO_4	9.05e+06	0.16	0.18	0.8	14.0	1.01e+00
	8.90e+06	0.16	0.18	1.6	15.4	1.06e+00
Avg. Err.				-5.9	-5.2	
Std. Dev.				15	10	

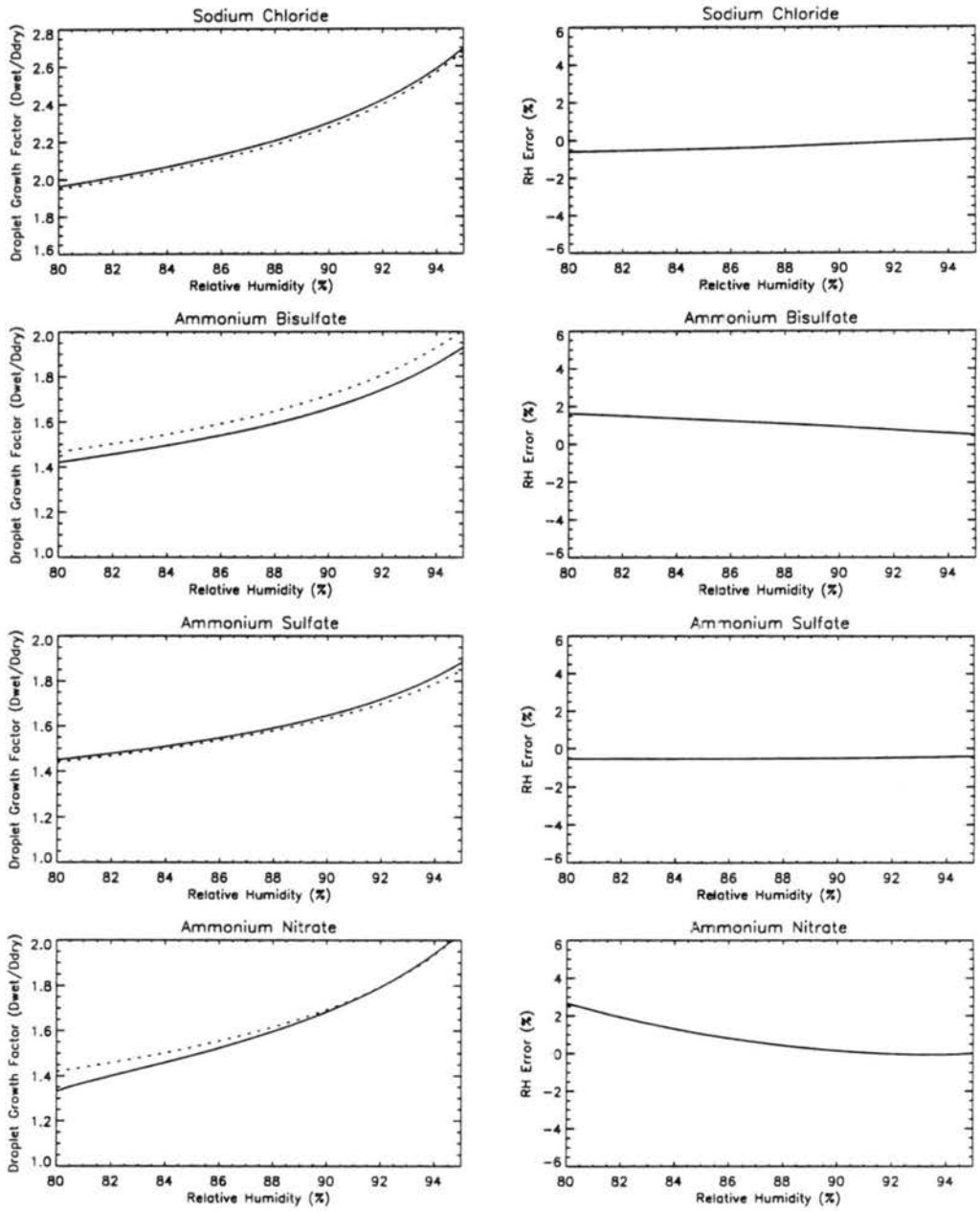

Figure 5.1: (a) Comparison of equilibrium RH's from the results of *Tang and Munkelwitz* [1994] and the reference Köhler model of this work for NaCl, NH_4HSO_4, $(NH_4)_2SO_4$, and NH_4NO_3. Dashed lines designate Tang's results, solid line indicates results from reference Köhler model. Right column shows the percent error between values of RH from *Tang and Munkelwitz* [1994] and the reference Köhler model.

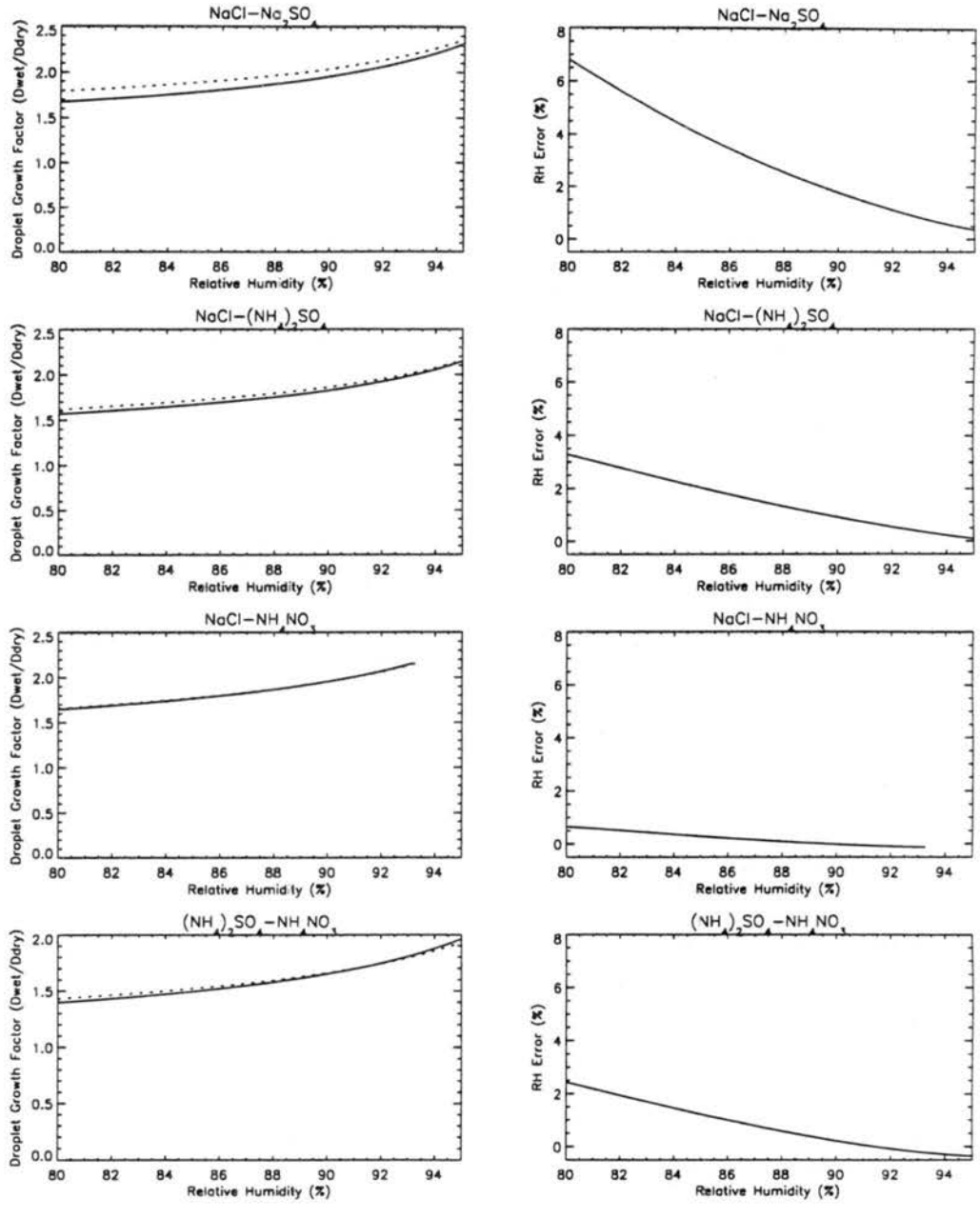

Figure 5.1: (b) Comparison of ZSR/Tang and reference/Pitzer Köhler model results for internally mixed solutes. Dashed lines designate results from ZSR model, solid line indicates results from reference Köhler model. Right column shows the percent error between values of RH from ZSR/Tang and the reference Köhler model. Extended ZSR/Tang model was used for internally mixed NaCl-Na_2SO_4 calculations.

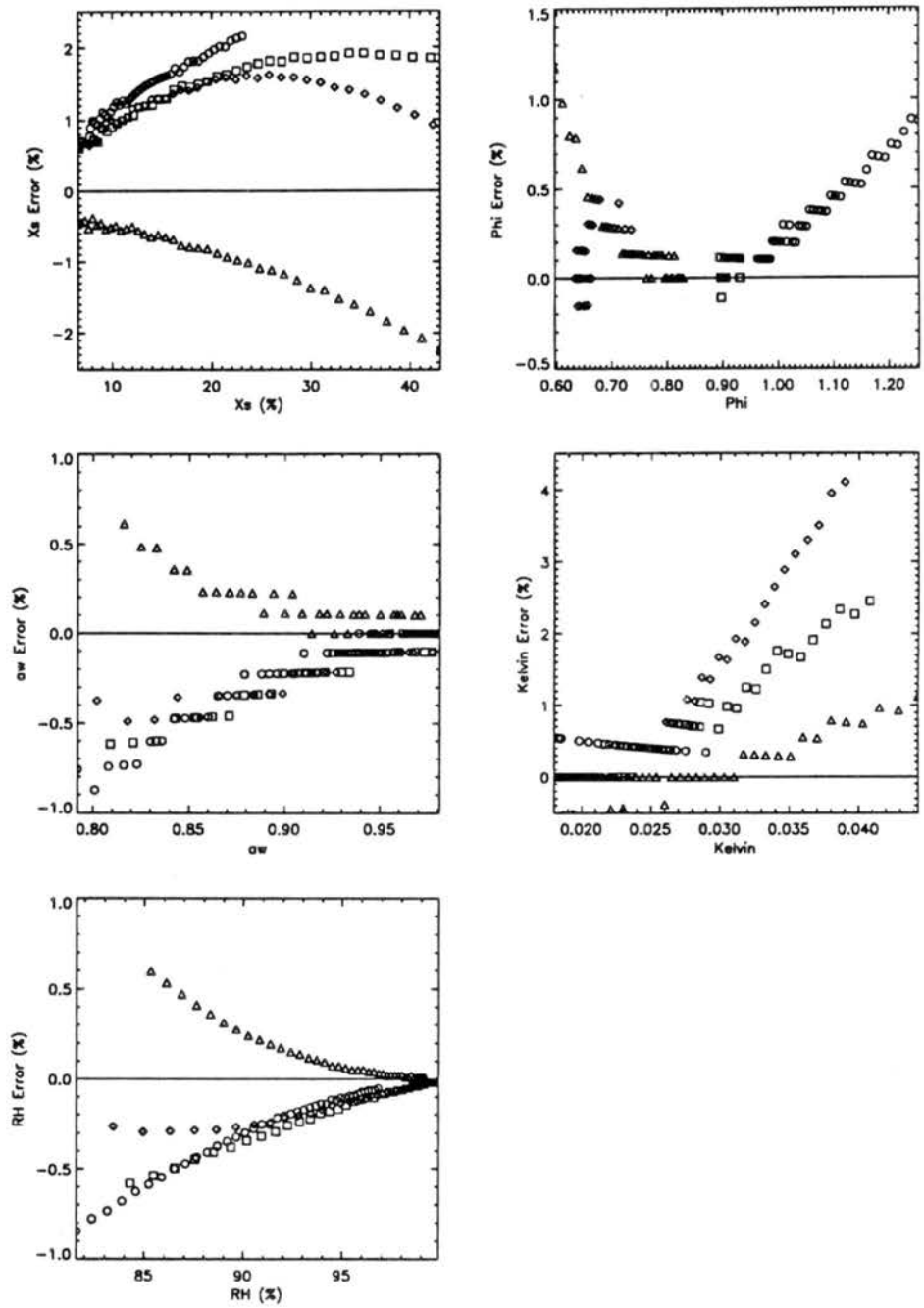

Figure 5.2: Sensitivity study results for volume additivity assumption. Errors (%) in x_s, Φ, a_w, natural log of Kelvin term, and RH due to assumption of volume additivity for different solute chemical compositions studied. Circles designate NaCl, squares designate NH_4HSO_4, diamonds designate $(NH_4)_2SO_4$, and triangles designate NH_4NO_3. A dry particle size of 40 nm was assumed for all calculations. Solid horizontal lines designate zero percent error.

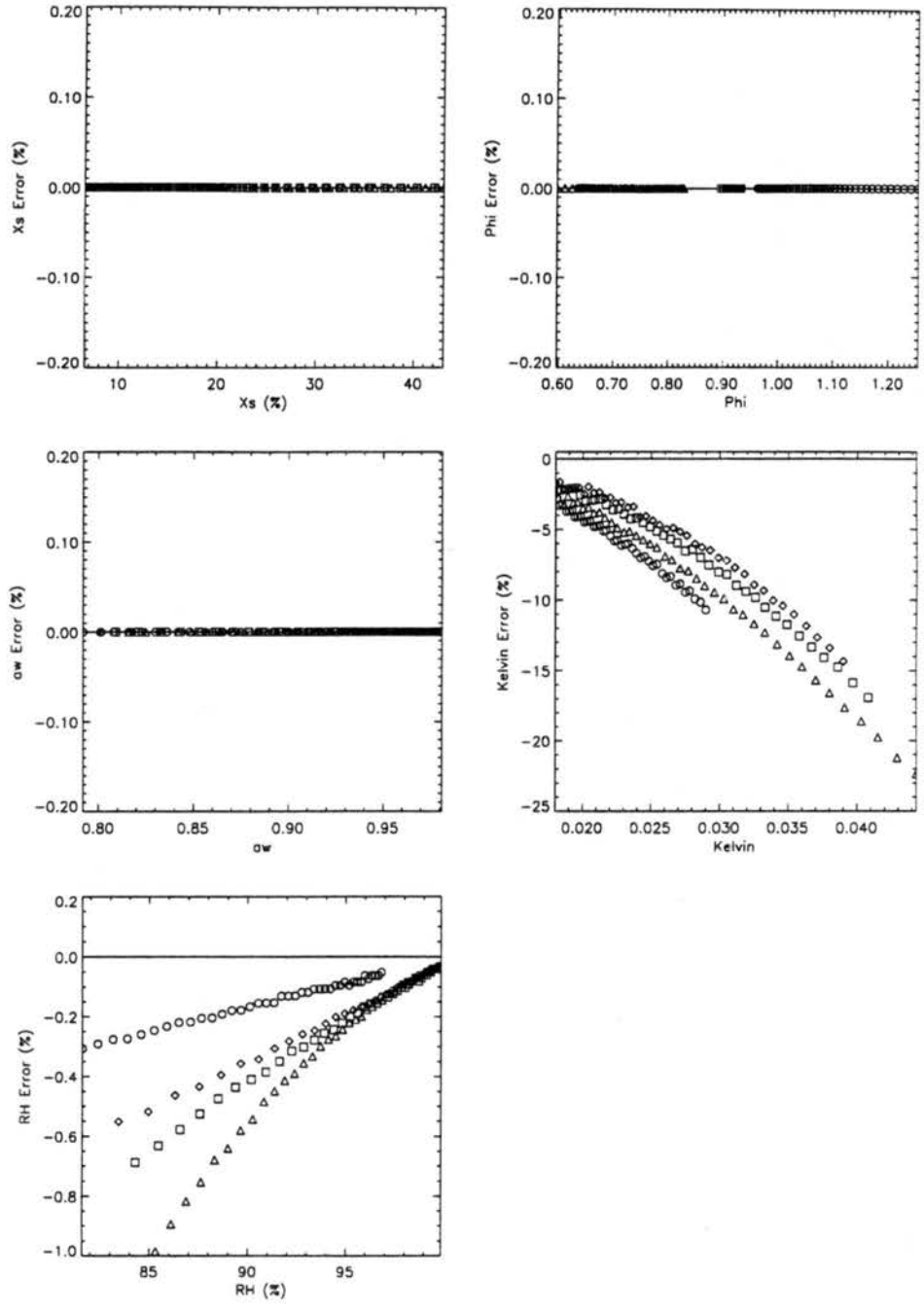

Figure 5.3: Sensitivity study results for surface tension assumption. Circles designate NaCl, squares designate NH_4HSO_4, diamonds designate $(NH_4)_2SO_4$, and triangles designate NH_4NO_3. A dry particle size of 40 nm was assumed for all calculations. Solid horizontal lines designate zero percent error.

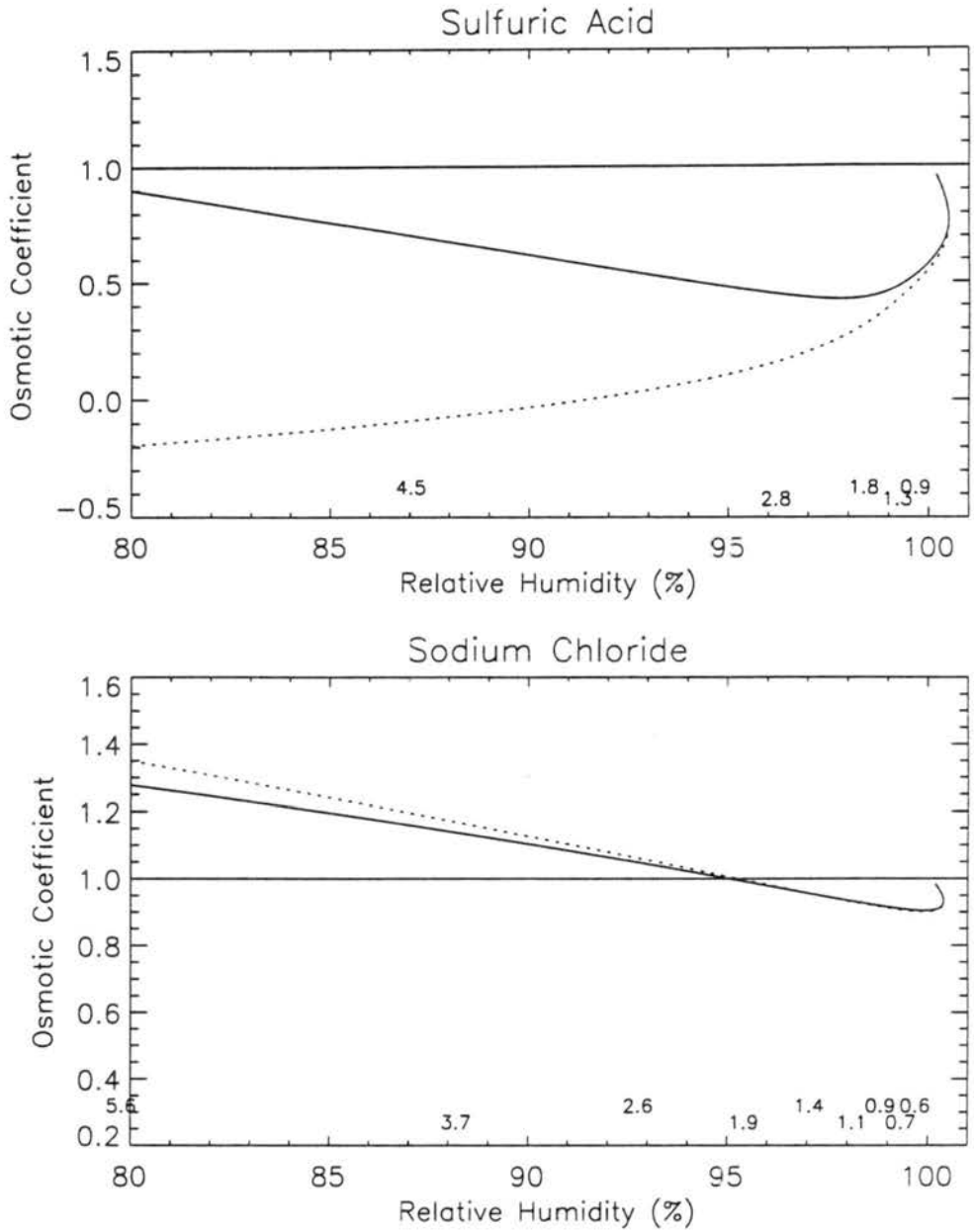

Figure 5.4: Values of the osmotic coefficient for compositions studied in this work. Values of solution molality are listed along x-axis. Solid curve represents calculations using the full Pitzer model. Dashed curve represents calculations using the simplified model of Φ neglecting terms involving m^2 and β_1. Solid horizontal line represents the value of Φ for infinitely dilute solutions, unity.

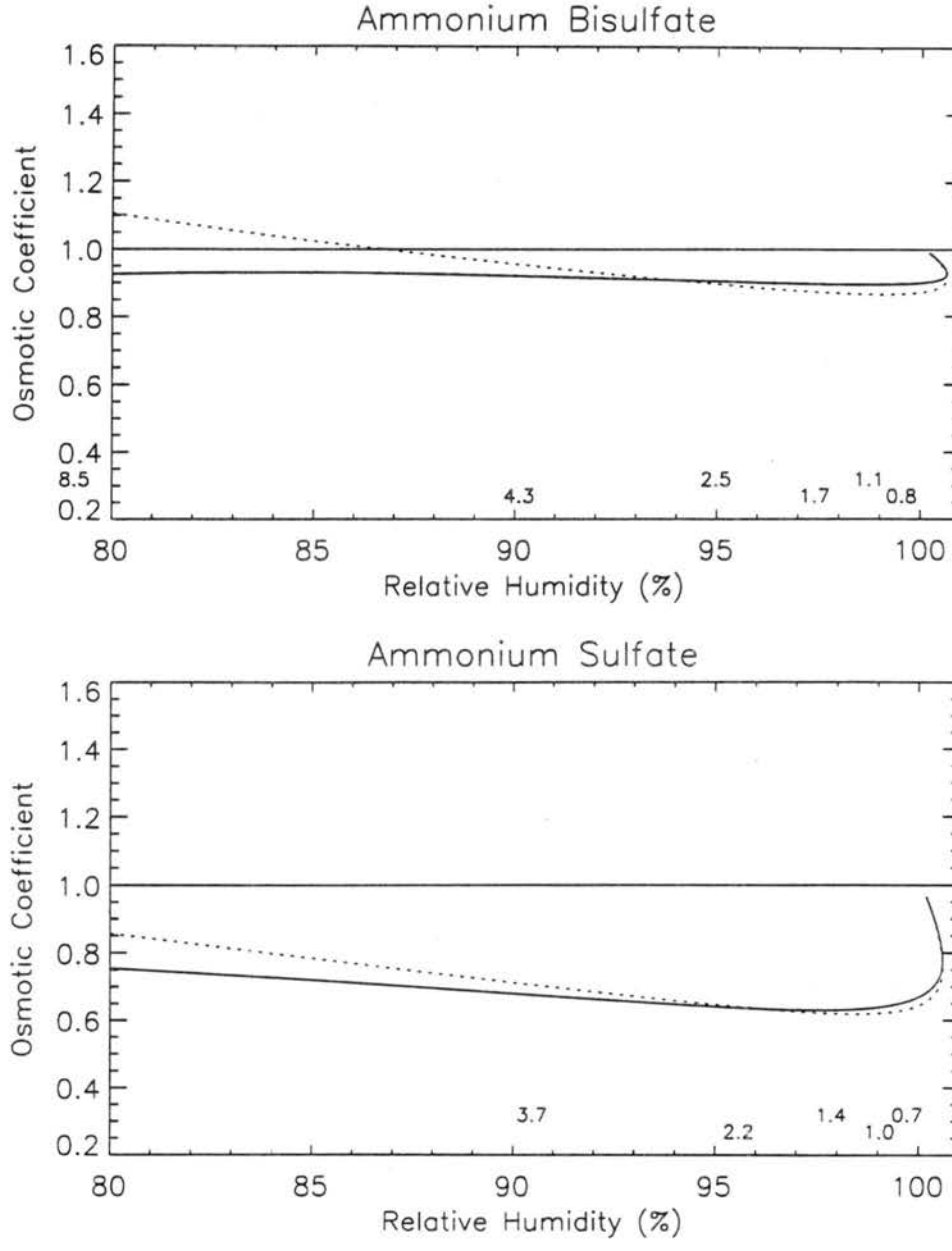

Figure 5.4: (cont.) Values of the osmotic coefficient for compositions studied in this work. Values of solution molality are listed along x-axis. Solid curve represents calculations using the full Pitzer model. Dashed curve represents calculations using the simplified model of Φ neglecting terms involving m^2 and β_1. Solid horizontal line represents the value of Φ for infinitely dilute solutions, unity.

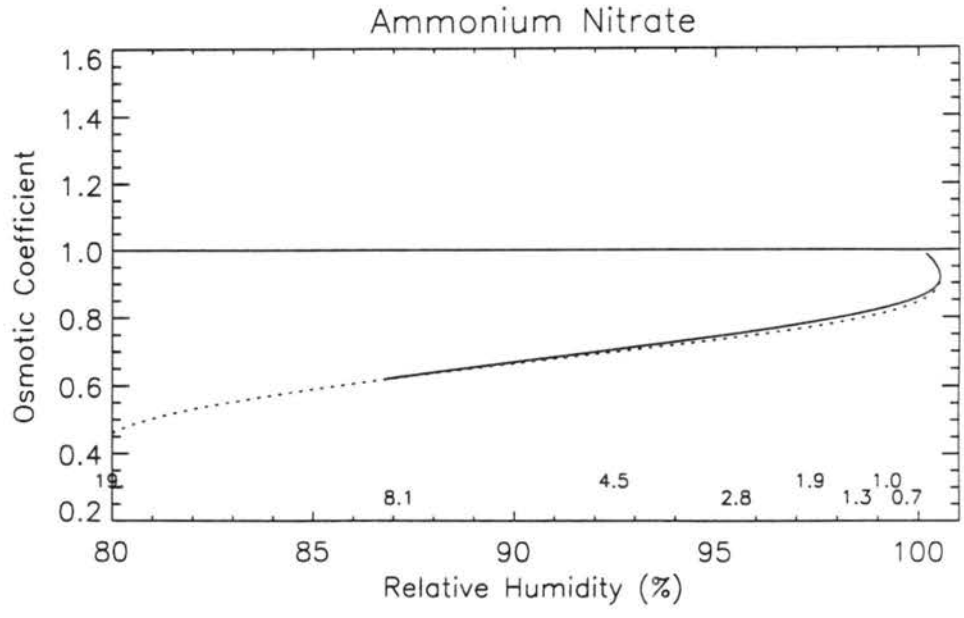

Figure 5.4: (cont.) Values of the osmotic coefficient for compositions studied in this work. Values of solution molality are listed along x-axis. Solid curve represents calculations using the full Pitzer model. Dashed curve represents calculations using the simplified model of Φ neglecting terms involving m^2 and β_1. Solid horizontal line represents the value of Φ for infinitely dilute solutions, unity.

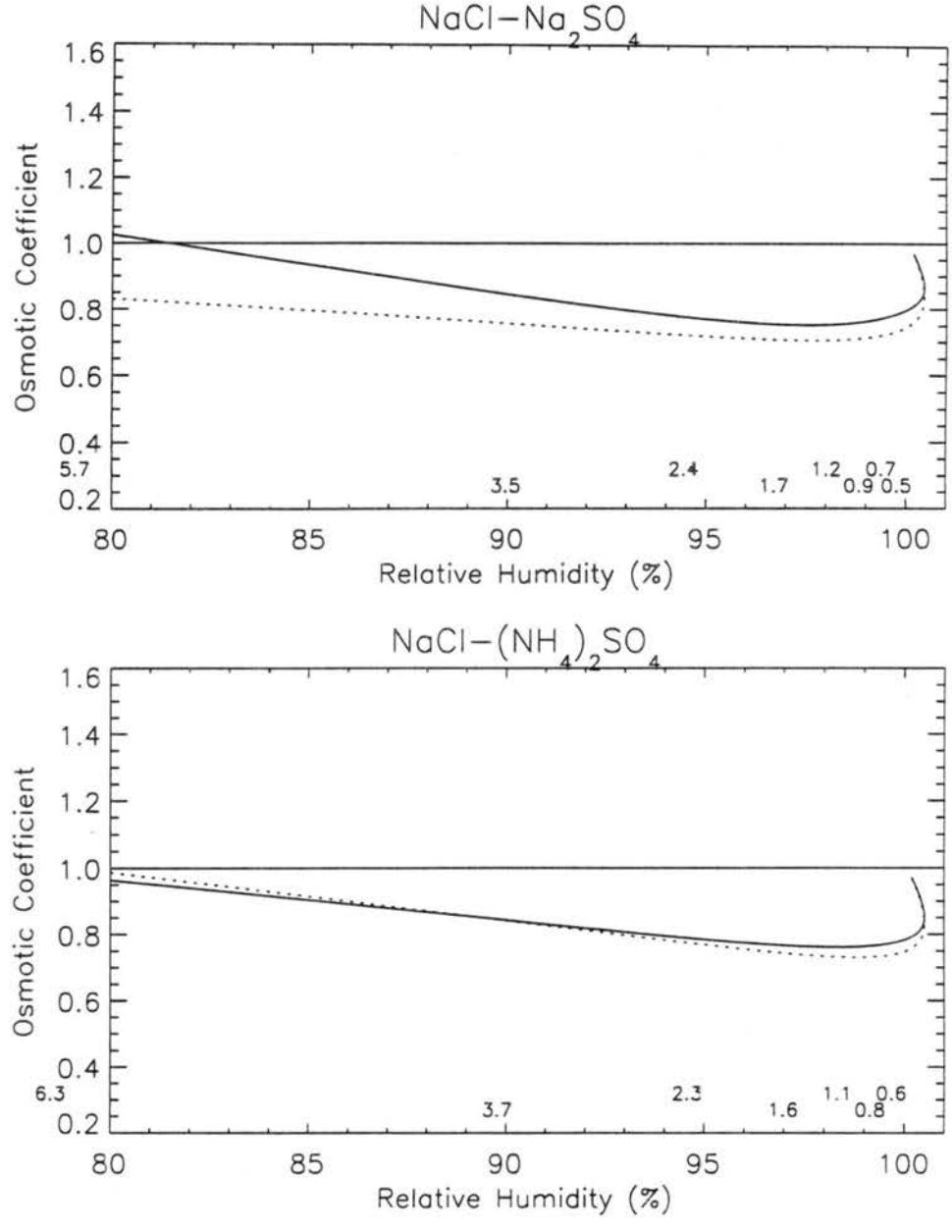

Figure 5.4: (cont.) Values of the osmotic coefficient for compositions studied in this work. Values of solution molality are listed along x-axis. Solid curve represents calculations using the full Pitzer model and the mole weighting approach outlined in chapter 4. Dashed curve represents calculations using the simplified model of Φ neglecting terms involving m^2 and β_1. Solid horizontal line represents the value of Φ for infinitely dilute solutions, unity.

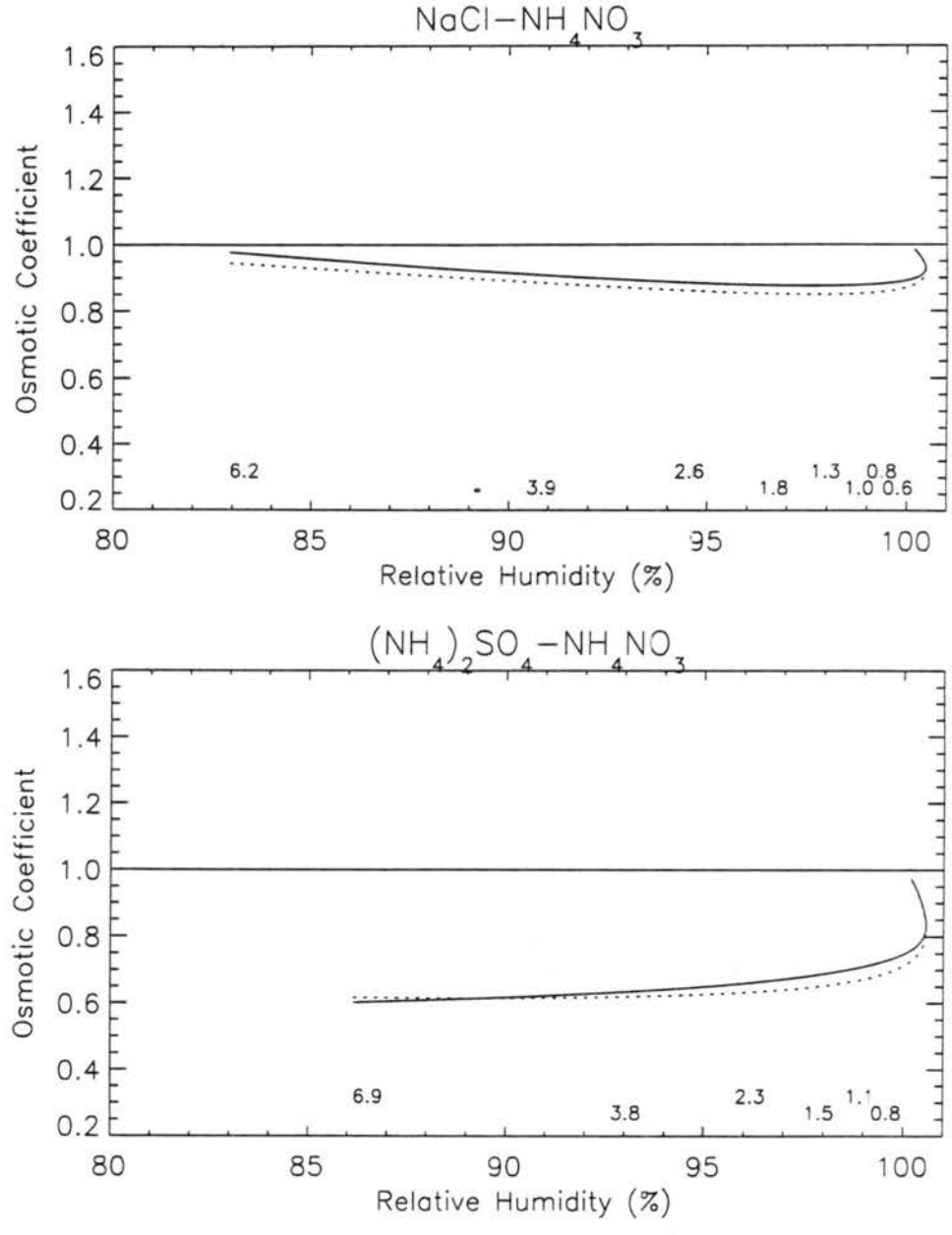

Figure 5.4: (cont.) Values of the osmotic coefficient for compositions studied in this work. Values of solution molality are listed along x-axis. Solid curve represents calculations using the full Pitzer model and the mole weighting approach outlined in chapter 4. Dashed curve represents calculations using the simplified model of Φ neglecting terms involving m^2 and β_1. Solid horizontal line represents the value of Φ for infinitely dilute solutions, unity.

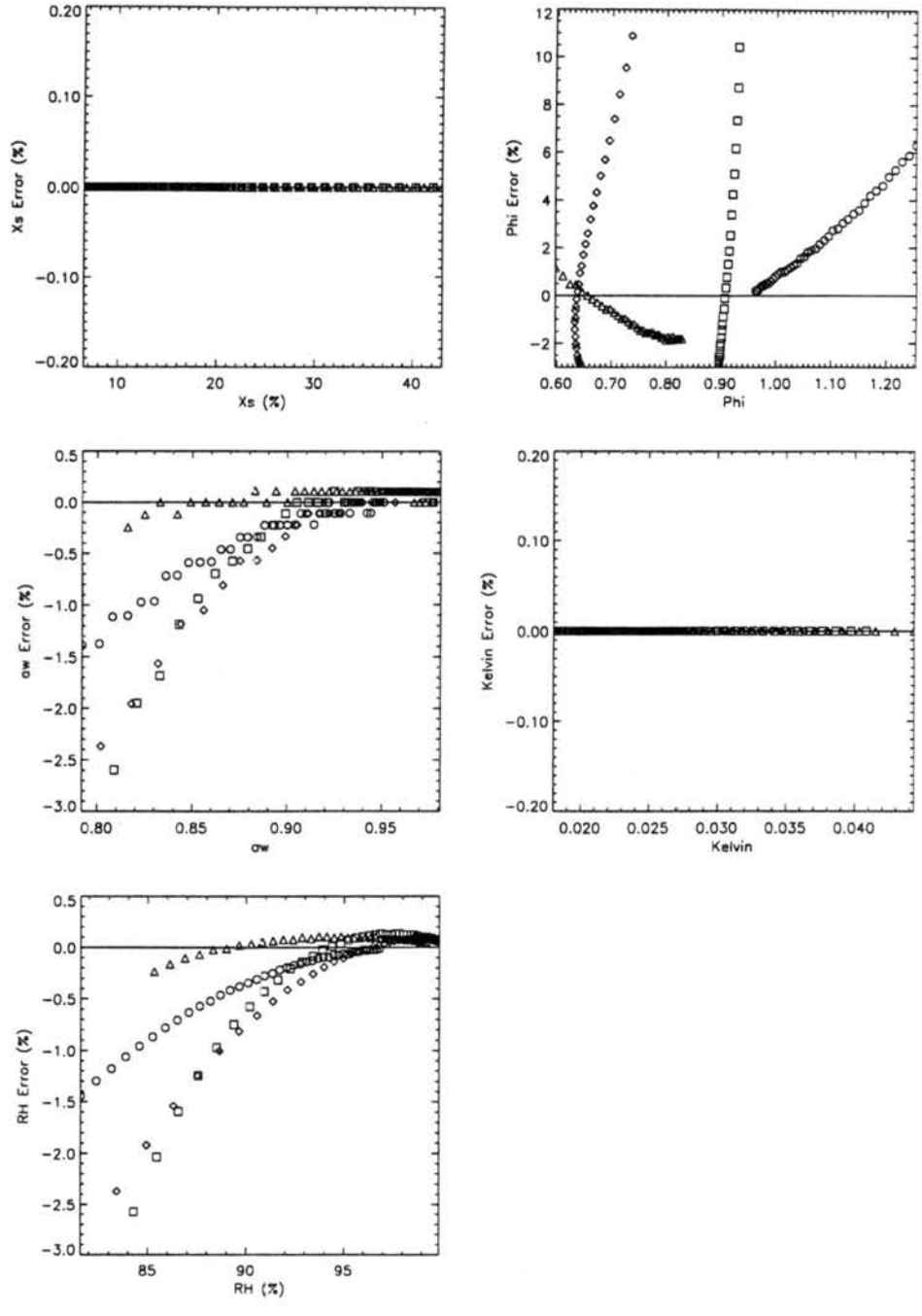

Figure 5.5: Sensitivity study results for simplified Eqn. 5.5. Circles designate NaCl, squares designate NH_4HSO_4, diamonds designate $(NH_4)_2SO_4$, and triangles designate NH_4NO_3. A dry particle size of 40 nm was assumed for all calculations. Solid horizontal lines designate zero percent error.

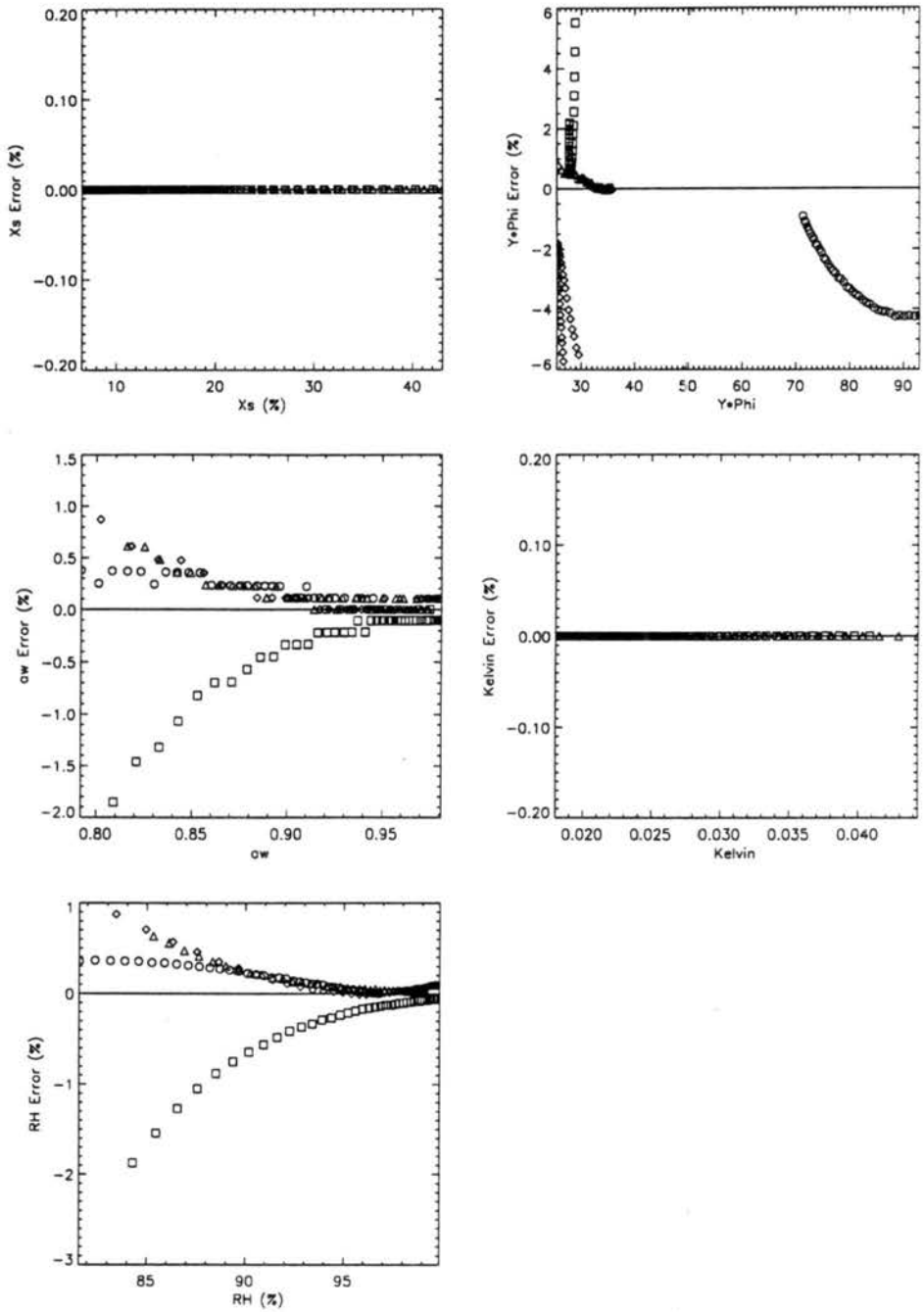

Figure 5.6: Sensitivity study results for assumption that $Y_f\Phi_f = Y\Phi$ where Y_f is determined from fit of $Y_f\Phi_f$ to $Y\Phi$ data. The values of Y_f and $\beta_{0,f}$ in Table 5.2 were used to calculate a_w. Circles designate NaCl, squares designate NH_4HSO_4, diamonds designate $(NH_4)_2SO_4$, and triangles designate NH_4NO_3. A dry particle size of 40 nm was assumed for all calculations. Solid horizontal lines designate zero percent error.

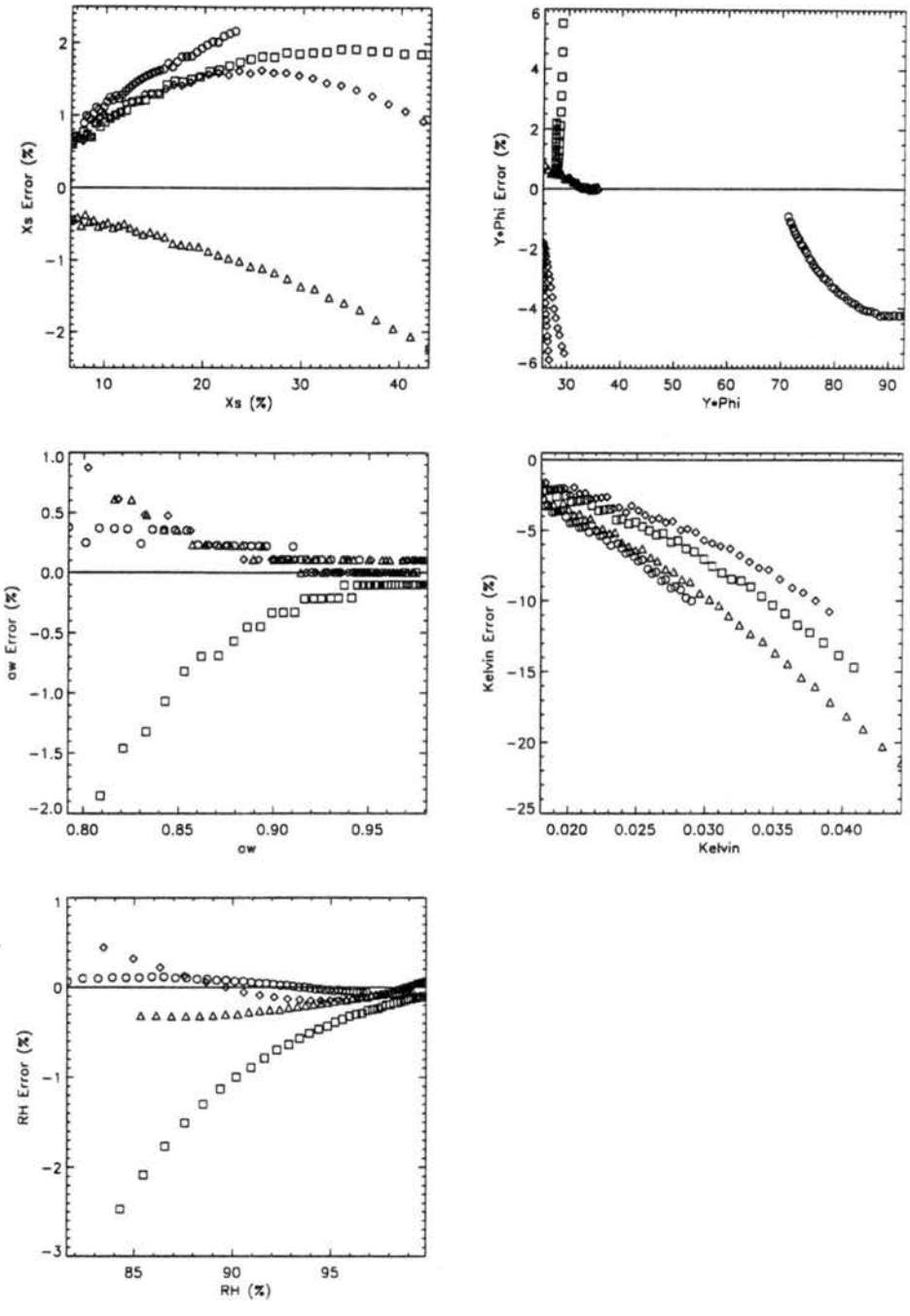

Figure 5.7: Sensitivity study results for all assumptions simultaneously. Circles designate NaCl, squares designate NH_4HSO_4, diamonds designate $(NH_4)_2SO_4$, and triangles designate NH_4NO_3. A dry particle size of 40 nm was assumed for all calculations. Solid horizontal lines designate zero percent error.

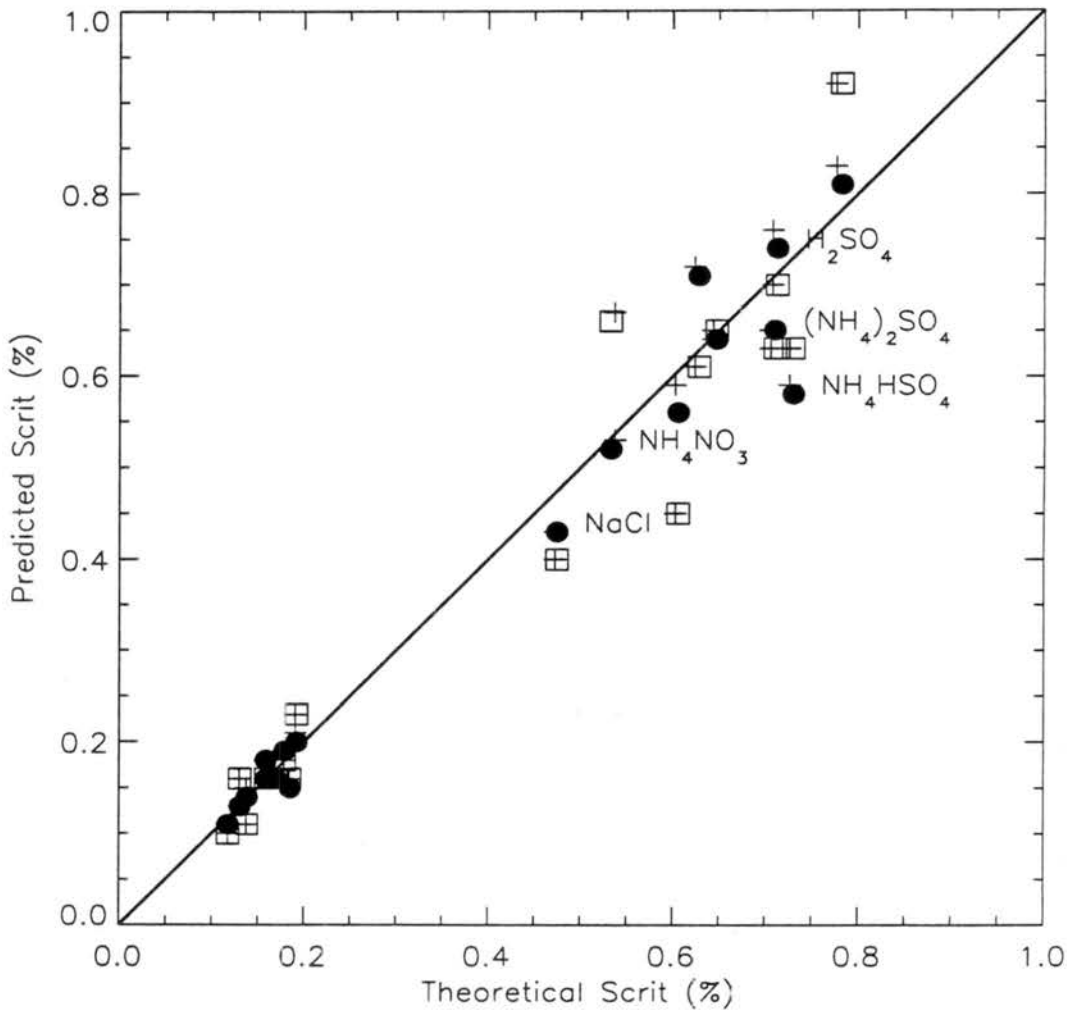

Figure 5.8: Comparison of theoretical and predicted values of S_{crit} from two Köhler models for all chemical compositions examined in this work and particle sizes of 40 nm and 100 nm (smaller values). Solid line is 1:1 line. Squares designate results from the model of *Weingartner et al.* and solid dots values from the model of this work. Plus symbols designate results of fit routine with no applied random uncertainties to the input data.

Chapter 6

Description of Measurement Techniques

6.1 *Introduction*

In this chapter the theory, operating characteristics and limitations of the individual instruments are described. The chapter includes subsections describing the particle generation system and particle sizing using the differential mobility analyzer. Then, a discussion of particle counting techniques using the continuous flow condensation particle counter (CPC) is provided. The operating characteristics of the thermal gradient diffusion cloud chamber used in this work are presented, and section six describes the theory of operation of the Humidified Tandem Differential Mobility Analyzer system in detail. Section seven presents the details of the important subsystems, including the RH and temperature measurement techniques and calibration procedures, the control and data acquisition system for the hygroscopicity system, flow measurements, and the algorithms used for control of the TDMA, DMPS and CCN systems. A discussion of how the various measurements were integrated together is provided in section eight. Experimental uncertainties in the various measurements are calculated in section nine.

6.2 *Particle Generation System*

A TSI Model 3760 Constant Output Atomizer (TSI Inc., Minneapolis, Minnesota) was used to generate particles of known chemical composition for all studies except those on ambient particles. Salt solutions were made by combining a known volume of Nanopure water with a known mass of salt. Only reagent grade chemicals were used to make the salt solutions, and all surfaces of the atomizer assembly that contacted the salt solution were thoroughly rinsed with Nanopure water before and after each use. Water volumes were measured using Erlenmeyer flasks to within ± 1 ml. Salt mass was measured with a Mettler Analytical Balance (Model AG204) to within ± 0.0001 g. The exact water volume and salt mass mixed were not important since the differential mobility analyzer selects the desired size from the polydisperse particle size distribution produced by the atomizer. However, to minimize the influence of larger, multiply charged particles the solutions were mixed to produce a polydisperse particle distribution with a number concentration peak at 40 nm dry particle diameter.

The atomizer operates by pulling the salt solution upwards out of a reservoir bottle and into a metal block using a venturi effect produced when dry, particle free, compressed air is passed through a nozzle with the air flow perpendicular to the hole supplying solution to the block. The atomizer was always operated at a clean air pressure of 30 psig. The air stream breaks up the exiting stream of salt solution into droplets with a nominal diameter of 0.35 μm and carries them out of the atomizer block and into an initial dilution and drying system. By controlling the concentration of the salt in the atomized solution, the final dry size of the particle that is produced when the droplets evaporate can be controlled. All air flows generated from the compressed air source were passed through a coalescing filter with a carbon membrane to remove oil droplets and organic vapors. The atomizer and dilution system air flows were dried to RH's between 2 and 10% using in-line Drierite^{TM} columns (W. C. Hammond Inc., Xenia, Ohio). The atomizer produces on the order

of 10^8 particles cm^{-3}, therefore it is necessary to dilute the output flow to produce acceptable particle concentrations. The output flow was first split so that some of the flow passed through a HEPA filter and the remainder passed through a metering valve used to regulate the flow passing through the filter. A water trap was used before the HEPA filter to capture large water drops. The two flows were recombined before passing into a diffusion dryer to remove water vapor and reduce the air flow RH to below 25%. Once dried, the particle stream was passed into a final dilution/drying system where the particle concentration was diluted with dry, particle free air with dilution ratios between 1:1 and 50:1.

The first DMA of the HTDMA system sampled directly from the final dilution system and the input RH at the polydisperse sample inlet of the DMA was monitored throughout the study. The polydisperse air flow RH entering DMA1 was kept below 10% for all studies except those on ammonium bisulfate and ambient particles, when the RH was kept below 2%. The amount of dilution required was determined by observing the output concentration from DMA1 using an Ultrafine Condensation Particle Counter (UCPC), the operation of which is described below. The dilution was set so that the output concentration of DMA1 was near 1000 cm^{-3}, to insure acceptable counting statistics in the CCN counter and after DMA2.

6.3 *The Differential Mobility Analyzer*

Determining the size of particles present in a sample of ambient or laboratory air is a critical part of the measurements performed in this work. Therefore, in this section the fundamental principles of operation of the instrument used to measure particle size, the differential mobility analyzer, are described in some detail.

The basic design of the DMA has remained essentially unchanged for several decades (see Hewitt, 1957). TSI Model 3071 DMA's were used in this study. The device consists of two concentric cylinders that are electrically isolated from each

other; an electric field of controlled voltage is maintained between the cylinders. Depicted schematically in Figure 6.1, there are four key air flows within the DMA: an aerosol sample inlet flow (q_a), a sheath air inlet flow (q_{sh}), a monodisperse aerosol outlet flow (q_s) and an excess air outlet flow (q_e). Because the DMA uses an electric field to move particles of a given size into the mondisperse outlet flow, and since the charge carried on the surface of an aerosol particle is not a function of the particle chemistry, the size classification of particles using the DMA does not depend on the chemical composition of the aerosol being studied. We do note, however, that the electrical mobility diameter does depend on the shape of the particle. Normally the particle is assumed to be spherical, however, a shape factor is necessary for non-spherical particles (e.g. NaCl). The use of an electric field in the DMA to size classify particles requires that the distribution of electrical charges on the aerosol as a function of size be well characterized before the aerosol encounters the electric field inside the instrument. This is accomplished using a source of beta particles, radioactive Krypton-85 gas, to bombard the particle with ions and force a known distribution of charge on the aerosol as a function of particle size before the particles enter the electric field. In our studies the work of *Wiedensohler* [1988] was used to calculate the distribution of charges on the aerosol as a function of size after the aerosol were passed through the Krypton-85 charge neutralizer.

Depending on the size of the particle selected by the DMA, only a relatively small fraction (between 5% and 20%) of the particles present in the original air sample are actually charged by the aerosol neutralizer so that they may be size classified by the DMA. Because the voltage of the DMA is only of a certain, single sign, about 50% of the charged particles, those with a charge opposite in sign to the voltage of the DMA, will actually be able to exit the monodisperse outlet flow. The result is that sizing particles using a DMA during low aerosol number concentration conditions can be very difficult and extremely time consuming in order to ensure that Poisson counting

statistical uncertainties are acceptably low. Diffusional losses of particles within the DMA, particularly for sizes below around 40 nm, also act to reduce the actual fraction of particles observed within a given size bin of the aerosol size distribution.

The way in which particle sizing is accomplished in the DMA is through a force balance between the electric field force which acts to pull particles with positive charge toward the negatively charged center rod, and the viscous, or friction, force which acts to retard the motion of the particles toward the center rod. The radial electric field in the DMA column has electric field vectors pointing from the outer rod toward the center rod, and therefore tends to push particles which have a sign opposite that of the center rod toward the center rod and eventually toward the monodisperse outlet sampling slits (see Figure 6.1). The viscous force which resists this motion can be expressed using a Stokes drag law formulation with the appropriate Cunningham correction factor to account for non-continuum effects for particles smaller than the mean free path of air molecules at the measurement conditions. The process by which particles of a known size are selected from an ambient or laboratory polydisperse distribution of aerosol proceeds as follows: first, the sample aerosol is dried as described in the previous section; this is done to ensure that sizing measurements are not influenced during the measurement process by variations in sample flow relative humidity. Second, the polydisperse aerosol is passed through the aerosol charge neutralizer with the Krypton-85 gas as described above and shown in Figure 6.1. As stated previously, the charge neutralizer insures that the particles of a certain size have known singly, doubly, triply and higher charged fractions. It should be noted that, in general, the majority of particles exiting the neutralizer actually have no net electrical charge and therefore cannot be size-classified by the DMA. Next the particles enter the annular space between the center rod and the outer rod and are separated from the outer diameter of the inner rod by the dried, filtered sheath air flow. For a certain value of the electric field strength (i.e. voltage) between the center and outer rods of the DMA

column, the electrical mobility of a particle is determined by the diameter of the particle, and by the temperature and pressure conditions that determine the air viscosity and mean free path, which are used to calculate the particle electrical mobility. The relationship between electrical mobility and particle size is given by

$$Z_p = \frac{neC_c}{3\chi\pi\nu_{air}D_p} \tag{6.1}$$

where Z_p is the electrical mobility, n is the number of charges carried by the particle, e is the elementary electric charge, χ is a shape factor that accounts for non-spherical particles [*Hinds*, 1982], ν_{air} is the dynamic viscosity of air, given by *Kinney et al.* [1991]

$$\nu_{air} = 1.83245x10^{-5}\left[\frac{T_{ref}+110.4}{T+110.4}\right]exp\left[1.5ln\left(\frac{T}{T_{ref}}\right)\right] \tag{6.2}$$

where T_{ref} is taken to be 23°C and T is the temperature inside the DMA. In Eqn. 6.1, D_p is the particle or droplet diameter, and C_c is the Cunningham slip correction factor taken from *Kinney et al.* [1991] to be

$$C_c = 1 + \frac{\lambda}{D_p}\left(2.514 + 0.8exp\left[\frac{-.55D_p}{\lambda}\right]\right) \tag{6.3}$$

where λ is the mean free path of air. The relationship between the DMA center rod voltage and Z_p is

$$V = \frac{q_{sh}}{2\pi LZ_p}ln\left[\frac{r_o}{r_i}\right] \tag{6.4}$$

where q_{sh} is the sheath air flow rate, L is the DMA column length, r_o is the inside diameter of the DMA column outer cylinder, and r_i is the outside diameter of the center rod. We will use these relations to calculate uncertainties in DMA sizing in section nine. The electrical mobility of a particle varies in a relatively linear fashion with particle diameter: the smaller the geometric size of a particle the greater its electrical mobility. This means that the voltage between the center and outer rods may be varied continuously from some small value to a large value, and, depending on the flow rates and mechanical characteristics of the particular DMA, result in rela-

tively monodisperse aerosol exiting the DMA starting with small sizes and gradually increasing in size as the voltage is increased.

The force balance previously discussed results in movement of particles of essentially a single size into the monodisperse outlet flow sampling slits positioned near the end of the DMA center rod and eventually out of the DMA and into a particle counting device. Although the term 'monodisperse' has been used to describe the aerosol exiting the DMA, this is somewhat of a misnomer since a strictly monodisperse aerosol can only exist theoretically, not in reality. This is primarily due to three different factors, the first two of which depend strongly on particle size. First, when the sampled aerosol passes through the charge neutralizer, there is a finite probability that some particles will obtain more than one charge. Since the interaction between the ions and particles is generally controlled by the particle surface area, the fraction of multiply charged particles is greater for larger particle sizes. Because the DMA selects particles from the polydisperse population of aerosols based on their electrical mobility, and since the electrical mobility of a particle is directly and linearly proportional to the charge carried by the particle, a relatively large particle with more than one charge can be selected by the DMA and move into the monodisperse outlet flow at the same time as smaller particles with only one charge. Empirical [*Wiedensohler,* 1988] and theoretical studies [*Fuchs,* 1964] of the aerosol charge distribution as a function of size show good agreement and indicate that the distribution is not a function of particle chemical composition, and only weakly varies with the thermodynamic state of the atmosphere within the charge neutralizer, at least over the ranges of temperature and pressure normally encountered when observing aerosol in the atmosphere near the earth's surface. The general result from these studies is that for particle sizes below 20 nm, the aerosol particles essentially hold only a single charge and below about 70 nm, the multiple charge correction is required only up to two charges per particle. For particle sizes greater than 70 nm, the full multiple

charge correction inversion should be applied. For the studies conducted here an inversion which accounted for up to six charges per particle was used. The number concentration of multiply charged particles was small enough relative to the number concentration of singly charged particles that the influence of the multiply charged particles on the results of CCN measurements could be neglected. This is discussed in more detail below. Therefore, the particle counts observed by the CPC can be inverted to correct for the presence of multiply charged particles for each size bin observed in order to arrive at the true aerosol size distribution.

A second process that increases the width of the geometric standard deviation of the distribution of particles exiting the DMA is diffusional broadening. Diffusion processes within the DMA result in a net loss of particles inside the DMA column and associated plumbing, and also broaden the observed 'monodisperse' aerosol, particularly for particle sizes below 20 nm. An improved understanding of this phenomenon has only recently been gained [*Kauffeldt et al.*, 1996]. The basic process is as follows: for extremely small particles, the characteristic diffusional length scale is relatively large compared to the length scales which define the DMA annular space and monodisperse sampling slits, therefore, particles with diameters between about 3 and 15 nm undergo motion due to diffusion that can cause them to enter the monodisperse sampling slits and subsequently be counted by the CPC. For example, if the DMA is configured to select 10 nm particles, a few 5 to 9 nm diameter particles will also be sampled through the monodisperse sampling slits, as will some 11 to 15 nm diameter particles, simply due to the diffusional motion of these particles. The theoretical transfer function calculations for a sheath-to-polydisperse aerosol flow rate ratio of 7:1, typical of that used in this study, indicate that for 10 nm particles, the ranges of sampled particle sizes should only be between 8.6 and 11.4 nm. For all of the studies performed here, distributions were only measured down to particle sizes of 30 nm, above the range of sizes where diffusional broadening significantly influences the

results. Therefore, the effects of diffusional broadening do not need to be considered in this study.

The final non-ideality involved with particle sizing by the DMA has to do with the physical characterisitics of the DMA itself. The problem is essentially one of instrument design - it is impossible to introduce the polydisperse aerosol into the electric field of the DMA in a way that does not result in a distribution of initial positions of the various size particles within the annular space of the column from which the particles are selected. This means that there are in reality infinitely many initial conditions that exist from which particle trajectories must be calculated to determine that range of particle sizes that will eventually exit through the monodisperse sampling slits. Furthermore, the monodisperse sampling slits at the bottom of the DMA center rod must themselves have a finite height along the center rod axis, so that not only are there infinitely many initial positions possible for the various particles, but there are also infinitely many final positions possible for each particle trajectory somewhere between the top and bottom of the monodisperse sampling slit opening. Fortunately, there are two limiting cases that define the range of particle sizes which are sampled through the monodisperse outlet for a given electric field strength (center rod voltage), and these are schematically represented in Figure 6.1. Particles which have a slightly smaller size, or greater electrical mobility, than the 'centroid' mobility for the given DMA center rod voltage, may be introduced into the electric field radially farther from the monodisperse sampling slit and still be sampled just at the top edge of the slit. This situation defines the smallest diameter particle, or the particle with the maximum electrical mobility, that will be sampled for a given voltage setting of the DMA and is depicted at the solid trajectory in Figure 6.1. Conversely, there will be some maximum particle size, or minimum electrical mobility, defined by the largest particle that, when introduced at the smallest possible radial position away from the center rod, will just enter the monodisperse sampling slit at

its bottom-most point. This scenario is shown as the dashed trajectory in Figure 6.1. For the DMA used in these studies and for the 7:1 flow ratio between sheath and polydisperse aerosol flow rates, the width of the sampled range is only ±14% of the centroid diameter value (for example, between 26 and 34 nm for a 30 nm centroid diameter [*Hoppel,* 1978]. Even though there is really a range of diameters drawn through the monodisperse sampling slits of the center rod, for the remainder of this work this will be taken as understood and the term 'monodisperse' aerosol will be used.

The theoretical transfer function for the DMA, or the probability that a particle of given mobility entering the DMA will exit through the monodisperse sampling slits, may be derived by considering the maximum and minimum mobilities discussed above. The radial electric field inside the DMA column at the center rod surface may be described by

$$E_r(r_i) = \frac{V}{r_i ln\left[\frac{r_o}{r_i}\right]}. \tag{6.5}$$

The radial motion of a particle with mobility Z_p is given by

$$\frac{dr}{dt} = Z_p E_r(r) = Z_p E_1 \frac{r_i}{r} \tag{6.6}$$

where

$$E_1 = \frac{E_r(r)}{E_r(r_i)}. \tag{6.7}$$

Assuming that air flows are only in the axial direction along the DMA column, we can write

$$r dr = Z_p E_1 r_i dt \tag{6.8}$$

which may be integrated from $r = r_{in},\ t = 0$ to $r = r,\ t = t$ to give

$$r^2(t) = r_{in}^2 + 2 Z_p E_1 r_i t \tag{6.9}$$

where r_{in} is the radial position of the particle when it enters the DMA column. The above relation can be solved for the time a particle requires to move from radial

position r_{in} to position r

$$t = \frac{r_{in}^2 - r^2(t)}{2Z_p E_1 r_i}. \tag{6.10}$$

The time for a particle to migrate from r_o to r_i is set by the axial flow rates q_{sh} and q_a

$$t(q_{sh} + q_a) = \pi(r_o^2 - r_i^2)L \tag{6.11}$$

which may be rewritten as

$$t = \frac{\pi(r_o^2 - r_i^2)L}{(q_{sh} + q_a)}. \tag{6.12}$$

The two relations for t may be set equal to each other and the maximum particle mobility sampled for the given flow rates derived assuming $r(t) = r_i$ and $r_{in}^2 = r_o$

$$Z_{p,max} = \frac{q_{sh} + q_a}{2\pi E_1 r_i L}. \tag{6.13}$$

The above relation defines the maximum particle mobility sampled for given values of q_a and q_{sh} since the particle was assumed to migrate from r_o to r_i and just be sampled at the monodisperse sampling slits located a distance L from the aerosol inlet to the DMA column.

In order to complete our derivation of the DMA transfer function, we must define the minimum particle mobility exiting through the monodisperse sampling slits. Referring to Figure 6.1, the minimum particle mobility is defined by a particle entering at radial position r_a and migrating to radial position r_s so that it just enters the bottom of the sampling slits. Analogous to the analysis presented above, based on the electric field force the time for this migration may be written

$$t = \frac{r_a^2 - r_3^2}{2Z_p E_1 r_i}. \tag{6.14}$$

Assuming that the minimum mobility particle is entrained immediately into the sheath air flow at the aerosol entrance to the DMA column, the migration time may also be written

$$t = \frac{\pi(r_a^2 - r_3^2)L}{q_{sh} - q_s}. \tag{6.15}$$

Setting the two expressions for the migration time equal to each other, the minimum particle mobility sampled for the given flow rates is

$$Z_{p,min} = \frac{q_{sh} - q_s}{2\pi E_1 r_i L}. \tag{6.16}$$

Only particles with mobilities between $Z_{p,min}$ and $Z_{p,max}$ will be sampled through the monodisperse slits, passing through the DMA to be counted by the CPC. The relative width of the mobility window, or monodispersity of the particles, can be derived by taking the ratio of the difference between the maximum and minimum mobilities and the centroid or average mobility

$$Z_{p,max} - Z_{p,min} = \frac{q_a + q_s}{2\pi E_1 r_i L} \tag{6.17}$$

and

$$Z_{centroid} = \frac{Z_{p,max} + Z_{p,min}}{2} = \frac{q_{sh}}{2\pi E_1 r_i L} \tag{6.18}$$

so that

$$\frac{Z_{p,max} - Z_{p,min}}{Z_{centroid}} = \frac{q_s + q_a}{q_{sh}}. \tag{6.19}$$

The DMA was operated with $q_a = q_s$ and q_{sh} between 6.9 and 10 times q_a. Therefore, the width of the mobility window sampled by the DMA was between $\pm 10\%$ and $\pm 14.4\%$ of the centroid mobility. *Knutson and Whitby* [1975] and *Hoppel* [1978] have shown that the fraction of particles with intermediate electrical mobilities between $Z_{p,min}$ and $Z_{p,max}$ that will pass through the sampling slits can be expressed as the DMA transfer function

$$\Omega = max\left[0, min\left(1, \frac{q_{sh} - q_s + K}{q_a}, \frac{q_a + q_{sh} + K}{q_a}, \frac{q_s}{q_a}\right)\right] \tag{6.20}$$

where $K = -2\pi r_i E_1 Z_p L$ [*Wang and Flagan,* 1990].

In summary, the procedure for sizing particles based upon their electrical mobility proceeds as follows. First the sample of air containing a polydisperse aerosol is exposed to ions in a radioactive charge neutralizer so that the charge distribution on the

sampled aerosol is a known function of size. Second, the polydisperse aerosol is drawn into the electric field in the annular space between the center rod and outer cylinder of the DMA. The electric field amplitude is varied in a systematic way so that particles of a single size, or a monodisperse aerosol, exit the sampling slits at the bottom of the center rod. It should be noted that the aerosol exiting through the monodisperse aerosol flow is not truly monodisperse, due to the instrumental limitations discussed previously. The monodisperse aerosol sample is drawn into a condensation particle counter so that the particles may be counted and a concentration determined for each voltage setting, or particle size, selected by the DMA. As the voltage within the DMA is varied, mono-mobility aerosol samples of different sizes are counted. These must be inverted to particle sizes by applying the transfer function. In this way a histogram of particle concentration verses particle size may be constructed which is called the aerosol number size distribution. How the particle concentration is determined is the subject of the next section.

6.4 *Condensation Particle Counter*

The basic principle for counting sub-micrometer particles is shown schematically in Figure 6.2. The air sample is pulled through the instrument using either an external vacuum pump (TSI Model 3010) or an internal pump (TSI Model 3025). The sample is introduced into a saturated butanol vapor environment within the saturator after passing through the inlet. The saturator is a warmed bath of liquid butanol that serves as a continuous source of butanol vapor to maintain saturation with respect to butanol within the saturator block. The sample air, along with butanol vapor introduced by the saturator, next passes into a condensing unit which cools the air stream causing the butanol vapor to rapidly condense onto the particles carried by the flow. The purpose of this condensation process is to grow the particles into liquid butanol droplets having diameters of several micrometers so they can be easily

detected and counted by a laser within the optical detection assembly of the counter. When a droplet passes through the laser beam, a pulse is detected by sensing electronics which then register the particle as a count in a counting buffer. The count buffer is allowed to accumulate counts for known periods of time before it is emptied by the data acquisition computer via communication through the RS-232 port. A more detailed discussion of the operating characteristics of the condensation particle counter may be found in *Agarwal and Sem* [1980].

For the studies presented here, there were actually two different types of condensation particle counters used. The TSI Model 3010 (referred to as 'CPC') was used to monitor the monodisperse outlet flow from DMA2. The larger sample flow rate of the CPC compared to the Model 3025 makes it the better choice for this application. The CPC has a nominal 50% counting efficiency for particles of 12 nm diameter and 100% counting efficiency for particle sizes greater than 28 nm. The second type of condensation particle counter used was the TSI Model 3025, an ultrafine condensation particle counter (referred to as 'UCPC'). It has a 50% counting efficiency for 3 nm particles. The UCPC uses a substantially lower sample flow rate and dilutes the air sample after it enters the counter, thereby allowing maximum concentration levels approximately ten times those of the CPC to be reliably measured. Unlike the CPC, in the UCPC only a portion (30 $cm^3\ min^{-1}$) of the total inlet sample flow (300 $cm^3\ min^{-1}$) actually passes through the saturator, condensor, and sensing optics. The remainder of the sample flow is filtered and used as sheath air to help focus the aerosol stream immediately before it passes through the optical sensing volume. The maximum concentration limit of the CPC, approximately $10^4\ cm^{-3}$, is attributable to coincidence of particles in the optical sensing volume, however, concentrations exiting DMA1 were measured using the UCPC, which has an upper concentration limit ten times that of the CPC. Maximum, monodisperse particle concentrations measured by the CPC after DMA2 were always below 1000 cm^{-3}, therefore, coincidence in the

CPC is not a problem for this study.

Even though the continuous flow CPC's are the most convenient and reliable method currently available for counting particles, there are four distinct limitations to this method: calibration, calibration drift, diffusional losses of particles within the instrument and sample flow tubing, and instrument response time. Absolute calibration of CPC's is made difficult by the need for an independent, calibrated standard for determing particle concentration. Typically, an electrometer is used as such a standard, but the question remains as to how the electrometer is to be calibrated. The detection efficiency of each individual particle counter as a function of particle size must be determined if the CPC is to be used for aerosol size distribution measurements. This requires a proper system for generating, sizing, and distributing calibration aerosol, which is not a trivial requirement. The counting efficiency curves for different CPC's of the same design, although similar, can demonstrate significant differences (see *Wiedensohler et al.* [1997]). Particularly in the UCPC, the calibration is extremely sensitive to a proper balance of flows inside the counter, which can be difficult to control. Also, over long-term continuous use, the optics and aerosol focusing mechanisms inside the CPC and UCPC can become clogged or coated with particles, particularly when operated at high particle number concentrations. This can result in instrument calibration drift over time, resulting in larger uncertainties and a general under-counting of particles in the sample flow. Particularly for particles with sizes below about 30 nm, diffusional losses of particles can also result in an undercounting of the particles which were present in the flow. This effect is implicitly accounted for in the calibration runs performed with aerosol of known size, therefore, the calibration should be viewed as accounting for two effects: first the inefficiency with which the optical sensor can detect the very smallest particle sizes which might not grow via condensation of butanol to droplet sizes that scatter a significant amount of light into the sensor, and second, the diffusional losses of particles with diameters

below about 30 nm inside the counter. Curves resulting from the calibration studies are not sharply defined, but are rather sigmoidal in shape and slowly increase with size for the CPC and increase more sharply with size for the UCPC. The calibration curves for the CPC's and UCPC used in this study are shown in Figure 6.3. The detection efficiency curve for the CPC takes the form [*Wiedensohler et al.*, 1997]

$$\eta_{cpc} = 1 - \frac{1.15}{exp\left[\frac{D_p - 11.3}{2.1}\right]} \tag{6.21}$$

where η is the detection efficiency (%/100) and D_p is the particle diameter in nm. For the UCPC, the relation is [*Wiedensohler et al.*, 1997]

$$\eta_{ucpc} = 1 - exp\left[\frac{2.22 - D_p}{0.28}\right]. \tag{6.22}$$

For the particle sizes studied here, the UCPC features a detection efficiency of 100%. However, an accounting had to be made of the diffusional losses in the 35 cm of sample line tubing to the UCPC from the point where both the UCPC and CCN counters sampled from the mondisperse outlet flow of DMA1. The UCPC data were corrected for these losses so that the correct particle number concentration could be compared to the droplet concentration determined by the TGDCC. The losses were quantified using the theory of *Reineking and Porstendörfer* [1986], and the minimum penetration efficiency for 15 nm particles amounted to 0.92. Therefore, to correct for diffusion losses to the UCPC, the UCPC data were divided by corrections between 0.92 and 1.0. Fifteen nanometer diameter particles were the smallest particles examined in the UCPC and TGDCC loss experiments. The smallest particle diameter examined during HTDMA studies was 25 nm. The penetration efficiency as a function of particle size is plotted in Figure 6.4 for the UCPC sample inlet tubing. The results from the theoretical diffusional loss calculations were fitted to an equation of the form

$$P_{ucpc} = c_0 + c_1 log_{10} D_p + c_2 (log_{10} D_p)^2 + c_3 (log_{10} D_p)^3 + c_4 (log_{10} D_p)^4 + c_5 (log_{10} D_p)^5. \tag{6.23}$$

The fit results are shown in Figure 6.4 and the c_i coefficients are listed in Table 6.1. The above relation was used to correct all UCPC data for a given particle size by

$$UCPC_{corrected} = \frac{UCPC_{measured}}{P_{ucpc}}. \tag{6.24}$$

Both the CPC and UCPC exhibit response times to step function changes in aerosol concentration at their inlets of around one second, that is, it takes the counters approximately one second to actually observe 63% (e-folding time) of the concentration of particles after the particles are sampled through the inlet. This finite response time can be important in aerosol studies using newer, scanning methods for determining the aerosol size distribution, where the size distribution is obtained relatively quickly compared to standard methods. In this study the scanning method was not used for obtaining the aerosol size distributions reported.

6.5 *Thermal Gradient Diffusion Cloud Chamber CCN Measurements*

The instrument used to measure the number concentration of dry particles activated to cloud droplets at a given supersaturation is called a Thermal Gradient Diffusion Cloud Chamber (TGDCC). The TGDCC provides an experimental value of water supersaturation, the critical supersaturation, required to activate a known dry particle. The experimental value of S_{crit} can then be compared to that derived from HTDMA measurement results. The Model M1 Cloud Condensation Nucleus Counter (referred to in the present work as the 'CCN counter' and the 'TGDCC'; DH Associates, Tucson, Arizona) used in this study is the same unit used by *Cruz and Pandis* [1997] in their studies of the CCN activity of organic compounds. The TGDCC consists of the thermal diffusion chamber, a laser used to illuminate droplets inside the chamber, a video camera to image the illuminated droplets, electronics to digitize and process the captured images, and various power supplies.

The diffusion chamber consists of two 1 cm thick, 9 cm diameter stainless steel plates separated by a glass ring 8 cm in diameter and 2 cm high. The glass ring maintains a 2 cm distance between the two metal plates. Wetted filter paper is placed on the lower metal plate, and a water reservoir is located inside the top plate. The top plate has a porous ceramic material as its bottom surface so that the bottom of the top metal plate (inside of the chamber) is kept moistened with water. Since both plate surfaces inside the chamber are kept wet, the RH above these surfaces is maintained at 100%. Only Nanopure water was used to wet the filter paper and fill the reservoir. A new piece of filter paper was used for each day of measurements. A thermoelectric cooler is used to cool the bottom plate, while the top plate temperature is allowed to equilibriate with the room temperature. When the bottom plate is cooled, a linear temperature gradient is created between the two plates. Both surfaces are kept at 100% RH, and since the saturation vapor pressure of water depends exponentially on temperature, the linear temperature gradient produces a quasi-parabolic water vapor supersaturation profile between the two plates. Although the maximum supersaturation between the plates cannot be measured directly, it can be calculated from the measured top and bottom plate temperatures using the following equation

$$S_{max} = 100\frac{\rho_s(T_t) + \rho_s(T_b) - 2\rho_s\left[\frac{T_t+T_b}{2}\right]}{2\rho_s\left[\frac{T_t+T_b}{2}\right]} \tag{6.25}$$

where ρ_s is the water vapor density at saturation for the indicated temperature. The laser passes through the glass ring and is directed through the chamber so that its position coincides with the location of maximum supersaturation in the chamber. Particles are introduced into the chamber by a pump which draws 1.5 l min^{-1} for 5 seconds through the chamber from the monodisperse outlet flow of DMA1. The sample flow is drawn through the chamber so that the particles enter through the top plate and later exit through a hole in the bottom plate. The five second pumping time is sufficient to draw 125 cm^3 of air through the chamber. The chamber volume is 100 cm^3. After the 5 second pumping time, 5 more seconds are allowed for the

supersaturation profile to be re-established. The remaining 20 seconds of the 30 second sampling period are used to obtain video images of droplets within the laser beam in the chamber. The sensing volume of the TGDCC is determined by the diameter of the laser and by the length along the laser viewed by the video camera. The volume and data processing algorithm are set by the manufacturer and cannot be changed. The sensing volume of the TGDCC is only 0.006 cm^3, and one sample takes 0.5 minutes, therefore, to sample a full cubic cm of air, 83.3 minutes are required. The extremely small sample volume of the TGDCC has important ramifications with respect to counting statistic uncertainties discussed below. The images are digitized and processed to remove spurious counts by the software within the instrument. Once processed, the number of droplets counted in the beam, the current accumulated 1/10th cm^3 and the current accumulated 1 cm^3 counts of droplets are sent through the parallel port of a PC running a QBasic program that acquires data.

At droplet concentrations around 1000 cm^{-3}, the video imaging system cannot resolve all of the individual droplets in the laser beam and the droplet number actually counted is reduced due to the coincidence of droplets in the sensing volume. Tabulated corrections for this effect have been provided by the manufacturer and the following polynomial was found to fit the tabulated data with a standard error of 1.84% and $r^2 = 0.999$

$$N_{true} = 8.71499x10^{-8} N_{act}^3 - 1.888063x10^{-5} N_{act}^2 + 1.10883 N_{act} - 1.560554x10^{1} \quad (6.26)$$

where N_{act} is the actual droplet number concentration reported by the TGDCC and N_{true} is the coincidence corrected CCN number concentration. The correction amounts to around 10% for N_{act} around 1000 cm^{-3}.

The TGDCC draws its sample air through a solenoid valve and 0.3 m of 0.4 cm inside diameter conductive tubing before the sample enters the diffusion chamber. The inlet through the top plate was expected to induce particle losses since the flow path was not directly into the chamber. In order to quantify the particle losses in the

TGDCC, a special plastic substitute ring for the glass ring was manufactured that had a sampling port through its side from which a CPC could sample. The instruments were arranged as shown in Figure 6.5. Because only monodisperse particles were sampled by both UCPC and CPC during this test, diffusional losses in the UCPC and TGDCC sampling tubing could be calculated based on the results of *Reineking and Porstendörfer* [1986]. The total loss in the TGDCC sample line, solenoid valve and top plate inlet was determined experimentally for particle sizes between 15 and 250 nm by measuring the monodisperse particle concentration in the diffusion chamber with a CPC while the DMA1 monodisperse outlet flow concentration was simultaneously measured with the UCPC. Identical, monodisperse particles were sampled by the UCPC and CPC to ensure equal counts prior to performing the loss experiments. Losses in the UCPC and TGDCC sampling lines, and losses inside the CCN unit as a function of particle size are shown in Figure 6.6. As can be seen from the figure, the CCN counter never passes more than approximately 75% of the input number concentration of particles supplied at its inlet. The UCPC concentrations were corrected for diffusional losses and then the following function was fitted to the ratio of UCPC and diffusion chamber particle concentrations

$$P_{ccn} = d_0 + d_1 log_{10}D_p + d_2(log_{10}D_p)^2 + d_3(log_{10}D_p)^3 + d_4(log_{10}D_p)^4 + d_5(log_{10}D_p)^5. \tag{6.27}$$

The best fit d_i coefficients are listed in Table 6.1. Results from the fitting exercise are shown in Figure 6.6. The above relation was used to correct the UCPC concentrations for a given input dry particle size to reflect the actual input particle concentration to the TGDCC diffusion chamber. After applying the coincidence correction, the final CCN-to-UCPC ratio could be determined for a given dry particle size and chamber S_{max} by

$$\frac{N_{CCN}}{N_{UCPC}} = \frac{P_{ucpc}N_{ccn,coinccorr}}{P_{ccn}N_{UCPC}}. \tag{6.28}$$

Technically, the output concentrations from DMA1 must be corrected for dou-

bly and higher charged particles larger than the desired diameter. The influence of larger, multiply charged particles could be particularly important when comparing CCN to UCPC concentrations because the ability of a particle to act as a CCN depends on both size and chemical composition, while all particles are counted in the UCPC. Therefore, for a given chamber S_{max}, larger, multiply charged particles would be counted as droplets as an artifact of the DMA selection technique, and should not be counted as CCN. In this work, particle sizes less than 130 nm are studied, therefore, doubly charged particles having diameters of around 260 nm and less need be considered. For this particle size range, less than 9% of the number of concentration of singly charged particles is doubly charged [*Wiedensohler,* 1988]. For our studies using 40 nm particles, the mode size of the polydisperse size distribution is set to 40 nm by controlling the atomizer salt solution concentration. Our studies of the polydisperse size distribution show that the concentrations of doubly charged particles for sizes greater than the mode diameter of the size distribution are between 100 and 1000 times lower than the singly charged number concentration corresponding to the doubly charged particles. Furthermore, the fraction of singly charged particles for the 30 to 130 nm size range is 12 to 21%, while the fraction of doubly charged particles for the 60 to 260 nm size range is only between 0.6 and 9%. Taken together, this means that the ratio of the number concentrations of singly to doubly charged particles for particle sizes near the mode diameter of the polydisperse size distribution is at least 20 (12/.6) when the number concentrations of 30 and 60 nm particles are approximately the same. A ratio of 20 implies that at most 5% of the input concentration is larger, doubly charged particles. For sizes larger than the mode size of the polydisperse input distribution, the ratio is even larger because the concentrations of the smaller particles is much larger than that of the larger particles and the ratio of the singly to doubly charged fractions is greater than 2. Together, the ratio of doubly to singly charged number concentrations are less than 0.005, or 99.5% of the total

number concentration is singly charged.

If studies are conducted on particles between 10 and 40 nm, we need to examine the fraction of doubly charged particles below around 80 nm. According to *Wiedensohler* [1988], the fraction of doubly charged particles near 80 nm is only around 2%, and the fraction is smaller than 0.1% for particles smaller than 30 nm. Even though the concentrations of particles having diameters less than 30 nm are smaller than concentrations of particles between 30 and 60 nm, the rapid decrease in the doubly charged fraction in the 30 to 60 nm size range overwhelms the differences in number concentrations so that the maximum correction for doubly charged particles in the sub-40 nm size range is 2%. Given that corrections between 2 and 5% are of the same order of magnitude and less than our measurement uncertainties, it was decided that corrections of CCN concentrations for multiply charged particles was unnecessary. Furthermore, both the UCPC and CCN number concentrations would require correction, and since we are examining the ratio of CCN-to-UCPC concentrations, the effect of the correction for multiply charged particles on our results would tend to be reduced and smaller than the conservative 5% estimate given above.

The thermocouples used to measure the top and bottom plate temperatures are not located at the wetted surfaces inside the chamber, but inside the top and bottom plates. Therefore, there is a question as to how representative the thermocouple temperatures are of the actual temperature gradient in the chamber. The value of the temperature gradient is critical for evaluating the maximum supersaturation of the diffusion chamber. We tested whether the thermocouple temperatures were representative of actual conditions inside the chamber by inserting two thermistors into the chamber through the sampling port in the special plastic substitute ring constructed for the particle loss study described above. One thermistor was positioned so that it contacted the top plate while the second thermistor rested on the dry bottom plate. The wetted filter paper was not placed on the bottom plate since condensational

heating of the cooled bottom plate would cause a positive temperature difference artifact. To prevent any influence of water condensation on the bottom thermistor, it was covered with parafilm and sealed with electrical tape to the bottom plate metal surface. The plastic ring used in place of the glass ring has a thermal conductivity about one-half that of glass, therefore, the thermal isolation between the two plates during this test should not have been affected by the substitute ring. Results from our study showed that the thermocouples inside the plates tended to overpredict the temperature difference by approximately 0.6°C . This effect was accounted for in our studies, and the chamber S_{max} corresponding to the thermocouple temperature difference minus 0.6°C was used in our calculations.

We included the TGDCC in our experiments to provide an experimental determination of S_{crit} for the same particle sizes and compositions used in the hygroscopic growth measurements in the HTDMA. Therefore, our goal with the TGDCC was to measure the dry particle size where 50% of the particle number concentration supplied to the TGDCC was counted as droplets for the maximum supersaturation in the chamber. In practice, this was accomplished by setting the cooler voltage on the unit for a certain supersaturation and waiting for the chamber to equilibrate. Thermistors attached to the outside of the plates using thermal paste and overlying insulation allowed the chamber temperatures and supersaturation to be monitored in real time during each experiment. The temperature gradient measured by the thermistors agreed very well with that measured by the thermocouples inside the plates after applying the correction discussed above. Once a constant supersaturation had been established within the chamber, the center rod voltage on DMA1 was set to supply a monodisperse aerosol to the TGDCC at a concentration near 1000 cm^{-3} and at a size twice as large as the expected 50% activation size, that is, the particle size for which the ratio of CCN to UCPC concentrations would be 0.5. Concentrations were kept near 1000 cm^{-3} in order to avoid vapor depletion and coincidence counting

problems in the TGDCC.

Because the TGDCC samples on a batch basis every 30 seconds, a solenoid valve was electronically interlocked with the sampling valve of the TGDCC so that a constant 1.5 lpm was drawn through the 1.5 m long electrically conductive sample line tubing from the 2.3 lpm DMA1 monodisperse output flow. Interactions between the opening and closing of the solenoid valve and flows in both DMA's were examined and found to be negligible. The UCPC sampled at 0.3 lpm from the same DMA1 output flow as the TGDCC using a 0.2 m long 0.41 cm ID stainless steel tube. After the required 83 minute sampling time, a smaller size was selected with DMA1, and the measurements repeated at the same chamber supersaturation. In this way, smaller and smaller sizes were selected with DMA1 so that a curve of the ratio of N_{CCN} to N_{UCPC} versus dry particle size could be constructed from each of the single particle size experiments. Between 10 and 13 points were obtained from each set of experiments, and the 50% activation diameter was determined by fitting the following equation to the data

$$\frac{N_{CCN}}{N_{UCPC}} = b - \frac{a}{\left[1 + exp\left(\frac{D_{p,sol} - D_1}{D_2}\right)\right]} \tag{6.29}$$

and solving the above equation for N_{CCN} over N_{UCPC} equal to 0.5. In the above relation, a, b, D_1 and D_2 are adjustable fit parameters.

The above relation was used to fit results from CCN studies where the chamber supersaturation was held constant and the input particle size was changed. The majority of CCN studies were conducted so that the chamber supersaturation was changed while the input dry particle size was varied so that ratios of N_{CCN} to N_{UCPC} between 0.2 and 0.9 could be observed. In this case, a linear fit to the chamber supersaturation-concentration ratio data pairs was performed and the supersaturation determined where the concentration ratio was equal to 0.5. A linear fit was used since the variation of the ratio of N_{CCN} to N_{UCPC} is expected to be linear over the narrow range of chamber supersaturations selected, and due to the relatively few

supersaturations that could be selected during a given study.

6.6 *The Humidified Tandem Differential Mobility Analyzer*

A schematic diagram of the HTDMA/CCN system is shown in Figure 6.7. The major components of the HTDMA system have been described in previous sections. In the HTDMA, dry (RH<2-10%), quasi-monodisperse particles are selected using the DMA from a polydisperse size distribution generated by the atomizer. The monodisperse particles are exposed to a controlled humidity environment before entering a second DMA. If the particles take up water, they will grow in size and exhibit a lower electrical mobility (larger size) in the second DMA. Recent work by *Weingartner et al.* [1997] suggests that a correction should be applied to the measured particle size when HTDMA studies are conducted at high RH values. The correction was primarily necessary in their study because the mass flow controller used to control the sheath air flow rate was positioned before the flow humidifier. The sheath air flow had to be corrected for the addition of water vapor mass to the air stream. In this work, the sheath air flow rate was measured using a volumetric flow meter after the sheath air humidifier. The mean free path, Cunningham slip correction, and subsequently the electrical mobility, are also influenced by high humidity conditions in the DMA. However, the effect is less than 0.4% for the electrical mobility diameter for RH's below 95%, therefore, this correction is not applied to the results from this study. A condensation particle counter is used to count the particles exiting the second DMA. By observing the electrical mobility where the CPC measures the maximum number of particles, the size of the wetted particles can be determined, and the water content derived from the difference between the wet and dry sizes. By controlling the second DMA aerosol in and sheath air flow RH's at several different values, the growth as a function of relative humidity may be determined for each input, dry monodisperse

particle size.

Maintaining constant air flows in the HTDMA is critical to obtain high quality data. Therefore, separate vacuum and regulated compressed air sources were used for all sample flows. Flows were controlled by precision needle valves and checked using an absolute volumetric flow meter before and after each set of measurements. Temperatures and relative humidities were monitored in real time during each experiment using LabView^{TM} application software that displayed and logged data every 5 seconds. Data were acquired from the HTDMA using a modified version of a QBasic program originally written by researchers at the Institute for Tropospheric Research in Leipzig, Germany to measure ambient size distributions. The HTDMA software was configured so that the measured centroid mobilities in adjacent mobility bins increased geometrically by a factor of 1.05 and between 7 and 15 bins were used to characterize the conditioned and unconditioned monodisperse aerosol exiting DMA1.

6.6.1 Inversion of HTDMA Data

TDMA and HTDMA data were inverted using two different inversion schemes and the results of log normal fits of the inverted data were compared. In the inversion routine developed by the Institute for Tropospheric Research [*Stratmann et al.*, 1996], the number of data points is increased using a smoothing spline interpolation routine. Second, the data are filtered and inverted to determine the number concentration as a function of particle mobility at the entrance to DMA2. A low pass, Fourier filter is used with an adjustable filter amplitude to remove unwanted noise from the input data. The mobility distribution in front of DMA2 is calculated iteratively by adjusting a guess for the distribution for an assumed triangular DMA transfer function shape and comparing the guess to the measured number concentration distribution. The guess is modified based on a least squares minimization technique that attempts to match the integral number concentration before DMA2 observed by the UCPC and

input to the code. Once the best solution is found, gaussian distributions are fitted to the inverted mobility distribution data so that mode sizes, standard deviations and number concentrations could be determined. No accounting is made for multiply charged particles in the inversion. A second, simpler technique was also applied to invert the data. The theoretical transfer function for an ideal DMA is 0.5 when the DMA is operated with the particle sample inlet flow equal to the monodisperse outlet flow. Therefore, the number concentration data in each bin were multiplied by two and divided by the difference between the base 10 logarithms of the bin diameter limits. The number size distribution data thus produced was fitted to log normal functions to determine the mode size of the dry or humidified particles. Results from both techniques for inverting the HTDMA data were compared and agreement between mode diameters was found to be better than 2%. Therefore, the simpler technique was used to invert all of the HTDMA data obtained during this study.

HTDMA scans were obtained over 10 minute intervals, however, the actual count data defining the number peak were typically measured over a two to three minute period within the total count time of ten minutes. Therefore, the RH and T data corresponding to the time period when the peak count data were obtained were used to determine the appropriate RH value corresponding to the measured droplet size. This was accomplished by synchronizing the computer clocks of the computers used for the various data acquisition tasks and using the scan start time, bin count times and the wait time between each size bin to determine the correct start and end times to calculate an average RH.

6.7 *Instrument Subsystems*

6.7.1 Relative Humidity Measurements

Relative humidity measurements are a key part of this work and considerable effort was expended to insure that accurate and precise RH measurements were made.

The same RH probe (Humitter 40, Vaisala Inc., Boston MA) was used for all RH measurements in this work. This sensor is shipped from the factory with a better than ±3% accuracy at 20°C for RH's between 10 and 90%. The temperature dependence of the sensor output is specified as less than ±2% for temperatures between -10°C and 60°C and the stability as ±1% over one year. Our calibrations before and after HTDMA studies showed that one DMA2 sensor exhibited drift greater than the manufacturer's specification. This is discussed further in chapter 7. There are four key issues that need to be accounted for in making RH measurements: sensor accuracy, sensor precision, control of temperature gradients in the measurement system, and control of RH by the computerized controller. Each of these issues is discussed below.

To improve the stated accuracy of the RH sensors, they were calibrated using known saturated salt solutions over which the RH could be calculated to within ±0.6% accuracy from the results of *Greenspan* [1977]. RH depends both on the absolute water vapor concentration and air temperature, and the solubility of the salts in solution also depends weakly on temperature, therefore, it was critical to perform the calibrations in as isothermal an environment as possible. A plexiglass enclosure (DMA2 box) was used to house the glass crystallization dish with the solution and the sensors. Six RH sensors and three (runs A and B) or four (run C) thermistors were held within 5 mm of the top surface of the salt solution using a rubber stopper with ten holes allowing access to the air over the saturated salt solution while forming an air tight seal around each sensor. The stopper fit snugly over a glass crystallization dish holding 20 cm^3 of salt solution. When inserted, the volume of the air space between the bottom of the rubber stopper and the top of the salt solution was 50 cm^3. A Mettler Analytical balance was used to weigh an excess amount of each of the crystalline salts to produce a saturated salt solution in 20 cm^3 of Nanopure water. A list of the salts used to calibrate the RH sensors is given in Table 6.2. Also shown in the table are average

temperatures and calculated RH values for the different solutions using the results of *Greenspan* [1977]. Four calibration runs were performed, A, B, and C before HTDMA growth studies and run D after HTDMA studies were completed to determine whether calibration drift had occurred.

The results from calibration run C were used for all HTDMA growth studies. Between 12 and 24 hours were required before the air over the saturated salt solution came to RH equilibrium with the solution. Once equilibrium had been achieved, the voltage from each RH sensor was recorded by the data acquisition system every five seconds for a 30 minute period. For calibration runs A and B, only five channels were available in the data acquisition system to record the voltages from six sensors, therefore the calibration was repeated for these two runs, swapping sensors four and six. For run C a circuit was constructed allowing all six sensors to be simultaneously logged by the DAQ system. Also for run C, a voltage follower circuit was incorporated into the signal processing circuit for the DMA2 monodisperse inlet and sheath air inlet sensors. This addition increased the signal-to-noise ratio by a factor of ten and improved the stability of RH's measured by these two sensors over previous runs. The voltages from each sensor for each RH were averaged and the following calibration equation was fit to the voltage data as a function of RH:

$$RH = a_0 + a_1 V + a_2 V^3 + a_3 V^5 \tag{6.30}$$

where V is the sensor voltage. A polynomial with only odd powers was found to give the best fit to calibration data. Once the best fit a_i coefficients were determined, the standard error of each of the fits for each sensor was calculated for the entire range of RH's used in the calibrations, for RH's between 8% and 54%, and for RH's between 75% and 97%. The calibration coefficients for each sensor, and for each calibration run (when available) are listed in Table 6.3. Plots of the results from each sensor are provided in Appendix A. The various standard errors of fit and estimates of the RH measurement accuracy from our RH calibrations are shown in Table 6.4.

Except for RH sensor number four, the results are consistent with the good agreement between theoretical and observed droplet growth factors during HTDMA studies on NaCl and $(NH_4)_2SO_4$ particles. Sensor four exhibited a drift in measured RH. The drift is discussed in more detail in chapter 7. The methods used to determine the errors in Table 6.4 will be discussed below. The χ^2 values in the table designate the goodness of fit of the above polynomial to the calibration data and are calculated as the sum of the squares of the differences between the fit-predicted values of RH and values of RH from *Greenspan* [1977].

The standard deviations of the voltages for each sensor for a given RH were calculated and the average voltage, plus and minus the standard deviation, was used in the above calibration equation to evaluate the precision of the RH measurements for each sensor as a function of RH. Results are tabulated in Table 6.5. The $\pm 1\sigma$ value provides 68% confidence that measured RH values are actually within plus-and-minus the values shown in Table 6.5. Our calibration results from runs A and B indicate that measured RH values are accurate to between $\pm 0.7\%$ and $\pm 1\%$ for the 75% to 97% RH range and have a precision of $\pm 0.02\%$ to $\pm 0.52\%$ (1σ, n=5) for the same RH range. The RH sensor precision was determined by calculating the standard deviation in the sensor voltage for constant RH conditions. The standard deviation was then added to and subtracted from the average sensor voltage for a given calibration RH value. The high and low voltage values thus determined were input into the calibration equation and the difference in the predicted RH values was defined as the sensor precision. The relatively higher uncertainties for sensors 4, 5 and 6 are due to the lower voltage amplitudes for these sensors during runs A and B, 50 mV compared to 1 V, compared to the other sensors. For run C, the average error for the entire RH range examined was between $\pm 0.44\%$ and $\pm 0.8\%$. The precision of the RH measurements for run C was determined by inputing the new calibration equations and re-exposing the RH sensors to the KNO_3 saturated salt solution with

a calibration RH of 93.15%. Over a 30 minute period, the standard deviations of the RH values from all of the sensors were less than 0.1% RH. The calibration equations from run C were used for all HTDMA studies.

Even though the temperatures of the different air flows outside of DMA2 varied, temperature gradients within DMA2 had to be kept to a minimum in order to insure that corresponding RH gradients were also small. Experience has shown that during HTDMA studies the maximum temperature difference between the 8 thermistors, 4 located within the air flows and 4 located at different axial positions along the outer cylinder, was 0.3°C , indicating that excellent thermal control could be maintained. The maximum temperature difference between the four DMA2 air flow temperatures was 0.1°C , corresponding to a maximum difference between entrance and exit RH's in DMA2 of 0.6% at the standard operating temperature of 29.5°C . Therefore, temperature gradients alone do not have a significant impact on RH control in DMA2.

The final issue with respect to determining RH measurement uncertainty is related to the control of the RH values for the monodisperse inlet and sheath air flow rates in DMA2. Experience with the controller used to control these RH's (Omega Model CN 3000 Dual Input Controller, Omega Engineering, Stamford, CT) has shown that the RH values can be controlled to between ± 0.4 and ± 0.9% RH of the setpoint values. The typical RH control capability, equal to one standard deviation of the RH values during the high number count period of the HTDMA scan, was ± 0.6% RH. Taken together, the sensor precision can be determined from the root mean sum of squares of the three experimentally determined values described above: 0.1% resulting from sensor repeatability, 0.6% resulting from the RH control capability of the Omega controller, and 0.6% resulting from the axial temperature gradient in DMA2. The nominal sensor precision is therefore ± 0.85% (1σ, n=5).

6.7.2 Temperature Measurements

Precision thermistors (YSI Inc., Model 44030) were used for all temperature measurements and shipped from the factory with a precision of ± 0.1°C. The thermistors were calibrated against a NIST traceable temperature standard (Hart Scientific Model 1504, Tweener Thermometer) in an isothermal chamber between 18 and 32°C with recirculating air to simulate actual measurement conditions. The temperature standard has a reported accuracy of ± 0.005°C and precision of ± 0.05°C [*Randy Horn, personal communication*]. All experiments in this work were conducted between 22 and 26°C. The thermistor calibration proceeded as follows: first, the traceable standard and 10 thermistors were bundled together to insure good thermal contact. The bundle was sealed inside the one liter air volume of a Vaportron^{TM} humidity instrument (Digilog Inst., Loveland, Colorado). The air volume was well stirred with a mixing fan and had microprocessor temperature control where cold and warm airstreams were mixed to create the desired temperature. All calibrations were conducted at 20% RH to avoid potential water vapor condensation. The isothermal chamber temperature was set to a value between 18 and 32°C and allowed to come to thermal equilibrium as indicated by the traceable standard. Third, once the chamber temperature had stabilized, the temperature of the traceable standard and all thermistor voltages were recorded every two seconds for a period of five minutes. This procedure was repeated for ten temperatures between 18 and 32°C , and twice repeated for each temperature. The voltages for each thermistor corresponding to a constant temperature were averaged and the standard deviation calculated. The ratio of the standard deviation to the average is defined as the experimental precision.

Thermistors operate by changing resistance with temperature. The change in resistance was converted to a voltage signal using a voltage divider circuit with a precision 10 volt reference source and 75 kΩ precision metal film resistors. The voltage across each thermistor was measured using a National Instruments Analog-to-Digital

(AD) convertor. The voltages for each thermistor for each setpoint temperature were averaged and the average value used to determine calibration coefficients in the following relation:

$$\frac{1}{T} = b_0 + b_1 ln(R) + b_2(ln(R))^2 + b_3(ln(R))^3 \tag{6.31}$$

where T is temperature in Kelvin, b_i are the calibration coefficients to be determined and R is the variable resistance of the thermistor determined by

$$R = \frac{R_{ref}}{\left[\frac{V_0}{V} - 1.0\right]} \tag{6.32}$$

whre R_{ref} is the nominal 75 kΩ resistance value, V_0 is the 10 volt precision reference voltage, and V is the measured voltage across the thermistor. A non-linear least squares fit routine was used to fit the above relation to the voltage versus temperature data. The calibration coefficients for each of the sensors are listed in Table 6.6. Plots of the calibration results for each sensor are given in Appendix B. The standard error of each fit, goodness of fit, and estimated accuracy for each sensor are shown in Table 6.7. The precision of each sensor was estimated using the same technique as for the RH sensors. Results from our calculations of the thermistor precision are listed in Table 6.8.

Our calibrations demonstrate that temperatures can be measured with an accuracy of ± 0.1°C and precision of ± 0.06°C .

6.7.3 Flow Rate Measurements

All DMA flows and flows into the CPC and CCN counters were determined using a NIST traceable primary volumetric flow meter (Gillibrator Model 11616-B, Gillian Inc., NJ). Two flow cells were used, a low-flow cell (Model 17218-S, 0.02-6 lpm) with accuracy of $\pm 0.196\%$ at 2 lpm, and a high-flow cell (Model 17073-H, 2-30 lpm) with accuracy of $\pm 0.198\%$ at 5 lpm.

6.7.4 Data Acquisition and RH Control

There were three personal computers used to acquire data during each experiment. An IBM 755C laptop computer running QBasic software controlled the DMA2 center rod voltage and logged dry and humidified number concentration versus size scans from the HTDMA. HTDMA scans were measured over approximately 10 minute intervals. A second IBM compatible desktop computer used a QBasic code to obtain data from the UCPC by communicating through the serial port. This computer was also used to log all temperature and RH voltage signals using a NI PCI-MIO-16XE analog-to-digital converter card with an AMUX-64T multiplexer (National Instruments, Austin, TX) allowing 64 total analog input channels to be read simultaneously. LabView^{TM} software was used to display the various sensor outputs to screen and to log the voltages to file. A Toshiba laptop computer was used to record the number of droplets counted in the current 30 second sample, the current per-tenth cubic centimeter droplet concentration, and the current full cubic centimeter droplet number concentration from the CCN counter. The clocks in each of the data acquisition computers were synched prior to each HTDMA/CCN study.

The humidities of the sheath and monodisperse input flows to DMA2 were controlled by an Omega Engineering Inc. Model CN-3000 Temperature Controller with PID control and two loop, simultaneous control capability. Humidification was accomplished by passing the sample flows through a porous tube (Accurel tubing, 0.2 μm pore size, Microdyn Technologies Inc., Raleigh, NC) surrounded by a larger stainless steel tube. The annular space between the two tubes was filled with recirculating Nanopure water by a peristaltic pump (Masterflex 'Unified' Drive 7520, Cole Parmer Instrument Co., Niles, Illinois). A heater was wrapped around the stainless steel tube, and the Omega controller pulsed the 120 VAC power to the heaters in order to drive water vapor through the porous tubing and into the sample air streams. No artifact particle counts were produced by the RH conditioners. The peristaltic pump was

operated at a speed setting of 3.5 corresponding to a water flow rate of 10 ml min^{-1}. Sample flow rates were measured after the RH conditioners. To allow for sufficient time for thermal equilibrium and droplet growth, 1.2 m of 4.1 mm I.D. copper tubing was installed after each conditioner inside the DMA2 enclosure. RH control sensors were positioned at the end of the copper tubing just before the air flows entered the DMA2 center rod assembly. By monitoring the monodisperse and sheath flow RH's and comparing them to the entered set point RH value, the controller could control the sample RH's to within ±0.7% RH at RH's below 92% and to within ±1.0% RH at RH's greater than 92%.

6.8 *Integrated System/Method*

Refer to Figure 6.7 for a schematic of the HTDMA/CCN system. Studies were conducted using the following procedures. First, a nominal supersaturation for the TGDCC was chosen and the cooler voltage set accordingly. Next, DMA1 monodisperse and sheath flows were set to 2.3 and 16 lpm, respectively, for a sheath-to-sample air flow ratio of 7:1. For the flow ratio in DMA1, the mobility window is ±14% of the midpoint mobility. The UCPC was turned on and set for a 0.3 lpm inlet flow. The polydisperse inlet flow to DMA1 and the excess air flow out of DMA1 were set equal to the monodisperse outlet and sheath flows, respectively. A new salt solution was mixed, the atomizer bottle and block were rinsed, the solution was added to the bottle, and the atomizer air flow was turned on. The DMA2 sheath and excess air flows were each set to 5 lpm, and the monodisperse inlet and outlet flows were each set to 1.0 lpm. Therefore, the sheath-to-sample air flow ratio in DMA2 was 5:1. For the flow ratio in DMA2, the mobility window is ±20% of the midpoint mobility.

The CCN bypass and inlet flows were set to 1.5 lpm. All flows were rechecked to verify all values. Center rod voltages on both DMA's were set equal to 0 v to verify that no counts were registered by the UCPC, CPC, and TGDCC. The am-

bient pressure was determined using the CSU Cloud Chamber pressure sensor and the DMA2 sample flow rate and exterior column temperatures were measured using precision thermistors. The pressure and temperature conditions were input to a QBasic code and the center rod voltage calculated for the flow rates in DMA1 and particle size selected for the study. The DMA1 particle size was chosen large enough so that all particles would be expected to activate in the TGDCC at the chamber supersaturation chosen for the study. The DMA1 center rod voltage was adjusted manually and maintained at a constant value throughout each HTDMA study. The two RH conditioners were set to their bypass 'dry' positions to measure dry particles in DMA2 as a way of verifying proper operation of the TDMA system. Three scans were performed with the system in the 'dry' configuration and the proper sizing of the classified DMA1 particles by DMA2 verified. For elevated RH scans, a QBasic program was used to control the DMA2 center rod voltage and scan voltages corresponding to particle diameters between 0.8 and 2.5 times that selected by DMA1.

The TGDCC was allowed to sample a full cubic centimeter of air from the monodisperse outlet flow of DMA1. Alternatively, if 400 droplets were counted before a full cubic centimeter of air had been sampled by the CCN counter, the CCN sampling was halted and a new chamber supersaturation was selected. During this time, between 10 and 40 elevated humidity scans in DMA2 were performed on the same particles sampled by the TGDCC. Between 4 and 8 different chamber supersaturations were selected, until no, or very few, drops were observed in the TGDCC. The entire sequence of measurements on the same DMA1 particle size lasted between 10 and 12 hours.

6.9 *Experimental Uncertainties*

In order to interpret the results presented here, it is important to understand the limitations and uncertainties of the various measurements [*Taylor* 1982].

6.9.1 Temperature Measurements

Relative humidity depends exponentially upon temperature (T), for example, at 29.5°C a ±0.1°C temperature uncertainty in the second DMA would correspond to an RH uncertainty (as percent error in RH) of ±0.6% based on the variation of the saturation vapor pressure of water with temperature. Furthermore, the mean free path, viscosity, and density of air all depend upon T and are used in calculating the particle size from electrical mobility in each DMA.

The characteristics and calibration of the precision thermistors used in this study were described above. The accuracy of the thermistors is assumed to be equal to the root mean sum of the squares of the accuracy of the NIST traceable standard (0.005°C) and the standard error of the calibration equation fit for the particular sensor (between 0.06 and 0.09°C). Using the above numbers, the accuracy of thermistor measured temperatures in this work is between ±0.06 and ±0.09°C, similar to the manufacturers specification of ±0.1°C. The precision of the temperature measurements was determined by calculating the standard deviation of the thermistor voltages for a constant temperature of 24°C as determined by the temperature standard. The precision was found to be ±0.06°C.

6.9.2 Relative Humidity Measurements

The accuracy of the RH measurements depends on four factors: 1. sensor design, 2. uncertainty in the RH over the calibration saturated salt solution due to uncertainties in the temperature, 3. standard error of the polynomial fits from *Greenspan* [1977] of RH as a function of temperature over the calibration solutions, 4. the standard error of the fit performed in this work of RH versus sensor voltage. The final RH accuracy, assuming all of the above sources of uncertainty are random in nature, is estimated by taking the root-mean sum of the squares of the uncertainties associated with each factor. The precision of RH measurements is determined by the sensor design as well

as two additional factors: temperature gradients in DMA2 and control precision of RH in DMA2.

To estimate the RH uncertainty due to uncertainties in the temperature over the saturated salt solution, the polynomials from *Greenspan* [1977] giving the dependence of RH on temperature for the various salts were differentiated with respect to temperature and the maximum temperature uncertainty of $\pm 0.09°C$ used to estimate the maximum RH uncertainty. The maximum RH uncertainties were associated with $NaCl$ (+0.04%) and KCl (-0.19%).

The primary factor limiting the accuracy of RH measurements in this work is the design of the sensor. The factory specified accuracy is $\pm 3\%$ RH. We tested the specified accuracy by performing four separate calibration runs and comparing the calculated RH values over the calibration salt solutions using the polynomials from *Greenspan* [1977] with those predicted from our derived calibration equations. The temperature of the saturated salt solution was measured and used in the polynomials from *Greenspan* [1977]. One of the four calibration runs was conducted after HTDMA studies were completed. Our comparisons indicate that for the 80 to 92% RH range, the range of all HTDMA studies performed here, the RH accuracy of the sensors is between ± 0.1 and $\pm 1.0\%$. The nominal RH accuracy as indicated from the fits of the calibration equations is $\pm 0.53\%$.

The uncertainties due to factors 3 and 4 above were estimated by *Greenspan* [1977]. The uncertainties for both of these factors were between $\pm 0.12\%$ and $\pm 0.55\%$ for the salts producing RH's between 80 and 92%. *Greenspan* [1977] reported $\pm 3\sigma$ uncertainties while $\pm 1\sigma$ values are reported here. Taking the maximum reported uncertainty of $\pm 0.55\%$ and dividing by three gives an estimated uncertainty for factors 3 and 4 of $\pm 0.18\%$.

Taking the root-mean-square sum of the above RH uncertainties, a final RH measurement accuracy of $\pm 1.0\%$ is determined. The precision of the RH measurements

made here were determined above to be ±0.85% (1σ).

6.9.3 Particle and Droplet Sizing in the HTDMA

The accuracy of the particle size determined by the DMA depends on many parameters. This is evident when one rewrites the relations presented above (Eqns. 6.1-6.4) in terms of particle diameter, D_p

$$D_p = \frac{2neLVC_c(D_p)}{3\chi q_{sh}\nu ln(r_o/r_i)} \tag{6.33}$$

e,L, r_o, and r_i are considered constants in this work and therefore do not contribute to uncertainties in D_p. n is the number of elementary electric charges on the particle. χ is the particle shape factor, and accounts for particle non-sphericity. Note that the Cunningham correction factor depends upon D_p. For the purposes of this analysis, we take C_c equal to its value for a 40 nm particle at T=24°C and a pressure of 840 mb. When estimating ΔC_c we include the derivative of C_c with respect to D_p and take the maximum D_p uncertainty of 0.6 nm for the 10-to-200 nm diameter range, as observed by *Rader and McMurry* [1986]. The uncertainty in D_p may be determined from

$$\Delta D_p = \frac{\partial D_p}{\partial \nu}\Delta\nu + \frac{\partial D_p}{\partial V}\Delta V + \frac{\partial D_p}{\partial C_c}\Delta C_c + \frac{\partial D_p}{\partial q_{sh}}\Delta q_{sh}. \tag{6.34}$$

The uncertainty in ν arises from its temperature dependence and the uncertainty in our temperature measurements of ±0.09°C . This term contributes very little to ΔD_p, as the magnitude is only 0.01 nm.

By manually adjusting and monitoring the DMA1 center rod voltage with a precision voltmeter, the uncertainty in sizing attributable to the uncertainty in the DMA column voltage was only 0.2 nm. The largest portion of the uncertainty in particle sizing is due to uncertainty in q_{sh}. Flow measurements of q_{sh} indicate that the flow rate can be controlled to within ±0.5% of a nominal value for flow rates between 5 and 16 lpm. The associated uncertainty in D_p is ±0.15 nm. The sizing uncertainty scales linearly with flow rate uncertainty. A ±0.5% variation in sheath flow rate is

typical of DMA operating conditions. The final uncertainty in sizing is due to the temperature, pressure and diameter dependence of C_c. For temperature, pressure and size uncertainties of 0.09°C , 1 mb, and 0.6 nm, respectively, an uncertainty in sizing of 0.57 nm is determined. Taking the square root of the sum of the squares of the above four uncertainties, the total uncertainty in particle size for a 40 nm diameter particle is ±0.6 nm or ±1.5%.

In addition to the random errors described above, *Rader and McMurry* [1986] determined that a systematic oversizing error in diameter measurements occured when two DMA's were used in series to measure the same particle size, as in the HTDMA. This systematic error has been attributed to flow uncertainties, diffusional broadening and unknown effects. The sizing error amounts to 0-2% and is most important for particle diameters less than 40 nm. This error can be accounted for by measuring the difference in the midpoint diameters determined from DMA1 and DMA2 when no aerosol conditioning is applied between the two DMA's. Studies of the systematic oversizing in our TDMA system showed that for the particle and droplet sizes examined in this work the effect was smaller than 1%.

The HTDMA uses a fitting procedure involving the number concentration of particles measured after the second DMA as a function of electrical mobility to determine the midpoint mobility (size) of the conditioned aerosols exiting DMA2. Therefore, uncertainties in number concentration, discussed below, affect the uncertainty in mode midpoint diameter determined from DMA2. *Rader and McMurry* [1986] determined that for a sheath-to-aerosol flow ratio of 8 and a 5% uncertainty in number concentration data, the uncertainty in measured midpoint size by DMA2 was 0.11 ±0.06% for particle diameters less than 200 nm. For 10% uncertainty in number concentration, the corresponding error in sizing was 0.22%. The estimated errors in particle sizing from *Rader and McMurry* [1986] were confirmed by experimental studies with a TDMA system. For particles smaller than 200 nm diameter, the experimental

precision was found to be better than 0.6 nm.

Using an identical RH conditioning system and a less advanced RH control system than employed in this study, *Berg et al.* [1998] have shown that the growth of ammonium sulfate and sea salt particles with RH in the HTDMA agree with published growth data [*Tang*, 1997] to within ±3%.

6.9.4 Particle and Droplet Number Concentration Measurements

Uncertainties in particle number concentrations are due primarily to Poisson counting errors, diffusional losses of particles in sample tubing, and uncertainties in condensation particle counter (CPC and UCPC) flowrates. Previous experience has shown that the CPC flowrate can be maintained within ±0.5%. An absolute, volumetric flowmeter traceable to a NIST standard, is used to measure the flowrate. The flowmeter has a reported accuracy of ±0.1% for the range of flow rates used in this study. The Poisson counting errors are large when a small number, N, of particles are counted in a given particle size bin after a DMA. The error is calculated as

$$Poisson\ Error = \frac{\sqrt{N}}{N}. \tag{6.35}$$

The HTDMA control software is configured to count a minimum of 1000 particles in each DMA size bin where a significant number of particles can be counted. Therefore, the Poisson counting error amounts to ±3.2%. The precision of particle number concentration measurements with the CPC, taking into account flow uncertainties and Poisson error, is estimated to be ±3.4%. This is smaller than the 5% error assumed by *Rader and McMurry* [1986] in their study of TDMA sizing errors.

Fluctuations in the UCPC sample flow rate occur and amount to a ±5% uncertainty in number concentration. UCPC data were obtained every five seconds at number concentrations near 1000 cm^{-3}, resulting in a total number of counted particles during a five second interval equal to about 2750 and an associated counting

uncertainty of 2%. Taking into account all of the above factors, the RMS UCPC number concentration uncertainty is therefore equal to ±6%.

Uncertainties in droplet number concentration measurements in the TGDCC are primarily due to Poisson counting statistical errors due to the very small sensing volume of the instrument. There is a small uncertainty (±2%) introduced through the application of a correction for droplet coincidence in the laser sensing volume. In order to derive S_{crit} from CCN measurements, the correct number concentration of dry particles entering the CCN chamber must be known. Studies found that the maximum fraction of particles entering the chamber was 75% for particle diameters greater than 80 nm, and the fraction decreased to 30% for 15 nm particles. The equation fitted to the loss study data exhibited a maximum error of 0.6%. For experiments performed here, a minimum of 400 droplets were counted for a given chamber supersaturation, except when the particles were too small to be activated at the chamber maximum supersaturation or during ambient studies when particle number concentrations were too low to count 400 droplets. Given the ±5% Poisson counting uncertainty based on counting 400 drops, the 0.6% diffusional loss correction uncertainty, and the 2% error introduced by the coincidence correction, the estimated uncertainty in N_{CCN} is estimated to be ±6%.

6.9.5 Number Size Distribution

The aerosol number size distribution of the polydisperse input aerosol to DMA1 was measured before and after each HTDMA study to insure that multiply charged particles could be ignored in the CCN and UCPC number concentrations. There are four basic uncertainties that conribute to the data uncertainty: the charging efficiency of the aerosol sampled by the DMA, diffusional losses within the DMA and sample inlet tubing, the DMA transfer function, and low counting efficiency of the CPC for particles with diameters less than 20 nm. Both the charging efficiency and the DMA

transfer function are accounted for by applying theoretical and empirical corrections to the data, however, these inefficiencies can increase the data uncertainty by greatly reducing the number of actual particles counted within any given size bin, resulting in poor Poisson counting statistics. This effect was minimized by counting at least 1000 particles in each size bin of the aerosol size distribution. The CPC counting efficiency is also accounted for by applying empirically determined correction factors as a function of particle size to the concentration data. The CPC efficiency correction is important for particles smaller than 20 nm. HTDMA studies reported here involved particle sizes greater than 20 nm where the CPC is 100% efficient at counting particles. Diffusional losses represent a significant fraction of the total correction factor which must be applied to the data and are a strong function of particle diameter. Again, for most of studies reported here, the relatively large particle sizes resulted in only small diffusional loss corrections. The charge correction calculation used to account for the charging efficiency of the particles entering DMA1 has an uncertainty of $\pm 2\%$ [*Wiedensohler,* 1988]. From the above analyses, uncertainties in number concentration data in a given size bin of a measured polydisperse size distribution are expected to be less than $\pm 10\%$, while the particle size has an estimated uncertainty of ± 0.6 nm as estimated previously.

6.9.6 S_{crit} Measurements

There are several factors that contribute to the experimental uncertainty in S_{crit}. These include: uncertainties in the top and bottom plate temperatures, variation of RH across the sensing volume of the laser, displacement of the chamber maximum supersaturation from the laser sensing volume centerline as a function of plate temperature difference, vapor depletion within the chamber during the course of a measurement, and the presence of larger diameter, multiply-charged particles in the aerosol sample that activate at values of S_{crit} lower than that for the singly-charged

particles.

The temperature uncertainty of the thermocouples in the CCN chamber provided by the manufacturer is ±0.3°C . For worst case conditions, where the bottom plate temperature is cooler by 0.3°C and the top plate is warmer by 0.3°C , the error in S_{crit} is -11% for S_{crit}=1% and -21% for S_{crit}=0.24%. The 0.24% to 1% S_{crit} range is similar to that experienced during HTDMA studies. We have attempted to improve on the measurement accuracy of the plate temperature difference by adding two precision thermistors to the CCN counter, measuring the top and bottom plate exterior temperatures. This was done for two reasons: first, the accuracy of the thermistors is estimated to be ±0.09°C , better than the thermocouples used in the CCN instrument; second, a 0.5 to 0.6°C offset between the thermistors and thermocouples was noticed that resulted in overestimation of the chamber supersaturation if the thermocouple temperature difference was used to calculate S_{crit}. When the instrument had been sitting idle for several days with the power off, the thermocouples registered a 0.5 to 0.6°C plate temperature difference, while the thermistors measured no temperature difference. Therefore, the thermocouple temperature gradient readings were assumed to have a 0.5°C offset. For the estimated accuracy of the thermistors, the uncertainties in S_{crit} are reduced from the values given above to ±4% for S_{crit}=1% and ±6.9% for S_{crit}=0.3%.

Another contributing factor to the uncertainty in S_{crit} is the stability of the temperature control in the CCN device. As the top plate temperature changes over the course of a measurement, the bottom plate temperature is controlled so that the plate temperature difference is held constant. Experimental studies with the TGDCC indicated that the temperature control could maintain a nominal plate temperature difference to within 0.1°C , resulting in an additional uncertainty in S_{crit} of between ±4% and ±6.9%.

For values of S_{crit} between 0.16 and 1%, the displacement of the peak supersatu-

ration from the centerline of the laser sensing volume is less than 1 mm [*CCN Design Review*, 1979]. The displacement can be calculated for experimental conditions of the CCN counter, and the actual maximum value of S_{crit} determined corresponding to the centerline of the chamber and of the laser sensing volume. Calculations indicate that for the largest displacement of the location of maximum supersaturation, the percent error between the maximum chamber supersaturation and the supersaturation in the middle of the laser sensing volume is less than -0.05% for chamber supersaturations near 0.16% and less than -0.36% for supersaturations near 1%. Given the relatively small uncertainty associated with this effect, we include the 0.36% uncertainty in our total uncertainty of S_{crit} but do not account for it in processing CCN study results.

Vapor depletion is expected to affect the growth of droplets within the chamber when concentrations of droplets exceed 2000 to 3000 cm^{-3}. For the studies performed in this work, concentrations were kept near or below 1000 cm^{-3} to avoid potential vapor depletion problems.

Larger size, multiply-charged particles will be present in the quasi-monodisperse particle sample input to the CCN counter. For particle sizes between 30 and 200 nm, the number fractions of doubly and triply charged particles that would be sampled at the same electrical mobility as singly charge particles are between 0.1 and 8% [*Wiedensohler,* 1988]. The number fractions of singly charged particles over the same size range is 12 to 20%. The larger, multiply-charged particles will appear in the CCN instrument as a droplet concentration peak before the smaller, singly-charged particles have activated and grown to detectable sizes. The potential for this effect to influence CCN study results has been determined by measuring the poly-disperse input size distribution to the first DMA before conducting HTDMA/CCN studies. Using this size distribution, the concentration of multiply-charged particles for each monodisperse particle size examined was estimated and determined to be small enough that a quantitative accounting of the effect was deemed unnecessary.

Assuming that the total uncertainty in S_{crit} is equal to the root-mean-square sum of the above errors, the estimated uncertainty in S_{crit} is between $\pm 6\%$ and $\pm 10\%$ for S_{crit} values between 0.2% and 1%.

6.9.7 Determination of Activation Size for TGDCC S_{max}

Some of the early studies conducted to verify proper operation of the CCN counter involved maintaining a constant chamber supersaturation and varying the input monodisperse particle size to the CCN instrument. For these studies, the activation size, $D_{act,50}$, is determined using an exponential fit to the ratio of the number concentration of CCN and UCPC verses dry particle size. The activation size is defined where the ratio is equal to 0.5. Once the activation size is known, the value of S_{crit} corresponding to the determined size and known composition can be calculated from Köhler theory. Therefore, uncertainties in $D_{act,50}$ will translate into uncertainties in S_{crit}. Uncertainty in $D_{act,50}$ will be due to uncertainties in $D_{p,sol}$ (0.6 nm, or 1.5% for a 40 nm dry diameter), number concentrations, and errors in the fit of the sigmoidal, exponential function to experimental data. Typical standard errors in the exponential fits were between 1 and 2%. $D_{act,50}$ is related to uncertainties in number concentrations through an exponential function, therefore, in order to determine how concentration uncertainties translate into $D_{act,50}$ uncertainties, the relation must be differentiated with respect to CCN and UCPC concentrations and the above number concentration uncertainties inserted to estimate uncertainty in $D_{act,50}$. Here, a 10% and 6% uncertainty in N_{CCN} and N_{UCPC} are assumed, respectively, based on previous analyses. The RMS uncertainty in $D_{act,50}$ is calculated to be $\pm 2.7\%$. A $\pm 2.7\%$ uncertainty in $D_{act,50}$ results in a $\pm 4\%$ uncertainty in S_{crit} for a 40 nm NaCl particle. Therefore, in addition to the $\pm 6\%$-to-$\pm 10\%$ uncertainty determined above for S_{crit} values from studies where the chamber supersaturation was varied at a constant input monodisperse particle size, an additional $\pm 4\%$ must be added to the

uncertainty in S_{crit} values determined from earlier CCN studies where the monodisperse input size was varied. The total RMS uncertainty in S_{crit} for the earliest CCN studies was therefore between ±8% and ±11%.

The ratio of the number concentrations of CCN and from the UCPC has uncertainty due to Poisson counting statistics, coincidence correction applied to the CCN droplet concentration, and from the diffusional loss corrections applied to the UCPC data. The RMS sum of the uncertainties in N_{CCN} and N_{UCPC} determined above results in an uncertainty of ±12% in their ratio.

The accuracy and precision of the various measureands in this work are summarized in Table 6.9.

6.10 *Summary*

In this chapter the theory, operating characteristics and limitations of the various, individual instruments have been described. The experimental procedures employed to measure particle hygroscopic growth in the HTDMA, CCN activity in the TGDCC, and for processing the data to determine S_{crit} have been presented. Uncertainties in all measureands have been determined assuming the various, individual uncertainties were random in nature and that their root-mean-square sum represented a good estimate of the overall uncertainty. In summary, it was found that overall experimental uncertainties were smaller than ±15%.

Table 6.1: Fit coefficients for N_{CCN} and N_{UCPC} penetration efficiency polynomials.

N_{UCPC} Coefficients					
c_0	c_1	c_2	c_3	c_4	c_5
-0.324	2.729	-2.344	1.037	-0.234	0.022
N_{CCN} Coefficients					
d_0	d_1	d_2	d_3	d_4	d_5
-5.909	15.093	-15.643	8.951	-2.687	0.327

Table 6.2: Values of air temperature and relative humidity over saturated salt solutions studied in this work. The standard error of the fit of *Greenspan [1977]* and the estimated RH accuracy are also shown. 'a', 'b' and 'c' correspond to different calibration runs. Results from run 'c' were used for all HTDMA studies.

Salt	T_a	T_b	T_c	RH_a	RH_b	RH_c	σ_{fit}	RH_{error}
KOH	24.80	24.61	24.77	8.27	8.31	8.28	0.28	0.75
$MgCl_2$	24.17	24.23	24.34	32.84	32.84	32.83	0.28	0.2
$Mg(NO_3)_2$	24.73	24.39	25.90	52.98	53.08	52.63	0.34	0.25
$NaCl$	24.61	24.47	26.10	75.31	75.32	75.25	0.21	0.12
$(NH_4)_2S0_4$	24.66	24.67	24.73	81.02	81.02	81.01	0.4	0.28
KCl	24.14	24.03	25.51	84.47	84.49	84.27	0.45	0.3
KNO_3	24.02	23.93	27.40	93.81	93.83	93.01	0.8	0.6
K_2SO_4	24.04	23.92	26.84	97.36	97.37	97.19	0.47	0.5

Table 6.3: RH calibration coefficients determined for each sensor for calibration runs 'a', 'b', and 'c'. Signal conditioning electronics were changed for sensors 4, 5, and 6 between runs 'b' and 'c'. This accounts for the large change in calibration coefficients for these three sensors.

Sensor	a_0	a_1	a_2	a_3
		Calibration Dataset 'C'		
3	-2.9574130e+01	6.9051478e+01	-1.4756261e+00	3.0276813e-01
2	-3.4904064e+01	8.6360322e+01	-4.0188176e+00	-9.4198238e-02
1	-3.2863645e+01	7.6569856e+01	-2.4489178e+00	-1.4563129e-02
6	-2.9732514e+01	1.0883087e+02	-4.5149298e+00	4.2831735e+00
4	-3.2512484e+01	1.0453021e+02	-8.4009120e+00	4.7501619e+00
5	-2.9709068e+01	1.0434909e+02	-3.5901012e+00	1.8280492e+00
		Calibration Dataset 'B'		
3	-2.4395003e+01	5.9873682e+01	3.9229174e+00	-6.1198656e-01
2	-2.5681544e+01	6.3899169e+01	2.5334505e+00	-4.6258133e-01
1	-2.0758681e+01	5.1397041e+01	9.2159696e+00	-1.6435676e+00
4	-2.3264873e+01	1.1279725e+03	4.2243580e+04	-2.1164163e+06
5	-2.3491389e+01	1.1669841e+03	4.3165584e+04	-2.6141737e+06
		Calibration Dataset 'A'		
3	-2.3050086e+01	5.7827108e+01	4.4692342e+00	-6.2459772e-01
2	-2.4336043e+01	6.1807681e+01	3.1244604e+00	-4.8334062e-01
1	-1.9218964e+01	4.8960107e+01	9.9779755e+00	-1.6966063e+00
6	-2.1964490e+01	1.0896339e+03	4.5824053e+04	-2.0785430e+06
5	-2.2146090e+01	1.1257020e+03	4.7586220e+04	-2.6353308e+06

Table 6.4: Standard error of fit and accuracy of RH measurements in plus/minus percent for different RH sensors for two calibration runs.

Sensor Number	σ_{fit} All RH's	σ_{fit} 8-54% RH	σ_{fit} 75-97% RH	χ^2	Error All RH's	Error 8-54% RH	Error 75-97% RH
			Calibration Dataset 'C'				
3	0.6659	0.9924	0.5163	0.7760	0.5591	0.1230	1.0229
2	0.6591	0.7593	0.6806	0.7601	0.5971	0.3445	0.9778
1	0.6800	1.0144	0.5237	0.8093	0.5639	0.0553	1.0600
6	0.6234	0.9669	0.4421	0.6802	0.5370	0.2150	1.0101
4	0.5061	0.7561	0.3895	0.4482	0.4432	0.1171	0.7963
5	0.6359	1.0691	0.3392	0.7077	0.5159	0.1272	1.1098
			Calibration Dataset 'B'				
3	0.5539	0.7644	0.4871	0.5369	1.1177	1.5433	0.9820
2	0.5596	0.7913	0.4772	0.5479	1.1289	1.5965	0.9624
1	0.9215	1.5624	0.4477	1.4862	1.8490	3.1319	0.9039
4	0.5862	0.8882	0.4385	0.6013	1.1817	1.7888	0.8856
5	0.6828	1.0533	0.4882	0.8158	1.3735	2.1172	0.9842
			Calibration Dataset 'A'				
3	0.5606	0.9018	0.3529	0.5501	1.1310	1.8159	0.7165
2	0.5118	0.7654	0.3911	0.4584	1.0343	1.5452	0.7918
1	0.9989	1.7381	0.3572	1.7462	2.0033	3.4827	0.7249
6	0.6295	0.9363	0.4694	0.6934	1.2676	1.8844	0.9468
5	0.6526	1.0473	0.3994	0.7453	1.3135	2.1051	0.8083

Table 6.5: Precision of RH measurements in plus/minus percent as a function of relative humidity and sensor for two calibration runs.

	Nominal Relative Humidity (%)							
Sensor Number	8	33	53	75	81	84.5	94	97
				Calibration Dataset 'B'				
3	0.0677	0.0263	0.0359	0.0621	0.0555	0.1026	0.0391	0.0388
2	0.0739	0.0569	0.0348	0.1300	0.0661	0.1026	0.0355	0.0349
1	0.0612	0.0305	0.0357	0.0620	0.0597	0.1046	0.0302	0.0273
4	0.3403	0.3441	0.4116	0.4328	0.4550	0.4445	0.4059	0.4439
5	0.3315	0.4199	0.4665	0.4952	0.4795	0.4766	0.4211	0.4534
				Calibration Dataset 'A'				
3	0.0428	0.0659	0.0352	0.1327	0.1156	0.1272	0.0321	0.0313
2	0.0558	0.0652	0.0330	0.1204	0.1202	0.0381	0.0317	0.0358
1	0.0396	0.0563	0.0391	0.1638	0.0769	0.1379	0.0268	0.0233
6	0.3240	0.4042	0.4131	0.5180	0.4691	0.4969	0.4934	0.4923
5	0.3768	0.3703	0.4239	0.4957	0.4770	0.4654	0.3932	0.4195

Table 6.6: Thermistor calibration coefficients determined for each sensor between 20 and 32°C .

Sensor	b_0	b_1	b_2
0	3.0938322e-03	2.3379076e-04	3.3449178e-06
1	3.0907097e-03	2.3690311e-04	2.9917922e-06
2	3.0896680e-03	2.3977041e-04	2.7174088e-06
3	3.0920681e-03	2.3524773e-04	3.4485357e-06
4	3.0835828e-03	2.4461117e-04	2.4253536e-06
5	3.0958356e-03	2.3167173e-04	3.5983090e-06
6	3.0877380e-03	2.3971577e-04	2.7673070e-06
7	3.0891577e-03	2.3805256e-04	3.0722130e-06
8	3.0892896e-03	2.3815654e-04	3.0361694e-06
9	3.0866160e-03	2.4133365e-04	2.7134389e-06

Table 6.7: Standard error of fit and goodness of fit of temperature measurements in plus/minus degrees celcius for different thermistors.

Sensor	σ_{fit}	χ^2
0	8.6937561e-02	7.5645719e-03
1	7.5135580e-02	5.6501599e-03
2	7.0001632e-02	4.9043989e-03
3	8.8871959e-02	7.9049469e-03
4	5.7700797e-02	3.3322155e-03
5	9.2143407e-02	8.4976334e-03
6	6.5505411e-02	4.2946108e-03
7	7.4703465e-02	5.5853572e-03
8	7.0290944e-02	4.9450218e-03
9	6.1521225e-02	3.7880823e-03

Table 6.8: Precision of temperature measurements in plus/minus degrees celcius for different thermistors.

Sensor	Precision
0	0.5394245e-01
1	0.4573173e-01
2	0.4861040e-01
3	0.6093519e-01
4	0.3379349e-01
5	0.5417099e-01
6	0.3913867e-01
7	0.4315035e-01
8	0.4667474e-01
9	0.4098088e-01

Table 6.9: Experimental uncertainties in major measureands.

Measureand	Experimental Uncertainty
T	0.09°C
RH	1%
$D_{p,sol}$	0.6 nm
N_{UCPC}	6%
N_{CCN}	6%
S_{crit}	6-11%
$\frac{N_{CCN}}{N_{UCPC}}$	12%

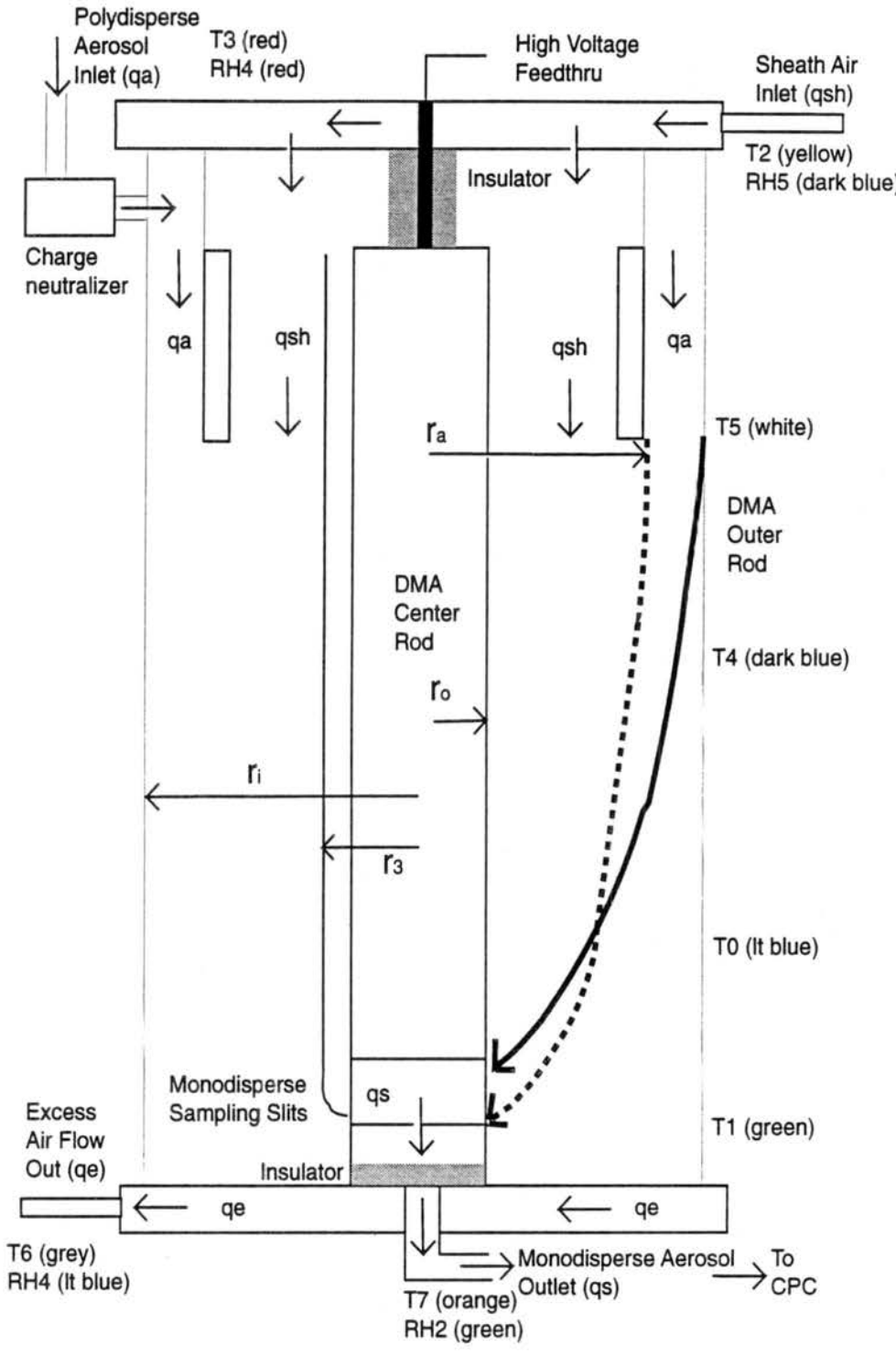

Figure 6.1: Schematic diagram of DMA. Arrows designate air sample flow pathways. 'RH4' designates RH sensor number 4. 'T4' designates thermistor number 4. Dashed trajectory indicates minimum sampled particle mobility while solid trajectory indicates maximum sampled particle mobility. Colors were used for identification purposes during data acquisition.

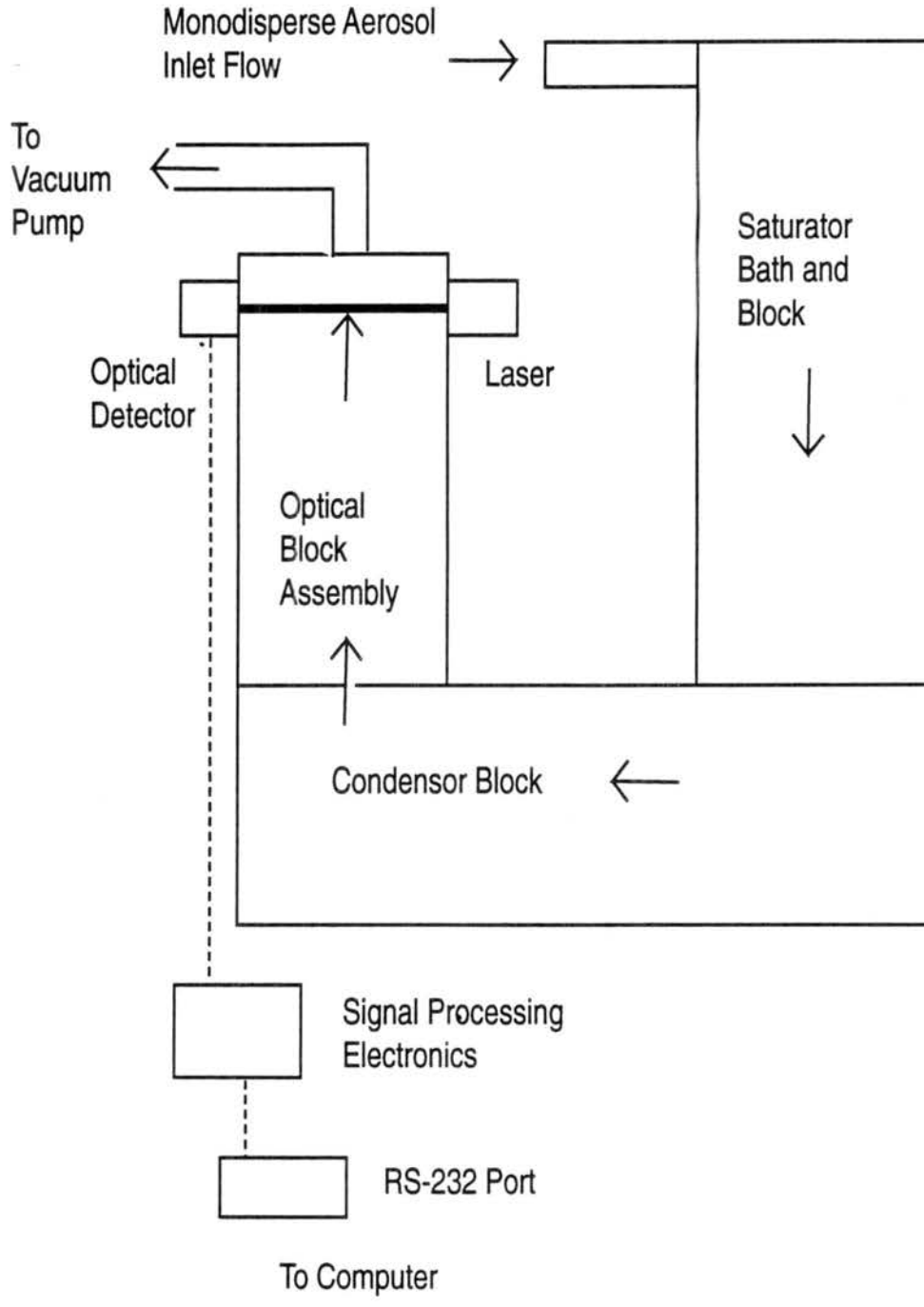

Figure 6.2: Schematic diagram of CPC. Solid lines with arrows designate air sample flow pathways.

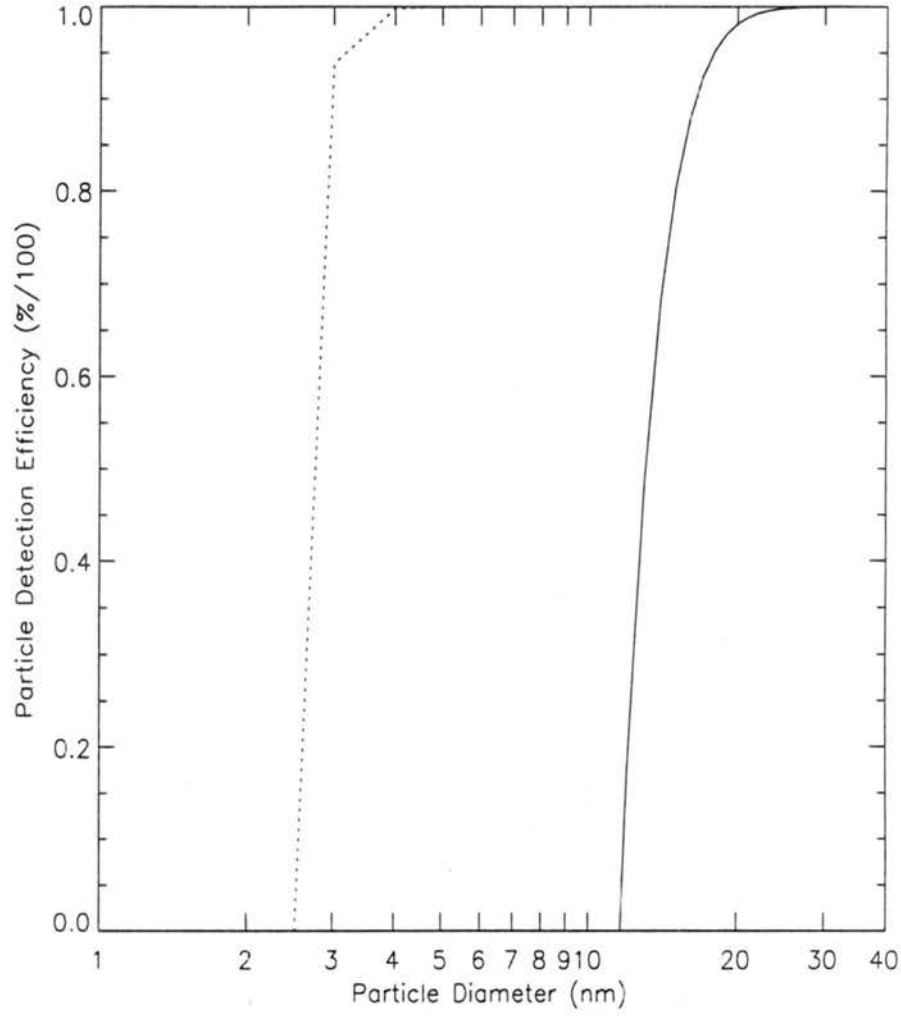

Figure 6.3: Counting efficiencies of CPC and UCPC as a function of particle size [*Wiedensohler et al.*, 1997]. Dashed line designates UCPC.

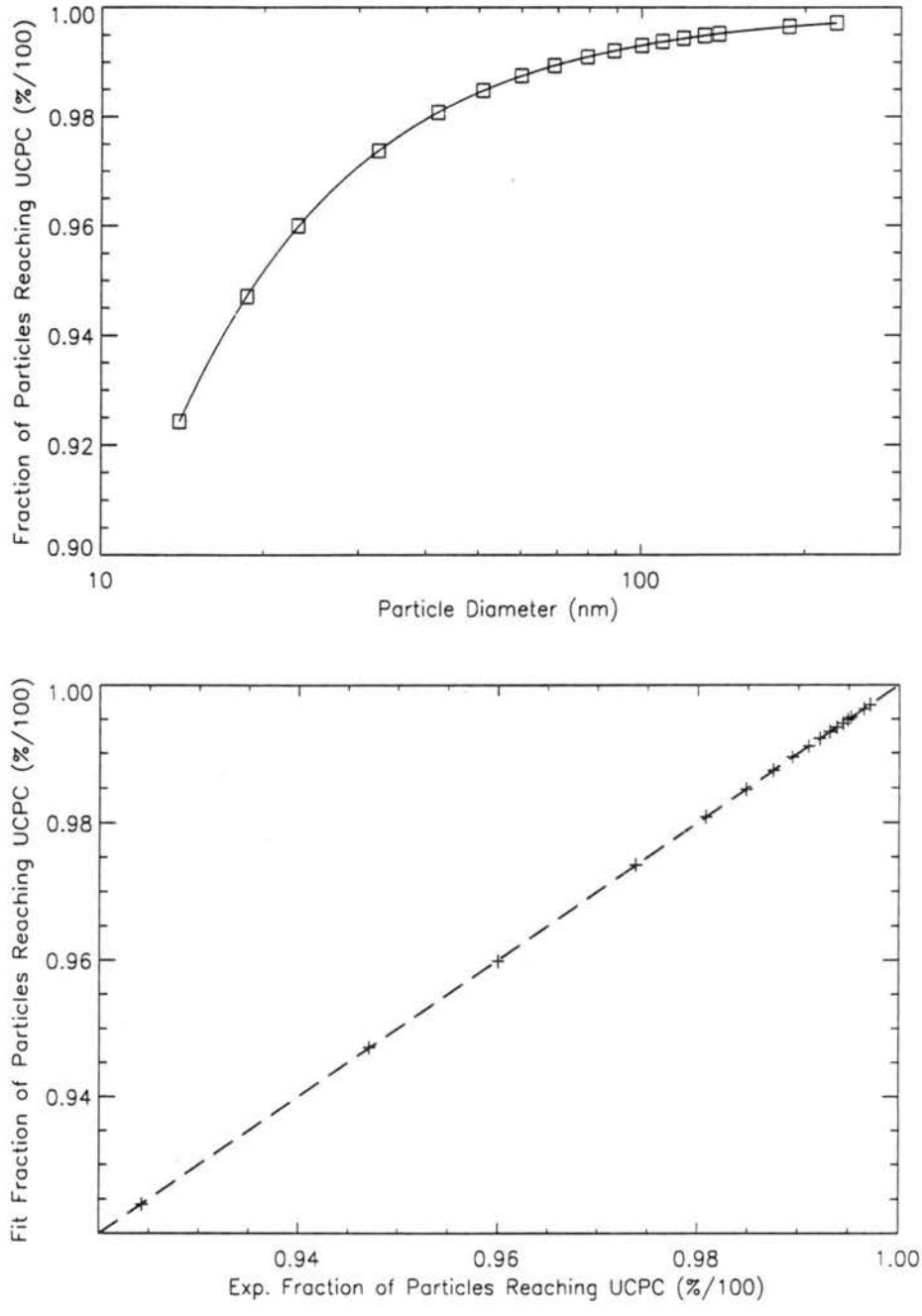

Figure 6.4: Theoretical particle diffusional losses in UCPC inlet (top), and (bottom) comparison of polynomial fit to theoretical diffusional loss results.

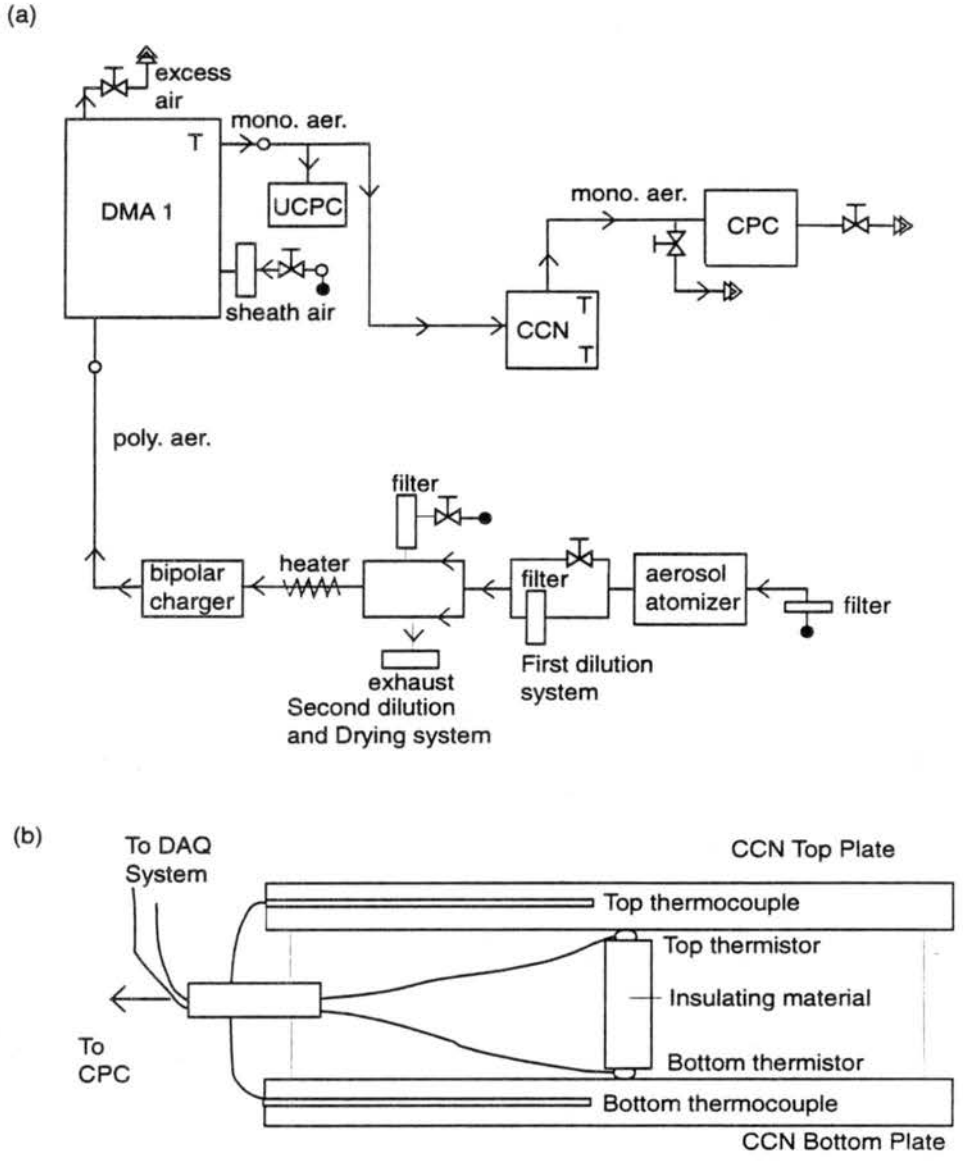

Figure 6.5: Schematic diagram of (a) system used to quantify particle losses and plate temperature difference in CCN counter. Solid lines with arrows designate air sample flow pathways. Solid dot designates particle free compressed air source. Double triangle designates vacuum source. Open dot designates RH sensor. 'T' designates location of thermistor temperature measurement; (b) system used to sample particles from the CCN diffusion chamber with CPC and for inserting thermistors inside chamber to measure inside plate temperatures.

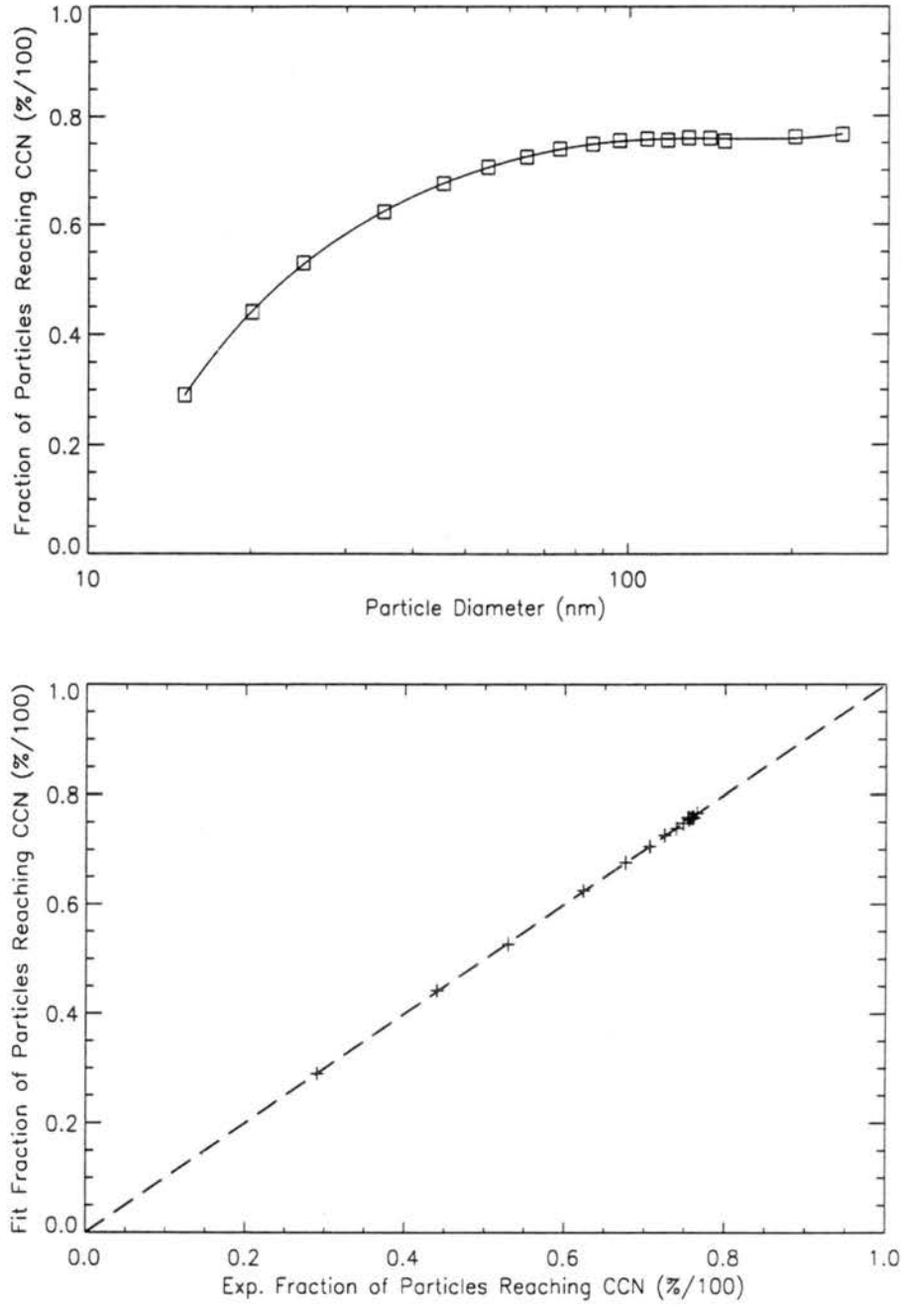

Figure 6.6: Particle losses (a) due to diffusion and losses in solenoid valve and top plate inlet in TGDCC, (b) comparison of polynomial fit to experimental particle loss data.

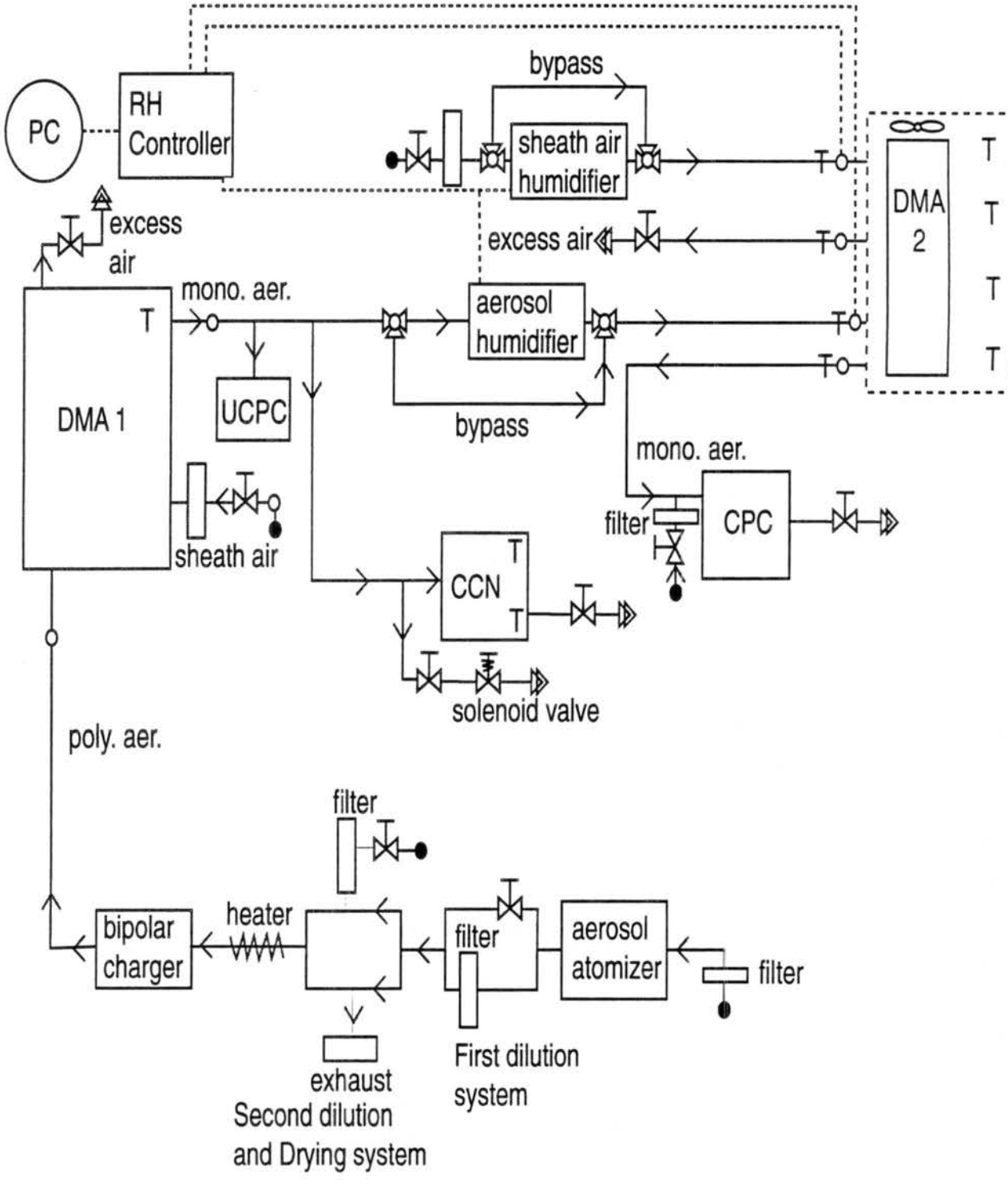

Figure 6.7: Schematic diagram of HTDMA system. Solid lines with arrows designate air sample flow pathways. Solid dot designates particle free compressed air source. Double triangle designates vacuum source. Open dot designates RH sensor. 'T' designates location of thermistor temperature measurement.

Chapter 7

Experimental Results

7.1 *Introduction*

In this chapter, results from the various laboratory studies are presented. Results from quality control experiments serve to validate the operation of the HTDMA and CCN instruments. The particle sizing capability of the HTDMA is validated by running without humidification to examine the observed dry particle size. The elevated RH runs on known chemical composition particles are compared to theoretical estimates of droplet growth to validate HTDMA operation. Hygroscopic growth results from studies on various particle chemical compositions are used in the fit routine to determine S_{crit} and the derived values are compared to those from TGDCC runs and, when possible, to theoretical S_{crit} values. Finally we present results from studies on ambient particle samples. A list of all HTDMA and TGDCC studies conducted for this work is given in Table 7.1.

7.2 *Quality Control Experiments*

Results from several of the quality control experiments conducted are presented in this section. The experiments include validation of zero counts, quantification of artifact particle number concentrations, and verification of accurate RH and temperature control.

7.2.1 Artifact Particles

In order to verify that unwanted particles were not contaminating the air samples via leaks, the HTDMA/CCN system was operated with no solution in the atomizer and size distribution measurements were performed using DMA1 and the UCPC. Results are shown in Figure 7.1. The solid curve represents a best-fit log normal distribution to the experimental data. There is some indication that artifact particles smaller than 30 nm are present in the system. However, for particles sizes between 20 and 100 nm, the number concentrations observed in any single size bin were between 0.03 and 0.09 cm^{-3}. The measurement was repeated and similar results were obtained. The observed artifact particle concentrations are two-to-five orders of magnitude smaller than concentrations observed during experiments where ambient and laboratory particles were sampled, respectively. Therefore, artifact particles have much smaller diameters and lower concentrations than actual particle samples, and should not influence the results of the HTDMA and CCN experiments conducted for this work.

A second test was conducted to examine the size distribution of artifact particles generated from atomization of Nanopure water containing no solute. The Nanopure water used for the atomizer solute solutions contains small amounts of impurities that could form particles after atomization and drying of the droplets, or influence the chemical composition of the atomized salt particles by becoming internally mixed with the salt particle. This would not occur during ambient samples where the atomizer and air flows associated with the dilution system were not used. To investigate this effect, pure Nanopure water was atomized and size distributions measured using DMA1 and the UCPC. The particle generation, dilution, and drying systems were operated using the same procedure as during HTDMA studies. All particle-free airstreams in the HTDMA system, including the atomizer and dilution chamber air flows, were filtered with HEPA filters prior to use. Results from the measurements

are shown in Figure 7.2. The solid curve represents a best-fit log normal number size distribution. The size distribution exhibits a mode size near 30 nm, a geometric standard deviation of 1.6, and a number concentration of 7000 cm^{-3}. The measurement was repeated with similar results. The concentrations of artifact particles in the 40 to 60 nm size range, representative of particles sampled in HTDMA studies on known composition particles, are between 180 and 450 cm^{-3}. For comparison, the range of concentrations of 40-to-60 nm salt particles sampled during HTDMA studies is two orders of magnitude higher than the observed concentration of artifact particles. Therefore, at most one-to-two percent of the total number concentration of atomized salt particles consisted of artifact particles with unknown chemical composition. Alternatively, some fraction of the total number concentration of atomized salt particles may have contained impurities from the Nanopure water. Based on the low relative monodisperse number concentrations and small sizes of the particles resulting from impurities in the Nanopure water, the assumption is made that they do not significantly influence the results of HTDMA growth or CCN activity studies conducted for this work.

7.2.2 RH and Temperature Control and Calibrations

The quality of droplet growth measurement results from the HTDMA depends in part on the accuracy and precision of the RH and temperature measurements. The accuracy and precision of S_{crit} values determined from CCN measurements depend upon the accuracy and precision of the measurements of the top and bottom plate temperatures in the instrument. Therefore, RH and T sensors were calibrated before experiments were conducted and the calibrations were checked after all experiments were completed. Except for a few early CCN validation studies, where HTDMA experiments were not performed, all experiments were conducted over a one month period.

As described in chapter 6, RH sensors were calibrated over saturated salt solutions. For calibration run 'D', where the RH calibrations were checked after experiments were completed, the RH sensors were exposed to three saturated salt solutions spanning the 80 to 93% RH range. This RH range represented the range of RH's experienced during HTDMA studies. The results from the RH calibrations before and after the HTDMA experiments are compared in Figure 7.3(a), (b), and (c) for saturated salt solutions of $(NH_4)_2SO_4$, KNO_3, and KCl, respectively. The theoretical calibration RH's are shown as solid lines in the figures with either 'C' or 'D' designating data from a particular calibration run. Values were calculated from the results of *Greenspan* [1977]. The theoretical RH's are not exactly the same for calibration runs 'C' and 'D' due to differences in the temperatures of the saturated salt solutions. Each of the six RH sensors are shown in separate plots for each of the saturated salt solution runs. In the figure, dashed lines with the letter 'C' designate the RH determined from the calibration equation for the particular RH sensor for run 'C'. Dashed lines with the letter 'D' designate the RH calculated using the same calibration equation derived from run 'C' for the saturated salt solution exposures in run 'D'. For all RH sensors used in determining DMA2 flow relative humidities, except that used for the excess air out flow, the relative humidities measured during runs 'C' and 'D' by each sensor agree with the theoretical calibration RH calculated for the saturated salt solution within $\pm 0.8\%$ for $(NH_4)_2SO_4$, $\pm 0.9\%$ for KCl, and $\pm 1\%$ for KNO_3. The agreement between RH values from the excess air RH sensor was not as good as for the other three DMA2 sensors. This sensor exhibited an offset of between 6% and 2% RH for RH's between 80% and 93% that monotonically decreased with increasing RH. This sensor offset was apparent in the excess air flow RH values observed during HTDMA studies, therefore, the excess air RH sensor data were not used in processing HTDMA results. The DMA1 inlet and outlet RH sensors also demonstrated some calibration drift, evident in Figure 7.3. The poorer performance of the DMA1 sensors

ws noted immediately after run 'C', therefore, they were purposely chosen to measure the inlet and outlet RH's of DMA1. The drift in the DMA1 RH sensors may be due to the relatively higher particle concentrations experienced by these sensors and the increased particle deposition onto the sensing surface relative to the other sensors. The DMA1 RH sensors were only used to measure RH's below 20%, therefore, the observed calibration drift for the 80 to 93% RH range is not representative of the performance of these sensors during laboratory experiments. Furthermore, the level of accuracy required for RH measurements in DMA1 was lower than that for DMA2. The DMA1 RH sensor calibrations were checked at an RH near 20% and agreement with the theoretical RH value for the saturated salt solution was found to be within $\pm 2\%$. The DMA 2 monodisperse in, monodisperse out, and sheath air flow sensors exhibited acceptable agreement with the theoretical saturated salt calibration RH's and were averaged to determine the RH corresponding to the observed droplet size. The calculated average RH value was used for plotting all HTDMA growth results. The results of the comparison of RH values from runs 'C' and 'D' indicate that RH measurements for all HTDMA studies exhibited an accuracy between $\pm 0.8\%$ and $\pm 1\%$ and precision of $\pm 0.6\%$.

The accuracy and precision of the thermistor temperature measurements were evaluated after experiments were completed by re-performing the calibration as outlined in chapter 6. Results from the new and old calibrations agreed within $0.1°C \pm 0.05°C$ for temperatures between 20°C and 32°C, the range of temperatures encountered in this study. Therefore, significant drift in the thermistor temperature measurements did not occur over the course of laboratory studies.

7.3 *Validation of CCN Counter Operation*

To validate proper operation of the CCN counter, the activation supersaturations of ammonium sulfate and sodium chloride particles were investigated for chamber supersaturations between 0.2 and 1.0%. The purpose of these studies was to evaluate the experimental uncertainties in the techniques for deriving experimental values of S_{crit} and also to verify the repeatability of the method. Several runs were performed for both chemical compositions. Two different experimental techniques were used to validate instrument operation. The first technique involved sampling progressively smaller, monodisperse NaCl or $(NH_4)_2SO_4$ particles with the CCN counter set for a constant chamber supersaturation. The diameter where 50% of the input particles were activated to droplets could be determined by fitting the sigmoidal function described in chapter 6 to the ratio of N_{CCN} to N_{UCPC} verses particle diameter. Using the experimentally determined value of $D_{act,50}$ and the known chemical composition, the theoretical value of S_{crit} could be calculated and compared to the average chamber maximum supersaturation for the experiment. N_{UCPC} data were corrected for sample line losses and for losses inside the CCN counter. N_{CCN} data were corrected for coincidence errors and the 1/10th cm^3 data were averaged to determine N_{CCN} for either a full cubic centimeter of air sampled by the TGDCC, or after 400 droplets had been counted, whichever came first. The percent error between the chamber and theoretical supersaturations defines the experimental accuracy and precision of the technique for estimating S_{crit} for a given particle chemical composition using this technique.

The second method for deriving S_{crit} from CCN measurements involved maintaining a constant input, monodisperse particle size and varying the chamber supersaturation so that values of the ratio of N_{CCN} to N_{UCPC} between 0.2 and 0.9 could be observed. The supersaturation where the ratio of N_{CCN} to N_{UCPC} was equal to 0.5 was then defined as the experimental estimate of S_{crit}. Although both methods for

deriving S_{crit} are equally valid for evaluating experimental uncertainties in derived S_{crit} values for particles of known composition, the second method was employed for all simultaneous HTDMA/CCN studies after and including day of year (DOY) 163. This choice was based on the fact that for ambient particles of unknown chemical composition, only the second method will allow valid experimental estimates of S_{crit} to be made.

Figure 7.4(a) shows results from a CCN study conducted on DOY 148 using the first method and $(NH_4)_2SO_4$ particles. The chamber was set for a supersaturation of 0.26% and the chamber supersaturation exhibited a standard deviation of 0.018% (7% variation) over the course of the measurement. Timelines of chamber supersaturation (diamonds), top and bottom plate temperatures (thin and thick lines), and the temperature difference between the top and bottom plate temperatures (dots; multiplied by 11) are shown in Figure 7.4(b). We show timelines of the CCN instrument temperatures and supersaturation for the CCN validation study results only to demonstrate the instrument's ability to control the chamber supersaturation. The estimates presented below of the experimental uncertainties in values of S_{crit} derived from CCN study results account for the effect of the variation in chamber supersaturation. In Fig. 7.4(b), as the top plate temperature increases over the course of the experiment, the bottom plate temperature also increases in order to maintain a relatively constant temperature difference between the two plates and a stable chamber supersaturation. The particle size corresponding to the point where 50% of the input dry particles are activated to droplets and counted as CCN (Fig. 7.4(a)) was determined by fitting the sigmoidal function described in chapter 6 to the ratio of N_{CCN} to N_{UCPC}. From the fit results, the observed value of $D_{act,50}$ was 65 nm. The theoretical S_{crit} value for a 65 nm $(NH_4)_2SO_4$ particle at the average chamber temperature was calculated to be 0.32%. In this, and all other comparisons, theoretical values of S_{crit} were calculated at the average chamber temperature for the particular CCN study. For this run, the

experimental estimate of S_{crit} is 17% lower than the theoretical value.

The results from a similar study, conducted on DOY 152 with NaCl particles are shown in Figure 7.5. For the nominal 0.255% chamber supersaturation during this study, the experimentally determined activation size for NaCl particles was 59 nm (Figure 7.5(a)). The timelines of chamber supersaturation and plate temperatures are shown in Figure 7.5(b). Chamber supersaturations ranged between 0.28% at the beginning of the study and 0.235% at the end of the study, representing a ±9% range about the nominal chamber supersaturation of 0.255%. The theoretical value of S_{crit} for a 59 nm NaCl particle at the average chamber temperature is 0.263%, within 3% of the experimentally determined nominal value of S_{crit}.

A final example from DOY 169, demonstrating the second method for determining S_{crit}, is shown in Figure 7.6. Experimental data are shown as asterisks and the solid line represents the best-fit line to the data. The sigmoidal function was not used for studies where the chamber supersaturation was varied because a narrow range of supersaturations was investigated and due to the fewer number of points obtained during experiments where the chamber supersaturation was varied. Between one and two hours were required for the chamber supersaturation to stabilize after being reset. The same amount of time was required to measure a significant number of droplets at a given supersaturation. Therefore, the two to four hour period required for each chamber supersaturation reduced the number of points that could be obtained during CCN studies where the chamber supersaturation was varied. Using the second method for determining S_{crit}, the input monodisperse size to the CCN chamber was kept constant at 57.2 nm, and the particles were composed of $(NH_4)_2SO_4$. The theoretical value of S_{crit} for this size and composition particle was 0.41%, and is shown in Fig. 7.6(a) as the solid dot. The experimentally determined value of S_{crit}, shown in Figure 7.6(a) by the intersection between the dotted line and the x-axis, was 0.42%. The agreement between theoretical and experimental values of S_{crit} is 3%.

In Fig. 7.6(a), the average value of S_{crit} from the fit routine run using all HTDMA data pairs with no applied random error is shown as the square. The plus symbol designates the average value of S_{crit} from the fit routine using all HTDMA data pairs with applied 1% random errors to the input parameters. The triangles represent the $\pm 1\sigma$ range of S_{crit} values predicted using the fit routine and all HTDMA growth results with applied error. These results will be discussed in section 7.5. Timelines of the chamber supersaturation and plate temperatures are shown in Figure 7.6(b) for the four different chamber supersaturations examined for this study. For chamber supersaturations between 0.3% and 0.54% for this study, the standard deviation in chamber supersaturation was less than 0.005% for each of the four different chamber supersaturations examined.

Results for all CCN studies are listed in Table 7.2 and have been plotted in Figure 7.7. The results from all CCN studies not presented as figures in this chapter are given in Appendix C. In Fig. 7.7, the solid line designates the 1:1 line, and represents perfect agreement between theoretical and experimental values of S_{crit}. The different compounds are designated by different symbol types: pluses for $(NH_4)_2SO_4$, asterisks for NaCl, diamonds for NH_4HSO_4, triangles for internally mixed NaCl-$(NH_4)_2SO_4$, and squares for externally mixed NaCl-$(NH_4)_2SO_4$. The vertical error bars represent the $\pm 21\%$ confidence interval in CCN-derived values of S_{crit}. The calculation of the confidence interval is described below. For all CCN studies conducted at supersaturations below 0.8%, the agreement between theory and experiment is very good.

The experimental uncertainty in the value of S_{crit} determined from CCN studies was evaluated by calculating the confidence interval as a percent of S_{crit} for a 95% confidence level. All confidence intervals in this work are calculated for a 95% confidence level. Henceforth, this will be taken as understood. Only results from studies on $(NH_4)_2SO_4$, NH_4HSO_4, and externally mixed $(NH_4)_2SO_4$ and NaCl particles were used in the calculation of the confidence interval since true replicate measurements

of S_{crit} are only available for these compounds. The two replicate measurements used were from studies on DOY's 169 and 176 for $(NH_4)_2SO_4$, DOY's 172 and 178 for NH_4HSO_4, and DOY's 177 and 181 for the externally mixed particles (see Table 7.2). Here we assume that the three different compounds represent three 'replicate' experiments to determine S_{crit}. Under these assumptions, the degrees of freedom (DOF) for calculating the pooled standard deviation is 6-3=3. The pooled standard deviation can be calculated [*Skoog et al.*, 1992]

$$s_{pooled} = \sqrt{\frac{\sigma_1^2(N_1 - 1) + \sigma_2^2(N_2 - 1) + \sigma_3^2(N_3 - 1)}{DOF}} \tag{7.1}$$

where σ_1, σ_2, and σ_3 are the standard deviations in values of S_{crit} for $(NH_4)_2SO_4$, NH_4HSO_4, and externally mixed NaCl-$(NH_4)_2SO_4$ for the replicate measurements, respectively, and N_1, N_2, and N_3 are the number of replicate CCN studies conducted on particles composed of $(NH_4)_2SO_4$ (2), NH_4HSO_4 (2), and externally mixed particles (2), respectively. Calculations using the data in Table 7.2 give a value for s_{pooled} of 0.029%. The units of s_{pooled} are the same as S_{crit}. For a 95% confidence level and a single set of measurements of S_{crit} (N=1), the t value required to calculate the confidence interval is 3.18 [DOF=3, *Skoog et al.*, 1992]. The t value is determined by the degrees of freedom in the calculation of s_{pooled}. The confidence interval can be calculated [*Skoog et al.*, 1992]

$$C.I._{95\%} = \pm\frac{t s_{pooled}}{\sqrt{N}}. \tag{7.2}$$

Using the above relation, the confidence interval for values of S_{crit} derived from CCN studies is $\pm 0.092\%$ (in units of S_{crit}). The confidence interval represents a coefficient of variation of approximately $\pm 21\%$. A second technique for determining the confidence interval was investigated. Assuming that the value of s_{pooled} determined above is representative of the true standard deviation in replicate measurements of S_{crit}, the calculated confidence interval value, in units of S_{crit}, is $\pm 0.056\%$. The coefficient of variation for the smaller confidence interval is $\pm 13\%$. The assumption that the

value of s_{pooled} is representative of the true population standard deviation is typically valid when greater than 20 replicate measurements have been performed. Only three replicate measurements were made here, therefore the more conservative ±21% value will be taken as the 95% confidence interval for S_{crit} in the remainder of this work.

The agreement between theoretical and experimental values of S_{crit} was also examined. For all CCN studies on particles composed of single, pure salts, the calculated average percent agreement is -0.6% (n=16). The simple standard deviation (67% confidence level) in the percent agreement between theoretical and experimental values of S_{crit} calculated from the same results is 11%. The standard deviation calculations were repeated with the results from the two different methods for determining S_{crit} treated separately. A total of ten CCN studies with NaCl and $(NH_4)_2SO_4$ particles were conducted where the chamber supersaturation was kept constant. Six studies were conducted on particles composed of NaCl, $(NH_4)_2SO_4$, and NH_4HSO_4 where the chamber supersaturation was varied. For studies where the chamber supersaturation was kept constant, the average and standard deviation of the percent agreement between theoretical and experimental values of S_{crit} were -5% and 11%, respectively. The corresponding values for studies where the chamber supersaturation was varied were 6.8% and 6%, respectively.

7.4 *Validation of HTDMA Hygroscopic Growth Measurements*

In order to validate HTDMA operation, two types of experiments were performed. First, to verify proper sizing, the humidity system was bypassed and dry particle size distributions were measured. These studies were performed on particles in the 40 to 100 nm size range composed of ammonium sulfate and sodium chloride. The purpose of these studies was to quantify the systematic oversizing of the TDMA system, as found by previous investigators (*Rader and McMurry,* [1986]). For the 25 size

distribution scans performed on 40 nm NaCl particles, the average mode diameter determined by fitting a Gaussian function to the number concentration data from DMA2 was 40.9 nm. The standard deviation of the average mode diameter was 0.13 nm, resulting in a coefficient of variation in the mean size of 0.33%. The ratio of the average mode size from DMA2 to the mean diameter selected by DMA1 was 1.02, or a systematic oversizing of 2% was found in the TDMA for 40 nm particles. This is consistent with previous results from *Rader and McMurry* [1986]. Similar results were obtained with ammonium sulfate particles. Studies performed on 50 nm $(NH_4)_2SO_4$ particles indicated that the oversizing decreased to around 1%. At 60 nm, the systematic oversizing again decreased to 0.7%. At 100 nm, no systematic oversizing was observed. Given that the systematic oversizing in the TDMA amounts to a very small correction for droplet sizes between 60 and 200 nm measured by DMA2, HTDMA data were not corrected for this effect. HTDMA studies on dry 40 nm particles demonstrated that the sizing precision of the system was $\pm 0.33\%$.

The second set of experiments involved controlled, elevated RH droplet growth studies on NaCl and $(NH_4)_2SO_4$ particles with diameters between 25 and 60 nm. The goal was to determine the experimental uncertainty in the observed droplet growth ratio. The uncertainty is defined as the confidence interval in percent error between droplet growth ratios measured with the HTDMA system and those reported by *Tang and Munkelwitz* [1994]. The confidence interval reported here is at the 95% confidence level. *Tang and Munkelwitz* [1994] measured the water uptake of NaCl, $(NH_4)_2SO_4$, and other particle compositions by levitating a dry particle in an electrodynamic balance and exposing it to known relative humidities. The water uptake could be determined from the balance voltage required to keep the droplet levitated. *Tang and Munkelwitz* [1994] measured the water uptake of single super-micrometer particles, where the Kelvin effect could be neglected. Therefore, in order to make the comparison with our observations, a Kelvin correction was applied to the results of *Tang*

and Munkelwitz [1994]. Results from all studies on NaCl and $(NH_4)_2SO_4$ particles are shown in Figures 7.8 and 7.9, respectively. All of the solutes used in this work contained less than 0.2% contaminants by mass and were certified by the Americal Chemical Society (Fisher Chemical, Fisher Scientific, Fair Lawn, New Jersey). In processing the results from these studies it was found that the RH of the monodisperse inlet flow to DMA2 had to be controlled within 2% of the sheath flow RH and that the standard deviations of both RH's had to be less than 1% in order for accurate growth measurements to be made. HTDMA results not satisfying the above RH control criteria were deemed unacceptable. Applying these criteria resulted in rejection of 17% of HTDMA study results. In these and subsequent figures, the thick dashed-dot line represents the measurements of droplet growth from *Tang and Munkelwitz* [1994] corrected for the Kelvin effect. The solid line designates theoretical growth curves calculated using the reference Köhler model. Experimental points are shown as solid dots; the vertical and horizontal bars designate calculated uncertainties in the measurement RH and particle and droplet sizes. Due to the cubic shape of NaCl particles, the dry particle electrical mobility diameter was reduced by a factor of 1.08, based on the work of *Kelly and McMurry* [1992]. No shape factor was applied to the dry diameter of $(NH_4)_2SO_4$ particles. RH measurement uncertainties were determined by calculating the root mean square sum of the standard deviations of the DMA2 sheath, monodisperse inlet, and monodisperse outlet flow RH's, as well as the 0.5% RH uncertainty atributable to the RH sensor calibration procedure. A $\pm 2\%$ uncertainty was assumed as a conservative estimate for droplet and dry particle size uncertainties, producing a $\pm 3.5\%$ overall uncertainty in the droplet growth factor. Uncertainties were calculated in the same manner for all HTDMA studies. The measured average HTDMA study temperature was used in the theoretical calculations of RH using the reference Köhler model. Dashed lines represent two-times the standard deviation in the percent agreement between observed and theoretical

droplet growth ratios added to and subtracted from the droplet growth curve from the results of *Tang and Munkelwitz* [1994]. The calculation of the percent agreement between observed and theoretical droplet growth is described below. All subsequent droplet growth figures use the same line style format.

Results in Figure 7.8 for NaCl show excellent agreement with the results of *Tang and Munkelwitz* [1994] and with theory. An uncertainty of ±5% was observed by *Rader and McMurry* [1986] in their growth ratio measurements on NaCl particles using the HTDMA technique. *Berg et al.* [1998] report a ±3% error in HTDMA derived growth factors, atributable to counting statistics and RH fluctuations inside the DMAs. Recall that the calculations with the reference Köhler model use Pitzer's full model for Φ in the Raoult term, and the partial molar volume of water and solute-corrected droplet surface tension in the Kelvin term. The results identified as Tang's in this and subsequent figures use the Kelvin term from the reference Köhler model, except water activities are calculated from polynomial regressions that depend upon the mass fraction of solute in solution, as given in *Tang and Munkelwitz* [1994]. The the percent error was calculated between droplet growth factors observed in this work and those observed by *Tang and Munkelwitz* [1994]. HTDMA experiments using NaCl particles were conducted on three separate days. A total of 40 HTDMA scans on NaCl particles were completed. In order to calculate the total percent error in the droplet growth factor, the percent errors in RH and D_{drop} had to be determined. First, the theoretical value of RH corresponding to the observed value of D_{drop} was calculated using the results from *Tang and Munkelwitz* [1994]. The percent error in RH was then calculated for each observed droplet size by taking the ratio of the difference between the observed RH and the theoretical RH and the theoretical RH. In order to calculate the percent error in D_{drop}, an iterative scheme was required to determine the theoretical value of D_{drop} corresponding to the observed RH. For a given value of observed RH, a value of D_{drop} was found by iteration that solved Tang's

polynomial as a function of solute mass fraction so that the value of RH from Tang's results equaled the observed value of RH. For HTDMA studies on particles composed of NaCl, the average percent agreement between observed and theoretical growth factors is 0.6% (1σ=1%, n=40). The average percent agreement between observed and theoretical RH and D_{drop} values are -1.2% (1σ=1.4%, n=40) and 0.5% (1σ=1.8%, n=40), respectively. The percent agreement between theoretical and observed droplet growth factors listed above is better than previously reported uncertainties in droplet growth factors.

Results in Figure 7.9 for $(NH_4)_2SO_4$ also show very good agreement with theory, however, there is a slight trend to underestimate growth (-3%) at RH's above 88%. A total of 63 HTDMA scans were conducted on four separate days on particles composed of $(NH_4)_2SO_4$. The average percent agreement between theoretical and observed droplet growth factor values is -0.3% (1σ=1.1%, n=63) for HTDMA studies on $(NH_4)_2SO_4$ particles. The average percent agreement between observed and theoretical RH and D_{drop} values are 0.2% (1σ=1.6%, n=63) and -0.8% (1σ=1.8%, n=63). Again, the agreement between theory and experiment reported here is better than found in previous similar studies.

Explanations for the lower observed growth of $(NH_4)_2SO_4$ particles at higher RH's include the possibility of contamination in the $(NH_4)_2SO_4$ used to mix the salt solutions, poorer RH control in DMA2, and the smaller relative DMA1 dry size selected during some of the $(NH_4)_2SO_4$ runs compared to other studies. A broader range of sizes was selected by DMA1 during $(NH_4)_2SO_4$ studies, 25 to 60 nm, compared to 40 to 50 nm for NaCl. Approximately one-half of the points in Figure 7.9 that lie near or below the lower dashed curve were determined when a DMA1 diameter between 24 and 30 nm was selected. When particles smaller than 40 nm are selected by the DMA, Brownian diffusion of the particles results in increased particle losses and an increase in the concentration of particles smaller than the midpoint mobility diameter exiting

the monodisperse sampling slits. The increased penetration of relatively smaller dry particles in DMA1 may have contributed to the underestimated growth for some of the high RH $(NH_4)_2SO_4$ studies. This explanation is supported to some extent by the better agreement between theory and experiment at elevated RH's for studies where 58 nm $(NH_4)_2SO_4$ particles were selected by DMA1, and by the better agreement observed during studies on externally mixed particles when a 40 nm dry size was selected. The possibility of poorer RH control during studies on $(NH_4)_2SO_4$ particles was investigated. It was found that the control was as good as during studies on NaCl particles, therefore this could not explain the lower observed growth at higher RH's. The likelihood that contamination may have contributed to the observed lower growth cannot be discounted. However, the same source of $(NH_4)_2SO_4$ was used to mix the atomizer solutions for HTDMA studies on $(NH_4)_2SO_4$ particles alone and for the externally mixed $(NH_4)_2SO_4$-NaCl studies. The results from all HTDMA studies presented in Appendix D.

In summary, the agreement between droplet growth factors for NaCl and $(NH_4)_2SO_4$ particles observed here and growth factors calculated from the results of *Tang and Munkelwitz* [1994] is estimated to be 0.6% and -0.3%, respectively. The standard deviations in observed agreement between theory and experiment were less than 2%. The good agreement between droplet growth factors observed in this study and those from *Tang and Munkelwitz* [1994] serves to validate the capability of the HTDMA system to accurately measure particle hygroscopic growth for RH's between 79% and 92%.

7.5 *Comparison of Measured, HTDMA Derived, and Theoretical Values of S_{crit} for Particles Composed of Single Solutes*

Having validated the HTDMA growth measurement technique and the use of the TGDCC to determine the experimental values of S_{crit}, we now test our method for deriving S_{crit} from HTDMA growth results using measured hygroscopic growth values in the fit routine. We then compare derived values of S_{crit} to theoretical values and to values determined from the CCN counter measurements. Theoretical values of S_{crit} may be determined for all particle types examined except for ambient particles where the chemical composition was unknown.

7.5.1 Sodium Chloride

Hygroscopic growth results for NaCl are shown in Figure 7.8. Several combinations of (RH, D_{drop}) pairs were chosen from those shown in the figure and input to the fit routine to derive S_{crit}. The different combinations of input data were chosen to examine the effect of the RH values and ranges of RH values chosen on the derived values of S_{crit}. The fit routine was also run on all available data pairs, with and without applied random uncertainties. The values of S_{crit} derived from the fit routine using all available HTDMA results with and without applied uncertainties are used as the predicted values of S_{crit} to be compared with experimental and theoretical S_{crit} values. The results from the fit routine from NaCl HTDMA studies are shown in Table 7.3. In Table 7.3, the data pair numbers indicate the first and last data pair used in the fit routine to derive S_{crit}. For example, for the first case with data pairs 0 to 19, 20 total pairs of data were selected, or all of the available data for this case. For each data pair selection there are two rows of results. Results in the first row correspond to the case where no random error was applied to the input data. Results in the second row for the same data pair are averages of the results from 20

runs where different random errors were applied to the input dry particle size, RH, and D_{drop} data simultaneously in each of the 20 runs. The values of input data for the fit routine will only be known to within the experimental uncertainties of the measureand. The 20 cases where random error was added to the input experimental data provide insight into the effect uncertainties have on the derived values of S_{crit}. For all cases where S_{crit} was derived from HTDMA results with applied error, the ratio of the standard deviation in the predicted value of S_{crit} to the predicted average value of S_{crit} was less than 0.15. The magnitude of the applied errors varied between -2% and 2% for droplet and dry particle sizes, and -1% and 1% RH for RH values. Also shown in Table 7.3, and in subsequent similar tables, are the values of derived fit parameters (Y_{fit} and $\beta_{0,f}$), the derived values of S_{crit} and D_{crit}, the percent error between derived and theoretical values of S_{crit} and D_{crit}, and the χ^2 convergence value of the fit. The value of χ^2 was calculated as the sum of the squares of the differences between fit-routine predicted values of RH and input values of RH.

In order to determine the confidence interval in predicted values of S_{crit} from the fit routine and HTDMA study results, four different sets of NaCl growth study results, each spanning the 78% to 92% RH range, were used as input to the fit routine and values of S_{crit} determined. Only results from DOY 164 were used in the calculation of the confidence interval since insufficient results from DOY 163 were available to form different RH-range sets and the data from DOY 146 were deemed less reliable than those from DOY 164. We note that the disagreement between predicted and theoretical values of S_{crit} in Table 7.3 is generally larger for the study on DOY 146. The HTDMA study on DOY 146 was one of the earliest studies, and the control of the sheath air flow RH was not as good as during later studies. It is possible that the relatively larger standard deviations in the sheath flow RH's during the study on DOY 146 resulted in worse agreement between experimentally derived and theoretical values of S_{crit} for this day. Similar sets of input data were assembled

using the results from HTDMA studies on particles composed of $(NH_4)_2SO_4$ (eight sets) and NH_4HSO_4 (five sets). The standard deviation in the predicted values of S_{crit} from the different sets of input data for each composition were calculated. The three standard deviations in predicted values of S_{crit} for the three different compounds were pooled and a confidence interval calculated at the 95% confidence level using the same relations outlined above. The calculated pooled standard deviation was 0.05% (RH units). For a degree of freedom of 14, the *'t'* value is 2.14 [*Skoog et al.*, 1992]. The calculated confidence interval for one set of HTDMA-derived values of S_{crit} (N=1) was ±0.1% (RH units). The calculated confidence interval represents a coefficient variation between ±16% (NH_4HSO_4) and ±28% ($(NH_4)_2SO_4$) in HTDMA-derived values of S_{crit}. The ±16%-to-±28% confidence interval range is a conservative estimate, since in practice two-to-three (RH, D_{drop}) data pairs are used at the same nominal RH in the fit routine to derive S_{crit}. For comparison, the confidence interval calculated for CCN-derived values of S_{crit} was ±0.092% (RH units; coefficient of variation of ±21%).

In Table 7.3, relatively larger errors in predicted values of S_{crit} are associated with cases where fewer than six data pairs were used as input to the fit routine. In some cases, larger errors in predicted values of S_{crit} correspond to larger values of the χ^2 parameter. Larger values of χ^2 correspond to cases where the simplified Köhler model did not fit the experimental data as well as in other cases. For example, on DOY 146, the largest error in a predicted value of S_{crit} corresponds to the largest value of χ^2, whereas on DOY's 163 and 164 this is not the case. The largest errors on DOY's 163 and 164 were associated with data pairs 28-33 and 22-27. On DOY 164, data pair 28-33 represented a very small range of RH: the values were between 79.5% and 81.9%. In contrast, data pair 33-39 on DOY 164 represented a range of RH values between 81.9% and 89.3%, and the errors in predicted S_{crit} are lower. The 2.4% RH range represented by data pair 28-33 is too small for the fit routine to

accurately predict S_{crit} because the curvature of the Köhler curve is not adequately represented by such a small RH range. The relatively smaller values of χ^2 for this data pair are most likely due to the very small RH range. On DOY 163, data pair 20-25 gave S_{crit} errors one-half those from data pair 22-27. Correspondingly, data pair 20-25 represented the RH range 81% to 90% with three of the six pairs between 81% and 83% RH, and the remaining pairs between 89% and 90% RH. In contrast, data pair 22-27 consisted of five data pairs between 81% and 83% RH, and only one pair at 90% RH. The larger predicted error in S_{crit} from the fit routine using data pair 22-27 is the result of the unequal spacing in the RH values over the RH range.

It is of interest to compare the derived values of Y_{fit} and $\beta_{0,f}$ with the theoretically perfect values listed in Table 5.2. The 'perfect' values of Y_{fit} and $\beta_{0,f}$ for NaCl are 74.1 and 0.11, respectively. The average values of Y_{fit} and $\beta_{0,f}$ determined from the fit routine using all HTDMA results from DOY's 163 and 164 are 61.6 (1σ=16, n=20) and 0.047 (1σ=0.049, n=20) respectively. The values in parentheses represent one standard deviation. Results from numerical studies in chapter 5 indicated that the sensitivity of the fit routine results to the value of $\beta_{0,f}$ was less than to the value of Y_{fit}. The numerical studies also demonstrated large standard deviations in predicted values of $\beta_{0,f}$ when data with assumed, random errors were input to the fit routine. The derived value of Y_{fit} is only 17% lower than the theoretically perfect value, suggesting that useful information concerning the chemical composition of the sampled particles may be derived from the fit routine parameters.

The results from all CCN studies on NaCl particles are listed in Table 7.2. Results from the CCN study on DOY 164 on NaCl particles are shown in Figure 7.10. Experimental results are shown as asterisks and the solid line represents the best-fit line to experimental data. The experimentally determined value of S_{crit} corresponds to the point on the solid line where the ratio of N_{CCN} to N_{UCPC} is equal to 0.5, and is represented in Figure 7.10 by where the dotted line intersects the x-axis. The large

triangles in the figure represent the average value of S_{crit} derived from HTDMA growth results with applied uncertainties and the fit routine $\pm 1\sigma$. The plus and square symbols represent the values of S_{crit} derived from the fit routine with and without errors applied to the input data, respectively. All subsequent CCN study figures use the same line and symbol notation. The theoretical value of S_{crit} for a 46 nm NaCl particle is 0.38%, and is designated in Figure 7.10 by the solid dot. The agreement between theory and experiment is very good, within 7%. The range of S_{crit} values predicted by the fit routine encompasses the theoretical value but tends to be too low. This can be explained using the results of numerical studies on 40 nm diameter NaCl particles shown in Table 5.3. For perfect input data, the simplified Köhler model tends to underpredict values of S_{crit}. Therefore, there is a built in propensity for the fit routine to produce lower than average S_{crit} values for NaCl.

7.5.2 Ammonium Sulfate

Hygroscopic growth results for $(NH_4)_2SO_4$ particles are shown in Figure 7.9. The RH, D_{drop} pairs were used in the fit routine to derive S_{crit} as described above for NaCl particles. Results for $(NH_4)_2SO_4$ particles are listed in Table 7.4 in the same format used for NaCl runs in Table 7.3. The fit routine was not run with data pairs 0 through 19 (DOY's 161 and 162) because the DMA1 diameter was varied during these studies, making it difficult to process the results using the fit routine. For the results shown in Table 7.4, the average agreement between values of S_{crit} predicted from the fit routine using all data pairs as input and theoretical values of S_{crit} is -16% with a standard deviation of 16% (n=20). For study results from DOY's 169 and 176, the agreement between HTDMA derived and theoretical S_{crit} values (-16%) is similar to the standard deviation in the average error in values of S_{crit} derived from CCN studies listed in Table 7.2 for $(NH_4)_2SO_4$ (-3%, 1σ=12%, n=9).

As found in the results for NaCl in Table 7.3, poorer agreement is found in

Table 7.4 between values of S_{crit} obtained using data pairs that either represent a relatively small range of RH values, or that are not equally spaced over the RH range of the data pairs. For example, poorer agreement is found for data pairs 35-45 and 30-40. These data pairs represent RH's between 85% and 90% (35-45), and between 80% and 85%, with one RH of 87% (30-40). The 5% RH range is too small for the Köhler model to predict accurate values of S_{crit}. In contrast, better agreement between predicted and theoretical values of S_{crit} is found for data pairs 20-30 and 30-50. These data represent RH ranges of 80% to 92% and 80% to 90%, respectively, and the RH values are more equally spaced across the RH ranges than for data pair 30-40. These results indicate that in order for the fit routine to return accurate values of S_{crit}, it is important that several HTDMA studies are conducted over a RH range spanning at least 10% to 15% RH. The χ^2 values in Table 7.4 tend to be larger for the aforementioned data pairs that produce better values of S_{crit} than for data pairs that result in less accurate values of S_{crit}. The χ^2 value depends on the total number of data pairs used, the relative uncertainties in the various data pairs, the specific data pairs used as input to the fit routine, and limitations in the Köhler model that do not allow it to capture the hygroscopic behavior of the sampled particles. Therefore, it is plausible that larger χ^2 values could be associated with more accurate predicted values of S_{crit}.

The 'perfect' values of Y_{fit} and $\beta_{0,f}$ for $(NH_4)_2SO_4$ are 40.2 and 0.048, respectively (Table 5.2). The average values of Y_{fit} and $\beta_{0,f}$ determined from the fit routine using HTDMA results from DOY's 169 and 176 are 34.2 (1σ=11, n= 20) and 0.001 (1σ=0.001, n=20) respectively. The derived value of Y_{fit} is 15% lower than the theoretically perfect value. To understand why values of S_{crit} from the fit routine are consistently lower than the theoretical values, one must recall the results from numerical sensitivity studies in chapter 5 on $(NH_4)_2SO_4$ particles. These results indicated that for 'perfect' input data pairs, the simplified Köhler model underpredicted

S_{crit} by 8% while underpredicting Y_{fit} (Y_f in Table 5.3) by 29%. Values of Y_{fit} were underpredicted, on average, by the fit routine with actual HTDMA results by only 15%. As the value of Y_{fit} is increased, the value of S_{crit} predicted by the fit routine decreases since the larger value of Y_{fit} effectively increases the vapor pressure lowering effect by the Raoult term. Therefore, the relatively larger values of Y_{fit} in Table 7.4 for the cases when all data pairs were input to the fit routine result in smaller predicted values of S_{crit}.

Results from the CCN study on DOY 176 on 57.2 nm $(NH_4)_2SO_4$ particles are shown in Figure 7.11. For the study on DOY 176, the experimental value of S_{crit} was 0.49%. The theoretical value of S_{crit} for a 57.2 nm $(NH_4)_2SO_4$ particle is 0.41%, designated in Figure 7.11 by the solid dot. The agreement between theory and experiment is 20%. The $\pm 1\sigma$ range of S_{crit} values derived from HTDMA results, shown as the large triangles in Figure 7.11, exhibits better agreement with the theoretical value of S_{crit} than the value derived from CCN measurements. The value of S_{crit} derived from CCN measurements lies outside of the range of S_{crit} values predicted by the fit routine.

7.5.3 Ammonium Bisulfate

Hygroscopic growth results for NH_4HSO_4 particles are shown in Figure 7.12. The format of Fig. 7.12 is slightly different than that of other similar figures. Tang's results for three different compounds: $(NH_4)_3H(SO_4)_2$ (letovicite, dotted with pluses), NH_4HSO_4 (dashed), and $(NH_4)_2SO_4$ (dashed with three dots), are shown in the figure. The reason for showing the droplet growth factors for these three compounds is that during HTDMA studies on NH_4HSO_4 on DOY's 172 and 178, a subset of particles did not grow at RH's between 68% and 72%. Furthermore, no controls were used to minimize the ammonia gas concentration in the particle production, dilution, or HTDMA system air flows. According to *Tang and Munkelwitz* [1994],

letovicite exhibits a deliquescence RH near 69%, while initially dry NH_4HSO_4 particles will deliquesce at 40% RH. The DMA1 RH during studies on NH_4HSO_4 was less than 2% on DOY 172 and less than 10% on DOY 178. According to *Tang and Munkelwitz* [1994], the crystallization RH for NH_4HSO_4 is near to, or less than, 2%. Therefore, the particles may not have been completely dry. The crystallization RH for $(NH_4)_3H(SO_4)_2$ is between 35% and 44% RH (Table 4.1). Therefore, particles composed of $(NH_4)_3H(SO_4)_2$ would initially have been completely dry in both HTDMA studies. Any particles composed of NH_4HSO_4 will grow at RH's between 40% and 69%, whereas initially dry particles composed of letovicite will not grow at these humidities. The solid line in Fig. 7.12 represents a best estimate of the droplet growth factor predicted using Pitzer's model of Φ for $(NH_4)_3H(SO_4)_2$. No parameters for $(NH_4)_3H(SO_4)_2$ were available for use in Pitzer's model, therefore values of β_0, β_1, and $C_{mx,\phi}$ were estimated following the work of *Kim et al.* [1993] by taking the square root of the products of the parameter values for $(NH_4)_2SO_4$ and NH_4HSO_4. As mentioned previously, the Pitzer model used here is less accurate for NH_4HSO_4. Therefore, experimental results in Fig. 7.12 should be compared with the curves generated from Tang's results.

As mentioned above, during HTDMA studies on NH_4HSO_4 a subset of particles did not grow at RH's between 68% and 72%, suggesting that initially dry particles composed of letovicite may have been present in the sample. Three HTDMA scans (not shown in Fig. 7.12) exhibited this behavior. There were too few data pairs and too small a range of RH's to attempt to use the fit routine on the results from these three HTDMA scans. At humidities above 72% all particles grew in a single mode. This is consistent with the similar droplet growth factors for NH_4HSO_4 and $(NH_4)_3H(SO_4)_2$ (Fig. 7.12) or with the ammoniation of the particles/droplets resulting in a growth more like $(NH_4)_2SO_4$. From the HTDMA results, it appears that the particles exhibited varying degrees of ammoniation between NH_4HSO_4 and

$(NH_4)_2SO_4$. It is also possible that the particles were internal mixtures of these compounds. The gas-phase partial pressure of ammonia will influence the composition of particles generated from an NH_4HSO_4 solution. Calculations show [*P. Demott, personal communication*] that, for reasonable estimates of levels of ammonia gas (1 to 3 ppbv) and temperatures experienced during HTDMA studies, solution droplets could become supersaturated with respect to letovicite and precipitate the crystal in solution. If contaminant particles from the Nanopure water were available to act as centers for heterogeneous nucleation of letovicite crystals, the formation of letovicite could also be favored. The process is highly temperature sensitive, and could be very sensitive to the availability of an impurity inclusion. This might explain why some of the particles behaved like NH_4HSO_4 while others appeared to be letovicite. Given the uncertainty in the particle chemical composition, the level of agreement between observed droplet growth and growth calculated from Tang's results is still very good: the average percent difference between theoretical and experimental data is 0.2% (1σ=1.1, n=30)% for an assumed $(NH_4)_2SO_4$ composition. The average percent error is ten times larger if an NH_4HSO_4 composition is assumed. The ammonium-to-sulfate ion ratio of the NH_4HSO_4 atomizer salt solution was analyzed by ion chromatography. Results indicated that a ratio of 1.0 was present, consistent with an NH_4HSO_4 composition [*Katherine Moore, personal communication*]. As found for $(NH_4)_2SO_4$, there is a trend for underprediction of droplet growth at RH's above about 86%.

RH, D_{drop} pairs were used in the fit routine to derive S_{crit} as described above for NaCl and $(NH_4)_2SO_4$ particles. Results for NH_4HSO_4 particles are listed in Table 7.5. For the results shown in Table 7.5, the average agreement for the two NH_4HSO_4 studies between experimentally derived and theoretical values of S_{crit} is -18% with a standard deviation of 3% (n=20). The -18% difference is close to the agreement observed between theoretical values of S_{crit} and values predicted in numerical studies conducted in chapter 5 (Table 5.3). The similarity between predicted

S_{crit} values in Table 7.5 and numerical study results in Table 5.3 indicates that limitations in the model are producing the larger disagreement between predicted and theoretical values of S_{crit}. This is supported by the larger values of χ^2 in Table 7.5 compared to values from studies on NaCl and $(NH_4)_2SO_4$.

The 'perfect' values of Y_{fit} and $\beta_{0,f}$ for NH_4HSO_4 listed in Table 5.2 are 30.9 and 0.045, respectively. The average values of Y_{fit} and $\beta_{0,f}$ determined from the fit routine using HTDMA results are 33.1 (1σ=2.3, n=20) and 0.004 (1σ=0.0004, n=20) respectively. The derived value of Y_{fit} is 7% higher than the theoretically perfect value, helping to explain why the average value of S_{crit} predicted by the fit routine is lower than the theoretical value for 40 nm NH_4HSO_4 particles. Theoretical values of S_{crit} calculated for NH_4HSO_4 using the reference Köhler model are not affected by the inaccuracy of Pitzer's model for Φ since the model accurately reproduces the behavior of Φ for the relatively dilute droplet solutions encountered at S_{crit}. The values of S_{crit} from the fit routine are consistently lower than the theoretical values partly because there is a bias in the simplified Köhler model to produce lower values for NH_4HSO_4 (Table 5.3). NH_4HSO_4 particles represent a more stringent test of the proposed method for deriving S_{crit} from HTDMA results as this compound dissociates into three ions, whereas the model is explicitly written only for solutes that dissociate into two ions. Furthermore, for conditions encountered during HTDMA studies, Pitzer's model of the osmotic coefficient is not as accurate for NH_4HSO_4 as for NaCl and $(NH_4)_2SO_4$ [*Kim et al.*, 1993].

Results from the CCN study on DOY 178 on 40 nm NH_4HSO_4 particles are shown in Figure 7.13. Results for DOY 176 were similar. For the study on DOY 178, the experimental value of S_{crit} was 0.735%. The theoretical value of S_{crit} for a 40 nm NH_4HSO_4 particle calculated using the reference Köhler model is 0.745%, designated in Figure 7.13 by the solid dot. The agreement between theory and CCN-derived values of S_{crit} is -1%. The range of S_{crit} values derived from HTDMA results

was very small for NH_4HSO_4, shown as the large triangles in Figure 7.13. As described above, values of S_{crit} derived from HTDMA results agre with the theoretical value of S_{crit} and with the value derived from CCN measurements within -20%.

7.6 *Comparison of Measured, HTDMA Derived, and Theoretical Values of S_{crit} for Particles Composed of Internally and Externally Mixed Solutes*

Results from three studies on mixed particles, conducted on DOY's 173, 177, and 181, are presented in this section. For the purposes of this study, an internally mixed solute is one where two salts with different chemical compositions are present within a single dry particle. An external mixture occurs when individual particles are composed of single solutes but different particles have different solute compositions in the same air sample. One purpose in applying the method for deriving S_{crit} from HTDMA data to mixed particles was to examine the ability of the method to predict S_{crit} for particles having a more complex chemical composition (internal mixture). A second goal of these measurements was to demonstrate that the HTDMA could distinguish between particles having different chemical compositions sampled simultaneously (external mixture).

7.6.1 Internally Mixed Ammonium Sulfate-Sodium Chloride

Hygroscopic growth results for internally mixed $(NH_4)_2SO_4$-NaCl particles are shown in Figure 7.14. The particles were atomized from an equimolar solution of $(NH_4)_2SO_4$ and NaCl. Only one study (on DOY 173) of internally mixed particles was conducted, therefore there are fewer experimental data points than for other studies. A shape factor of 1.25 was applied to the dry particle size selected by DMA1 so that experimental growth would match the theoretically predicted growth. This value is consistent with shape factor values reported by *Hinds* [1982]. Good agree-

ment between RH values predicted by the reference Köhler model and the ZSR relation [*Zdanovskii,* 1936; *Stokes and Robinson,* 1966] for internally mixed $(NH_4)_2SO_4$-NaCl was shown in chapter 5. Direct comparison with growth results from *Tang* [1997] is not possible since this mixture was not tested. The use of a shape factor is supported by transmission electron micrographs of deposited particles showing that they were of irregular shape with protrusions. The micrographs did not allow a quantitative assesment of the shape factor to be made, but qualitatively supported the need for a shape factor. The agreement between experimental and theoretical growth is very good: the average percent difference between theoretical and experimental data is -0.7%±1.2%, n=17. Values of RH calculated using the reference Köhler model agree within 4% of those determined using the ZSR relation with Tang's results for solution densities and water activities of binary solutions. The lower predicted growth from Tang's results is most likely due to the simplified ZSR relation used to calculate the equilibrium water activity. As pointed out by *Tang and Munkelwitz* [1994], interactions between the different solute ions in solution are neglected in the form of the ZSR relation used in this work.

RH, D_{drop} pairs were used in the fit routine to derive S_{crit} for internally mixed particles, and results are listed in Table 7.6. The fit routine was run using all 17 data pairs as input and the predicted values of S_{crit} from 20 cases of applied random error were averaged. The average agreement between experimentally derived and theoretical values of S_{crit} is -8% with a standard deviation of 10%. The fit routine returned a value of S_{crit} 10% larger than the theoretical value for the case where no error was applied to the input data and all data were used as input. The percent difference between HTDMA derived and theoretical S_{crit} values is the same as the percent difference listed in Table 7.2 for CCN studies on internally mixed particles (-8%).

The 'perfect' value of Y_{fit} for the internally mixed, equimolar composition is 49.2.

The average value of Y_{fit} determined from the fit routine using HTDMA results was 53.0 (1σ=11). The derived value of Y_{fit} is 8% higher than the theoretically perfect value. The relatively good agreement between theoretical and fit routine derived Y_{fit} values for internally mixed particles suggests that the simplified Köhler model is capable at predicting Y_{fit} values for the more complex chemical composition. The predicted value of $\beta_{0,f}$ in Table 7.6 is 67% smaller than the 'perfect' value listed in Table 5.2. We note that only one study on internally mixed particles was conducted for this work. Internally mixed particles represent a more stringent test of the proposed method for deriving S_{crit} from HTDMA results compared to runs with single solutes, as internally mixed particles dissociate into three or more ions, whereas the model is explicitly written only for solutes that dissociate into two ions.

Results from the CCN study on DOY 173 on 32 nm particles are shown in Figure 7.15. The experimental value of S_{crit} was 0.65%. The theoretical value of S_{crit} for a 32 nm equimolar, internally mixed NaCl-$(NH_4)_2SO_4$ particle is 0.709%, designated in Figure 7.15 by the solid dot. The agreement between theory and experiment is -8%. The range of S_{crit} values derived from HTDMA results, shown as the large triangles in Figure 7.15, exhibit reasonable agreement with the theoretical value of S_{crit} and with the value derived from CCN measurements. We note that the theoretical critical supersaturation of an internally mixed $(NH_4)_2SO_4$-NaCl particle without the applied shape factor (i.e., 40 nm diameter) is 0.51%, 40% lower than the value of S_{crit} determined from the CCN study on internally mixed particles and the value predicted by the fit routine.

7.6.2 Externally Mixed Ammonium Sulfate-Sodium Chloride

Hygroscopic growth results for externally mixed $(NH_4)_2SO_4$-NaCl particles are shown in Figure 7.16. The externally mixed particles were created by operating two atomizers in parallel and combining their output flows in the dilution and drying chamber

so that approximately equal number concentrations of each composition was present. One atomizer was operated with a $(NH_4)_2SO_4$ solution and the second atomizer with a NaCl solution. The first study of externally mixed particles was conducted on DOY 177, and the second on DOY 181. A shape factor of 1.08 was applied to the NaCl dry particle size selected by DMA1 as described previously. The HTDMA results clearly demonstrate that particles of different chemical composition sampled simultaneously can be distinguished based on differences in their hygroscopic growth. The agreement between experimental and theoretical growth is very good for both solutes. The average percent difference between theoretical and experimental data is 1.3%±0.7% (n=34) for NaCl, and 0.7%±1.4% (n=34) for $(NH_4)_2SO_4$.

RH, D_{drop} pairs were used in the fit routine to derive S_{crit} for externally mixed particles, and results are listed in Table 7.7 for $(NH_4)_2SO_4$ and NaCl. The average agreement between experimentally derived and theoretical values of S_{crit} is -23% (1σ=5%, n=34) for $(NH_4)_2SO_4$ and -25% (1σ=6%, n=34) for NaCl. The poorer average agreement is reflected in the larger average χ^2 values in Table 7.7 compared to previous studies on $(NH_4)_2SO_4$ and NaCl particles. The values of Y_{fit} in Table 7.7 derived from the fit routine for $(NH_4)_2SO_4$ and NaCl are clearly different. This demonstrates that the technique for deriving S_{crit} from HTDMA results can differentiate between particles of different chemical composition sampled at the same time. The percent difference between HTDMA derived and theoretical S_{crit} values is larger than the percent uncertainty listed in Table 7.2 for CCN studies on NaCl and $(NH_4)_2SO_4$ particles, 4.2 and -2.7%, respectively.

The 'perfect' values of Y_{fit} for NaCl and $(NH_4)_2SO_4$ are 74.1 and 40.2, respectively. The average values of Y_{fit} determined from the fit routine using HTDMA results were 96.2 (1σ=12, n=20) and 41.8 (1σ=5, n=20), respectively. The poor agreement between values of $\beta_{0,f}$ predicted by the fit routine and values listed in Table 5.2 demonstrates the lack of sensitivity of the fit routine results to the predicted

value of $\beta_{0,f}$. The derived values of Y_{fit} are 30% higher and 4% higher than the theoretically perfect values, for NaCl and $(NH_4)_2SO_4$, respectively. For NaCl, the higher the predicted value of Y_{fit}, the larger the negative difference between theoretical and predicted values of S_{crit}. This trend is consistent with the physical argument that higher values of Y_{fit} correspond to higher values of solute mass per unit volume. Therefore, for the same particle size, the Raoult effect will be more effective and reduce the equilibrium water vapor pressure in equilibrium with a given size droplet, resulting in lower values of S_{crit}. This helps explain the -25% difference between the predicted and theoretical S_{crit} values for NaCl in Table 7.7. Also evident in Table 7.7 is that the choice of different data pairs influences the predicted value of Y_{fit} and the degree of underprediction of S_{crit}. For example, data pairs 17 through 33 and 15 through 25 produced the greatest underpredictions of S_{crit}. Data pairs 15 through 25 represented a very narrow total RH range of 5% (81 to 86% RH), while pairs 17 through 33 represented RH values between 81% and 90%. However, pairs 17 through 33 were represented by higher than average growth values, resulting in a poorer fit.

Results from the CCN study on DOY 177 on 40 nm $(NH_4)_2SO_4$ and 37 nm NaCl particles are shown in Figure 7.17. The CCN counter was not able to distinguish between the different S_{crit} values of the externally mixed particles, and the experimental values of S_{crit} listed in Table 7.2 represent average values for the sampled NaCl and $(NH_4)_2SO_4$ particles. Interestingly, the agreement between the experimentally determined value of S_{crit} and the average of the theoretical values of S_{crit} for 40 nm $(NH_4)_2SO_4$ and 37 nm NaCl particles is extremely good, within -7%. The experimental value of S_{crit} was 0.58% for the study on DOY 177. The average of the two theoretical values of S_{crit} for DOY 177 was 0.62%, and is designated in Figure 7.17 by the larger solid dot. The smaller solid dots in the figure represent the S_{crit}values for 40 nm $(NH_4)_2SO_4$ and 37 nm NaCl particles. The $\pm 1\sigma$ range of the average S_{crit} values for 40 nm $(NH_4)_2SO_4$ and 37 nm NaCl particles derived

from HTDMA results, shown as the large triangles in Figure 7.17, exhibit reasonable agreement with the theoretical values of S_{crit} and with the value derived from CCN measurements. As discussed above, the S_{crit} values derived from HTDMA results are lower than those from CCN measurements and theory.

7.6.3 Summary of Results from HTDMA and CCN Studies on Particles of Known Chemical Composition

The results of validation studies to determine the experimental uncertainty in values of S_{crit} derived from CCN studies indicate that the confidence interval expressed as a percent error in S_{crit} for a 95% confidence level is ±21%. The average agreement between CCN-study derived and theoretical values of S_{crit} for studies conducted on $(NH_4)_2SO_4$, NaCl, and NH_4HSO_4 particles was -0.6% (1σ=11%, n=16). The 1σ value was calculated from the percent differences between CCN-derived and theoretical values of S_{crit}. Confidence interval calculations were performed for the value of S_{crit} predicted by the fit routine for three replicate studies on NaCl, $(NH_4)_2SO_4$, and NH_4HSO_4 particles without applied error. The confidence interval as a percent error in S_{crit} derived from the fit routine was calculated to be between ±16% (NH_4HSO_4) and ±28% ($(NH_4)_2SO_4$), similar to the value determined for CCN-study derived values of S_{crit}. For particles composed of the single and internally mixed solutes examined here, the fit routine derived values of S_{crit} agreed with theoretical values to within between -6% and -18%. The agreement for externally mixed particles was -25%. These results indicate that values of S_{crit} can be successfully derived from HTDMA results for particles that completely dissociate in solution.

7.7 *Comparison of Measured, HTDMA Derived, and Theoretical Values of S_{crit} for Ambient Particles of Unknown Chemical Composition*

Ambient air samples were drawn from above the roof of the laboratory through a 1.2 cm inside diameter, electrically conductive, plastic sampling line 8 m long. The flow rate in the inlet tubing was 8 lpm. No dilution air was added to the ambient sample, as the ambient concentrations were already significantly lower than during laboratory studies of atomized salt particles. The particle sample was drawn into DMA1 through a diffusion dryer and the operation of other components of the HTDMA/CCN system was analogous to studies on atomized salt particles. The relative humidity of the DMA1 sample inlet flow was between 2% and 9% for all studies on ambient particles. Hygroscopic growth results for ambient particles are shown in Figure 7.18. Three studies of ambient particles were conducted on DOY's 174, 175, and 182 (the last study). The particle size selected by DMA1 was different for the three studies: 85 nm diameter particles were selected on DOY 174, 68.4 nm particles were examined on DOY 175, and 120 nm particles were selected on DOY 182. Local meteorological data have been plotted in Figures 7.19, 7.20, and 7.21 for DOY's 174, 175, and 182, respectively. The data were collected at the CSU Department of Atmospheric Science Christman Field meteorological data station, located approximately 100 m from the sample inlet used to draw the ambient sample into the laboratory. Timelines of concentrations of monodisperse particles observed by the UCPC have been plotted in Figure 7.22 to help interpret changes in the observed hygroscopic growth. The average concentrations on DOY's 174, 175, and 182 were 34.5, 22.1, and 48.1 cm^{-3}, respectively. However, concentrations reached 80 cm^{-3} on DOY 182, whereas maximum concentrations were only 60 cm^{-3} during the other two studies. Highest concentrations appear during periods where winds are easterly and light and when winds are from the south. Lowest concentrations were observed when winds were high

and from the west and northwest. The most obvious change in UCPC concentration occurred at DOY 175.57 (Fig. 7.22), about the same time as the wind direction shifted from easterly to southwesterly and wind speeds increased. The variability in UCPC concentration on DOY 182 was associated with fluctuating wind directions between DOY 182.6 and 182.78, and finally a shift in wind direction to northerly at DOY 182.8.

A shape factor is likely required for the sampled particles, however, we have no way of estimating an appropriate value. The ambient RH during the three ambient studies was between 8% and 60%. The particles were dried to RH's below 9% before entering DMA1. If the particles were still droplets at these low RH's then they would most likely be spherical and a shape factor not required. The hygroscopic growth results from the three different study days are shown as different symbols in Fig. 7.18. DOY 174 is shown as solid dots, DOY 175 is shown as asterisks, and DOY 182 is shown as squares. Data pairs have been numbered. A striking feature of the results from the ambient studies is the much lower observed growth. $(NH_4)_2SO_4$ and NaCl particles exhibit growth that is between 26% and 52% greater at 80% RH and between 21% and 72% greater at 90% RH than observed for ambient samples. Assuming that the particle chemical compositions were similar on the three days, the results also suggest that larger particles (120 nm, squares) are more hygroscopic than smaller particles (other symbols). On DOY 174 (solid dots), the observed growth is less than that on DOY 175 (asterisks) at RH's greater than around 88%. Of the 54 total HTDMA scans conducted, two distinct growth modes could only be discerned in eight. Of the eight observed cases, only one was observed at the highest study RH on DOY 174 (data pair 18, DOY 174.76), three were observed at the highest RH's examined on DOY 175 (data pairs 21, 22, and 24, DOY 175.57-175.61), and four were observed at RH's between 81% and 90% on DOY 182 (data pairs 33 through 36, DOY 182.49-182.54). On DOY 182, two distinct growth modes were observed in the first

four HTDMA scans at RH's between 82 and 90% (data pairs 33-36), but not during HTDMA scans at these same RH's later in the study (i.e., data pairs 40-53, DOY 182.6-182.85). Possible explanations for the observed change in hygroscopic behavior are discussed below.

A more hygroscopic mode appears in the data of DOY 175 around data pair 21 (DOY 175.57), corresponding to a sudden decrease in number concentration (Fig. 7.22), a shift in wind direction from easterly to southerly (Fig. 7.20), and an increase in wind speed from 2 to 6 m s^{-1}. On DOY 174, the local wind direction was more easterly, whereas on DOY 175 the wind direction was southerly and southwesterly. The one scan where a more hygroscopic mode was observed occured at DOY 174.76, and could be related to the changes in wind direction or the slight increasing trend in number concentration observed at this time. The highest observed growth factor was for the 120 nm particles sampled on DOY 182. Because of their relatively larger size, it is likely that these particles were aged particles from anthropogenic sources, and had had sufficient time for gas-to-particle conversion to modify, and possibly increase, their hygroscopicity. The more hygroscopic mode observed between DOY 182.49 and 182.54 occured during northeasterly flow and fairly stable number concentrations. At the same RH's later in the study on DOY 182, a more hygroscopic mode was not observed and winds were more northwesterly, and number concentrations were relatively higher and more variable.

Although the chemical composition of the ambient particles was unknown, possible compositions were examined by assuming the sampled particles consisted of internal mixtures of $(NH_4)_2SO_4$, NH_4NO_3, and an insoluble compound. The insoluble compound was assumed to have a dry density of 1000 kg m^{-3} and a molecular weight of 40 g $mole^{-1}$. The choice of soluble compounds is supported by filter and impactor sampling results of ambient particles outside the laboratory that showed $(NH_4)_2SO_4$ and NH_4NO_3 were present. Recent measurements of the chemical com-

position of ambient particles along the Front Range of Colorado have shown that $(NH_4)_2SO_4$ and NH_4NO_3 constitute between 34% and 50% of the ambient sub-2.5 μm particulate mass, respectively [*NFRAQS Executive Summary,* 1998]. Carbonaceous particles were found to comprise between 33% and 48% of the ambient sub-2.5 μm mass. Equilibrium RH's were calculated as a function of droplet size for various mass fractions of the three constituents and the particle sizes selected during each of the three ambient studies. Curves of RH verses D_{drop} were compared to observed (RH, D_{drop}) data pairs for each ambient study. The mass fraction values were determined that provided the best fit to observed (RH, D_{drop}) data pairs. The fit was validated visually. Once the mass fractions were determined, hypothetical S_{crit} values could be calculated for each ambient study. The results of this calculation have been listed in Table 7.2. The observed droplet growth factors are compared with values calculated for different hypothetical compositions (solid line) in Figure 7.23. For the studies on DOY's 174 and 175, the same combination of the three compounds provided a reasonable fit to observed droplet growth factors. For these studies, the mass fractions of $(NH_4)_2SO_4$, NH_4NO_3, and insoluble material were 0.14, 0.09, and 0.77, respectively. Therefore, the volume fraction of soluble material in the sampled particles is estimated to be only 14%. For comparison, a 48% mass fraction of carbonaceous material (ρ_s=1000 kg m^{-3}) corresponds to a volume fraction of approximately 70%, for a mixture of $(NH_4)_2SO_4$, NH_4NO_3, and carbonaceous material consistent with results from the NFRAQS study. It should be noted that the NFRAQS study quantified the sub-2.5 μm mass, while monodisperse, 68 to 120 nm particles were sampled with the HTDMA. The calculated values of S_{crit} for the assumed chemical compositions on DOY's 174 and 175 differ from values derived from CCN studies by 10% and -23%, respectively. This level of agreement is similar to that found in other CCN studies. For the study on DOY 182, a different mixture of compounds best simulated the observed hygroscopic behavior. The mass fractions of $(NH_4)_2SO_4$, NH_4NO_3, and

insoluble material that give the solid line in Fig. 7.23(c) are 0.25, 0.15, and 0.6. The estimated volume fraction of soluble material in the 120 nm diameter particles is 27%. Correspondingly, the predicted value of S_{crit} for DOY 182 is 0.2%, much lower than the value of 0.53% derived from CCN studies. Interestingly, the hypothetical value of S_{crit} derived for the assumed chemical composition agrees very well with the value from the fit routine for this study (0.18%). It is possible that variability in the ambient particle characteristics, for example chemical composition and number concentration, on DOY 182 adversely affected the value of S_{crit} derived from CCN studies.

RH, D_{drop} pairs were used in the fit routine to derive S_{crit} for ambient particles, and results are listed in Table 7.8. For the eight cases where two hygroscopic modes were observed in a single scan, the more hygroscopic mode was chosen to be used in the fit routine. For cases where more and less hygroscopic modes were present, values of S_{crit} derived from the CCN counter studies are less reliable due to the inability to distinguish between droplets formed on the more and less hygroscopic particles. For the three studies, the average agreement between values of S_{crit} derived from CCN studies and values of S_{crit} derived from HTDMA results is -38% with a standard deviation of 5% (n=20). Furthermore, the χ^2 values of the fits listed in Table 7.8 are generally larger than those from studies on known salts, indicating that the simplified Köhler model does not simulate the growth of ambient particles as well as particles composed of the other compositions examined in this work. The largest error, -65%, was found for the study on DOY 182, and may be due to the variability in number concentration during the study. As mentioned above, the calculated value of S_{crit} for a hypothetical chemical composition that exhibits droplet growth similar to that observed on DOY 182 is closer to the value predicted from the fit routine than to the value from CCN studies. The percent difference between HTDMA derived and CCN measurement derived S_{crit} values is larger than the -0.6% (1σ=11%, n=16)

uncertainty in S_{crit} values derived from CCN studies on known composition particles. For the study on DOY 175, the agreement between HTDMA derived (0.47%) and CCN derived (0.5%) values of S_{crit} is much better: -6(4)%, closer to the experimental uncertainty in the value of S_{crit}. For the study on DOY 175, the error in predicted values of S_{crit} is much larger for the case where data pairs 27 to 31 are used as input to the fit routine. These data represent RH's between 77 and 84%, a range too small to derive accurate values of S_{crit}. They demonstrate again the importance of the choice of RH values for determining S_{crit}. For comparison, data pairs 19 to 26 include only 8 data pairs, but the RH range spanned by these points is 80 to 90%.

The values of Y_{fit} derived for the ambient particle samples are shown in Table 7.8. It is of interest to note that most of the values are between one-half and one-tenth of those derived for the pure salts, consistent with the lower observed hygroscopic growth of the ambient particles compared to the salts. Using the results from data pairs 33 to 36 on DOY 182, an attempt was made to derive values of S_{crit} for each of the two observed growth modes. Data pair 35 was not used in the analysis of the less hygroscopic mode because the observed growth of the less hygroscopic mode was very different from data pairs 33, 34, and 35. The fit routine would not converge for the case where no error was applied to the more hygroscopic mode data, as shown in Table 7.8 by 'NA'. When error was applied, the fit routine converged and the derived value of S_{crit} was 0.21%. When the fit routine was run on the less hygroscopic mode results, the resulting value of S_{crit} was lower (0.1%), not higher, and the value for Y_{fit} was approximately five times that derived from the more hygroscopic mode data. This can be explained mainly by the sparsity of data points (3) that were available to run the fit routine. Another likely explanation for the poor performance of the model on the ambient data is that the particles were composed of internal mixtures of materials that did not fully dissociate in solution or somehow inhibited the condensation process (for example, coatings). The current version of the simplified Köhler model did not

capture the hygroscopic growth behavior of the ambient particles as well as for the pure salts studied here.

Results from the three CCN studies on ambient particles are shown in Figures 7.24, 7.25, and 7.26. Results for the study on DOY 174 on 85 nm ambient particles are shown in Figure 7.24. The experimental value of S_{crit} was 0.51%. The range of S_{crit} values derived from HTDMA results is shown as the large triangles in Figure 7.24. For this study, the HTDMA derived values of S_{crit} are 32% lower than the value of S_{crit} derived from CCN measurements. Results from the CCN study on DOY 175 on 68.4 nm ambient particles are shown in Figure 7.25. The experimental value of S_{crit} was 0.5%. The range of S_{crit} values derived from HTDMA results is shown as the large triangles in Figure 7.25. The HTDMA derived value of S_{crit} (0.47%) agrees very well with the value of S_{crit} derived from CCN measurements. Results from the CCN study on DOY 182 on 120 nm ambient particles are shown in Figure 7.26. The experimental value of S_{crit} was 0.53%. Number concentrations varied considerably during the CCN study. The range of S_{crit} values derived from HTDMA results is shown as the large triangles in Figure 7.26. The HTDMA derived values of S_{crit} are much smaller than the value of S_{crit} derived from CCN measurements and more consistent with the calculated value derived for the hypothetical chemical composition described above.

There are several possible explanations for the large differences between predicted and observed values of S_{crit} from the three ambient studies. The poorer agreement in the ambient studies on DOY's 174 and 182 may be due in part to the more erratic behavior in the number concentration and wind direction observed during these two studies compared to that on DOY 175. The fluctuating number concentrations and wind direction may indicate changes in air mass source region and particle chemical composition. The poorer agreement during ambient studies may also be due to the very long period of time required to complete the study, given that ambient conditions

likely changed during the study period. If the aerosol properties changed significantly over the twelve hour period required to perform each HTDMA/CCN study, then combining the results from the different supersaturations examined and different RH's in the HTDMA would be inappropriate. The relatively lower number of droplets that were counted due to the low number concentrations of particles exiting DMA1 brings into question the reliability of the CCN results. Number concentrations sampled by the CCN counter were between one and two orders of magnitude lower than during studies conducted on known composition particles. Only between ten and fifty drops were counted during the two hours required for a full cubic centimeter sample of air to be processed by the CCN counter during ambient studies. The corresponding Poisson counting errors are between 14% and 32%. Furthermore, the number concentration of ambient particles varied during all studies, but particularly during the study on DOY 182. Limitations in the current, simplified Köhler model may preclude the prediction of accurate values of S_{crit} from HTDMA results for ambient particles of unknown composition. For example, as pointed out by *Schulmann et al.* [1996], certain surface-active organic compounds can influence the critical supersaturation of a particle by inhibiting the uptake of water. This effect is not accounted for in our model.

7.8 *Effect of Multiply Charged Particles on Hygroscopic Growth Measurements With the HTDMA*

There is an interesting aspect to measuring the hygroscopic growth of particles of known and unknown chemical composition that has not previously been discussed. When particles are selected with DMA1 in the HTDMA, it is unavoidable that larger diameter, multiply charged particles will also be present in the monodisperse particle sample exiting the DMA. For the purposes of this discussion, only doubly, and not higher, charged particles are assumed to be present at a high enough number

concentration to be considered. The doubly charged particles are physically larger than the singly charge particles and carry two charges per particle. The reason that higher charged, larger diameter particles could influence the observed singly charged droplet mode size is that the variation of particle size with electrical mobility is not the same as the variation of particle size with relative humidity. During studies on known salt particles, the number concentration of doubly charged particles could be kept below 5% of the number concentration of singly charged particles by controlling the number size distribution of the polydisperse particle distribution from the atomizer and the dry size selected by DMA1. However, during ambient studies, there was no control over the number concentration of doubly charged particles and the ratio of the number concentration of doubly charged to singly charged particles was as high as 0.2. The ratio was determined by examining the polydisperse ambient size distribution measured before and after the HTDMA/CCN study and calculating the number concentrations of singly and doubly charged particles using the results of *Wiedensohler* [1988]. Therefore, the influence of the higher number fraction of doubly charged particles on the observed droplet mode size was investigated. The investigation was also motivated by the desire to determine if an increased doubly charged fraction could be responsible for some of the trend observed in the growth data for $(NH_4)_2SO_4$ and NH_4HSO_4, where a tendency for growth to be lower than theoretical estimates at higher RH's was observed.

Numerical studies of this effect demonstrated that when the singly and doubly charged particles have the same composition and growth ratios, the influence on the fitted mode size is quite small, only between -0.1% and -0.4% for 40 nm dry particles, with doubly charged number fractions between 10% and 20%, and growth ratios between 1.3 and 2.25. However, the effect can be more important for larger particle sizes where the relative fraction of doubly charged particles can be larger. During the studies of the influence of doubly charged particles on observed growth

modes for particles of known composition, it became clear that if the growth factors of the doubly charged and singly particles with increasing RH were different, then a significant change in the results of the analysis would be observed. An example is illustrated in Figure 7.27. A singly charged 40 nm particle will have the same electrical mobility as a doubly charged 58.1 nm particle. A ratio of doubly-to-singly charged particles of 0.2 was assumed in the example calculation, the singly charged particle number concentration was set to 1000 cm^{-3}, and a standard deviation of 1.08 was assumed for both singly and doubly charged particles. If both particles are exposed to a relative humidity of 85%, and the 40 nm particle is composed of NaCl while the larger particle consists of $(NH_4)_2SO_4$, then the 40 nm particle will grow to 84 nm while the 58.1 nm particle will grow to 88.6 nm. The growth process is depicted in Figure 7.27(b), where the actual droplet sizes (not mobility diameters) of the grown singly and doubly charged droplets are shown. The electrical mobility of a doubly charged 88.6 nm droplet is equivalent to a singly charged droplet size of 60.7 nm, significantly smaller than the 84 nm singly charged droplet size. The distribution observed will appear bimodal, with one mode size identified as 60.7 nm under the assumption that they are singly charged droplets, and a second mode size equal to 84 nm. The mobility diameters of the two modes, as observed by the HTDMA, is depicted in Fig. 7.27(c), where the bimodality resulting from the chemical composition and hygroscopic growth factor differences between the singly and doubly charged particles is clearly evident. It is worth pointing out that the magnitude of the effect of doubly charged particles on observed hygroscopic growth modes depends on differences in the hygroscopic growth of the singly and doubly charged particles and on the relative number concentration of doubly compared to singly charged particles. This effect was not observed during HTDMA studies on externally mixed $(NH_4)_2SO_4$ and NaCl particles because the concentrations of doubly charged particles were less than 5% of the singly charged particle number concentrations and the droplets formed on

doubly charged $(NH_4)_2SO_4$ and NaCl particles would exhibit electrical mobilities very similar to the singly charged droplets formed on singly charged $(NH_4)_2SO_4$ and NaCl particles, respectively. It is when the hygroscopic growth factors of the singly and doubly charged particles are different that a bimodality is introduced in the HTDMA results. This effect is very important to consider for ambient particle samples when the chemical composition, and therefore hygroscopic growth factors, are very likely to be different for different particle sizes. In fact, this effect could, in some cases, be responsible for observed 'less' and 'more' hygroscopic growth modes in ambient samples in previous work. The two growth modes may not be the result of externally mixed particles with the same aerodynamic diameter, but rather the result of externally mixed particles of the same electrical mobility diameter (i.e. singly and doubly charged particles).

The potential effect of multiply charged particles on observed HTDMA growth results could be tested by observing the polydisperse size distribution and calculating the maximum number concentration of doubly charged particles that could have been sampled with the singly charged monodisperse particles. If the ratio of doubly-to-singly charged number concentrations is much lower than the ratio of the number concentrations observed in the less and more hygroscopic growth modes, then the influence of doubly charged particles can most likely be neglected. Alternatively, if the number concentration of doubly charged particles is relatively high, their influence on the observed growth modes could be important. In this case, observations of the chemical compositions of the singly and doubly charged particles could elucidate potential differences in their hygroscopic growth. Furthermore, the hygroscopic growth of the doubly charged particles could be observed directly and then compared to the observed growth of the singly charged particles.

7.9 *Comparison of S_{crit} Values Derived Using the Model from Weingartner et al. and the Simplified Köhler Model*

In a recent paper by *Weingartner et al.* [1997], a method for deriving S_{crit} from HTDMA growth data was proposed similar to that used in this work. The primary difference between the model used by *Weingartner et al.* and that in this work is that only one free fit parameter was used. The basic equation used by *Weingartner et al.* was

$$RH = 100exp\left[\frac{\alpha}{D_{drop}}\right] exp\left[\frac{-\beta N_i}{D^3_{drop} - D^3_{p,sol}}\right] \tag{7.3}$$

where α was taken equal to 2.155 nm, β was set equal to 5.712x10^{-2} nm^3, and the droplet and particle sizes were in nanometers [*Weingartner et al.,* 1997]. In order to compare results from the model of *Weingartner et al.* [1997] to S_{crit} values from our model, α and β were re-calculated for the temperatures of the HTDMA studies in this work. Typical values were similar to those used by *Weingartner et al.* N_i denoted the number of dissociated molecules in the water layer of the droplet, and was the one unknown in the model. *Weingartner et al.* fit the above relation to HTDMA growth data from studies of combustion particles and derived values of N_i for particles with various pretreatments and produced from different fuels. These values of N_i were then used in Eqn. 7.1 to derive values of S_{crit} for the combustion particles. No simultaneous CCN measurements were available against which the derived S_{crit} value could be compared. However, the derived values of S_{crit} were similar to those measured by previous investigators for particles from combustion sources. Their results indicated that combustion particles with diameters between 50 and 110 nm exhibited values of S_{crit} between 0.8% and 2.7%, with higher values associated with the smaller particles. They also found that the derived values of S_{crit} decreased for particles generated from fuels with higher sulfur content. Another interesting finding in their study was that particles aged in storage bags exhibited

increased hygroscopicity with increasing storage time.

The values of S_{crit} and D_{crit} predicted by the model of *Weingartner et al.* were compared to those derived from the model in this work for each of the particle types studied. Results are listed in Table 7.9. The values of S_{crit} that are compared in Table 7.9 are predicted using all of the HTDMA study results for each compound with applied error. The values of S_{crit} predicted by the two models have been plotted in Figure 7.28. The solid line represents perfect agreement with theory. Solid dots in the figure represent S_{crit} values from CCN studies. Diamonds represent the values of S_{crit} predicted by the model in this work and squares represent the results from the model of *Weingartner et al.* The vertical uncertainty bars represent the $\pm 28\%$ confidence interval in HTDMA-derived values of S_{crit}. The $\pm 21\%$ confidence interval is shown for CCN-derived values of S_{crit}in Figure 7.28. Both methods for predicting S_{crit} from HTDMA results always underpredict values of S_{crit} over the supersaturation range examined. The average agreement between theoretical and predicted values of S_{crit} for particles of known chemical composition is -20% (1σ=8%, n=8) for the model proposed by *Weingartner et al.* and -16% (1σ=7%, n=8) for the model from this work. The similarity of the average agreement from the two models is surprising, since the model of *Weingartner et al.* does not make any accounting for the variation of the osmotic coefficient with droplet molality, which can be important for the relative humidities between 80% and 90% typical for HTDMA studies.

For many of the particles composed of single solutes studied here, the osmotic coefficient varies between values slightly above one and values slightly below one (NaCl) or is less than one ($(NH_4)_2SO_4$, NH_4HSO_4, NH_4NO_3, internally mixed solutes) for the RH range and molalities experienced during HTDMA studies (1 to 6 molal). For example, for $(NH_4)_2SO_4$ the osmotic coefficient is near 0.75 for molalities greater than 6 molal, decreases from to 0.65 for molalities between 6 and 1, and then exponentially approaches unity as the molality decreases below 1 molal. In the model of *Weingart-*

ner et al. the product $\frac{\nu\rho_s\Phi}{M_s}$ is assumed to be constant as the one free fit parameter in the model (N_i). Therefore, the assumption is made that Φ does not vary with RH. As mentioned above, for HTDMA conditions and many of the compounds studied here, the osmotic coefficient value varies about unity or does not vary significantly, and the simpler model of *Weingartner et al.* can do a reasonable job of predicting S_{crit}. This is true as long as measurements are made in the appropriate molality range where Φ does not vary significantly. However, in general, compounds do not have osmotic coefficient values that vary about unity or are constant for droplet molalities experienced during HTDMA measurements. A good example is NH_4NO_3, where the osmotic coefficient demonstrates a monotonic decrease from a value of 0.8 for a 1 molal solution, to a value of 0.65 for a 6 molal solution. Correspondingly, the model of *Weingartner et al.* exhibits a much larger error in predicted S_{crit} in Tables 5.5 and 5.6 for the numerical studies on particles composed of NH_4NO_3.

Values of Y were derived from the values of N_i reported in Table 7.9 using Eqn. 5.20. For particles composed of single solutes, the agreement between values of Y reported in Table 5.2 and values derived from the N_i values in Table 7.9 was 26% for NaCl, -32% for $(NH_4)_2SO_4$, and -6% for NH_4HSO_4. This comparison suggests that some information regarding the chemical composition can be obtained from the N_i values. For internally mixed NaCl-$(NH_4)_2SO_4$, the value of Y derived from N_i in Table 7.9 was 20% larger than the theoretical value of Y for this composition. Values of Y derived from *Weingartner et al.'s* model were smaller for the ambient particle studies, consistent with the smaller values of Y_f shown in Table 7.8.

7.10 *Summary*

The experimental results from all laboratory studies conducted in this work were presented in this chapter. Results from several quality control experiments were outlined, including tests for leaks, Nanopure water impurities, RH and T control, and

TDMA sizing studies. The results from these initial experiments revealed that the results from HTDMA studies are not influenced by artifact particles, that RH and T control was maintained at acceptable levels during HTDMA studies, and that the sizing precision of the TDMA system was 0.13 nm for 40 nm particles. The ability to predict values of S_{crit} from CCN measurements was validated and the average agreement between theoretical values of S_{crit} for known particle diameters and chemical compositions and those derived from CCN studies was calculated. For particles composed of pure salts, the average agreement was found to be -0.6% with a standard deviation of 11% (n=16). The confidence interval in S_{crit} values determined from CCN studies was determined at the 95% confidence level by pooling data from studies on $(NH_4)_2SO_4$, NH_4HSO_4, and externally mixed NaCl-$(NH_4)_2SO_4$. The calculated confidence interval expressed as a percent of S_{crit} was found to be $\pm$21%.

The operation of the HTDMA system was validated by comparing observed droplet results with theory for particles composed of NaCl and $(NH_4)_2SO_4$. Agreement between experiment and theory was found to be 0.6% (1σ=1%, n=40) for NaCl and -0.3% (1σ=1.2%, n=63) for $(NH_4)_2SO_4$. The excellent agreement between observed hygroscopic growth and theoretical droplet growth factors verified proper operation of the HTDMA. Results for other known compounds exhibited similar agreement between theory and experiment. Confidence intervals in HTDMA-derived values of S_{crit} were calculated by pooling the standard deviations in predicted values of S_{crit} from sets of (RH, D_{drop}) pairs. For particles composed of NaCl, $(NH_4)_2SO_4$, and NH_4HSO_4, and RH's between 78% and 92%, the confidence interval expressed as a percent of S_{crit} at the 95% confidence level was between $\pm$16% and $\pm$28%.

Values of S_{crit} were derived using the fit routine and observed droplet growth from the HTDMA for particles composed of NaCl, $(NH_4)_2SO_4$, NH_4HSO_4, internally mixed NaCl-$(NH_4)_2SO_4$, externally mixed NaCl-$(NH_4)_2SO_4$, and for ambient particles of unknown chemical composition. Particle diameters between 25 and 120 nm were

examined. The derived and theoretical values of S_{crit} agreed within -8% for NaCl, -16% for $(NH_4)_2SO_4$, -18% for NH_4HSO_4, -8% for internally mixed NaCl-$(NH_4)_2SO_4$, -23% for externally mixed $(NH_4)_2SO_4$, and -25% for externally mixed NaCl. Numerical studies in chapter 5 demonstrated that the model itself has a tendency to underpredict values of S_{crit}. Therefore, the simplifications described in chapter 5 that were introduced into the Köhler model are partly responsible for the underprediction of S_{crit}. Although there is a bias for the fit routine to underpredict values of S_{crit} relative to theoretical values, the underpredictions are smaller than, or similar to, uncertainties in values of S_{crit} derived from CCN studies. For HTDMA studies conducted on particles composed of known, pure salts the average agreement between predicted values of S_{crit} and theoretical values is -12% (1σ=5%, n=5). This value is equal to the uncertainty in experimentally derived values of S_{crit} from CCN studies. Therefore, the method proposed here to derive S_{crit} from HTDMA measurements has been validated for particles composed of known pure salts.

The sensitivity of the values of S_{crit} predicted by the fit routine to the choice of RH values was investigated. As expected, when the HTDMA growth data used as input to the fit routine consisted of very few points (3 or 5), or represented too narrow a range of RH (<5-10%), the predicted values of S_{crit} exhibited greater error. For small numbers of data pairs and small ranges of RH, the fit routine is less capable at deriving accurate values of S_{crit}, particularly when one considers the experimental uncertainties in the input data and the inability to capture the hygroscopic growth behavior for these conditions.

For the three ambient samples, only one showed good agreement (-6%, DOY 175) between the value of S_{crit} derived from HTDMA studies and that from simultaneous CCN studies. The value of S_{crit} derived from the fit routine for results from DOY 182 was only 10% smaller than the value calculated for a hypothetical chemical composition determined by matching calculated hygroscopic growth for the assumed

composition with observed droplet growth. Possible reasons for the poorer agreement in the ambient studies include changes in air mass source region and particle chemical composition during the long period of time required to complete the studies, and more uncertainty in the data arising from the relatively lower number of droplets that were counted due to the low number concentrations of particles exiting DMA1. Limitations in the simplified Köhler model used in the fit routine may also be responsible for the poorer agreement between predicted values of S_{crit} for particles of unknown composition and those determined from simultaneous CCN studies.

Table 7.1: Summary of all HTDMA and CCN studies conducted for this work. Study numbers designate day of year of study and are used in text to designate particular studies.

Chemical Composition	D_p Range (nm)	HTDMA Study Numbers	Number of RH Scans	CCN Study Numbers
		Single Solutes		
Ammonium Sulfate	25-102	161,162 169,176	85	74[a],75[a], 147,148, 162,169,176
Sodium Chloride	37-96	146,163 164	49	76,77,152, 163,164
Ammonium Bisulfate	40	172,178	43	172,178
		Mixed Solutes		
Internally Mixed $NaCl$-$(NH_4)_2SO_4$	32	173	16	173
Externally Mixed $NaCl$-$(NH_4)_2SO_4$	37-40	177,181	47	177,181
		Ambient Samples		
Unknown	65-120	174,175 182	42	174,175,182
Total Studies		15	282	22

[a]Two CCN studies conducted on this day.

Table 7.2: Summary of all CCN studies from this work. Study numbers designate day of year of study and are used in text to designate particular studies. Calculated average error is shown with standard deviation in parentheses. 'NS' designates day when HTDMA study was conducted with no simultaneous CCN study. Studies conducted before DOY 163 involved changing the monodisperse dry size sampled by the CCN counter and maintaining a constant chamber supersaturation. Later studies involved maintaining a constant input dry size and changing the chamber supersaturation.

Study Number	D_p (nm)	S_{crit} Exper.	S_{crit} Theory	S_{crit} Percent Error
		Ammonium Sulfate		
74a	45.8	0.58	0.57	+0.9
74b	102.3	0.17	0.165	+3
75a	30.8	1.01	1.06	-4.7
75b	53.2	0.39	0.45	-13
147	74.1	0.27	0.26	+0.4
148	65.0	0.26	0.32	-17
162	29.8	0.90	1.12	-20
169	57.2	0.42	0.41	+3
176	57.2	0.49	0.41	+20
Average	Error			-3.0(12)
		NaCl		
76	96.2	0.15	0.128	+17
77	51.7	0.28	0.326	-14
146	37.0	NS	0.475	NS
152	59.0	0.255	0.263	-3
163	44.0	0.47	0.411	+14
164	46.3	0.407	0.381	+7
Average	Error			4.2(13)
		Ammonium Bisulfate		
172	40.0	0.729	0.742	-2
178	40.0	0.735	0.745	-1
Average	Error			-1.5(0.7)
Average All Conf. Interval				-0.6(11) ±21.4%
		Internal Mixture-NaCl -$(NH_4)_2SO_4$		
173	32.0	0.65	0.709	-8
		External Mixture-NaCl -$(NH_4)_2SO_4$		
177	40.0	0.577	0.617	-6.5
181	40.0	0.571	0.617	-7.5
Average	Error			-7.0(1)
		Ambient		
174	85.0	0.513	0.35	-32
175	68.4	0.497	0.47	-6
182	120.0	0.530	0.20	-62

Table 7.3: Summary of theoretical S_{crit} values, Y_{fit} and $\beta_{0,f}$ fit parameters, and D_{crit} values determined HTDMA study results on particles composed of NaCl. The confidence interval of HTDMA-derived values of S_{crit} is ±28%. Data pair numbers designate which HTDMA scans were used in the fit routine. The difference between the two values is the total number of data points used in the fit routine. Each data pair is shown twice: the first fit routine run was performed without added random error, the second set of results for the same data pair represent the average of 20 runs of the fit routine with assumed random error added to the input data pairs. Ratios of standard deviations in predicted values of S_{crit} to average values of S_{crit} were less than 0.16 for the cases with applied errors. The theoretical values and experimental values of S_{crit} for NaCl particles are listed in Table 7.2.

Data Pairs	Y_{fit}	$\beta_{0,f}$	S_{crit} (%)	S_{crit} Err. (%)	D_{crit} (nm)	Error D_{crit} (%)	χ^2
NaCl 37 nm DOY 146							
0 19	84.767	0.01611	0.42	-21	321	12	8.00e-01
0 19	93.656	0.01114	0.40	-24	334	17	1.04e+00
0 10	107.122	0.00593	0.38	-29	357	25	5.37e-01
0 10	121.272	0.00274	0.34	-35	392	37	1.38e+00
10 19	63.286	0.04046	0.47	-11	285	0	3.14e-01
10 19	94.190	0.02336	0.40	-24	335	17	6.96e-01
5 15	100.163	0.00856	0.39	-26	344	20	1.69e-01
5 15	110.808	0.00407	0.36	-32	373	30	6.03e-01
0 5	105.446	0.00439	0.37	-30	364	27	9.36e-01
0 5	179.628	-0.00098	0.29	-45	465	62	1.84e+00
5 10	121.920	0.00120	0.35	-34	383	34	5.08e-02
5 10	140.032	-0.00125	0.33	-38	408	42	6.82e-01
10 15	84.419	0.01879	0.43	-20	317	11	1.27e-01
10 15	120.029	0.00439	0.34	-35	393	37	5.88e-01
NaCl 46 nm DOY 164							
28 39	45.787	0.08943	0.40	6	337	-15	2.44e+00
28 39	55.641	0.06072	0.36	-6	379	-5	1.73e+00
28 33	59.701	0.03544	0.35	-9	390	-2	7.19e-01
28 33	127.280	0.00710	0.24	-37	569	42	1.37e+00
33 39	52.072	0.05124	0.37	-2	366	-8	1.74e+00
33 39	63.570	0.04438	0.34	-11	403	0	2.02e+00
NaCl 44 nm DOY 163							
20 27	65.292	0.03302	0.37	-10	368	0	1.31e+00
20 27	67.561	0.03248	0.36	-11	372	0	9.81e-01
20 25	65.279	0.03474	0.37	-10	365	-1	1.78e+00
20 25	62.043	0.05105	0.37	-10	367	0	1.01e+00
22 27	80.924	0.01252	0.32	-21	416	12	3.49e-01
22 27	94.865	0.00807	0.31	-25	440	18	8.70e-01

Table 7.4: Summary of theoretical S_{crit} values, Y_{fit} and $\beta_{0,f}$ fit parameters, and D_{crit} values determined HTDMA study results on particles composed of single solutes. The confidence interval of HTDMA-derived values of S_{crit} is ±28%. For $(NH_4)_2SO_4$, the theoretical and experimental S_{crit} values are shown in Table 7.2. In this and subsequent similar tables, data pair numbers designate which HTDMA scans were used in the fit routine. The difference between the two values is the total number of data points used in the fit routine. Each data pair is shown twice: the first fit routine run was performed without added random error, the second set of results for the same data pair represent the average of 20 runs of the fit routine with assumed random error added to the input data pairs. Ratios of standard deviations in predicted values of S_{crit} to average values of S_{crit} were less than 0.16 for the cases with applied errors.

Data Pairs	Y_{fit}	$\beta_{0,f}$	S_{crit} (%)	S_{crit} Err. (%)	D_{crit} (nm)	Error D_{crit} (%)	χ^2
Ammonium Sulfate 57 nm DOY's 169 & 176							
20 62	33.353	0.00247	0.35	-13	388	5	1.72e+00
20 62	34.225	0.00101	0.33	-16	403	9	2.35e+00
20 30	21.548	0.02164	0.42	4	320	-12	4.21e+00
20 30	25.850	0.02066	0.39	-2	342	-6	5.48e+00
30 40	37.211	0.00138	0.33	-18	410	11	7.44e-01
30 40	41.538	-0.00125	0.31	-21	429	16	1.60e+00
40 50	28.269	0.01183	0.38	-5	353	-3	5.55e-01
40 50	35.772	-0.00075	0.33	-18	410	11	9.83e-01
20 40	29.108	0.00593	0.36	-9	371	1	2.75e+00
20 40	34.415	0.00250	0.35	-13	388	5	3.84e+00
30 50	26.786	0.01755	0.39	-2	344	-6	1.25e+00
30 50	27.477	0.01408	0.39	-4	349	-4	1.54e+00
25 35	17.621	0.06540	0.48	19	284	-22	4.85e+00
25 35	23.843	0.03085	0.41	2	329	-10	4.92e+00
35 45	31.111	0.00721	0.36	-10	373	1	6.62e-01
35 45	35.232	0.00416	0.33	-18	410	11	1.04e+00

Table 7.5: Summary of theoretical S_{crit} values, Y_{fit} and $\beta_{0,f}$ fit parameters, and D_{crit} values determined HTDMA study results on particles composed of NH_4HSO_4. The confidence interval of HTDMA-derived values of S_{crit} is ±28%. Ratios of standard deviations in predicted values of S_{crit} to average values of S_{crit} were less than 0.16 for the cases with applied errors. The theoretical and experimental S_{crit} values for NH_4HSO_4 are shown in Table 7.2.

Data Pairs	Y_{fit}	$\beta_{0,f}$	S_{crit} (%)	S_{crit} Err. (%)	D_{crit} (nm)	Error D_{crit} (%)	χ^2
Ammonium Bisulfate 40 nm DOY's 172 & 178							
0 29	31.289	0.00596	0.62	-16	217	5	2.51e+00
0 29	33.059	0.00398	0.61	-18	222	8	3.21e+00
0 14	34.282	0.00406	0.60	-19	226	10	3.02e+00
0 14	34.365	0.00372	0.58	-21	232	13	3.68e+00
15 29	27.921	0.00758	0.64	-13	209	1	1.47e+00
15 29	31.212	0.00668	0.62	-16	216	5	2.29e+00
0 10	33.585	0.00397	0.60	-19	224	9	3.32e+00
0 10	33.904	0.00376	0.58	-21	231	12	4.44e+00
10 20	38.288	0.00008	0.55	-26	245	19	1.45e+00
10 20	49.484	-0.00224	0.50	-33	271	32	2.46e+00
20 29	33.275	0.00336	0.60	-18	222	8	1.56e+00
20 29	42.581	-0.00170	0.53	-28	252	22	2.39e+00
5 15	32.037	0.00562	0.61	-17	219	6	3.89e+00
5 15	33.153	0.00465	0.59	-20	228	11	5.55e+00

Table 7.6: Summary of theoretical S_{crit} values, Y_{fit} and $\beta_{0,f}$ fit parameters, and D_{crit} values determined HTDMA study results on internally mixed particles composed of $(NH_4)_2SO_4$ and NaCl. The confidence interval of HTDMA-derived values of S_{crit} is ±28%. Ratios of standard deviations in predicted values of S_{crit} to average values of S_{crit} were less than 0.16 for the cases with applied errors. Study numbers designate day of year of study and are used in text to designate individual studies.

Data Pairs	Y_f	$\beta_{0,f}$	S_{crit} (%)	Error w/ Theory (%)	D_{crit} (nm)	D_{crit} Error (%)	χ^2
Internally Mixed Ammonium Sulfate - NaCl 32 nm DOY 173							
0 16	37.791	0.05239	0.78	10	175	5	2.11e+00
0 16	53.002	0.02558	0.65	-8	207	25	2.51e+00
0 9	71.267	0.00297	0.56	-21	238	43	1.29e+00
0 9	92.463	-0.00089	0.50	-29	266	60	2.08e+00
5 16	63.873	0.00565	0.61	-14	221	33	9.72e-01
5 16	75.263	0.00131	0.57	-20	237	43	1.39e+00
10 16	63.893	0.00529	0.61	-14	218	31	1.89e-01
10 16	67.881	0.02274	0.59	-17	227	37	6.80e-01
0 5	112.273	-0.00318	0.46	-35	291	75	8.40e-01
0 5	122.780	-0.00264	0.44	-38	307	85	1.17e+00
5 10	112.413	-0.00466	0.46	-35	293	77	6.84e-01
5 10	115.132	-0.00330	0.45	-37	296	78	7.26e-01

Table 7.7: Summary of theoretical S_{crit} values, Y_{fit} and $\beta_{0,f}$ fit parameters, and D_{crit} values determined HTDMA study results on externally mixed particles composed of $(NH_4)_2SO_4$ and NaCl. The confidence interval of HTDMA-derived values of S_{crit} is ±28%. Ratios of standard deviations in predicted values of S_{crit} to average values of S_{crit} were less than 0.16 for the cases with applied errors. Study numbers designate day of year of study and are used in text to designate individual studies. The theoretical S_{crit} value for a 40 nm $(NH_4)_2SO_4$ particle at the HTDMA study temperature is 0.71%. The theoretical S_{crit} value for a 37 nm NaCl particle is 0.534%.

Data Pairs	Y_f	$\beta_{0,f}$	S_{crit} (%)	Error w/ Theory (%)	D_{crit} (nm)	D_{crit} Error (%)	χ^2
Externally Mixed Ammonium Sulfate 40 nm DOY's 177 & 181							
0 33	39.751	-0.00141	0.55	-22	245	16	3.16e+00
0 33	41.757	-0.00242	0.54	-23	249	18	3.76e+00
0 16	39.673	-0.00161	0.55	-21	242	15	2.93e+00
0 16	38.844	-0.00171	0.56	-20	239	14	3.27e+00
17 33	24.835	0.02702	0.70	0	193	-7	2.72e+00
17 33	28.720	0.01282	0.63	-10	213	1	3.13e+00
5 21	28.999	0.00623	0.63	-11	214	2	3.64e+00
5 21	33.019	0.00506	0.59	-16	227	8	4.28e+00
22 33	9.527	0.31310	1.02	43	142	-32	1.56e+00
22 33	21.608	0.06569	0.74	4	185	-11	1.96e+00
0 9	52.469	-0.00422	0.48	-31	278	32	3.37e+00
0 9	51.649	-0.00424	0.47	-33	284	35	2.38e+00
10 25	31.038	0.00508	0.61	-13	220	5	4.42e+00
10 25	35.417	0.00431	0.58	-17	230	9	5.37e+00
10 15	42.219	-0.00509	0.53	-24	251	19	1.32e+00
10 15	48.381	-0.00598	0.48	-31	278	32	1.70e+00
15 25	41.029	-0.00221	0.52	-25	255	21	4.83e+00
15 25	44.346	0.00027	0.52	-25	255	21	5.50e+00

Table 7.7: (cont.) Summary of theoretical S_{crit} values, Y_{fit} and $\beta_{0,f}$ fit parameters, and D_{crit} values determined HTDMA study results on externally mixed particles composed of $(NH_4)_2SO_4$ and NaCl. The confidence interval of HTDMA-derived values of S_{crit} is ±28%. Ratios of standard deviations in predicted values of S_{crit} to average values of S_{crit} were less than 0.16 for the cases with applied errors. Study numbers designate day of year of study and are used in text to designate individual studies. The theoretical S_{crit} value for a 40 nm $(NH_4)_2SO_4$ particle at the HTDMA study temperature is 0.71%. The theoretical S_{crit} value for a 37 nm NaCl particle is 0.534%.

Data Pairs	Y_f	$\beta_{0,f}$	S_{crit} (%)	Error w/ Theory (%)	D_{crit} (nm)	D_{crit} Error (%)	χ^2
Externally Mixed NaCl 37 nm DOY's 177 & 181							
0 33	90.184	0.01185	0.41	-24	330	15	1.72e+00
0 33	96.198	0.00919	0.40	-25	337	18	2.01e+00
0 16	67.687	0.03800	0.47	-11	284	0	1.55e+00
0 16	74.788	0.02597	0.45	-15	299	4	1.91e+00
17 33	100.885	0.00835	0.39	-27	346	21	1.84e+00
17 33	105.348	0.00488	0.38	-29	356	24	2.24e+00
5 21	79.565	0.02015	0.43	-18	310	8	2.10e+00
5 21	90.481	0.01545	0.41	-23	331	15	2.47e+00
22 33	76.775	0.02835	0.44	-17	305	6	1.09e+00
22 33	80.187	0.03182	0.42	-21	320	12	1.33e+00
0 9	48.856	0.07945	0.54	0	253	-11	1.61e+00
0 9	83.175	0.05910	0.41	-23	331	16	2.23e+00
10 25	78.923	0.01648	0.42	-21	319	11	2.15e+00
10 25	89.263	0.01247	0.40	-25	339	18	2.52e+00
10 15	83.535	0.00993	0.41	-23	327	14	3.23e-01
10 15	99.668	0.01575	0.39	-27	348	21	7.20e-01
15 25	103.918	0.00605	0.38	-29	354	23	2.50e+00
15 25	105.413	0.00817	0.36	-31	369	29	3.21e+00
Avg	86.381	0.02230	0.42	-22	326	14	1.86e+00
Sigma	14.744	0.01975	0.04	7	28	9	6.95e-01

Table 7.8: Summary of theoretical S_{crit} values, Y_{fit} and $\beta_{0,f}$ fit parameters determined HTDMA study results on ambient particles. The confidence interval of HTDMA-derived values of S_{crit} is ±28%. Ratios of standard deviations in predicted values of S_{crit} to average values of S_{crit} were less than 0.16 for the cases with applied errors. The theoretical S_{crit} value is not available for any of the ambient samples. The S_{crit} values derived from CCN studies on monodisperse 68.4, 85, and 120 nm ambient particles were 0.497, 0.513, and 0.53%, respectively.

Data Pairs	Y_f	$\beta_{0,f}$	S_{crit} (%)	Error w/ CCN (%)	χ^2
Ambient 85 nm on DOY 174					
0 18	8.824	-0.00404	0.37	-27	4.21e+00
0 18	9.332	-0.00450	0.35	-32	3.54e+00
0 10	65.861	0.03236	0.13	-75	5.21e+00
0 10	49.531	0.02096	0.15	-71	5.84e+03
9 18	2.740	0.11584	0.15	-71	3.20e+00
9 18	6.873	0.00338	0.42	-18	5.08e+00
0 14	73.316	0.04175	0.13	-75	5.10e+00
0 14	29.133	0.00662	0.21	-59	2.46e+03
Ambient 68.4 nm on DOY 175					
19 32	10.743	-0.00444	0.47	-6	1.35e+01
19 32	10.808	-0.00434	0.47	-6	1.05e+01
19 26	9.322	-0.00497	0.50	1	7.74e+00
19 26	9.157	-0.00514	0.51	2	5.35e+00
27 31	63.146	0.02883	0.19	-61	1.93e+00
27 31	43.596	0.01639	0.22	-54	6.64e+03
Ambient 120 nm on DOY 182					
33 50	13.617	-0.00260	0.18	-65	4.44e+00
33 50	13.772	-0.00299	0.18	-65	4.61e+00
33 36	NA	NA	NA	NA	NA
33 36	9.843	0.02293	0.21	-59	2.64e+00
38 50	9.476	0.00897	0.21	-58	1.14e+00
38 50	10.185	0.00325	0.21	-60	2.64e+00
35 40	15.047	-0.00268	0.17	-67	1.71e+00
35 40	14.564	-0.00255	0.17	-66	2.19e+00
49 53	16.737	-0.00417	0.16	-69	2.07e+00
49 53	17.086	-0.00405	0.15	-70	1.88e+00
38 44	7.060	0.01694	0.24	-53	1.35e+00
38 44	8.926	0.01258	0.22	-57	3.19e+00
45 50	11.021	0.00216	0.20	-61	5.56e-01
45 50	11.313	0.00245	0.19	-62	1.53e+00

Table 7.9: Comparison of S_{crit} values derived using the Köhler model in *Weingartner et al.* [1997] and those derived using the Köhler model from this work. All HTDMA growth results for each compound from this study were used in deriving values of S_{crit} from both models. N_i is the number of ions produced from dissociation of the solute and is the single unknown in the Köhler model of Weingartner. $S_{crit,th}$ designates theoretical value of S_{crit} for indicated composition and dry particle size. $S_{crit,w}$ designates the S_{crit} value derived from Weingarter's equation, $S_{crit,tw}$ is the value of S_{crit} from this work derived from the fit routine. Errors in S_{crit} for ambient studies are calculated with respect to the values derived from CCN studies (Table 7.2) and not hypothetical $S_{crit,th}$ values shown below. The confidence interval of HTDMA-derived values of S_{crit} is ±28%. Ratios of standard deviations in predicted values of S_{crit} to average values of S_{crit} were less than 0.16 for the cases with applied errors. Reported averages and standard deviations do not include results from ambient particle studies.

Compound	$D_{p,sol}$ (nm)	N_i (ions)	$S_{crit,th}$ (%)	$S_{crit,w}$ (%)	$S_{crit,tw}$ (%)	$S_{crit,w}$ Err (%)	$S_{crit,tw}$ Err (%)
NaCl	46.3	2.70e+06	0.38	0.29	0.36	-25	-6
NaCl	37.0	1.50e+06	0.48	0.38	0.40	-28	-24
NaCl	44.0	2.31e+06	0.41	0.31	0.36	-25	-12
$(NH_4)_2SO_4$	57.2	1.61e+06	0.41	0.37	0.35	-8	-14
NH_4HSO_4	40	5.85e+05	0.74	0.61	0.62	-17	-17
Int. Mix.	32	6.14e+05	0.71	0.60	0.65	-15	-8
Ext. Mix. NaCl	37	1.44e+06	0.53	0.39	0.41	-27	-24
Ext. Mix. $(NH_4)_2SO_4$	40	5.63e+05	0.71	0.62	0.55	-12	-23
Ambient	68.4	5.79e+05	0.65	0.61	0.47	22	-6
Ambient	85.0	9.83e+05	0.47	0.47	0.37	-8	-27
Ambient	120	4.89e+06	0.20	0.21	0.18	-59	-66
Average						-20	-16
Sigma						8	7

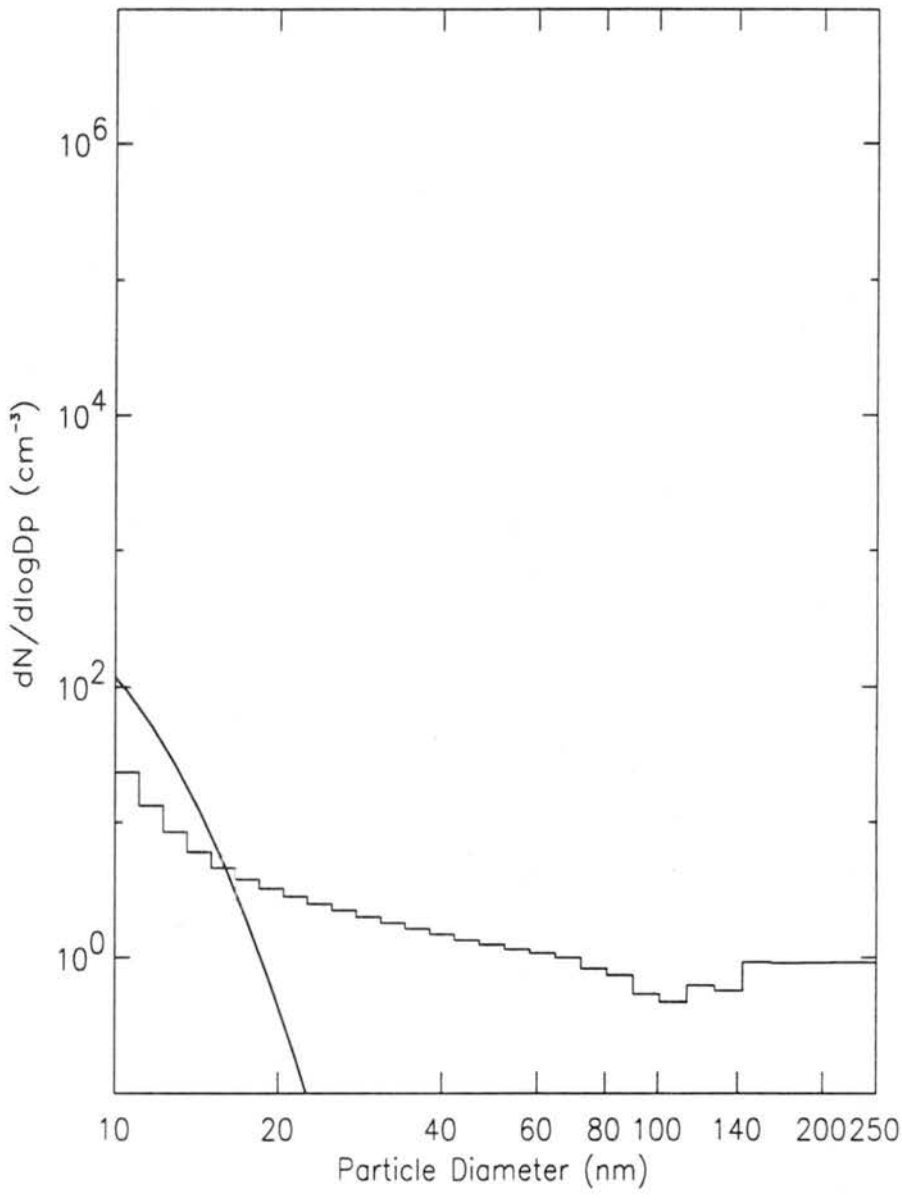

Figure 7.1: Size distribution measured with DMA1 and UCPC with no solution in atomizer to test for system leaks and artifact particles. Solid curve designates fit of log normal size distribution to experimental data.

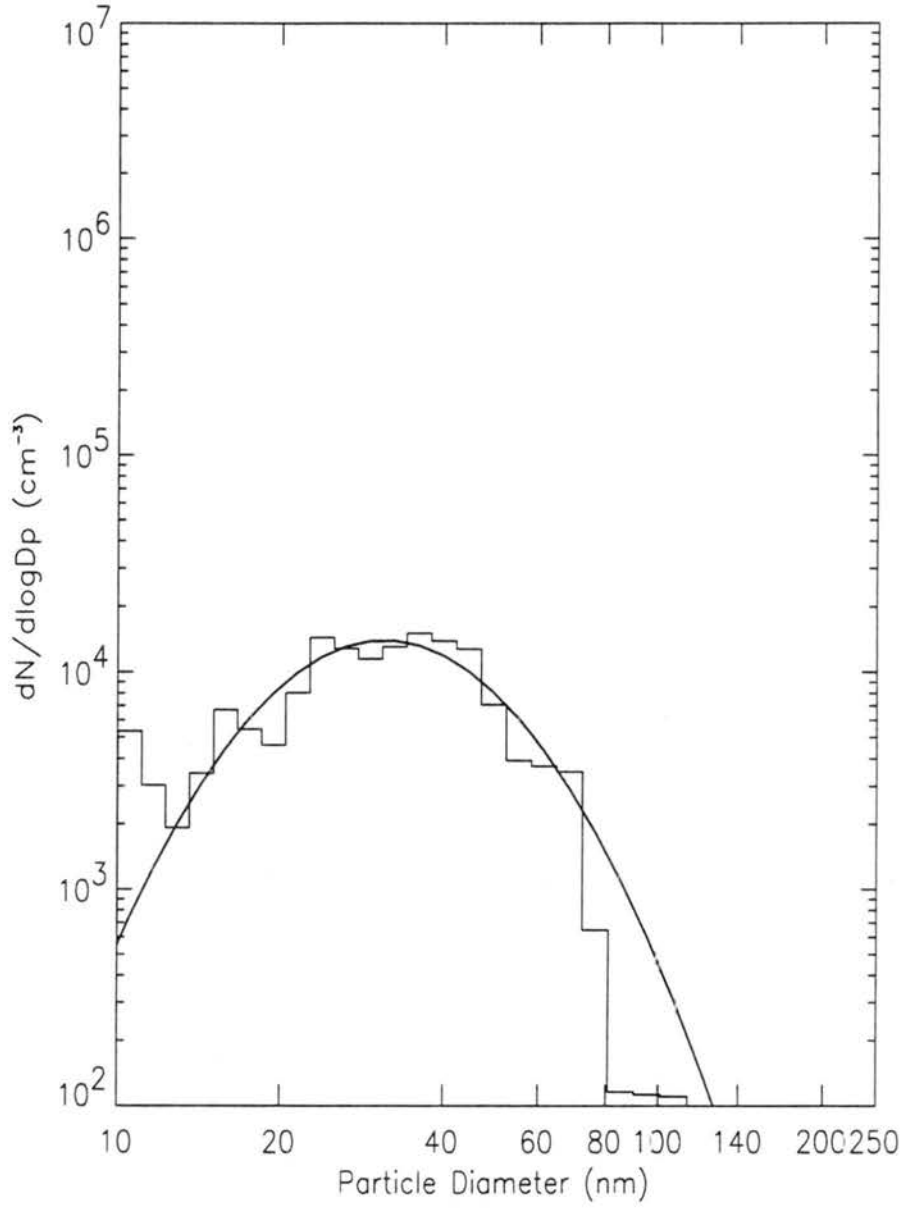

Figure 7.2: Size distribution measured with DMA1 and UCPC with Nanopure water in atomizer and no solute in solution. Solid curve designates fit of log normal size distribution to experimental data.

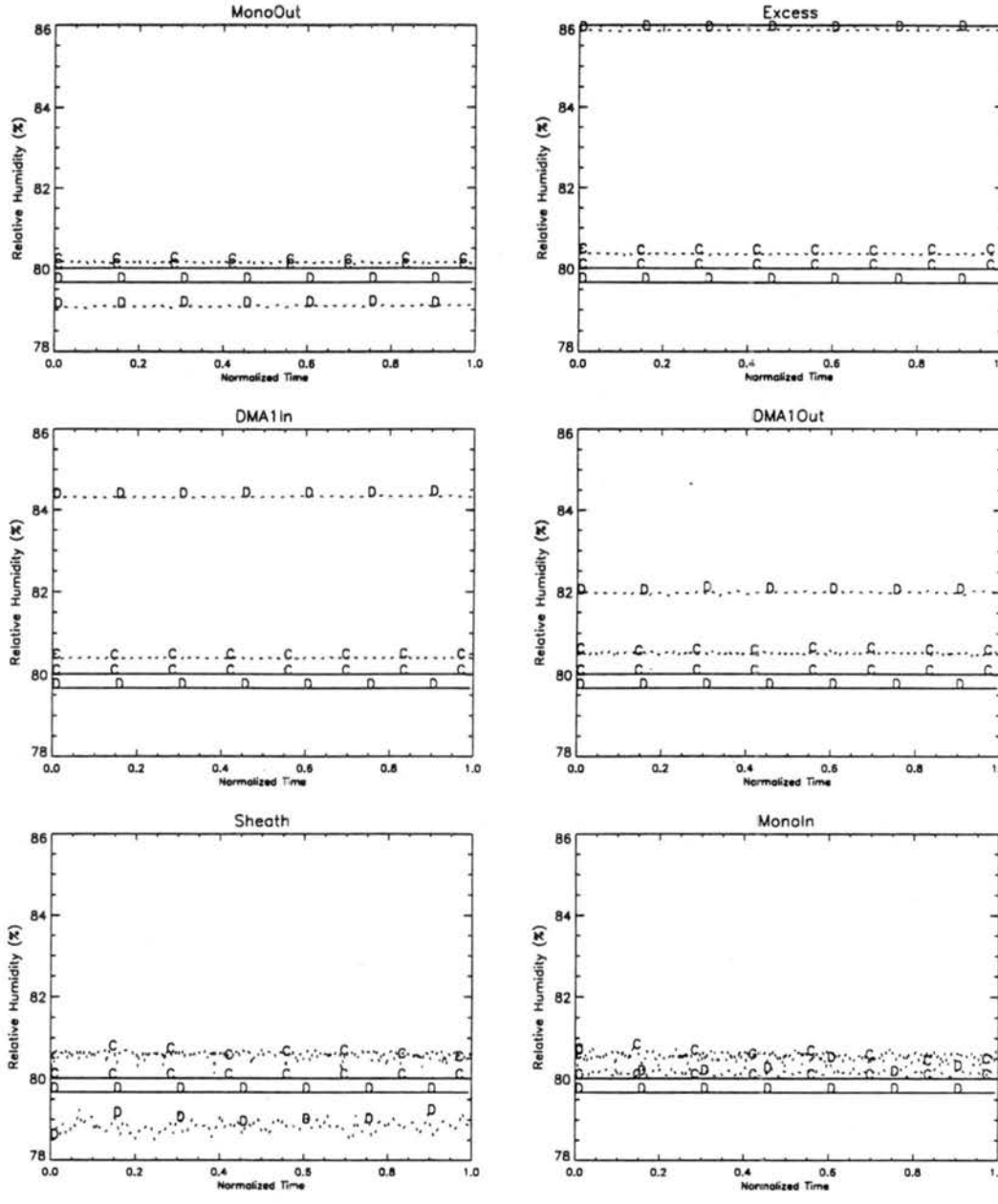

Figure 7.3: (a) RH sensor calibration check using $(NH_4)_2SO_4$ saturated salt solution. Results from calibration runs 'C' and 'D' are shown for each of the six sensors. Solid lines designate theoretical RH over the salt solution calculated from *Greenspan* [1977]. Dashed lines designate RH calculated during sensor exposure to salt solution.

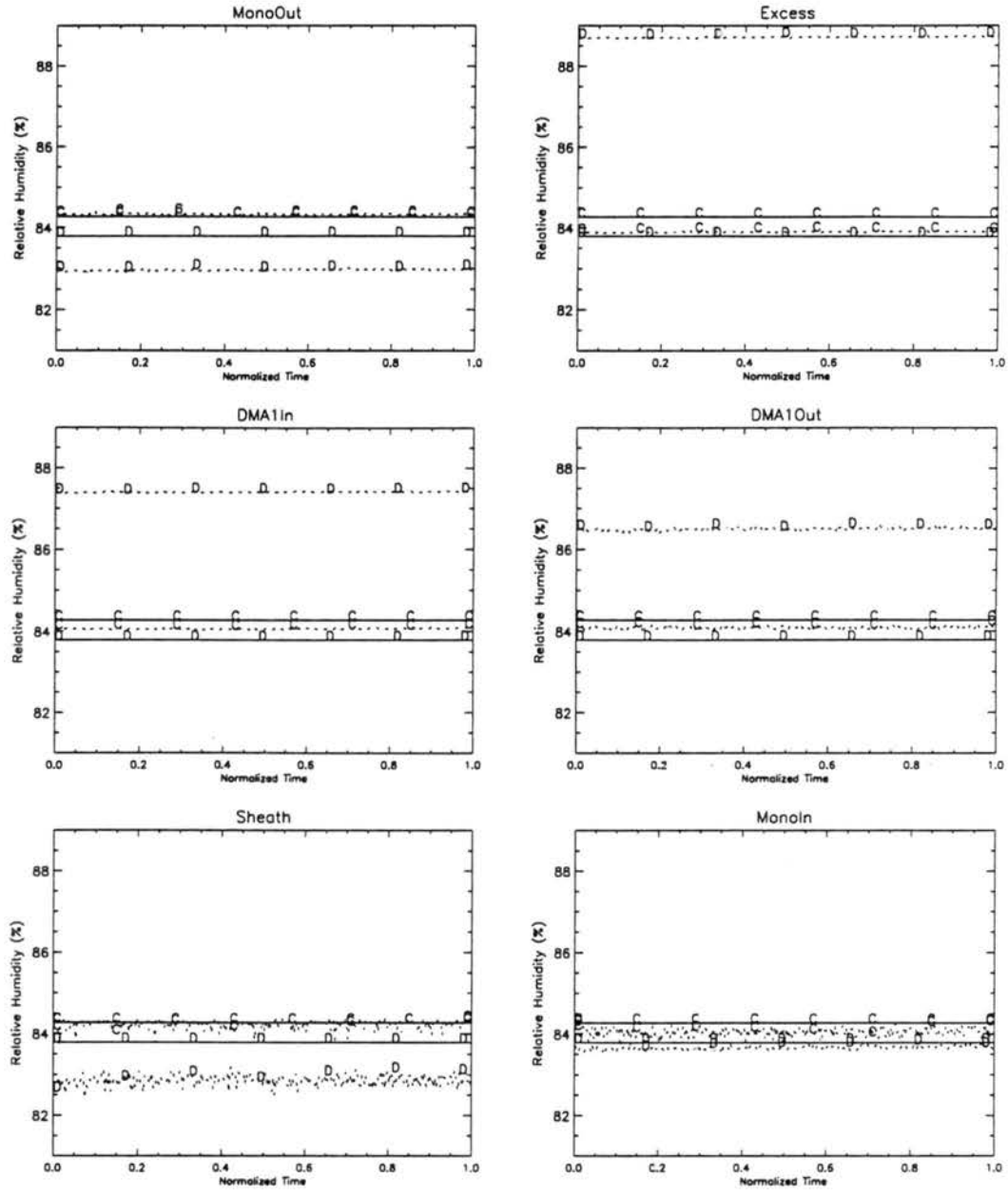

Figure 7.3: (b) RH sensor calibration check using KNO_3 saturated salt solution. Results from calibration runs 'C' and 'D' are shown for each of the six sensors. Solid lines designate theoretical RH over the salt solution calculated from *Greenspan* [1977]. Dashed lines designate RH calculated during sensor exposure to salt solution.

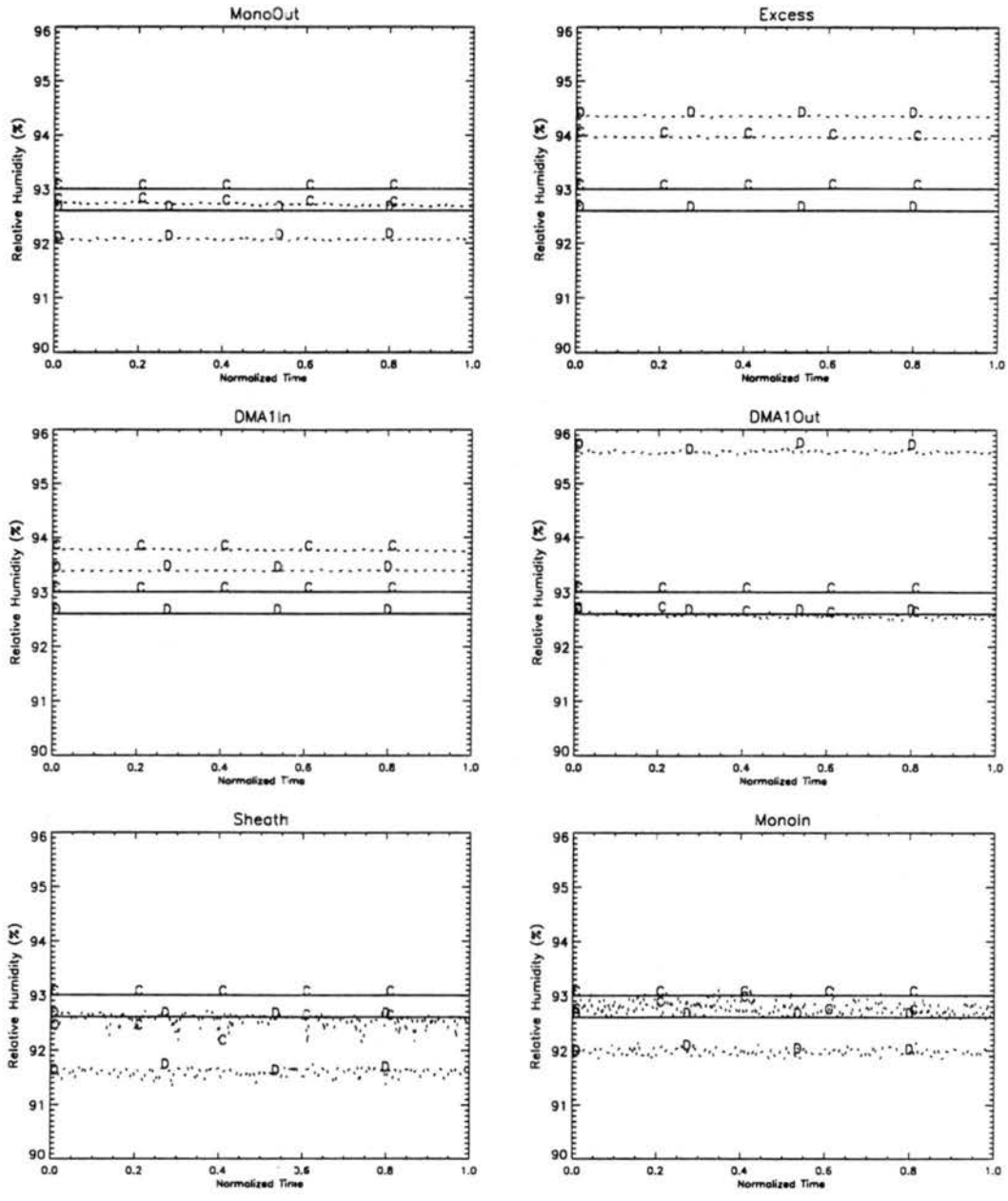

Figure 7.3: (c) RH sensor calibration check using KCl saturated salt solution. Results from calibration runs 'C' and 'D' are shown for each of the six sensors. Solid lines designate theoretical RH over the salt solution calculated from *Greenspan* [1977]. Dashed lines designate RH calculated during sensor exposure to salt solution.

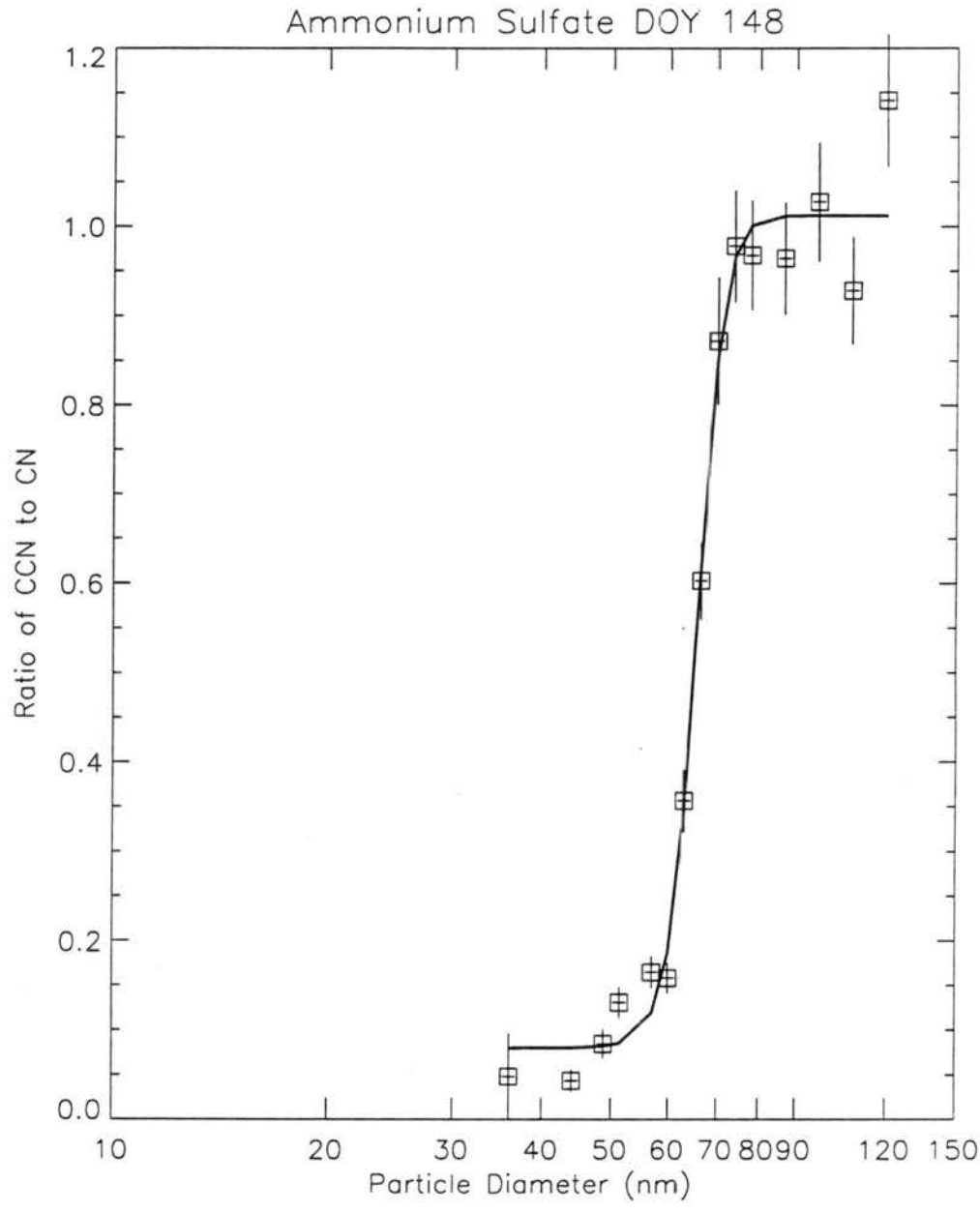

Figure 7.4: (a) CCN validation study results for $(NH_4)_2SO_4$ particles on DOY 148. Solid line designates fit of sigmoidal function to experimental data designated by squares. Vertical uncertainty bars represent Poisson counting error in CCN droplet concentration. The nominal CCN chamber maximum supersaturation was 0.27%. The confidence interval for CCN-derived values of S_{crit} is $\pm 21\%$.

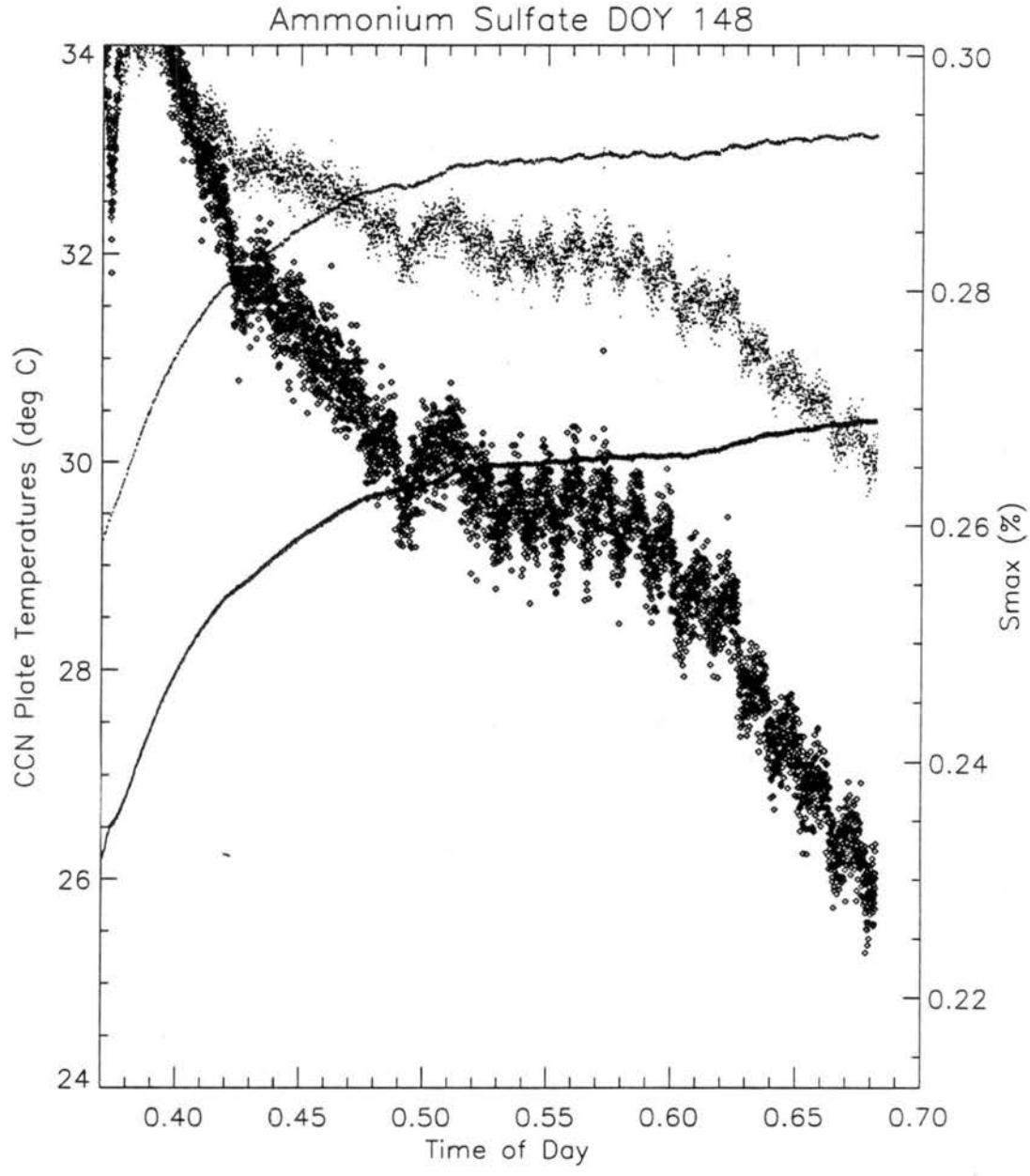

Figure 7.4: (b) Timelines of diffusion chamber top (thin solid) and bottom (thick solid) plate temperatures, temperature difference between top and bottom plates (dots) multiplied by 11, and chamber maximum supersaturation (diamond) for CCN validation study on $(NH_4)_2SO_4$ particles on DOY 148.

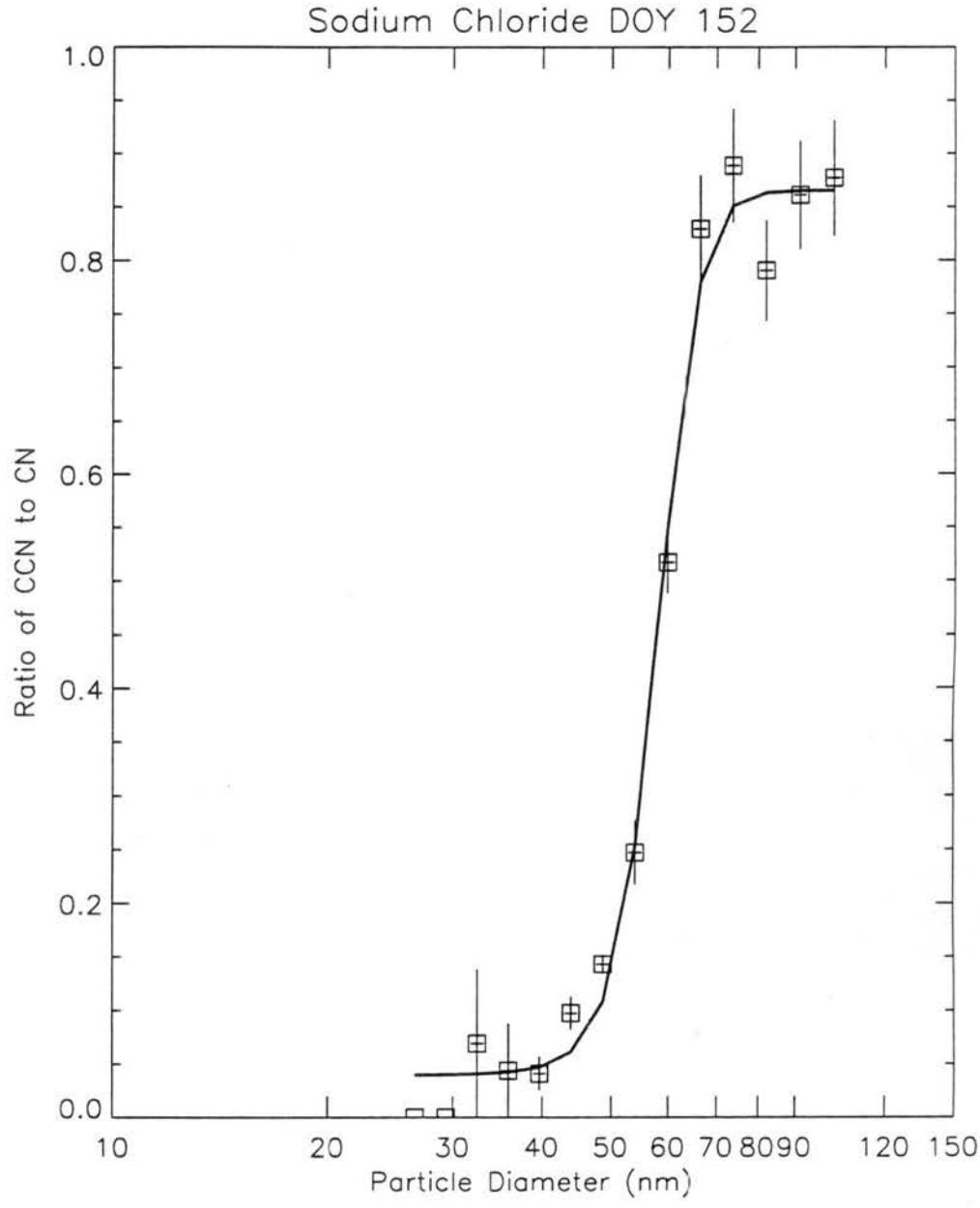

Figure 7.5: (a) CCN validation study results for NaCl particles on DOY 152. Solid line designates fit of sigmoidal function to experimental data designated by squares. Vertical uncertainty bars represent Poisson counting error in CCN droplet concentration. The nominal CCN chamber supersaturation was 0.26%. The confidence interval for CCN-derived values of S_{crit} is ±21%.

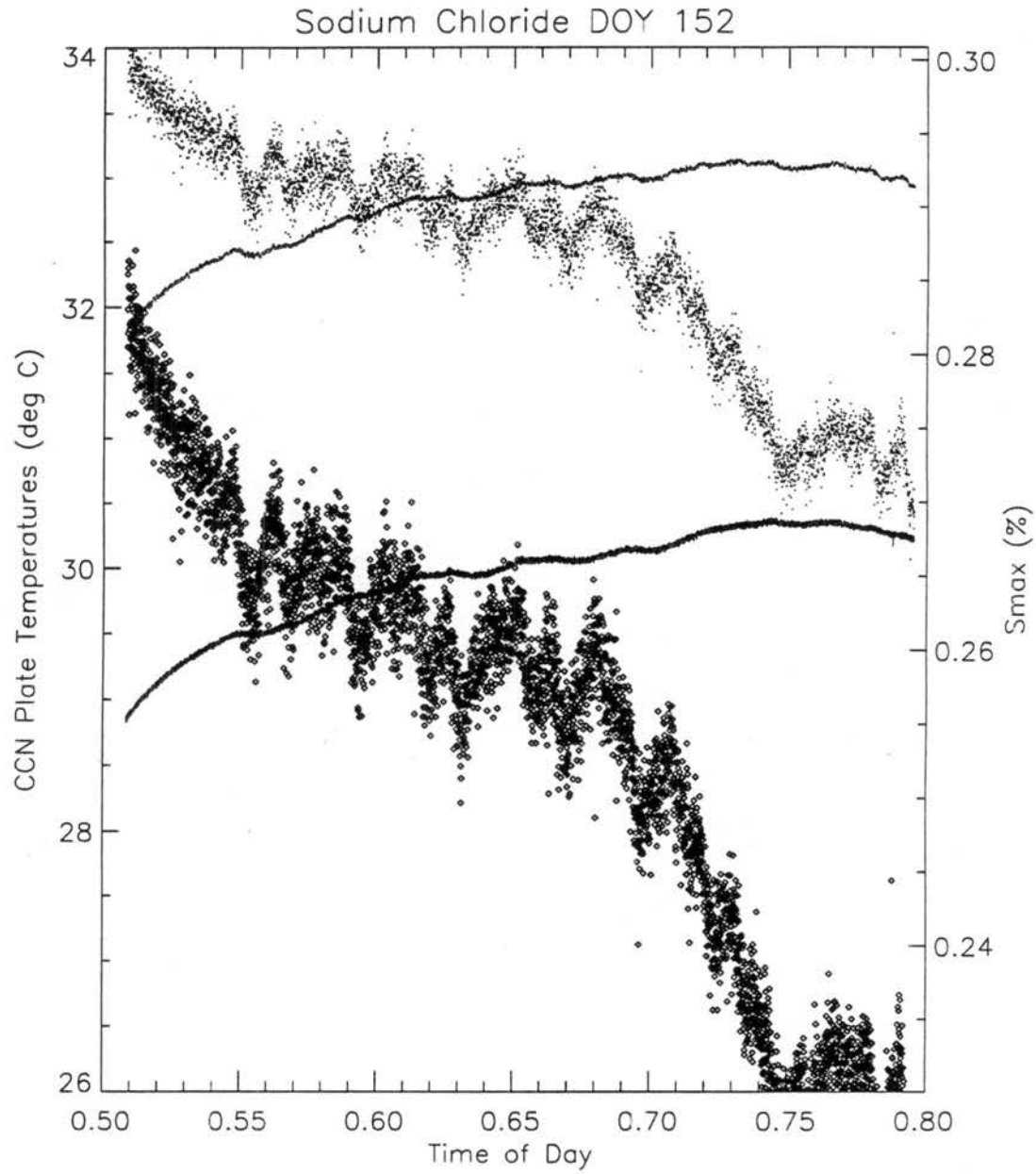

Figure 7.5: (b) Timelines of diffusion chamber top (thin solid) and bottom (thick solid) plate temperatures, temperature difference between top and bottom plates (dots) multiplied by 11, and chamber maximum supersaturation (diamond) for CCN validation study on NaCl particles on DOY 152.

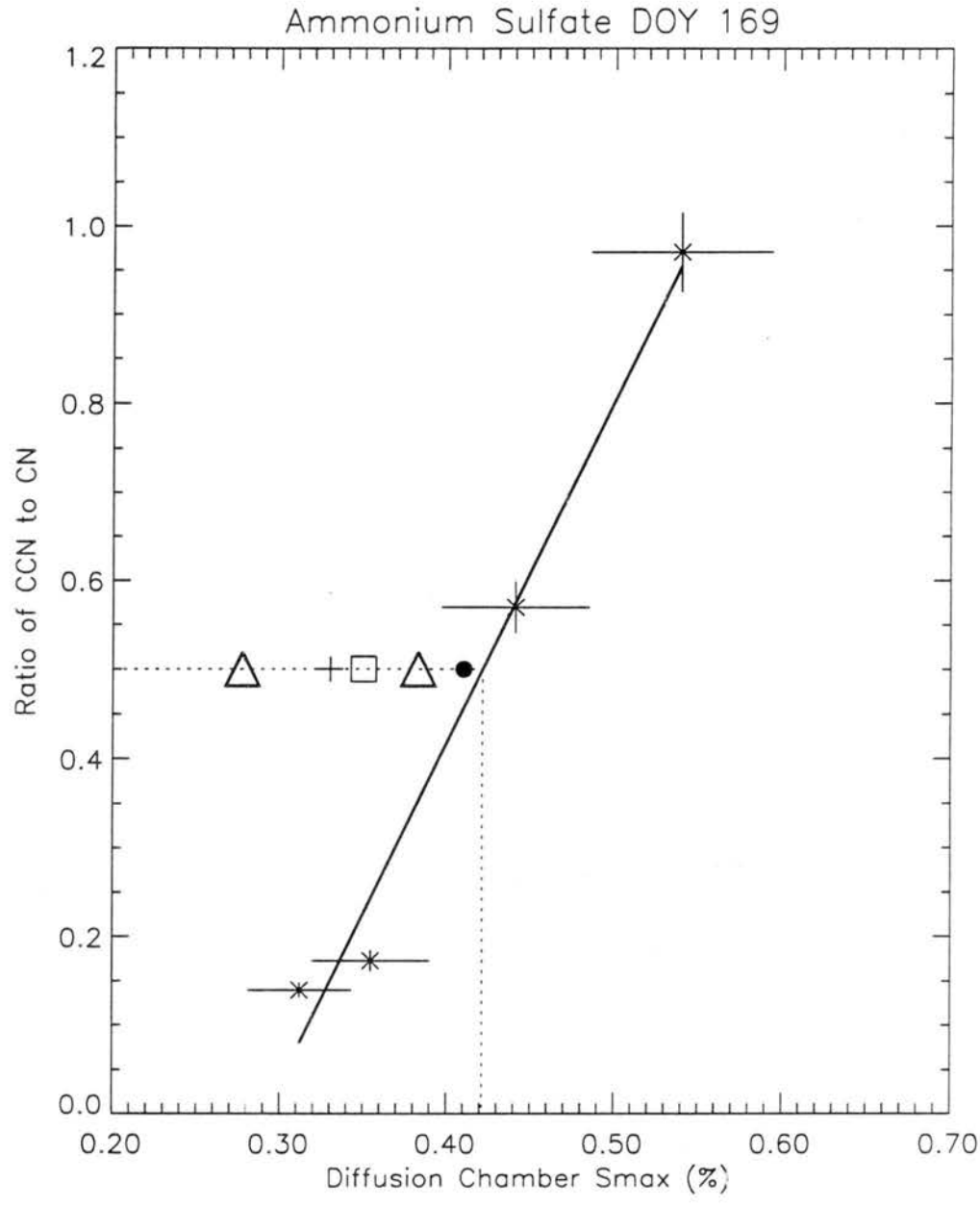

Figure 7.6: (a) CCN validation study results for 57.2 nm $(NH_4)_2SO_4$ particles on DOY 169. Solid line designates best-fit line to experimental data designated by asterisks. Vertical uncertainty bars represent Poisson counting error in CCN droplet concentration. Horizontal uncertainty bars represent ±10% uncertainty in chamber S_{max}. Triangles designate 1σ range of S_{crit} values predicted by fit routine from HTDMA growth results. The square represents the value of S_{crit} from the fit with all data pairs and no applied error, while the plus symbol represents the average value from the fits with applied error. Dotted lines designate experimentally observed value S_{crit}. Solid dot represents the theoretical value of S_{crit} for a 57.2 nm diameter $(NH_4)_2SO_4$ particle. The confidence interval for CCN-derived values of S_{crit} is ±21%.

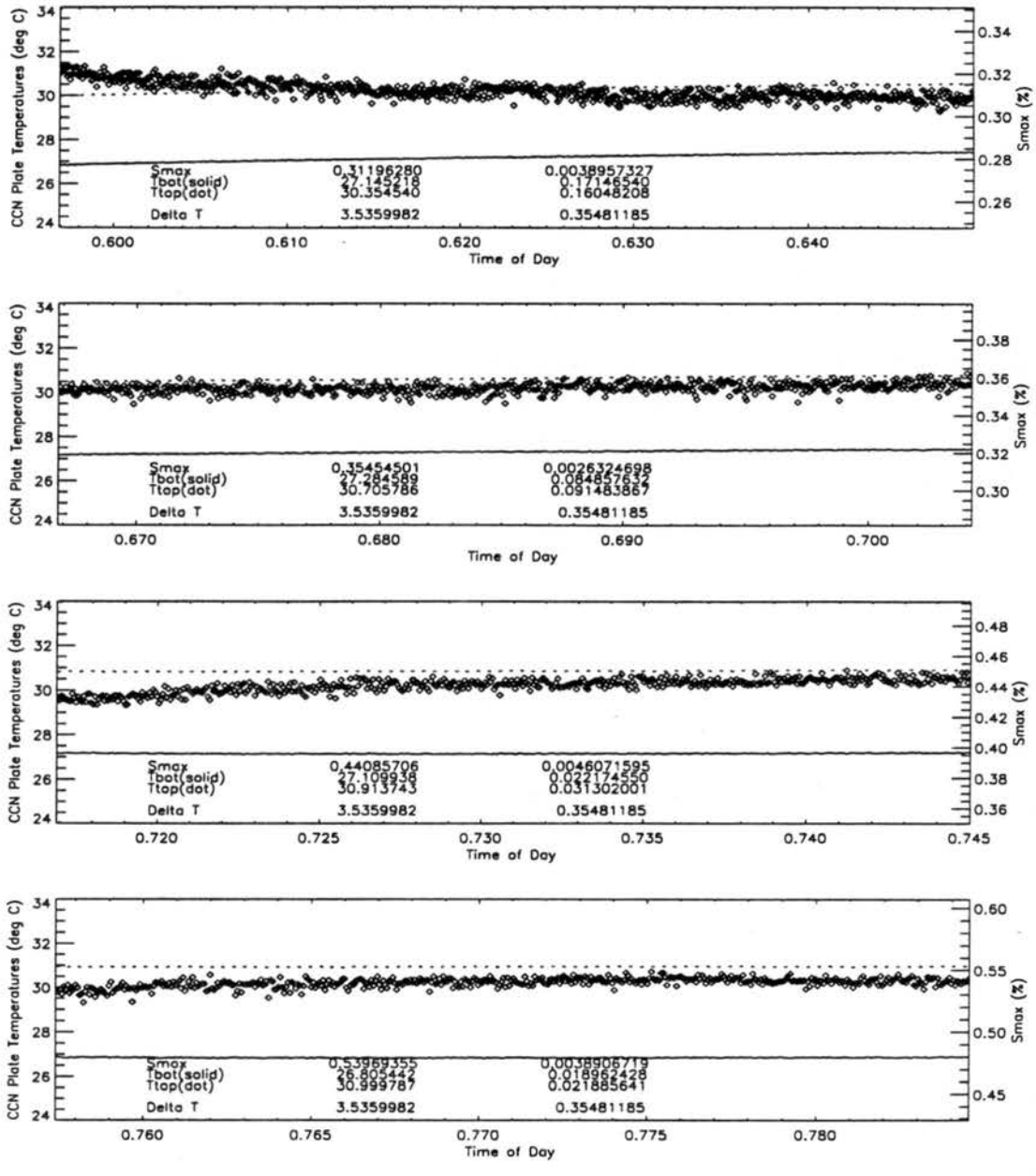

Figure 7.6: (b) Timelines of diffusion chamber top (dotted) and bottom (solid) plate temperatures and chamber maximum supersaturation (diamond) for CCN validation study on $(NH_4)_2SO_4$ particles on DOY 169. Average values and standard deviations of various study parameters are shown for each supersaturation.

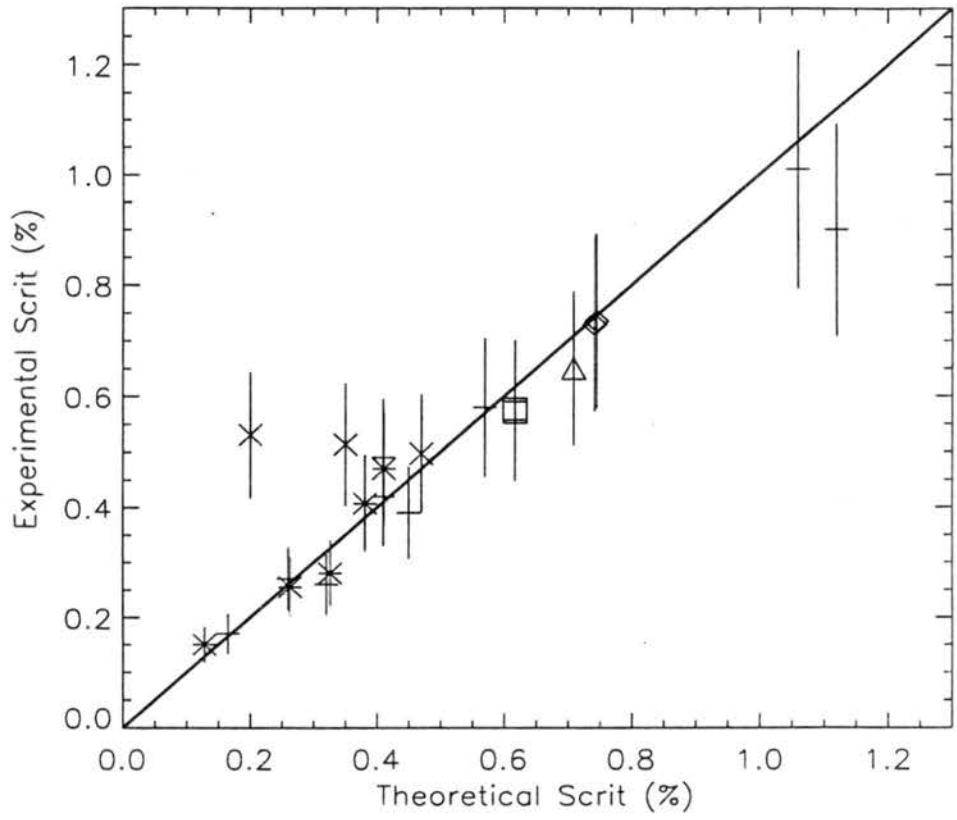

Figure 7.7: Comparison of values of S_{crit} determined from all CCN studies in this work and theoretical values of S_{crit} calculated using the reference Köhler model for the temperature conditions of each CCN study. Solid line is 1:1 line and designates perfect agreement between theory and experiment. Symbols represent: plus for $(NH_4)_2SO_4$, asterisk for NaCl, diamond for NH_4HSO_4, triangle for internally mixed NaCl-$(NH_4)_2SO_4$, square for externally mixed NaCl-$(NH_4)_2SO_4$, and 'X' for ambient samples. Vertical error bars represent the ±21% confidence interval in CCN-derived values of S_{crit}. For ambient samples, the x-axis S_{crit} value is that predicted from hygroscopic growth data and the y-axis S_{crit} value is from CCN counter measurements.

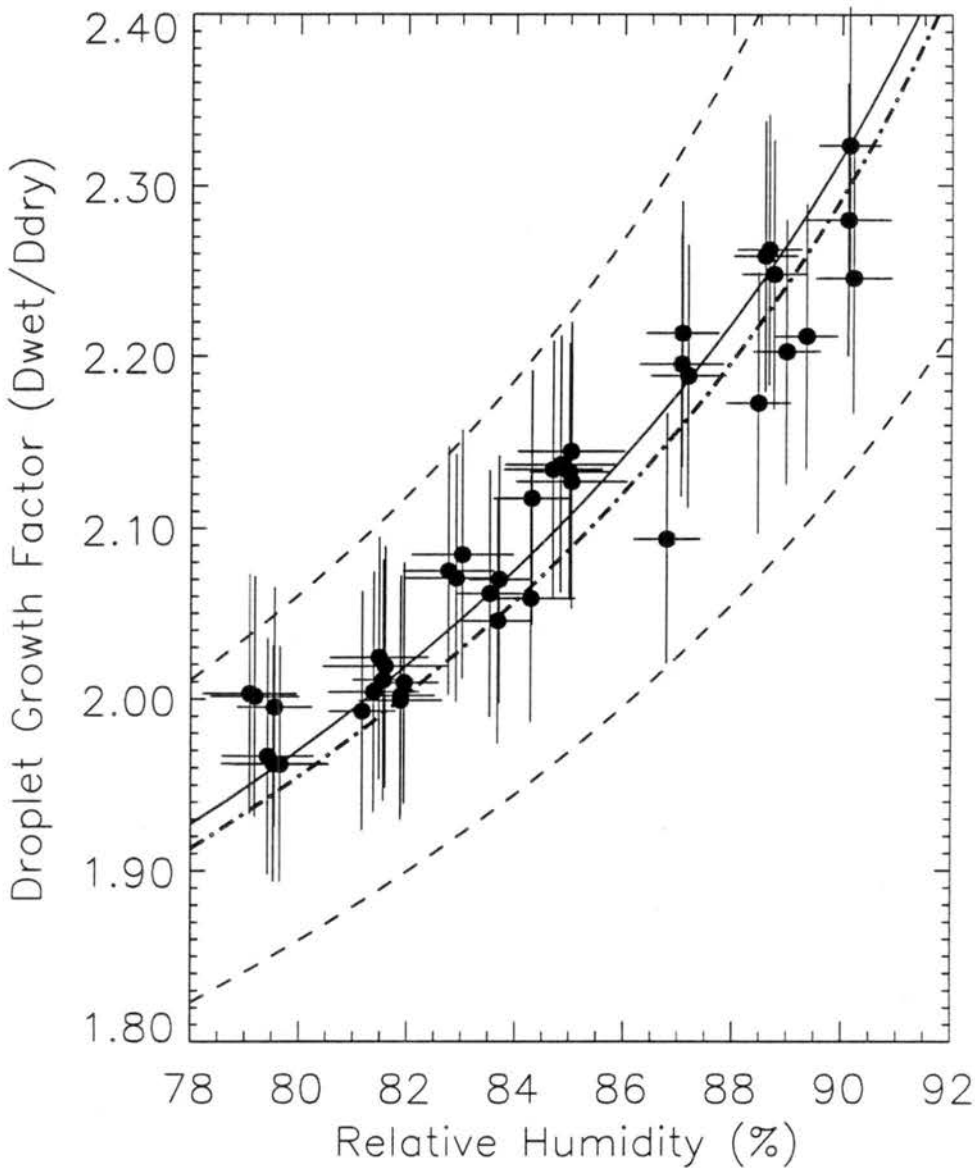

Figure 7.8: Hygroscopic growth study results from all HTDMA experiments conducted on NaCl particles. Solid line designates RH calculated using the reference Köhler model. Thick dashed-dot line represents results from *Tang and Munkelwitz* [1994] for NaCl particles. Dashed lines represent the confidence interval added and substracted from the dashed-dot line. Experimental data are designated by solid dots. Vertical uncertainty bars represent a ±3.5% uncertainty in the observed growth factor. Horizontal uncertainty bars are calculated using the observed standard deviations in the sheath, monodisperse inlet, and monodisperse outlet RH's, and the 0.5% RH uncertainty attributable to the RH sensor calibration procedure.

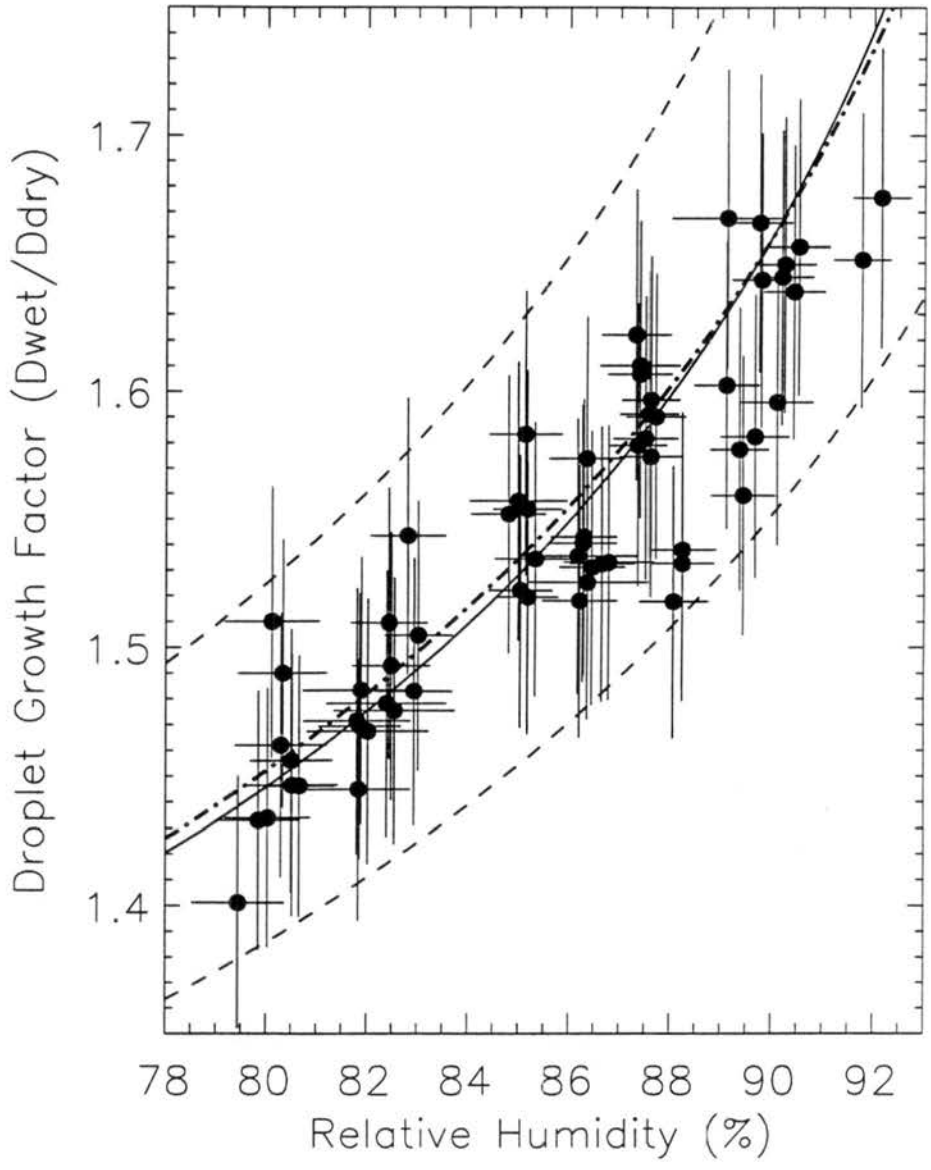

Figure 7.9: Hygroscopic growth study results from all HTDMA experiments conducted on $(NH_4)_2SO_4$ particles. Solid line designates RH calculated using the reference Köhler model. Thick dashed-dot line represents results from *Tang and Munkelwitz* [1994] for $(NH_4)_2SO_4$ particles. Dashed lines represent the confidence interval added and substracted from the dashed-dot line. Experimental data are designated by solid dots. Vertical uncertainty bars represent a $\pm 3.5\%$ uncertainty in the observed growth factor. Horizontal uncertainty bars are calculated using the observed standard deviations in the sheath, monodisperse inlet, and monodisperse outlet RH's, and the 0.5% RH uncertainty attributable to the RH sensor calibration procedure.

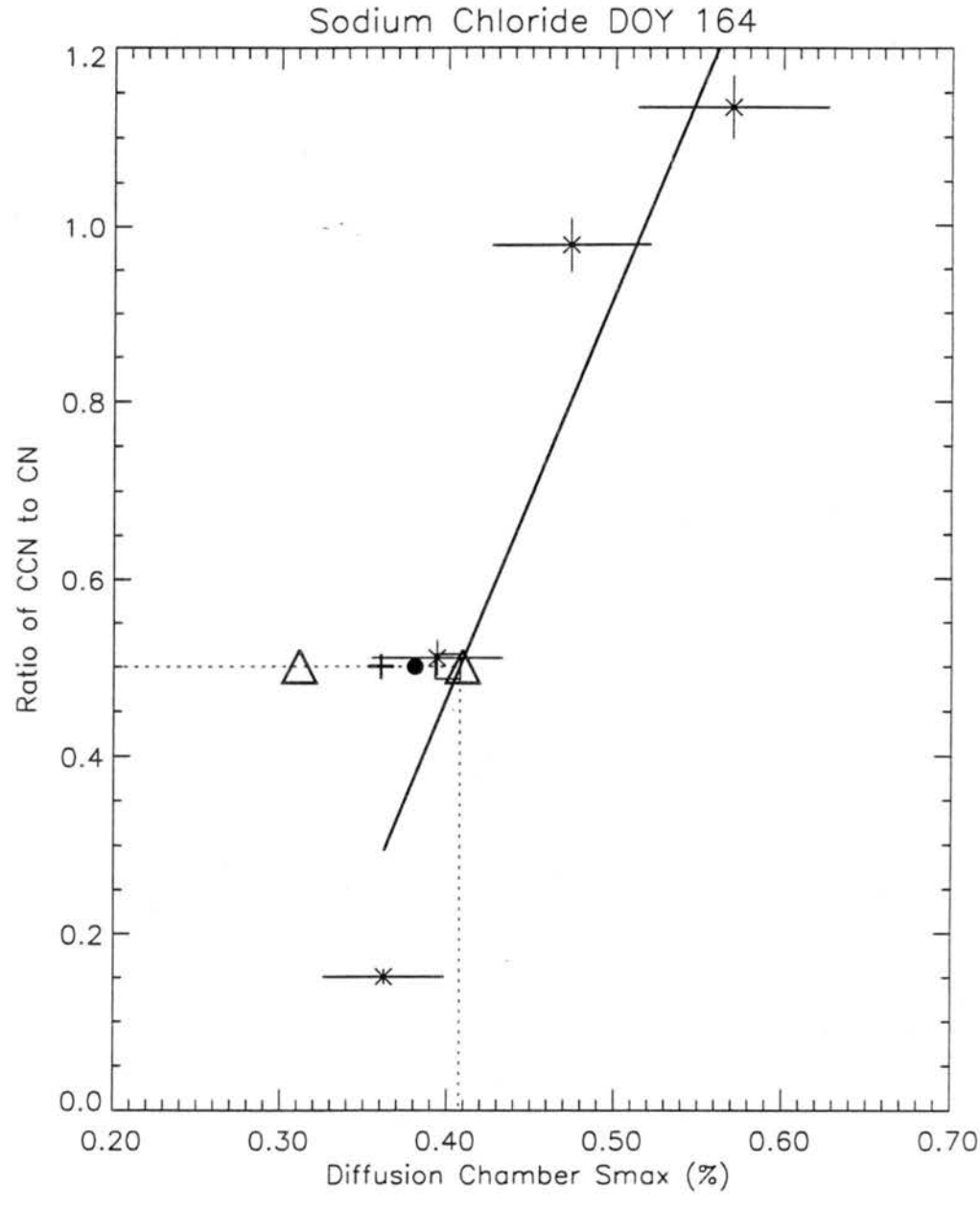

Figure 7.10: CCN validation study results for 46.3 nm diameter NaCl particles on DOY 164. Solid line designates best-fit line to experimental data designated by asterisks. Vertical uncertainty bars represent Poisson counting error in CCN droplet concentration. Horizontal uncertainty bars represent ±10% uncertainty in chamber S_{max}. Triangles designate 1σ range of S_{crit} values predicted by fit routine from HTDMA growth results. The square represents the value of S_{crit} from the fit with all data pairs and no applied error, while the plus symbol represents the average value from the fits with applied error. Dotted lines designate experimentally observed value S_{crit}. Solid dot represents the theoretical value of S_{crit} for a 46.3 nm diameter NaCl particle. The confidence interval for CCN-derived values of S_{crit} is ±21%.

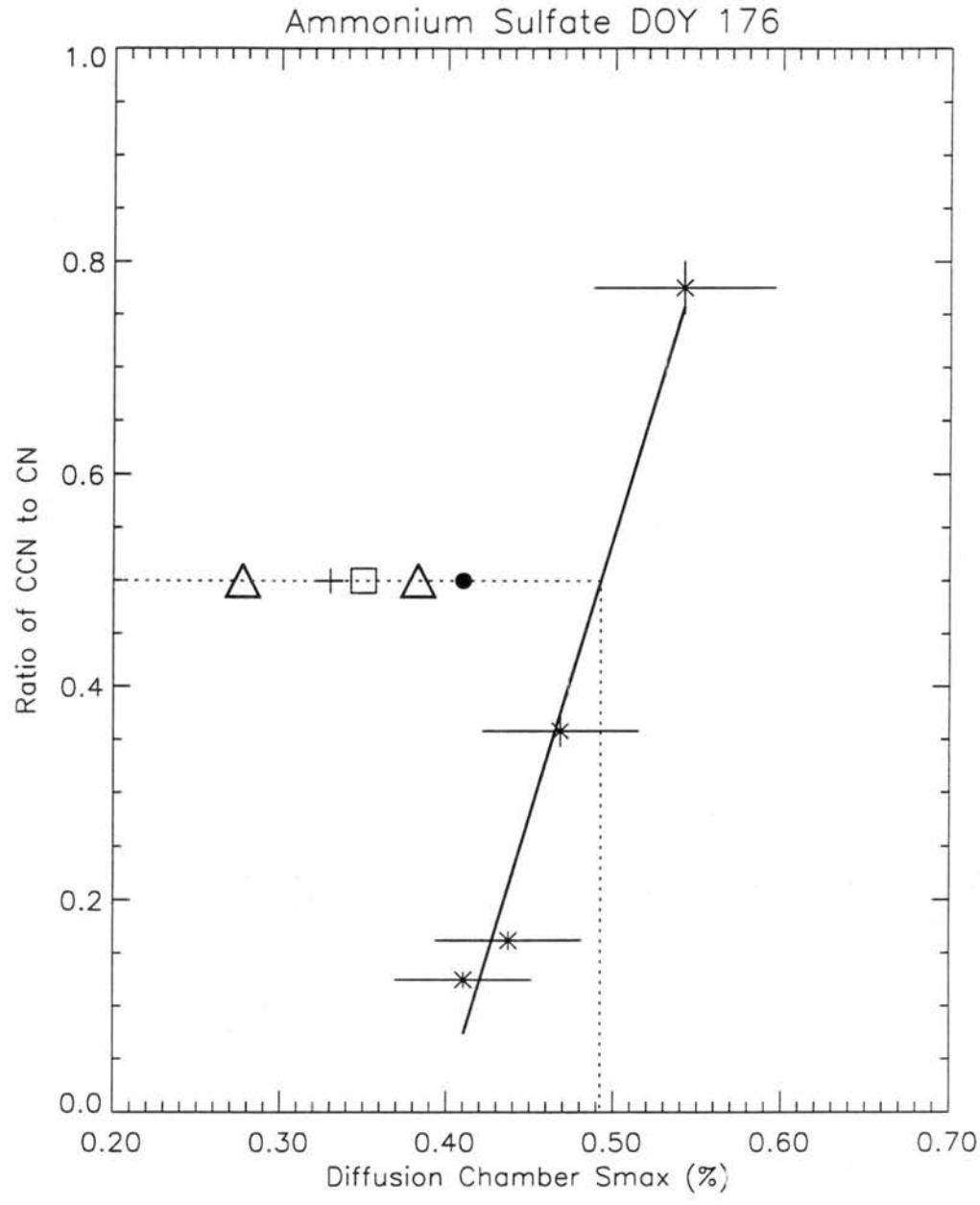

Figure 7.11: CCN validation study results for 57.2 nm diameter $(NH_4)_2SO_4$ particles on DOY 176. Solid line designates best-fit line to experimental data designated by asterisks. Vertical uncertainty bars represent Poisson counting error in CCN droplet concentration. Horizontal uncertainty bars represent $\pm 10\%$ uncertainty in chamber S_{max}. Triangles designatem 1σ range of S_{crit} values predicted by fit routine from HTDMA growth results. The square represents the value of S_{crit} from the fit with all data pairs and no applied error, while the plus symbol represents the average value from the fits with applied error. Dotted lines designate experimentally observed value S_{crit}. Solid dot represents the theoretical value of S_{crit} for a 57.2 nm diameter $(NH_4)_2SO_4$ particle. The confidence interval for CCN-derived values of S_{crit} is $\pm 21\%$.

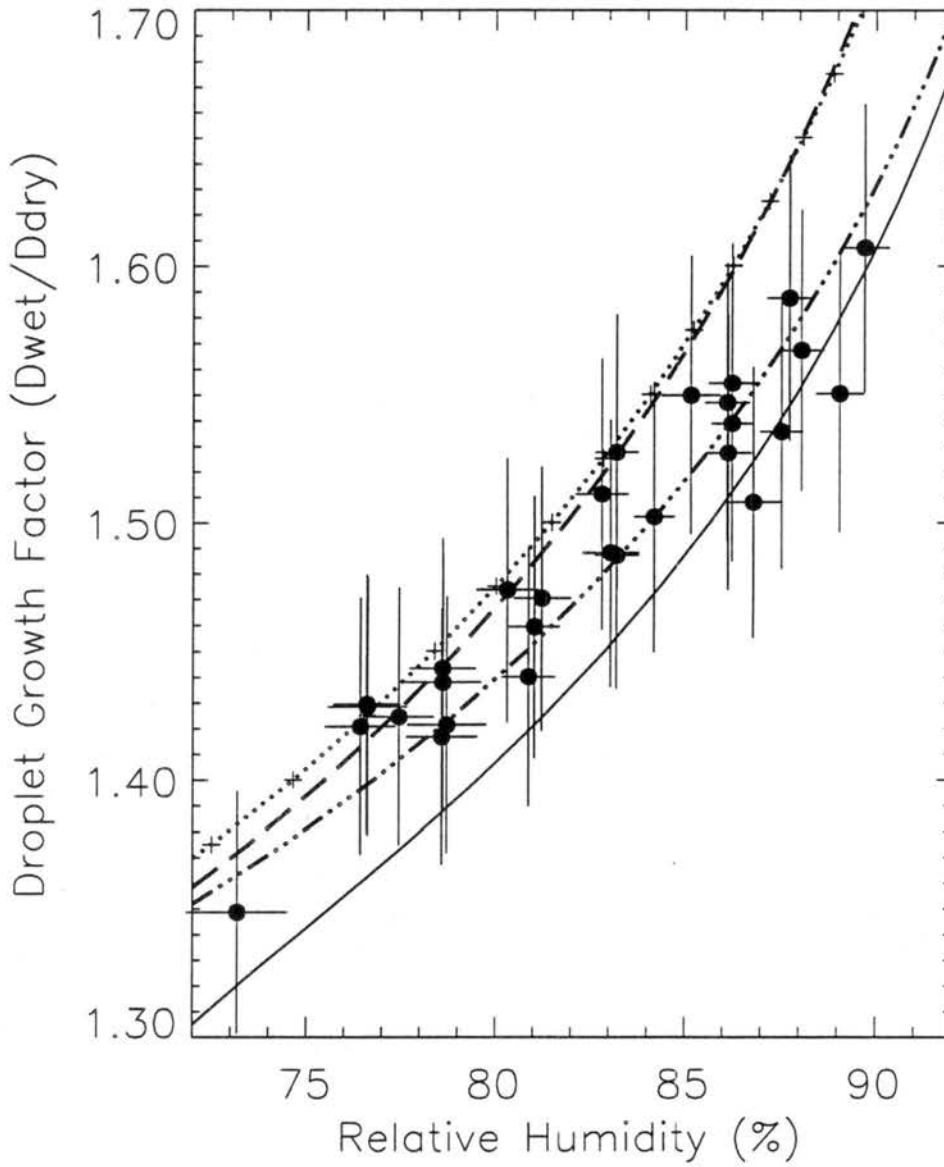

Figure 7.12: Hygroscopic growth study results from all HTDMA experiments conducted on NH_4HSO_4 particles. Solid line designates RH calculated using the reference Köhler model for $(NH_4)_3H(SO_4)_2$. Thick dashed, dashed-three-dots, and dotted with plus symbol lines represent results from *Tang and Munkelwitz* [1994] for NH_4HSO_4, $(NH_4)_2SO_4$, and $(NH_4)_3H(SO_4)_2$, respectively. Experimental data are designated by solid dots. Vertical uncertainty bars represent a $\pm 3.5\%$ uncertainty in the observed growth factor. Horizontal uncertainty bars are calculated using the observed standard deviations in the sheath, monodisperse inlet, and monodisperse outlet RH's, and the 0.5% RH uncertainty attributable to the RH sensor calibration procedure.

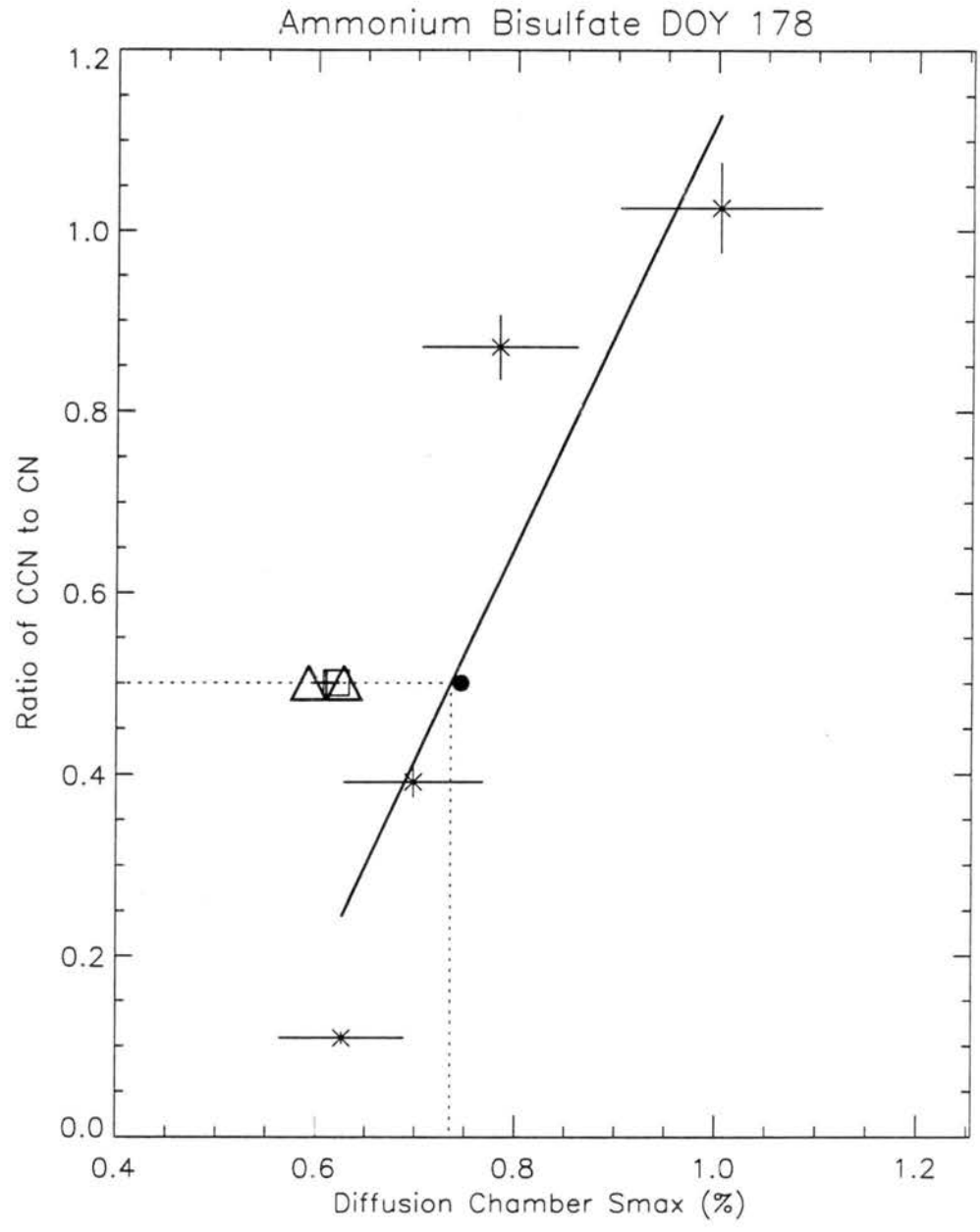

Figure 7.13: CCN validation study results for 40 nm diameter NH_4HSO_4 particles on DOY 178. Solid line designates best-fit line to experimental data designated by asterisks. Vertical uncertainty bars represent Poisson counting error in CCN droplet concentration. Horizontal uncertainty bars represent ±10% uncertainty in chamber S_{max}. Triangles designate 1σ range of S_{crit} values predicted by fit routine from HTDMA growth results. The square represents the value of S_{crit} from the fit with all data pairs and no applied error, while the plus symbol represents the average value from the fits with applied error. Dotted lines designate experimentally observed value S_{crit}. Solid dot represents the theoretical value of S_{crit} for a 40 nm diameter NH_4HSO_4 particle. The confidence interval for CCN-derived values of S_{crit} is ±21%.

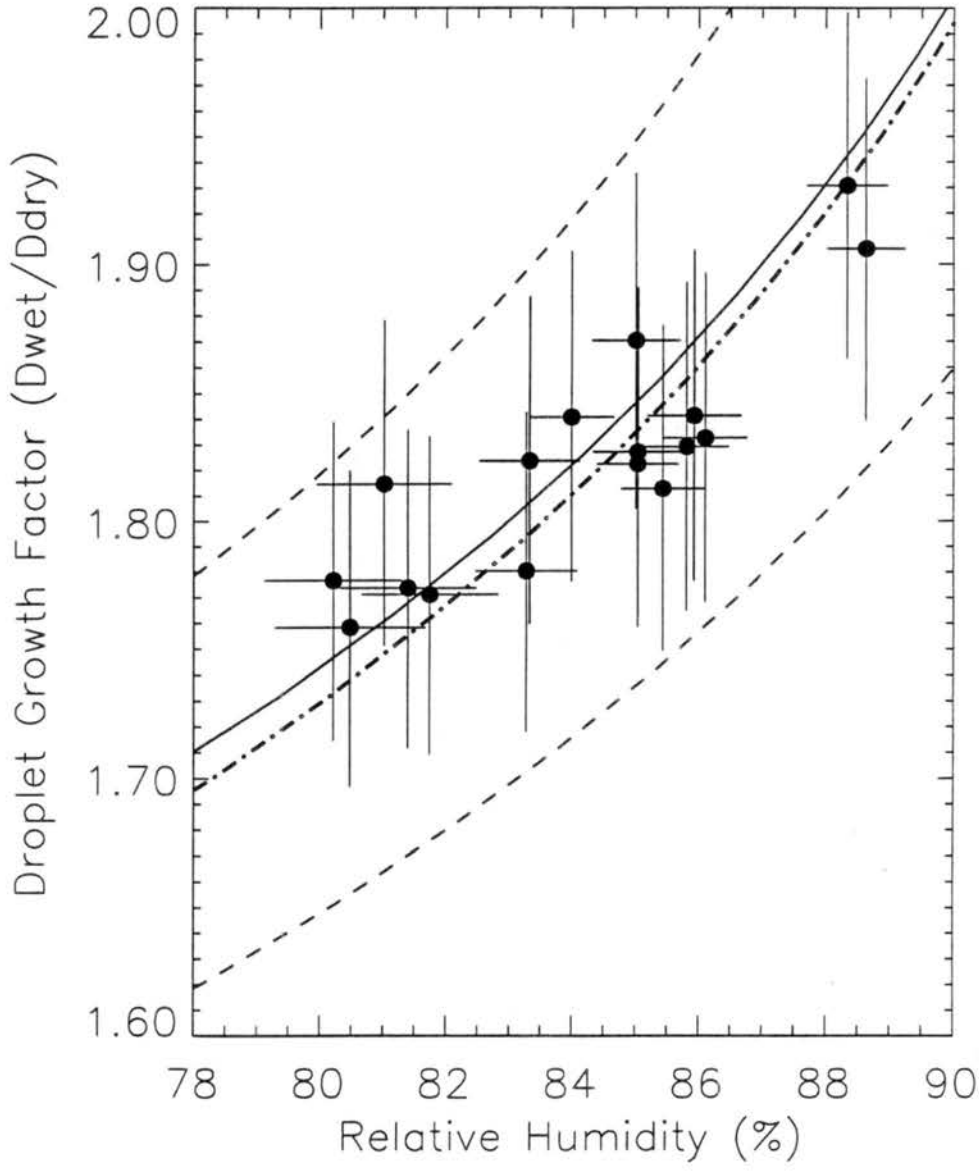

Figure 7.14: Hygroscopic growth study results from all HTDMA experiments conducted on internally mixed 32 nm diameter equimolar $(NH_4)_2SO_4$ -NaCl particles. Solid line designates RH calculated using the reference Köhler model. Thick dash-dot line represents results from ZSR relation using Tang's measurements of the variation of water activity with solution molality for $(NH_4)_2SO_4$ and NaCl particles. Dashed lines represent the confidence interval added and substracted from the dashed-dot line. Experimental data are designated by solid dots. Vertical uncertainty bars represent a $\pm 3.5\%$ uncertainty in the observed growth factor. Horizontal uncertainty bars are calculated using the observed standard deviations in the sheath, monodisperse inlet, and monodisperse outlet RH's, and the 0.5% RH uncertainty attributable to the RH sensor calibration procedure.

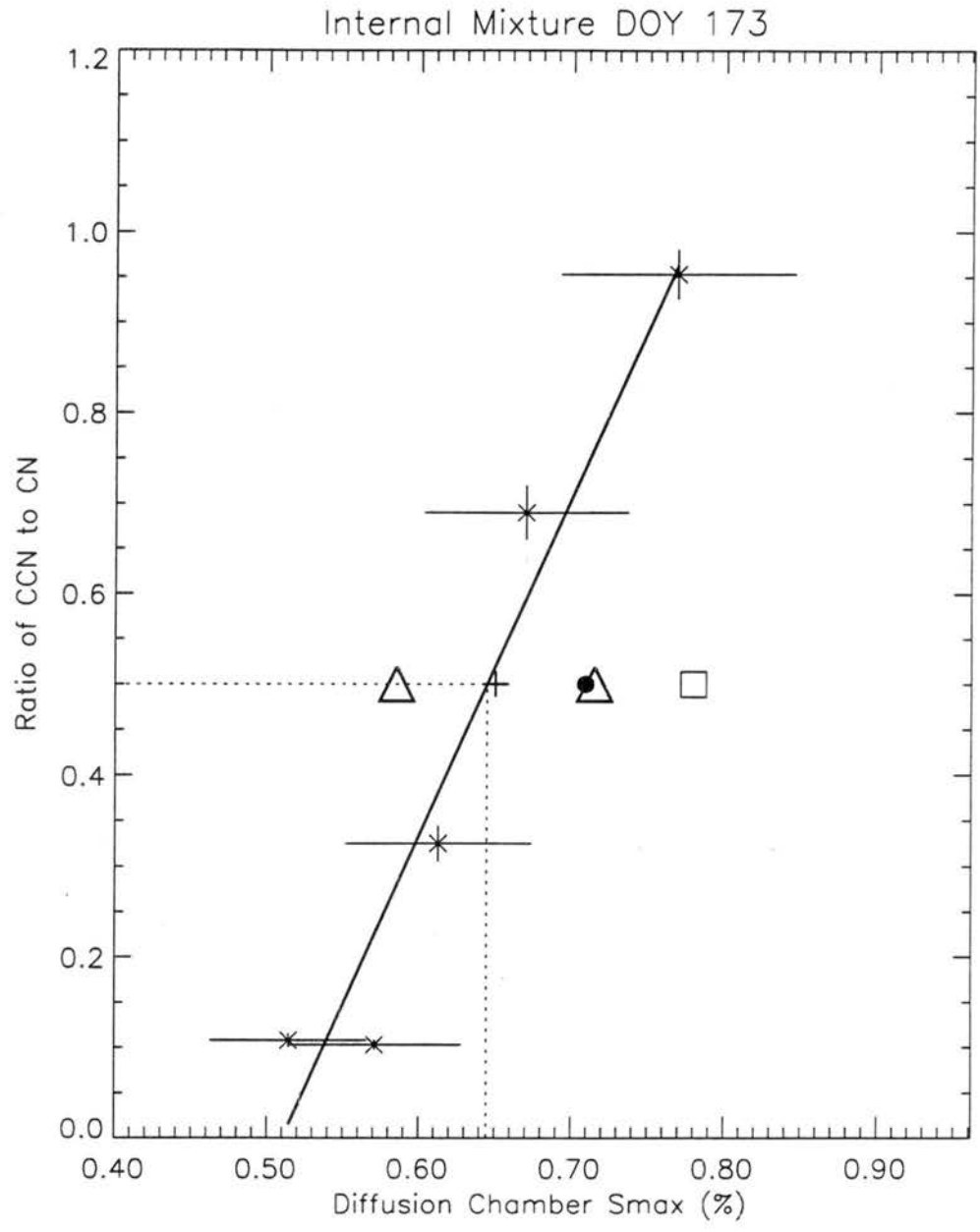

Figure 7.15: CCN study results for internally mixed 32 nm diameter $(NH_4)_2SO_4$ - NaCl particles on DOY 173. Solid line designates best-fit line to experimental data designated by asterisks. Vertical uncertainty bars represent Poisson counting error in CCN droplet concentration. Horizontal uncertainty bars represent ±10% uncertainty in chamber S_{max}. Triangles designate 1σ range of S_{crit} values predicted by fit routine from HTDMA growth results. The square represents the value of S_{crit} from the fit with all data pairs and no applied error, while the plus symbol represents the average value from the fits with applied error. Dotted lines designate experimentally observed value S_{crit}. Solid dot represents the theoretical value of S_{crit}. The confidence interval for CCN-derived values of S_{crit} is ±21%.

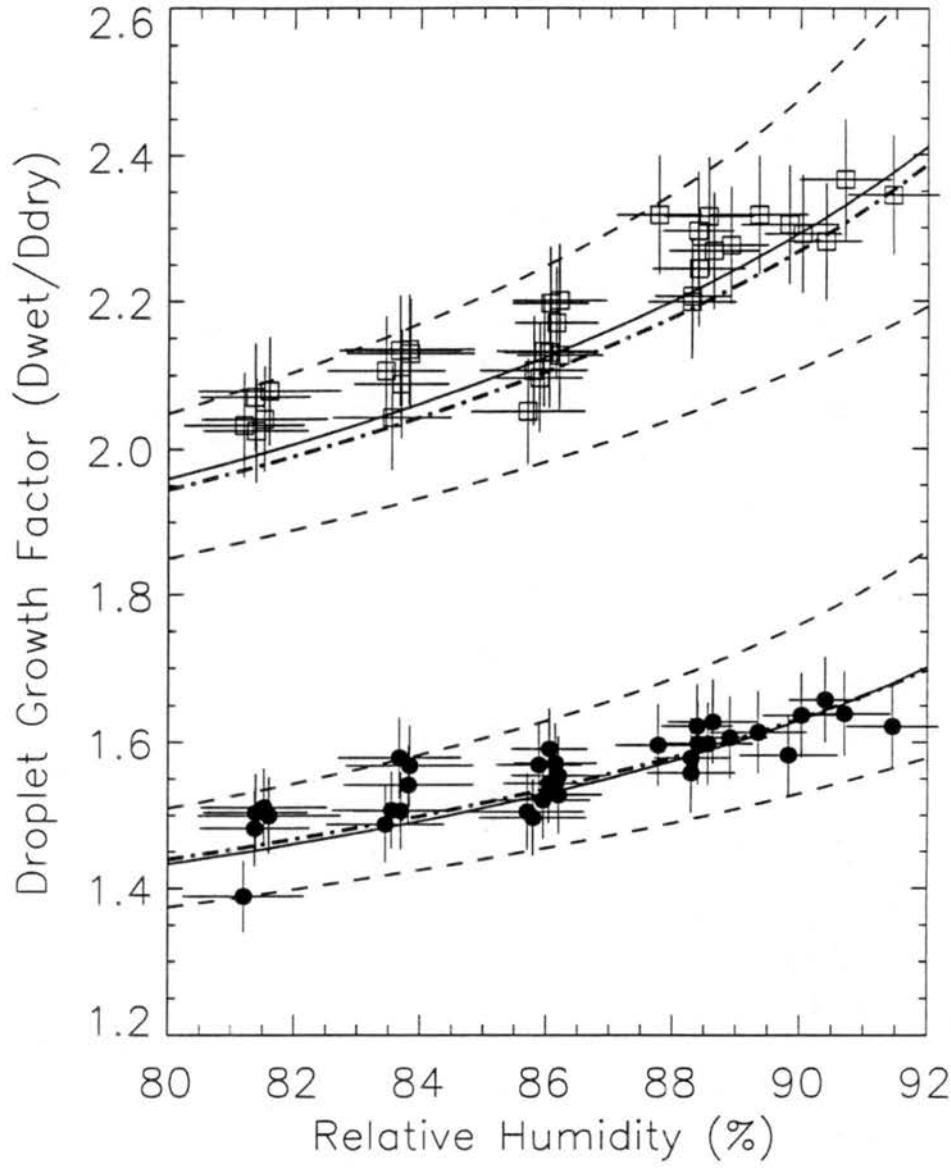

Figure 7.16: Hygroscopic growth study results from all HTDMA experiments conducted on externally mixed $(NH_4)_2SO_4$ (dot) and NaCl (square) particles. Solid line designates RH calculated using the reference Köhler model. Thick dashed-dot line represents results from *Tang and Munkelwitz* [1994] for NaCl and $(NH_4)_2SO_4$ particles. Dashed lines represent the confidence interval added and subtracted from the dashed-dot line. Experimental data are designated by solid dots. Vertical uncertainty bars represent a $\pm 3.5\%$ uncertainty in the observed growth factor. Horizontal uncertainty bars are calculated using the observed standard deviations in the sheath, monodisperse inlet, and monodisperse outlet RH's, and the 0.5% RH uncertainty attributable to the RH sensor calibration procedure.

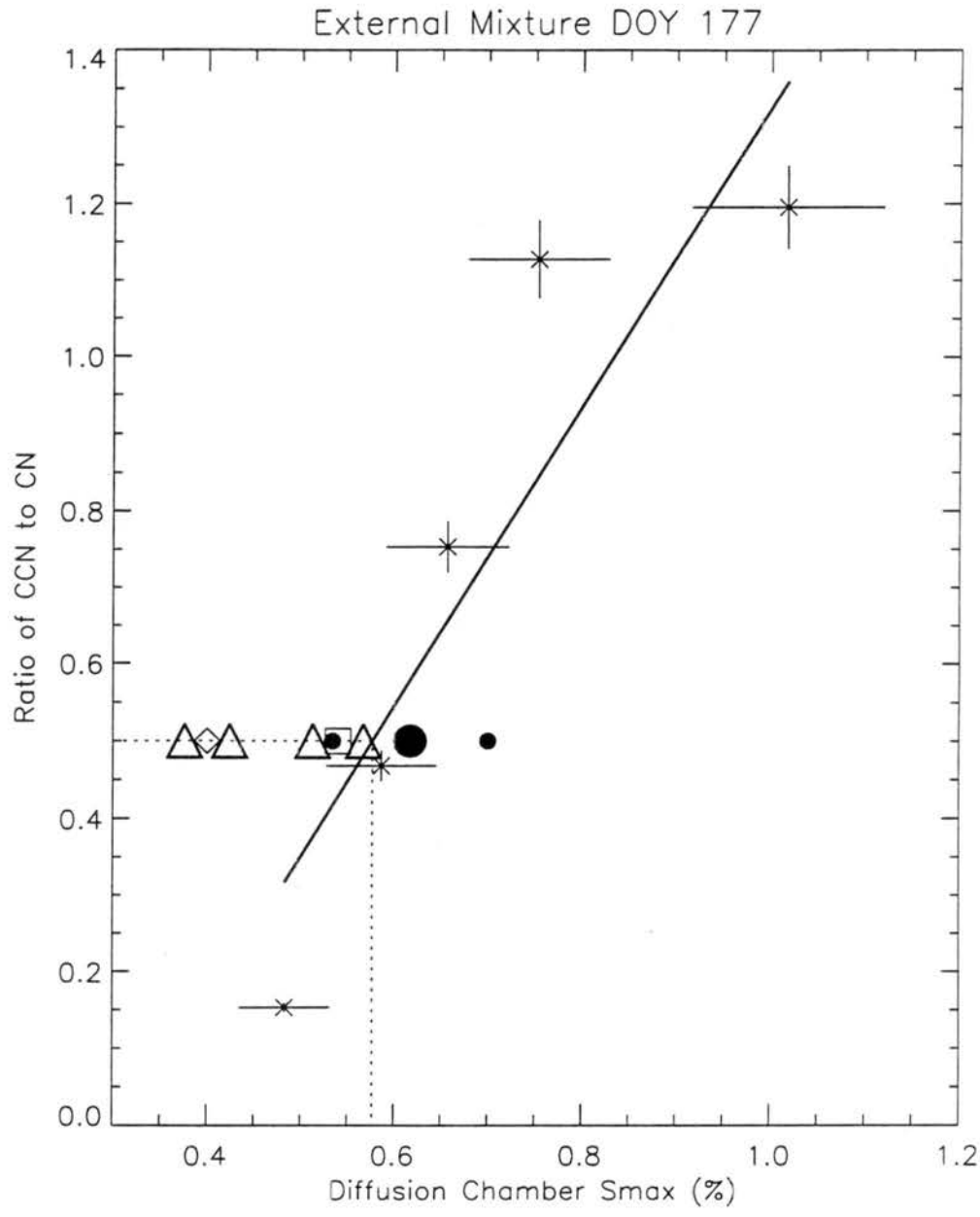

Figure 7.17: CCN study results for externally mixed 40 nm diameter $(NH_4)_2SO_4$ and 37 nm diameter NaCl particles on DOY 177. Solid line designates best-fit line to experimental data designated by asterisks. Vertical uncertainty bars represent Poisson counting error in CCN droplet concentration. Horizontal uncertainty bars represent $\pm 10\%$ uncertainty in chamber S_{max}. Triangles designate 1σ range of S_{crit} values predicted by fit routine from HTDMA growth results. Dotted lines designate experimentally observed value S_{crit}. The larger solid dot represents the average of the theoretical values of S_{crit} for the two dry particle types (designated by the smaller solid dots). Open diamond designates the value of S_{crit} predicted by the fit routine for sampled NaCl particles. Open square designates the value of S_{crit} predicted by the fit routine for sampled $(NH_4)_2SO_4$ particles. The confidence interval for CCN-derived values of S_{crit} is $\pm 21\%$.

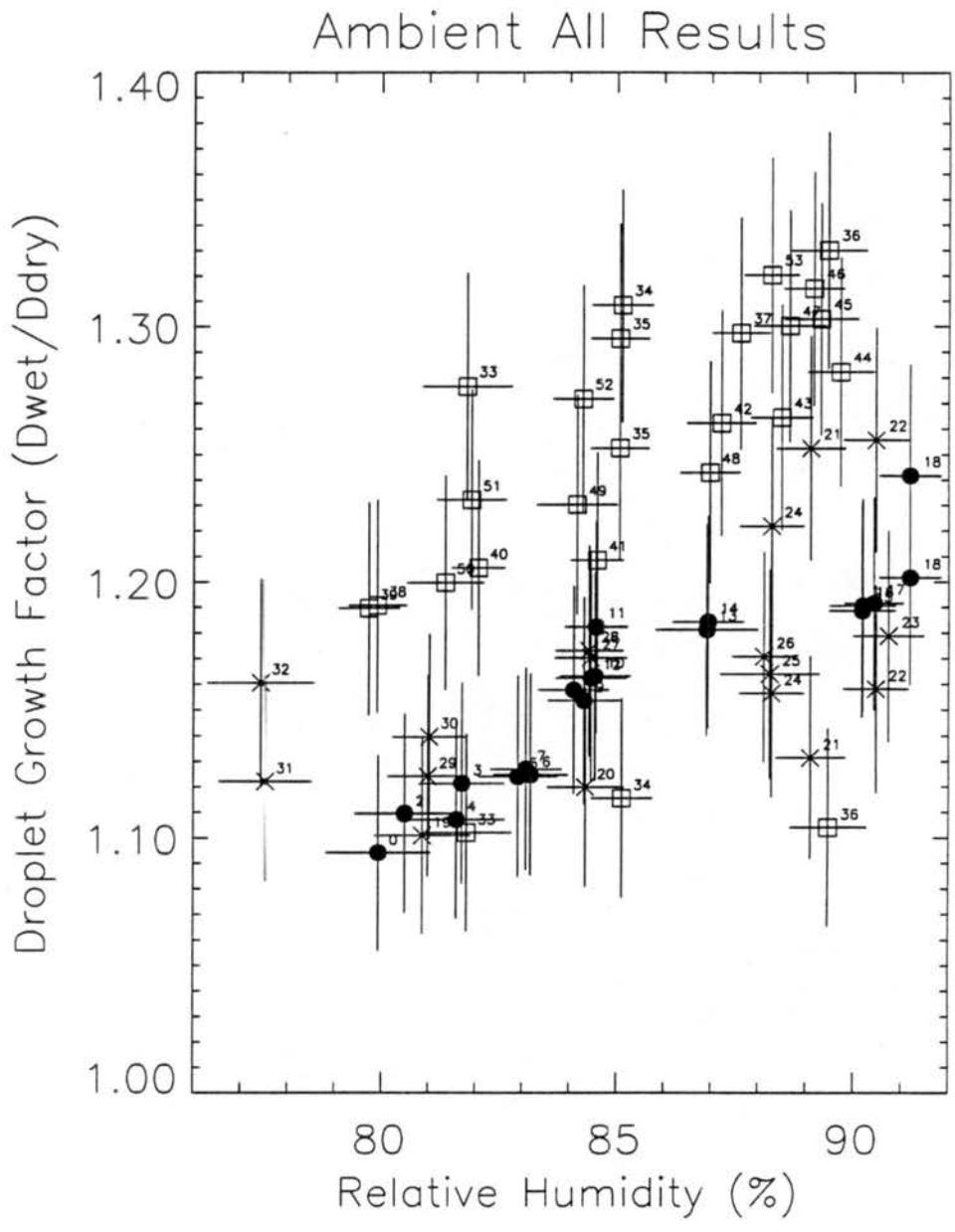

Figure 7.18: Hygroscopic growth study results from all HTDMA experiments conducted on ambient particles. Experimental data are designated by solid dots. Vertical uncertainty bars represent a ±3.5% uncertainty in the observed growth factor. Horizontal uncertainty bars are calculated using the observed standard deviations in the sheath, monodisperse inlet, and monodisperse outlet RH's, and the 0.5% RH uncertainty attributable to the RH sensor calibration procedure. Results from DOY 182 designated by squares, results from DOY 174 by designated solid dots, and DOY 175 results are shown as asterisks.

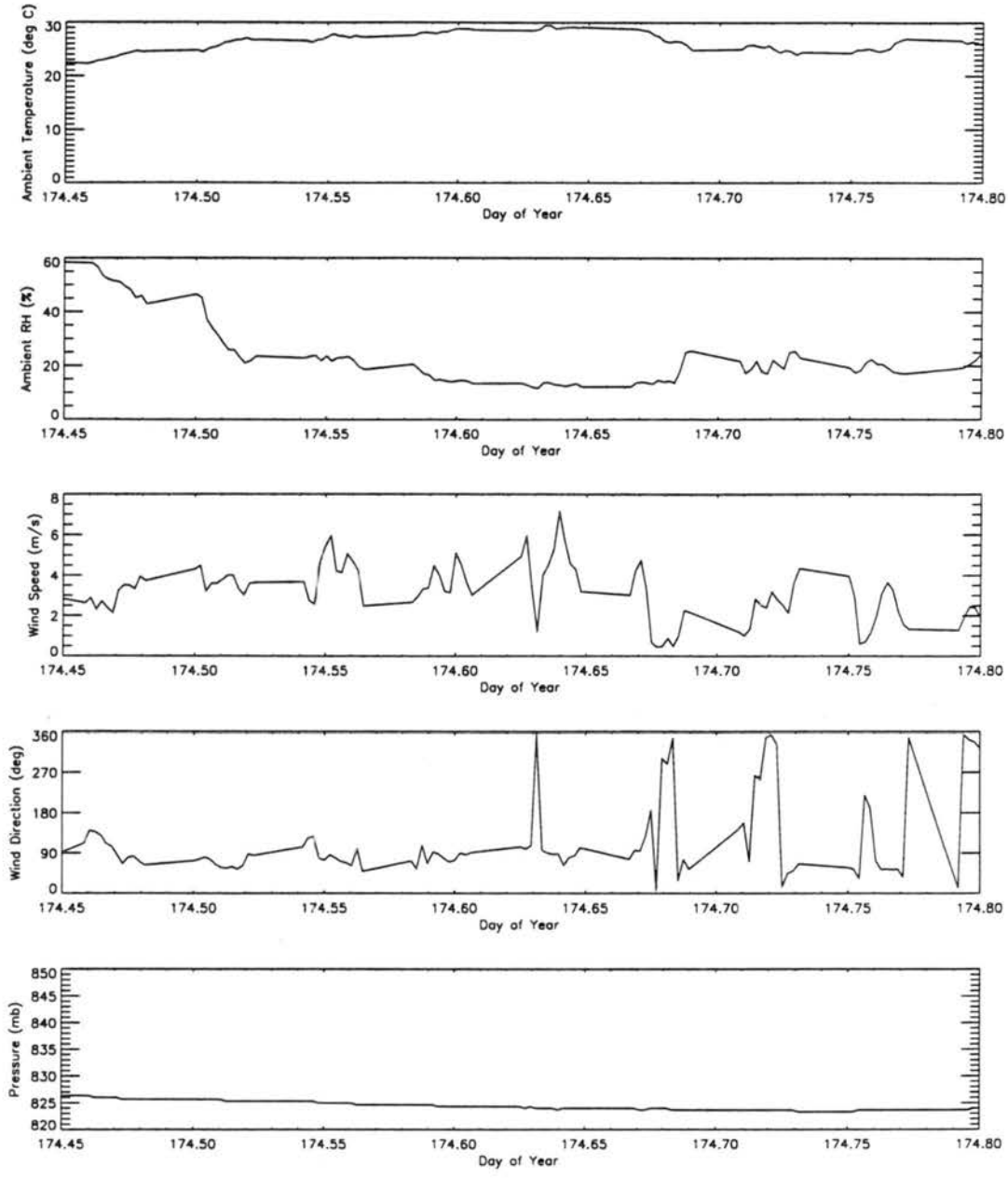

Figure 7.19: Ambient temperature (°C), relative humidity (%), wind speed (m s^{-1}), wind direction (degrees from North), and pressure (mb) during the HTDMA study on DOY 174 on 85 nm diameter ambient particles.

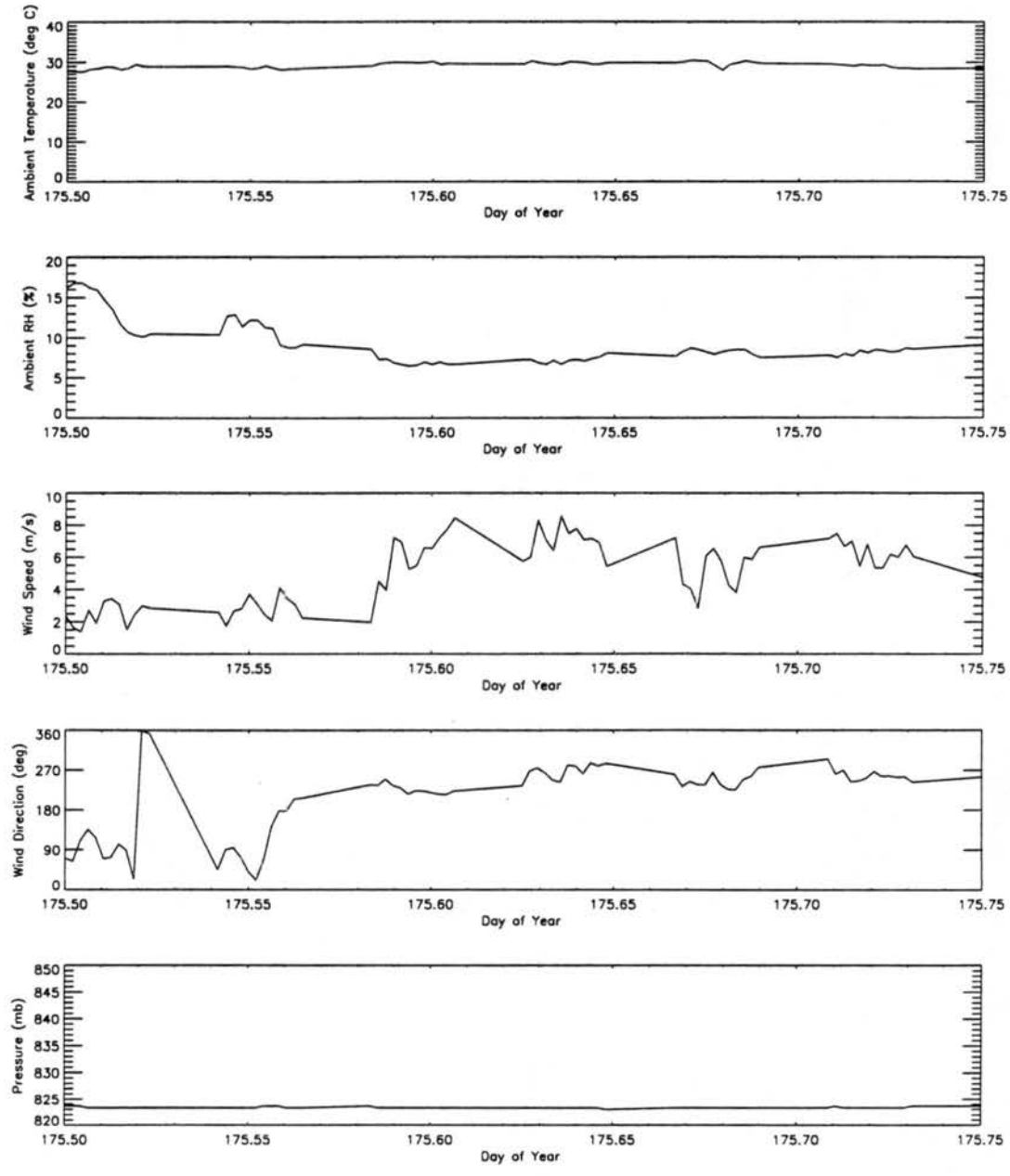

Figure 7.20: Ambient temperature (°C), relative humidity (%), wind speed (m s^{-1}), wind direction (degrees from North), and pressure (mb) during the HTDMA study on DOY 175 on 68 nm diameter ambient particles.

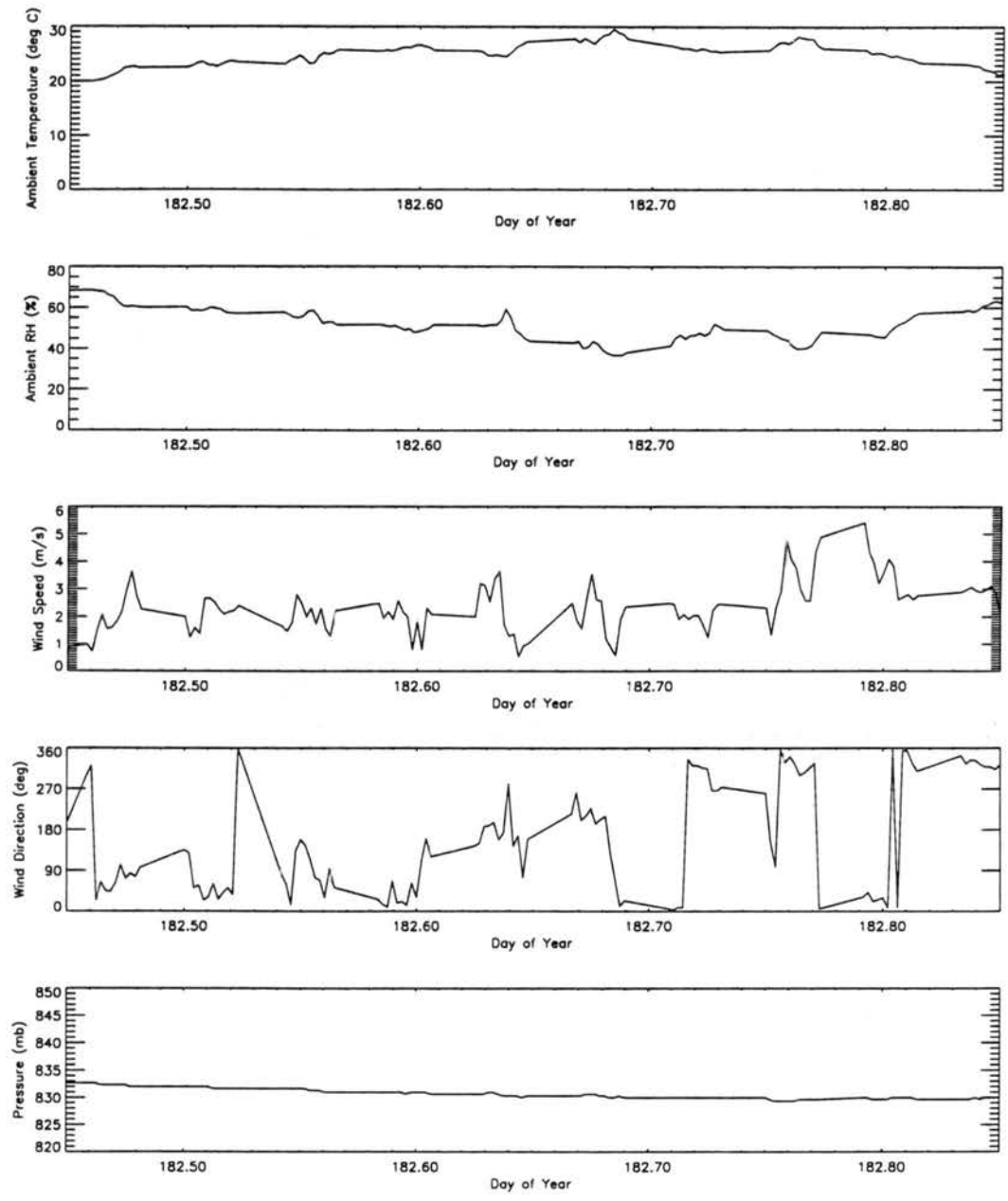

Figure 7.21: Ambient temperature (°C), relative humidity (%), wind speed (m s^{-1}), wind direction (degrees from North), and pressure (mb) during the HTDMA study on DOY 182 on 120 nm diameter ambient particles.

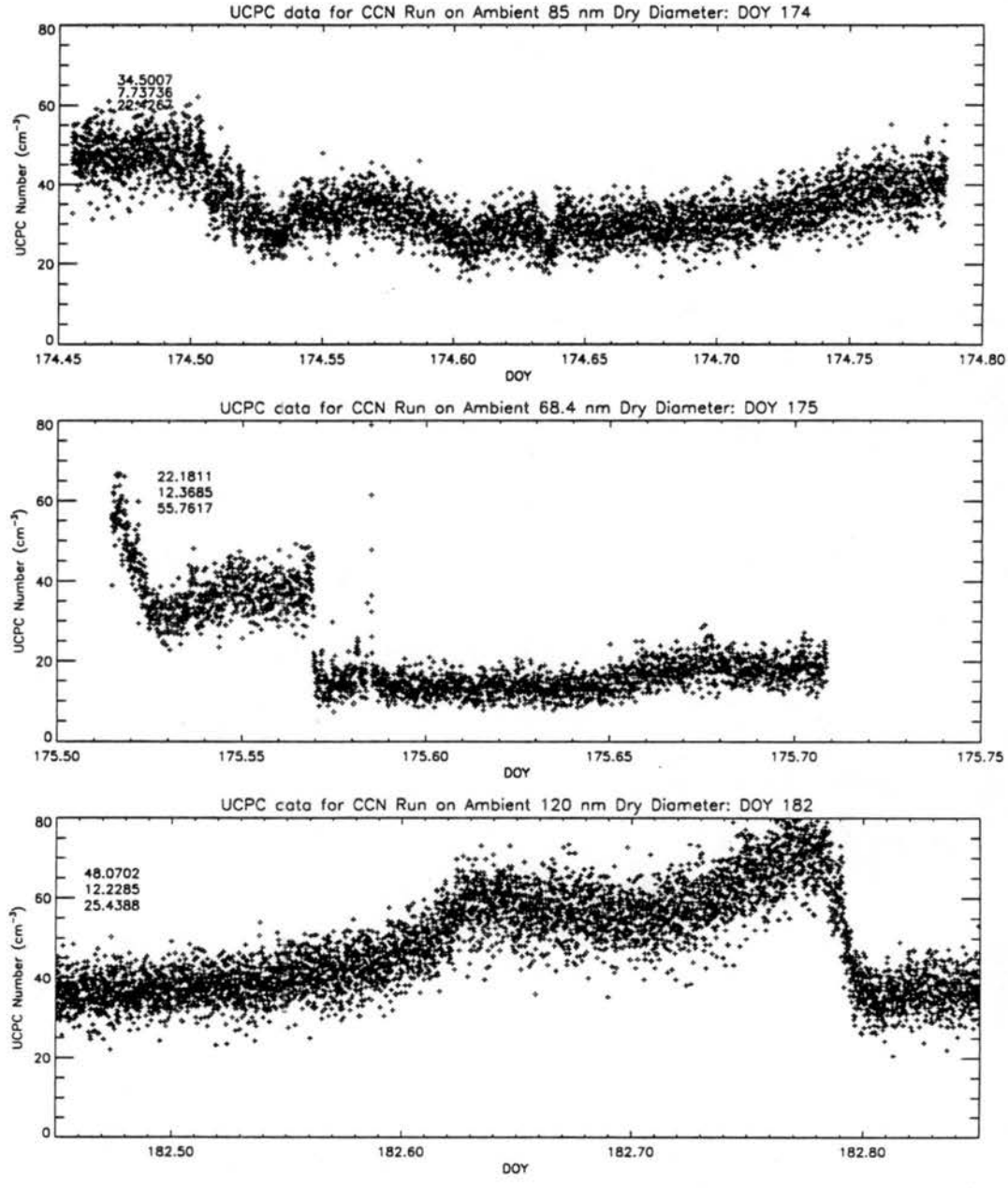

Figure 7.22: UCPC monodisperse number concentrations during all studies on ambient particles. Average number concentration, standard deviation, and coefficient of variation (%) are arranged in a column from top to bottom in each plot.

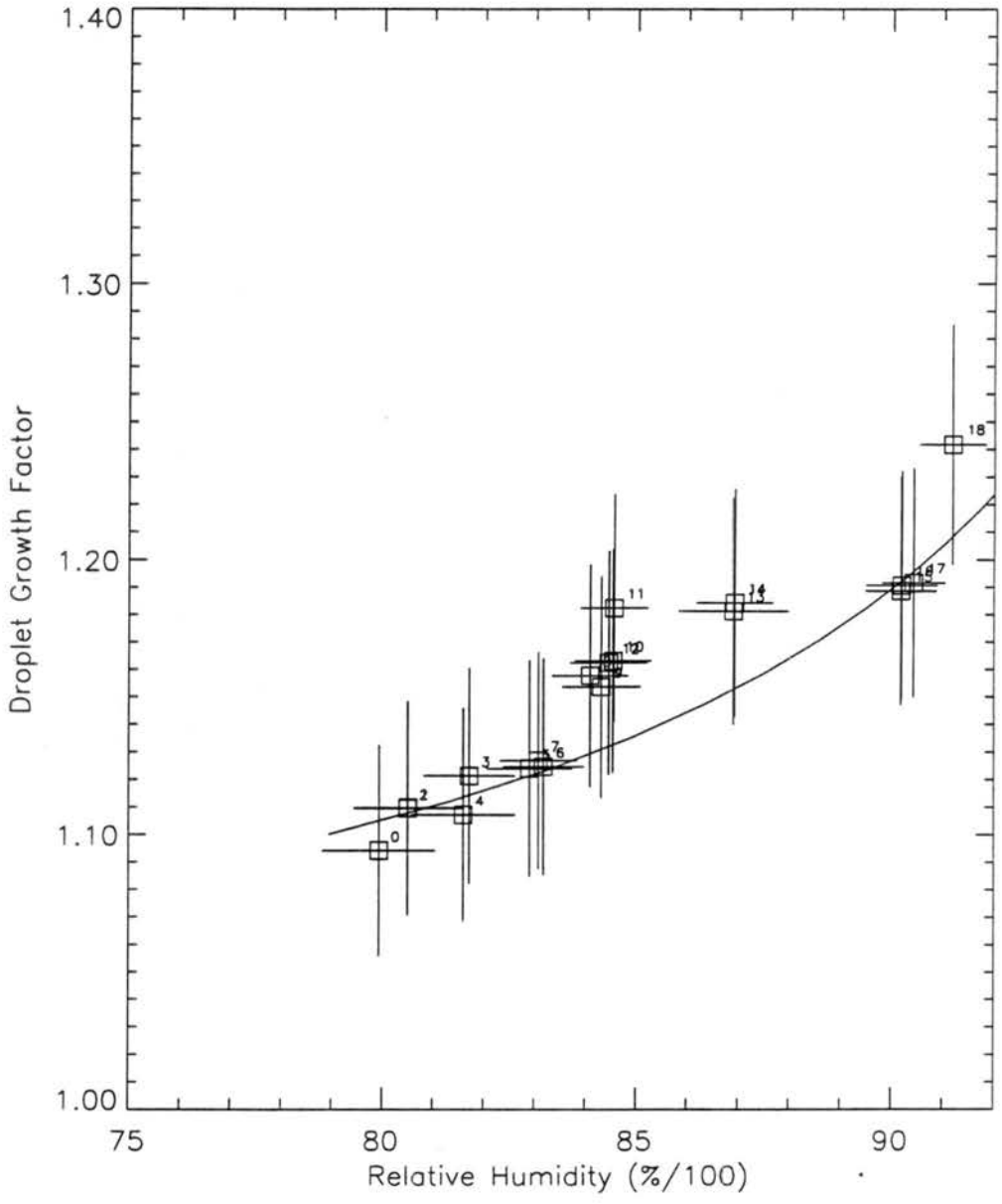

Figure 7.23: (a) Observed and calculated growth for a hypothetical internally mixed $(NH_4)_2SO_4$, NH_4NO_3, and insoluble material composition for ambient study on DOY 174.

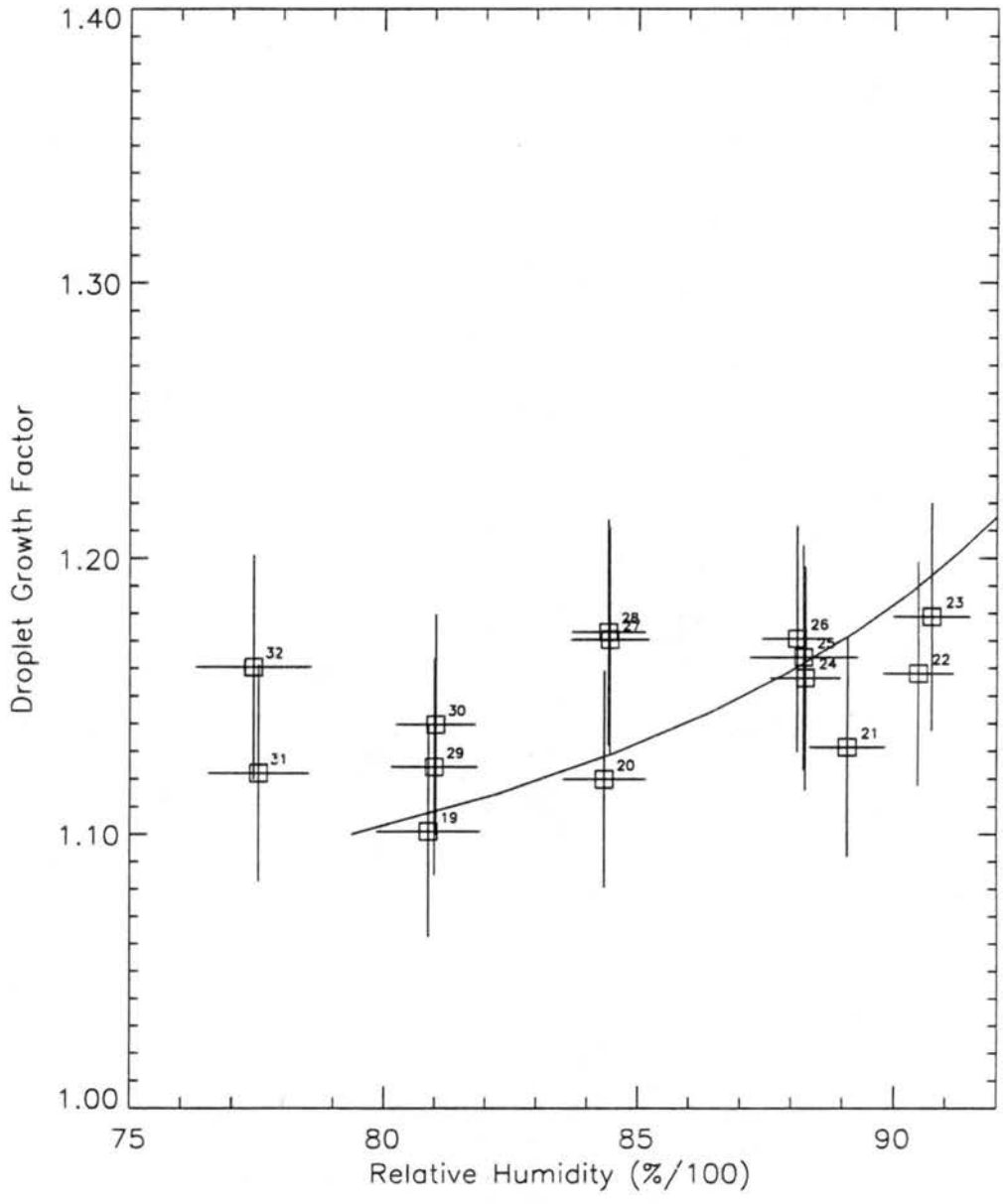

Figure 7.23: (b) Observed and calculated growth for a hypothetical internally mixed $(NH_4)_2SO_4$, NH_4NO_3, and insoluble material composition for ambient study on DOY 175.

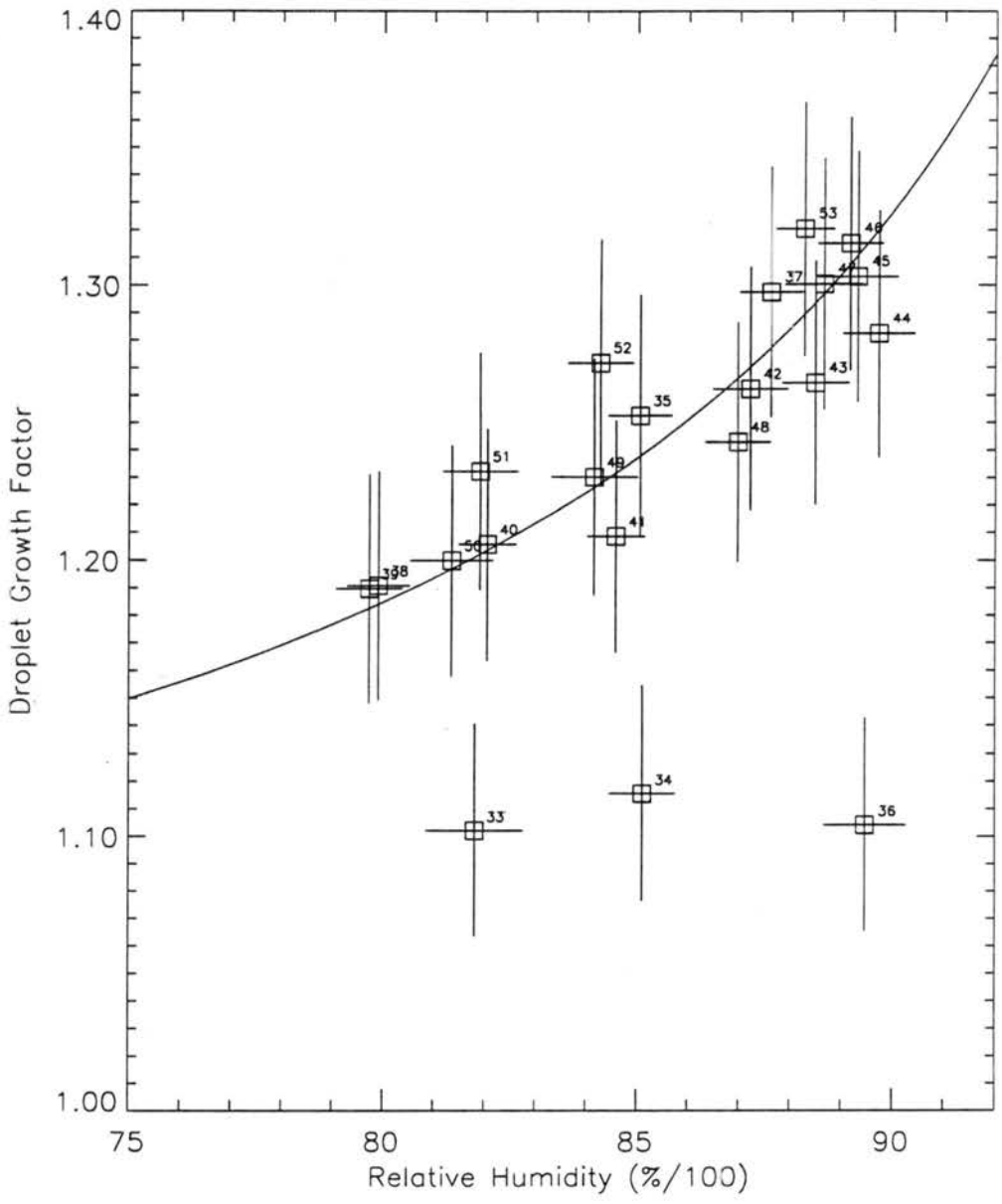

Figure 7.23: (c) Observed and calculated growth for a hypothetical internally mixed $(NH_4)_2SO_4$, NH_4NO_3, and insoluble material composition for ambient study on DOY 182.

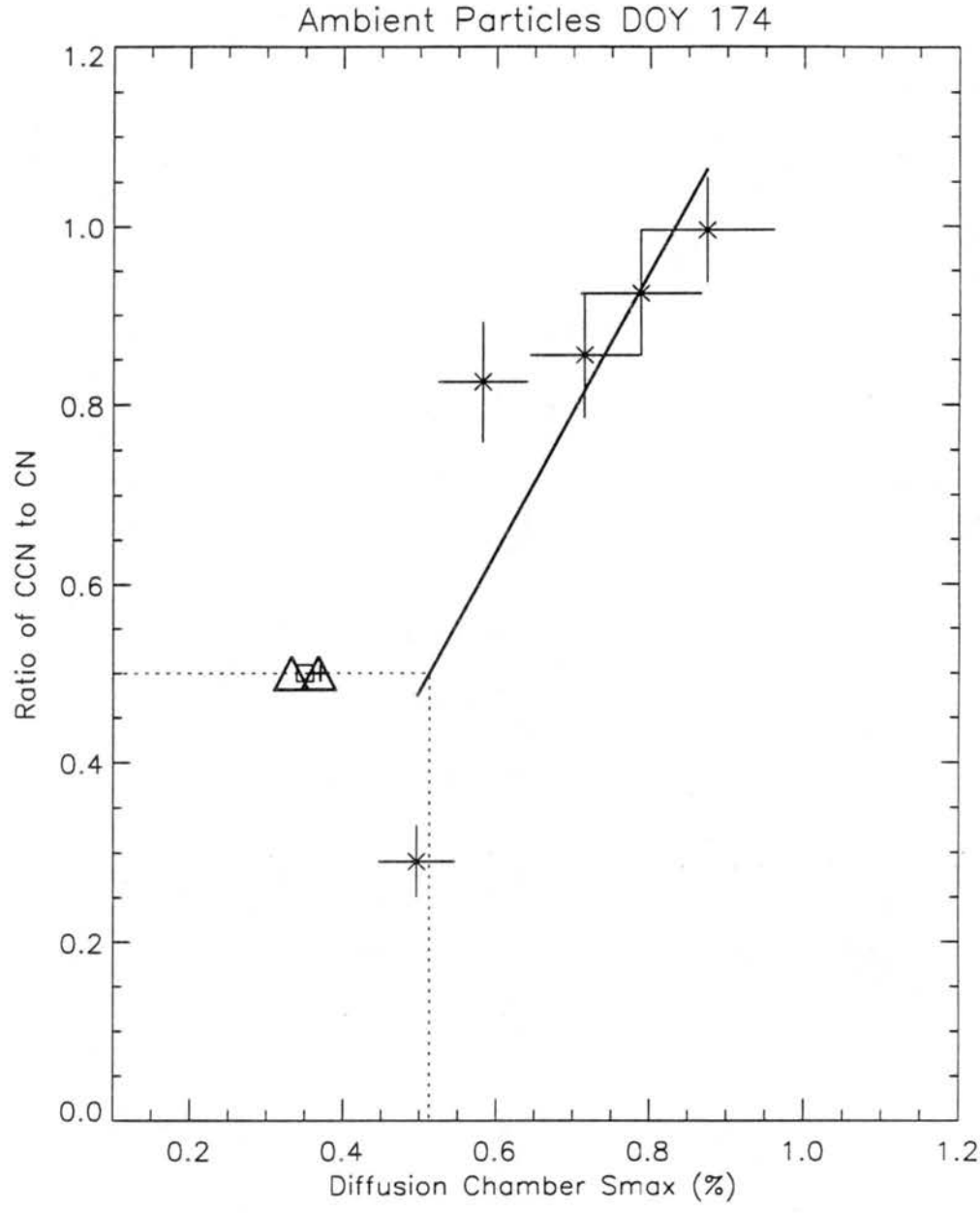

Figure 7.24: CCN study results for 85 nm diameter ambient particles on DOY 174. Solid line designates best-fit line to experimental data designated by asterisks. Vertical uncertainty bars represent Poisson counting error in CCN droplet concentration. Horizontal uncertainty bars represent $\pm 10\%$ uncertainty in chamber S_{max}. Triangles designate 1σ range of S_{crit} values predicted by fit routine from HTDMA growth results. The square represents the value of S_{crit} from the fit with all data pairs and no applied error, while the plus symbol represents the average value from the fits with applied error. Dotted lines designate experimentally observed value S_{crit}. The confidence interval for CCN-derived values of S_{crit} is $\pm 21\%$.

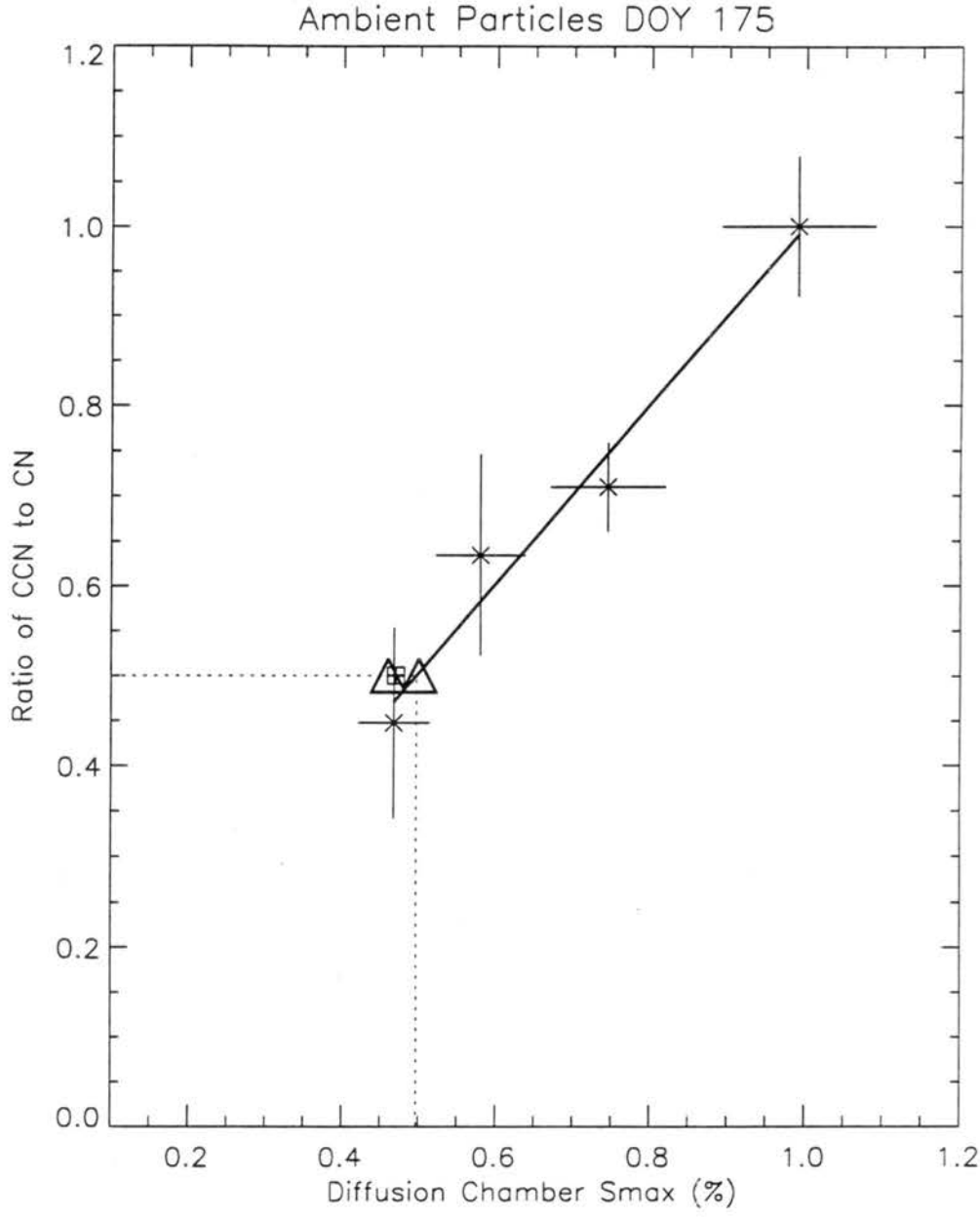

Figure 7.25: CCN study results for 68.4 nm diameter ambient particles on DOY 175. Solid line designates best-fit line to experimental data designated by asterisks. Vertical uncertainty bars represent Poisson counting error in CCN droplet concentration. Horizontal uncertainty bars represent $\pm 10\%$ uncertainty in chamber S_{max}. Triangles designate 1σ range of S_{crit} values predicted by fit routine from HTDMA growth results. The square represents the value of S_{crit} from the fit with all data pairs and no applied error, while the plus symbol represents the average value from the fits with applied error. Dotted lines designate experimentally observed value S_{crit}. The confidence interval for CCN-derived values of S_{crit} is $\pm 21\%$.

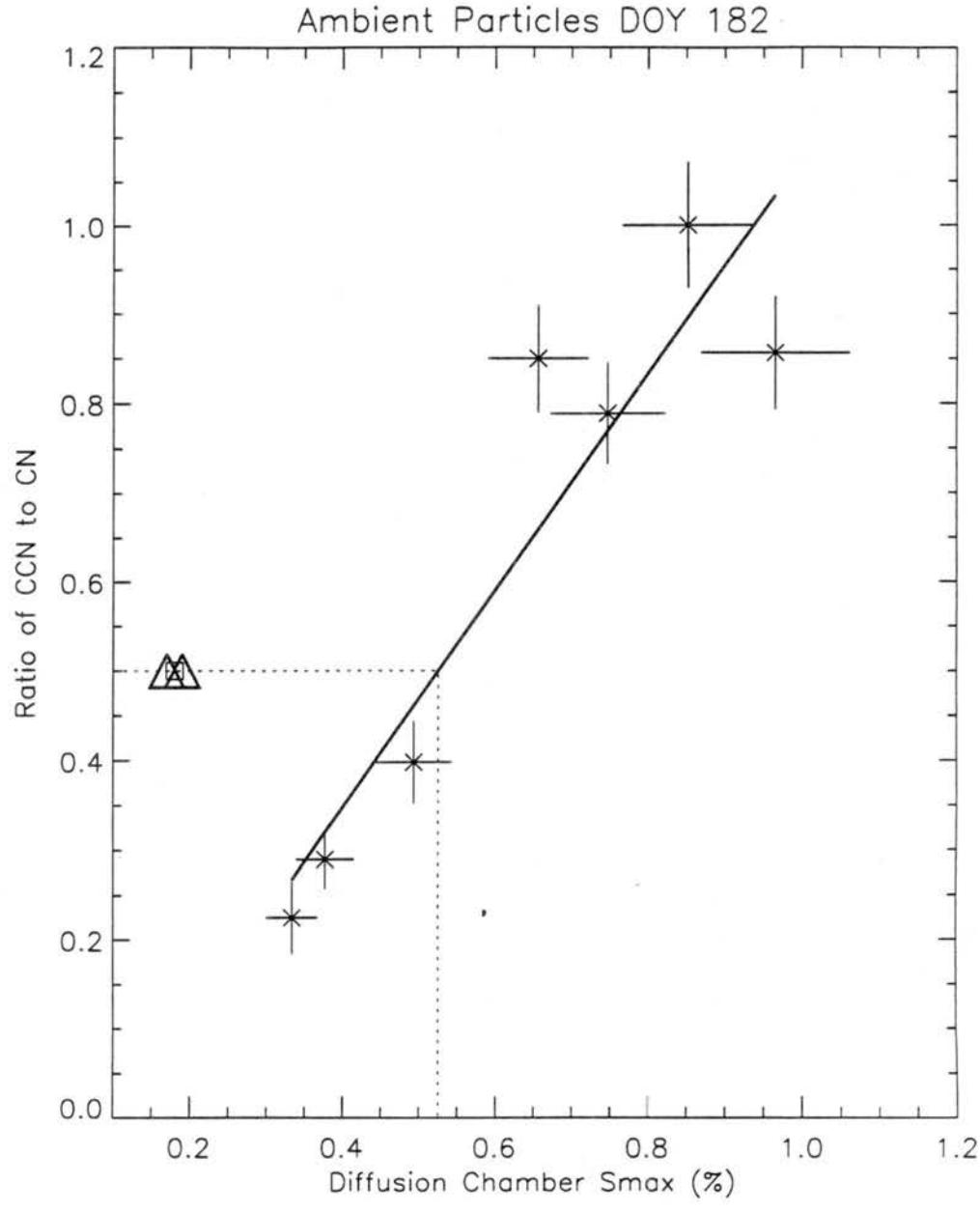

Figure 7.26: CCN study results for 120 nm diameter ambient particles on DOY 182. Solid line designates best-fit line to experimental data designated by asterisks. Vertical uncertainty bars represent Poisson counting error in CCN droplet concentration. Horizontal uncertainty bars represent ±10% uncertainty in chamber S_{max}. Triangles designate 1σ range of S_{crit} values predicted by fit routine from HTDMA growth results. The square represents the value of S_{crit} from the fit with all data pairs and no applied error, while the plus symbol represents the average value from the fits with applied error. Dotted lines designate experimentally observed value S_{crit}. The confidence interval for CCN-derived values of S_{crit} is ±21%.

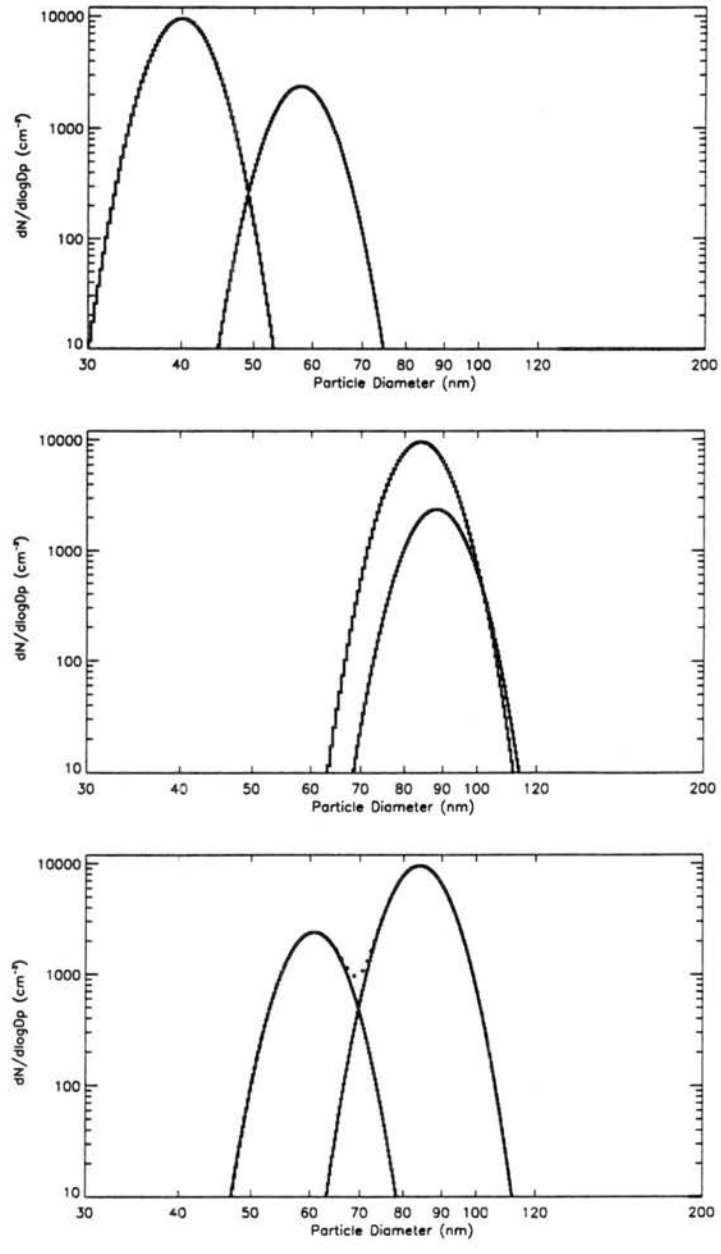

Figure 7.27: Example of the effect doubly charged particles can have on observed HT-DMA growth when doubly charged particles have a different chemical composition than singly charged particles. Top panel, (a), shows 40 nm singly charged NaCl particles and 58.1 doubly charged $(NH_4)_2SO_4$ dry particles selected by DMA1. Middle panel, (b), shows droplet sizes at 85% RH for singly and doubly charged populations. Bottom panel, (c), shows the mobility diameters measured by DMA2 of the doubly charged droplets formed on $(NH_4)_2SO_4$ particles (60.7 nm), and the singly charged droplets formed on NaCl particles (84 nm).

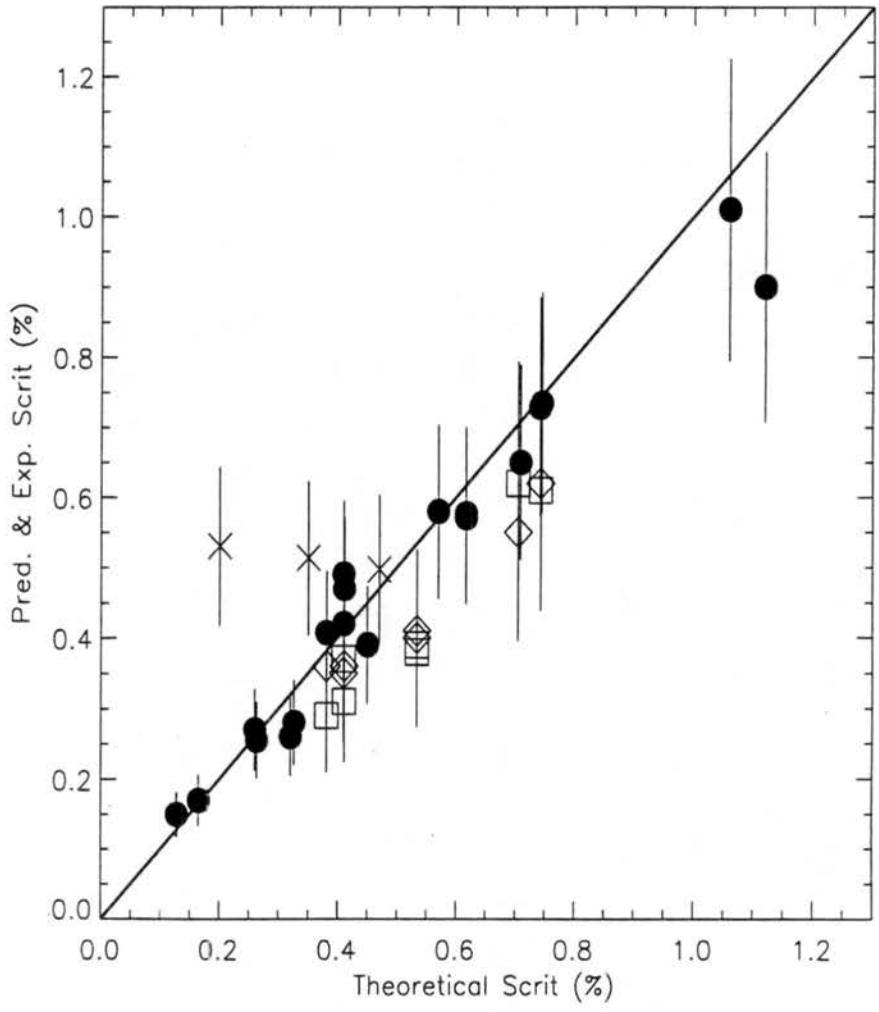

Figure 7.28: Comparison of values of S_{crit} derived from CCN studies (solid dots), the Köhler model in this work (diamonds), and the Köhler model from *Weingartner et al.* [1997] (squares), for all known composition particles studied in this work. The solid line designates perfect agreement between experimental and theoretical values of S_{crit}. 'X' designates results from ambient studies. For ambient studies, CCN-derived value of S_{crit} is shown on y-axis and HTDMA-derived value of S_{crit} is plotted on x-axis. Vertical error bars for CCN-derived values of S_{crit} represent the $\pm 21\%$ confidence interval. For HTDMA-derived values of S_{crit}, the vertical error bars represent a $\pm 28\%$ confidence interval. Confidence intervals are at the 95% confidence level.

Chapter 8

Summary and Conclusions

8.1 *Summary*

In this chapter, we summarize the work and results presented in previous chapters, present key conclusions, and provide some suggestions for future work.

In chapter 2, a review of previous work on bulk and monodisperse particle hygroscopicity and CCN activity was presented. Bulk measurements were found to be incapable of allowing unambiguous, quantitative assesments of the contributions to observed hygroscopic growth and CCN activity by particles of different sizes. HTDMA studies can be used to determine the size-dependent hygroscopic growth of particles, but the need for simultaneous chemical composition data to derive S_{crit} from HTDMA results has been one limitation of previous work where this was attempted. The first studies involving concurrent measurements of hygroscopic growth and CCN activity were performed in 1995 [*Covert et al.,* 1998]. Results from numerous HTDMA studies demonstrated the complex chemical composition of ambient particles and therefore the distinct advantage of a technique for determining S_{crit} that does not rely on information about the particle chemical composition. If only measurements of hygroscopic growth were required to determine the critical supersaturation of a particle, then the inability to accurately determine particle chemical composition would no longer be a significant deterrent to determining CCN concentrations.

The scientific questions and hypotheses addressed by this research were presented

in chapter 3. Experiments to test the various hypotheses were outlined. The fundamental scientific question addressed by this work is: 'Can the S_{crit} of monodisperse particles be predicted within experimental uncertainty using measurements of particle growth at RH's between 80 and 92%?' Subsequent chapters presented theoretical and laboratory results that demonstrated the feasibility of the proposed technique for deriving S_{crit} from HTDMA growth measurements on particles of known chemical composition.

In order to perform the numerical studies, a 'reference' Köhler model of particle growth as a function of RH was developed from first principles in chapter 4. In chapter 5, three key simplifications to the reference model were explored: volume additivity of solute and solvent, setting the surface tension of the droplet solution equal to that for pure water, and assuming a simplified version of Pitzer's model of the osmotic coefficient for electrolyte solutions [*Pitzer*, 1973]. We tested the sensitivity of predicted values of RH to each of the three assumptions. Our analyses showed that the simplifying assumptions may be used in the reference model to derive a simplified Köhler model that still accurately predicts RH to within $\pm 0.4\%$ for moderate solution molalities (< 6 molal) and for solutes that do not produce ions that associate in solution. From the simplified Köhler model, in chapter 5 we showed how S_{crit} could be derived from HTDMA study results and explored numerically the sensitivity of derived values of S_{crit} to experimental uncertainties in all input measureands. A simpler Köhler model, proposed by *Weingartner et al.* [1997], was also tested in our numerical simulations. For droplet solutions where the osmotic coefficient maintained values near unity over the range of RH's during HTDMA studies, values of S_{crit} predicted by the two models were similar. However, for one compound examined, NH_4NO_3, where the value of the osmotic coefficient monotonically decreases with increasing solution molality, the simpler Köhler model was less effective. Results from our sensitivity studies indicated that accurate values of S_{crit}, within ~7.5%

(1σ=10%, n=6) of theoretical values, could be derived for particles composed of single and two inorganic salts using simulated HTDMA study results with applied values of experimental uncertainties determined from laboratory HTDMA studies.

A detailed discussion of the theories of operation of the HTDMA, TGDCC and the various other instruments used in the laboratory studies was given in chapter 6. Quality control procedures were outlined. The experimental uncertainties in each measurement were quantified. In chapter 7, results from the laboratory studies of the hygroscopic growth and CCN activity of particles composed of pure and mixed salts and of ambient particles were presented. Excellent agreement between observed and theoretical droplet growth was found for particles composed of NaCl and $(NH_4)_2SO_4$. The error in droplet growth factors for studies on NaCl and $(NH_4)_2SO_4$ particles was calculated to be less than $\pm$1.65%. These results validated HTDMA operation.

Values of S_{crit} derived from CCN studies on particles of known chemical composition agreed with theoretical values within -0.6% with a standard deviation of 11%. Experimental uncertainties in values of S_{crit} were estimated in chapter 6 to be between $\pm$6% and $\pm$11%. The confidence interval in S_{crit} values derived from CCN studies was $\pm$21%. Values of S_{crit} derived from the fit routine using observed droplet growth from HTDMA studies on particles of known composition agreed with theoretical values of S_{crit} within -12% with a standard deviation of 5% (n=5). The confidence interval in S_{crit} values derived from HTDMA results was between $\pm$16% and $\pm$28%. The good agreement between values of S_{crit} derived from HTDMA results, those derived from CCN studies, and theoretical values serves to validate the method for deriving S_{crit} from hygroscopic growth results and the simplified Köhler model. The tendency for the fit routine to underpredict S_{crit} is due in part to assumptions made in the model that produce low values of S_{crit} even for perfect input data. Values of S_{crit} were also derived from HTDMA study results using the Köhler model proposed by *Weingartner et al.* [1997]. Slightly better agreement was found between theoret-

ical and predicted values of S_{crit} from the model of the present work than values predicted by the model of *Weingartner et al.* S_{crit} values from CCN studies did not agree within experimental uncertainties with those from HTDMA studies for two of the three ambient particle studies conducted for this work. The poorer agreement for the ambient studies is believed to be due to the variability in ambient particle concentration and chemical composition during the study, the low number concentrations of particles that were available to be sampled, and the likely complex mixture of more and less hygroscopic material in the ambient particles resulting in hygroscopic behavior that could not be captured by the simplified Köhler model.

Numerous previous HTDMA studies [*McMurry and Stolzenberg,* 1989; *Covert et al.,* 1993; *Svenningsson et al.,* 1994] have found that monodisperse samples of ambient particles often exhibit two hygroscopic growth modes and that the more hygroscopic particles typically grow less than particles composed of pure salts. These results suggest that the particles are chemically externally mixed at a single size and that the more hygroscopic particles are also internally mixed, containing a mixture of materials of lower hygroscopicity than pure inorganic salts. An alternative explanation for the observed two growth modes was examined numerically. Doubly, and higher, charged particles with a different chemical composition than the singly charged particles can grow more, or less, than the singly charged particles at a given RH. The change in droplet size produced through water condensation at elevated RH will not conserve the 2:1 ratio of the electrical mobilities of the doubly and singly charged droplets because the rate of change of electrical mobility with particle size does not match the rate of change of particle size with RH. For doubly and singly charged particles with the same composition and diameters less than 60 nm, the effect is small, less than -0.4% for growth factors between 1.3 and 2.1. The effect increases to -6% for a growth factor of 2.5, particle diameter equal to 80 nm, and a ratio of doubly-to-singly charged particles of 0.3. However, when the doubly and singly charged particles have

different chemical compositions, and therefore different growth factors, the effect can produce a bimodal distribution very similar to what is often observed with ambient particles where the chemical composition of the doubly and singly charged particles are possibly different. Therefore, in some situations, it may be incorrect to claim that the singly charged monodisperse particles are chemically externally mixed based on observations of less and more hygroscopic growth modes. It is possible that chemical differences between the singly and doubly charged particles are responsible for the observed bimodal hygroscopic response. If insignificant number concentrations of higher charged particles are present in the sample, then this effect is negligible. However, in some cases it may be important to consider that at a given size the particles may not be externally mixed with respect to their chemical composition, but that the physically larger, doubly charged particles have a different chemical composition than their singly charged counterparts. Techniques to discriminate the effects of doubly from singly charged particles were presented.

The following major conclusions may be drawn from this work:

- By applying the necessary corrections to the input particle number concentrations, systematic studies on particles of known size and chemical composition have demonstrated that a thermal gradient diffusion chamber CCN instrument can be used to determine the critical supersaturation of monodisperse particles within -0.6% of theoretical values. Approximately six to eight hours are required to complete such a study.

- A simplified form of the Köhler equation can be fit to HTDMA hygroscopic growth results from particles composed of known salts and values of S_{crit} derived that agree with theory within -12% (1σ=5%, n=5). Only 30 to 60 minutes are required to acquire the data necessary to derive a value of S_{crit}.

- For ambient particles, the agreement between values of S_{crit} predicted by the

current Köhler model and CCN study-derived values is poorer than that for known composition particles. This may be due to fluctuations in particle number concentration and chemical composition during the long period of time required for the CCN measurements, the low number concentrations and relatively few droplets counted in the CCN counter, or limitations in the Köhler model that did not allow it to capture the hygroscopic behavior of the ambient particles.

8.2 *Recommendations for Future Work*

The studies conducted for this work have motivated many interesting questions that could be addressed by future research. These main suggestions are offered:

1. Proper sizing with the HTDMA system depends critically on accurate and precise flow control. The HTDMA system could be improved by installing volumetric flow meters to measure three of the four DMA air flows in each DMA during HTDMA studies.

2. The role of impurities in the atomizer salt solutions should be examined, particularly with respect to the formation of letovicite in droplets of ammonium bisulfate. The nanopure water could be filtered or distilled in order to reduce the number of impurity particles.

3. The goodness of the log-normal fit to observed droplet growth data from the HTDMA depends upon the number of size bins with which the droplet mode is resolved. In the present work, the droplet mode was resolved with between five and ten size bins. For ambient studies, observed less and more hygroscopic modes often exhibited similar growth and could not be separately resolved by the log-normal fit routine. Future versions of the HTDMA data acquisition program could use a 'fast scan' approach, where an initial fast scan is conducted

to find the nominal droplet mode size. After the fast scan, new bin midpoint mobilities and DMA voltages could be calculated centered about the nominal mode size determined from the fast scan. In this way, the number of size bins used to resolve the grown particle size distribution could be increased. A preliminary version of the 'fast scan' data acquisition program has already been completed.

4. The HTDMA and UCPC data acquisition programs should be integrated into the LabView program used to measure temperatures and relative humidities. A pressure sensor should be installed in each DMA and the pressure and temperature measurements for each DMA should be integrated into the mobility calculations for each scan by the HTDMA program. The center rod voltages of each DMA should be measured and recorded by the LabView program to validate proper operation of the HTDMA system.

5. Studies on the sensitivity of HTDMA-derived values of S_{crit} to the number of (RH, D_{drop}) data pairs and the range of RH used as input to the fit routine demonstrated that best agreement between HTDMA-derived and theoretical values of S_{crit} occured when between five and ten data pairs were input to the fit routine spanning a RH range of approximately 10%. Fewer data pairs and input RH ranges smaller than 5% RH resulted in poorer agreement between HTDMA-derived and theoretical values of S_{crit}.

6. The poorer agreement between predicted and observed values of S_{crit} for ambient particles and laboratory NH_4HSO_4 particles suggests that future work should focus on improving the simplified Köhler model so that it can be applied to particles with more complex chemical compositions typical of the ambient aerosol. Efforts to improve the Köhler model should focus first on improving the parameterization of Φ so that it may be applied to particles composed of

mixtures of salts and insoluble material. Furthermore, future work involving ambient particles should include simultaneous chemical composition measurements: monodisperse particles could be deposited onto transmission electron microscope grids. Simultaneous, ambient polydisperse size distribution measurements during HTDMA studies would be useful for determining changes in ambient particle number concentrations with size over the course of the study.

7. The results of laboratory studies on particles composed of NH_4HSO_4 were uncertain due to the lack of any controls on ammonia gas concentrations and the potential neutralization of the particles. The levels of ammonia in the HTDMA air flows can be reduced by using bottled nitrogen gas to supply the DMA and atomizer flows. Alternatively, a scrubber system could be employed.

8. The finding that accurate and precise RH and temperature control in DMA2 is required for accurate HTDMA growth results indicates that future work on improving the RH control, particularly of the monodisperse inlet flow, is warranted. Specifically, a shorter humidification section for the monodisperse inlet flow humidifier might improve the RH control of this flow.

9. More replicate CCN studies on particles composed of single, pure salts, internally mixed salts, organic compounds, and particles composed of mixtures of organics and inorganic salts would allow even better estimates of the confidence interval in CCN-derived values of S_{crit} to be made.

10. HTDMA and CCN laboratory studies on particles composed of organic compounds and internal mixtures of salts and insoluble compounds are required to test the applicability of the fit technique to more complex chemical compositions.

11. If the Köhler model can be made to work with a more generic composition particle, there are some novel potential future applications of the method for deriving S_{crit} from observed particle hygroscopic growth. First, hygroscopic growth measurements could be used together with CCN measurements to quantify the CCN activity of ambient particles. A second possibility is that the hygroscopic growth of ambient particles could be measured from satellite for the same air mass experiencing different, known RH conditions. The results from the remotely observed hygroscopic growth might be used in a future version of the fit routine to derive an average S_{crit} for the sampled particle population. In order for this to work, the dry, ambient particle size distribution must also be observed remotely (i.e. at extremely low ambient RH) in the same air mass experiencing different values of RH. The observed dry and wet size distributions would need to be parameterized in terms of log-normal functions because information on monodisperse particle sizes would most likely not be available. For a given RH and mode diameter of the dry size distribution, the average droplet size could be represented by the mode size of the observed wet size distribution. The fit routine could then be applied as with HTDMA data, except with the wet mode size, RH data pairs as input for the observed dry mode size.

Chapter 9

REFERENCES

Agarwal, J. K., and G. J. Sem, Continuous Flow, Single-Particle-Counting Condensation Nucleus Counter, *J. Aerosol Sci.*, 11, 343-357, 1980.

Atkins, P. *Physical Chemistry, Fifth Edition*, W. H. Freeman and Company, New York, 1994.

Berg, O. H., E. Swietlicki, and R. Krejci, Hygroscopic growth of aerosol particles in the marine boundary layer over the Pacific and Southern Oceanss during ACE 1, *J. Geophys. Res., 103*, 16,535-16,545, 1998.

Brechtel, F. J. and S. M. Kreidenweis, A Preliminary Study of the Volatility of Aerosol at a Remote Mid-Latitude Mountain Site, *Poster presented at the International AAAR Conference, Aug. 1994.*

Byers, H. R., *Elements of Cloud Physics*, University of Chicago Press, Chicago, IL., 1965.

Carstens, J. C., J. Podzimek, and H. Andriambeloma, Assessment of the Impact of Insoluble and Surface Active Pollutants on Fog Evolution, *Proceedings of the 10th Annual Cloud Physics Conf., AMS, 1986.*

Charlson, R. J., J. E. Lovelock, M. O. Andreae, and S. G. Warren, Oceanic Phytoplankton, atmospheric sulfur, cloud albedo and climate, *Nature, 326*, 655-661,

1987.

Chen, J-P., Theory of Deliquescence and Modified KöhlerCurves, *J. Atmos. Sci., 51*, 3505-3516, 1994.

Cohen, M. D., R. C. Flagan, and J. H. Seinfeld, Studies of Concentrated Electrolyte Solutions Using the Electrodynamic Balance. 1. Water Activities for Single-Electrolyte Solutions, *J. Phys. Chem., 91*, 4563-4574, 1987.

Cohen, M. D., R. C. Flagan, and J. H. Seinfeld, Studies of Concentrated Electrolyte Solutions Using the Electrodynamic Balance. 2. Water Activities for Mixed-Electrolyte Solutions, *J. Phys. Chem., 91*, 4575-4582, 1987.

Cohen, M. D., R. C. Flagan, and J. H. Seinfeld, Studies of Concentrated Electrolyte Solutions Using the Electrodynamic Balance. 3. Solute Nucleation, *J. Phys. Chem., 91*, 4583-4590, 1987.

Covert, D. S. and J. Heintzenberg. Measurement of the degree of internal/external mixing of hygroscopic compounds and soot in atmospheric aerosols, *Sci. Total Environ., 36*, 347-352, 1984.

Covert, D. S., J. L. Gras, A. Wiedensohler and F. Stratmann, Comparison of Directly Measured CCN with CCN Modeled from the Number-Size Distribution in the MBL during ACE-1 at Cape Grim, *J. Geophys. Res., 103*, 16,597-16,608, 1998.

Covert, D. S., and J. Heintzenberg, Size Distributions and Chemical Properties of Aerosol and Ny Alesund, Svalbard, *Atmos. Env., 27A*, 2989-2997, 1993.

CDRD ACPL: Critical Design Review Data for Atmospheric Cloud Physics Laboratory, Prepared for George C. Marshall, Space Flight Center ACPL Project by General Electric Company under contract NAS 8-32668, October, 1979.

Cruz, C. N. and S. N. Pandis, A Study of the Ability of Pure Secondary Organic Aerosol to Act as Cloud Condensation Nuclei, *Atmos. Env., 31*, 2205-2214, 1997.

Dua, S. K., and P. K. Hopke, Hygroscopic Growth of Assorted Indoor Aerosols, *Aer. Sci. Tech., 24*, 151-160, 1996.

Duce, R. A., V. A. Mohnen, P. R. Zimmerman, D. Grosjean, W. Cautreels, R. Chatfield, R. Jaenicke, J. A. Ogren, E. D. Pellizzari, and G. T. Wallace, Organic Material in the Global Troposphere, *Rev. Geophys. Space Phys., 21*, 921-952, 1983.

Fitzgerald, J. W., W. A. Hoppel, and M. A. Vietti, The Size and Scattering Coefficient of Urban Aerosol Particles at Washington, D. C. as a Function of Relative Humidity, *J. Atmos. Sci., 39*, 1838-1852, 1982.

Fletcher, N. H., *The Physics of Rainclouds*, Cambridge University Press, 1962.

Fuchs, N. A., *The Mechanics of Aerosols*, Pergamon, 1964.

Gerber, H. E., W. A. Hoppel, and T. A. Wojciechowski, Experimental Verification of the Theorectical Relationship Between Size and Critical Supersaturation of Salt Nuclei, *J. Atmos. Sci., 34*, 1836-1841, 1977.

Gill, P. S., and T. E. Graedel, Organic Films on Atmospheric Aerosol Particles, Fog Droplets, Cloud Droplets, Raindrops, and Snowflakes, *Rev. Geophys. Space Phys., 21*, 903-920, 1983.

Gorbunov, B., and R. Hamilton, Water Nucleation on Aerosol Particles Containing Both Soluble and Insoluble Substances, *J. Aer. Sci., 28*, 239-248, 1997.

Gras, J. L., CN, CCN and particle size in Southern Ocean air at Cape Grim, *Atmos. Res., 35*, 233-251, 1995.

Greenspan, L., Humidity Fixed Points of Binary Saturated Aqueous Solutions, *J. Res. NBS A, 81A*, 89-95, 1977.

Hagen, D., M. Alcorn, J. Kassner, J. Carstens, R. Hopkins, J. Schmitt, M. Trueblood, W. Walker, and D. White, UMR Cloud Simulation Studies of Droplet Growth:

Investigation fo Condensation Coefficient, *Proceedings of the 10th Annual Cloud Physics Conf., AMS, 1986.*

Hallberg, A., J. A. Ogren, K. J. Noone, K. Okada, J. Heintzenberg, and I. B. Svenningsson, The influence of aerosol particle composition on cloud droplet formation, *J. Atmos. Chem., 19*, 153-171, 1994.

Hallett, J., B. Gardiner, J. Hudson, and F. Rogers, Cloud Condensation and Ice Nucleation of a Range of Carbonaceous Aerosols, *Proceedings of the 10th Annual Cloud Physics Conf., AMS, 1986.*

Hämeri, K., M. Rood, and H.-C. Hansson, Hygroscopic Properties of a NaCl Aerosol Coated with Organic Compounds, *J. Aer. Sci., 23*, S437-S440, 1992.

Hänel, G., The Properties of Atmospheric Aerosol Particles as Functions of the Relative Humidity at Thermodynamic Equilibrium with the Surrounding Moist Air, *Rev. of Geophys., 17*, 73-188, 1976.

Hänel, G. and M. Lehmann, Equilibrium size of aerosol particles and and relative humidity: new experimental data from various aerosol types and their treatment for cloud physics application. *Beitr. Phys. Atmos., 54*, 57-71, 1981.

Hansson, H.-C., A. Wiedensohler, M. J. Rood, and D. S. Covert, Experimental Determination of the Hygroscopic Properties of Organically Coated Aerosol Particles, *J. Aer. Sci., 21*, S241-S244, 1990.

Harrison, L., and H. Harrison, The Segregation of Aerosols by Cloud- Nucleating Activity. Part I: Design, Construction, and Testing of A High-Flux Thermal Diffusion Cloud Chamber for Mass Separation, *J. Clim. Appl. Met., 24*, 302-310, 1985.

Harrison, L., The Segregation of Aerosols by Cloud-Nucleating Activity. Part II: Observation of an Urban Aerosol, *J. Clim. Appl. Met., 24*, 312-321, 1985.

Heintzenberg, J., and D. S. Covert, Chemically resolved submicrometric size distribution and external mixing of the Arctic haze aerosols, *Tellus, 39B*, 374-382, 1987.

Hegg, D. A., Yuen, P. F., and T. V. Larson, Modeling the Effects of Heterogeneous Cloud Chemistry on the Marine Particle Size Distribution, *J. Geophys. Res., 97*, 12927-12933, 1992.

Hewitt, G. W., The Charging of Small Particles for Electrostatic Precipitation, *AIEE Transactions,* Paper 57-90, 300-306, 1957.

Hinds, W. C.,*Aerosol Technology: Properties, Behavior, and Measurement of Airborne Particles*, John Wiley & Sons, 1982.

Hoppel, W. A., Measurement of the Size Distribution and CCN Supersaturation Spectrum of Submicron Aerosols over the Ocean, *J. Atmos. Sci., 36*, 2006-2015, 1979.

Hudson, J. G., X. Da, Volatility and size of cloud condensation nuclei, *J. Geophys. Res., 101,* 4435-4442, 1996.

Hudson, J. G., Y. Xie, and S. S. Yum, Vertical distributions of cloud condensation nuclei spectra over the summertime Southern Ocean, *J. Geophys. Res., D13*, 16609-16624, 1998.

IPCC, Intergovernmental Panel on Climate Change, 1995. Radiative Forcing of Climate Change. In *Climate Change 1994*, Cambridge University Press, New York.

Juozaitis, A., Ulevicius, V., and Girgzdys, A., and Willeke, K., Differentiation of Hydrophobic from Hydrophylic Submicrometer Aerosol Particles, *Aer. Sci. Tech., 18*, 202-212, 1993.

Kelly, W. P., and P. H. McMurry, Measurement of Particle Density by Inertial Classification of Differential Mobility Analyzer-Generated Monodisperse Aerosols, *Aer.*

Sci. Tech., 17, 199-212, 1992.

Kim, Y. P., J. H. Seinfeld, and P. Saxena, Atmospheric Gas-Aerosol Equilibrium I. Thermodynamic Model, *Aer. Sci. Tech., 19*, 157-181, 1993.

Kinney, P. D., D. Y. H. Piu, W. Mulholland, and N. P. Bryner, Use of the electrostatic classifier method to size 0.1 mm SRM particles - A feasibility study, *J. Res. Natl. Inst. Stand. Technol., 96*, 147-175, 1991.

Konopka, P., A Reexamination of the Derivation of the Equilibrium Supersaturation Curve for Soluble Particles, *J. Atmos. Sci., 53*, 3157-3163, 1996.

Kulmala, M., A. Laaksonen, R. J. Charlson and P. Korhonen, Clouds without supersaturation, *Accepted in Nature, 1997.*

Leaitch, W. R., J. W. Bottenheim, T. A. Biesenthal, S.-M. Li, P. S. K. Liu, K. Asalien, H. Dryfhout-Clark, F. Hopper, and F. J. Brechtel, A Case Study of Gas-to-Particle Conversion in an Eastern Canadian Forest. Accepted, *Journal of Geophysical Research,* August, 1998.

Liu, B. Y. H., D. Y. H. Pui, K. T. Whitby, D. B. Kittelson, Y. Kousaka and R. L. McKenzie, The Aerosol Mobility Chromatograph: A New Detector for Sulfuric Acid Aerosols, *Atmos. Env., 12*, 99-104, 1978.

Low, R. D. H., A Generalized Equation for the Solution Effect in Droplet Growth, *J. Atmos. Sci., 26*, 608-611, 1969.

Malm, W. C., J. F. Sisler, D. Huffman, R. A. Eldred and T. A. Cahill, Spatial and seasonal trends in particle concentration and optical extinction in the United States. *J. Geophys. Res. , 99,* 1347-1370, 1994.

McDonald, J. E., Erroneous Cloud-Physics Applications of Raoult's Law, J. Meteor., 10, 68-70, 1953,

McMurry, P. H. and M. R. Stolzenburg, On the Sensitivity of Particle Size to Relative

Humidity for Los Angeles Aerosols, *Atmos. Env., 23*, 497-507, 1989.

McMurry, P. H., M. Litchy, P. Huang, X. Cai, B. J. Turpin, W. D. Dick, and A. Hanson, Elemental composition and morphology of individual particles separated by size and hygroscopicity with the TDMA, *Atmos. Env., 30* , 101-108, 1996.

Meszaros, A., On the variation of the size distribution of large and giant atmospheric particles as a function of the relative humidity, *Tellus, 23*, 436-440, 1971.

Murphy, D. M., J. R. Anderson, P. K. Quinn, L. M. McInnes, F. J. Brechtel, S. M. Kreidenweis, A. M. Middlebrook, M. Posfai, D. S. Thomson and P. R. Buseck, Influence of sea-salt on aerosol radiative properties in the Southern Ocean marine boundary layer, *Nature, 392*, 62-65, 1998.

Northern Front Range Air Quality Study (NFRAQS), Executive Summary, Available from *http://www.charon.cira.colostate.edu/FinalReports.html.*

Neumann, A. W., and J. K. Spelt eds., *Applied Surface Thermodynamics*, Marcel Dekker, Inc., New York, 1996.

Novakov, T. and J. E. Penner, Large Contribution of Organic Aerosols to Cloud-Condensation-Nuclei Concentrations, *Nature, 365*, 823-826, 1993.

Pitchford, M. L., and P. H. McMurry, Relationship Between Measured Water Vapor Growth and Chemistry of Atmospheric Aerosol for Grand Canyon, Arizona, in Winter 1990, *Atmos. Env., 28*, 827-839, 1994.

Pitzer, K. S., Thermodynamics of Electrolytes. I. Theoretical Basis and General Equations, *J. Phys. Chem., 77*, 268-277, 1973.

Pitzer, K. S., and G. Mayorga, Thermodynamics of Electrolytes. II. Activity and Osmotic Coefficients for Strong Electrolytes with One or Both Ions Univalent, *J. Phys. Chem., 77*, 2300-2308, 1973.

Podzimek, J., M. B. Trueblood, and D. E. Hagan, Condensation Nuclei Activation

or Deactivation by Deposited Insoluble Particles, *Atmos. Env., 25A*, 2587-2591, 1991.

Pruppacher, H. R., and J. D. Klett, *Microphysics of Clouds and Precipitation*, Dordrecht Publishers, 1997.

Quinn, T. and T. S. Bates et al., Disco Chem Observations, *Poster presented at Final ACE-1 Data Workshop, Hilo, HI, Mar. 1997.*

Rader, D. J. and P. H. McMurry, Application of the Tandem Differential Mobility Analyzer to Studies of Droplet Growth or Evaporation, *J. Aerosol Sci., 17*, 771-787, 1986.

Reid, R. C., J. M . Prausnitz and B. E. Poling, *The Properties of Gases & Liquids, 4th Ed.*, McGraw-Hill, Inc., New York, 1987.

Reineking, A., and J. Porstendörfer, Measurements of Particle Loss Functions in a Differential Mobility Analyzer (TSI, Model 3071) for Different Flow Rates. *Aerosol Sci. and Technol., 5,* 483-486, 1986.

Robinson, R. A., and R. H. Stokes, 1959: *Electrolyte Solutions.* 2d ed. Butterworths, 571 pp.

Rogers, R. R., and M. K. Yau, 1989: *A Short Course in Cloud Physics*, 3d ed. Pergamon Pres, 293 pp.

Rogge, W. F., M. A. Mazurek, L. M. Hildemann, G. R. Cass, and B. R. T. Simoneit, Quantification of Urban Organic Aerosols at a Molecular Level: Identification, Abundance and Seasonal Variation, *Atmos. Env., 27A*, 1309-1330, 1993.

Rood, M. J., D. S. Covert and T. V. Larson, Hygroscopic properties of atmospheric aerosol in Riverside, California, *Tellus, 39B*, 383-397, 1987.

Saxena, P. S., L. M. Hildemann, P. H. McMurry, and J. H. Seinfeld, Organics alter hygroscopic behavior of atmospheric particles, *J. Geophys. Res., 100* , 18755-

18770, 1995.

Saxena, P. and L. M. Hildemann, Water-Soluble Organics in Atmospheric Particles: A Critical Review of the Literature and Application to Thermodynamics to Identify Candidate Compounds, *J. Atmos. Chem., 24*, 57-109, 1996.

Schulmann, M. L., M. C. Jacobsen, R. J. Charlson, R. E. Synovec, and T. E. Young, Dissolution behavior and surface tension effects of organic compounds in nucleating cloud droplets, *Geophys. Res. Lett., 23*, 277-280, 1996.

Seinfeld, J. H. *Atmospheric Chemistry and Physics of Air Pollution*, J. Wiley & Sons, 738 pp, 1986.

Seinfeld, J. H. and S. N. Pandis. *Atmospheric Chemistry and Physics, From Air Pollution to Climate Change*, J. Wiley & Sons, 1326 pp, 1997.

Sekigawa, K., Estimation of the Volume Fraction of Water Soluble Material in Submicron Aerosols in the Atmosphere, *J. Met. Soc. Jpn., 61*, 359- 367,1983.

Shaw, M. A., and M. J. Rood, Measurement of the Crystallization Humidities of Ambient Aerosol Particles, *Atmos. Env., 24A*, 1837-1841, 1990.

Skoog, D. A., D. M. West, and F. J. Holler, *Fundamentals of Analytical Chemistry*, Sixth ed., Saunders College Publishing, 1992.

Sloane, C., and G. T. Wolff, Prediction of ambient light scattering using a physical model responsive to relative humidity: validation with measurements from Detroit, *Atmos. Env., 19*, 669-680, 1985.

Stokes, R. H., and R. A. Robinson, Interactions in aqueous nonelectrolyte solutions, *J. Phys. Chem., 70*,2126-2131, 1966.

Stratmann, F., and A. Wiedensohler, A new data inversion algorithm for DMPS measurements, *J. Aerosol Sci., 27*, S1, 339-340, 1996.

Kauffeldt Th., F. Stratmann and H. Kleinwechter, Development and Experimental Verification of a New Straight Forward Inversion Algorithm for Differential Mobility Analysers, *J. Aerosol Sci., 27 (S1)*, 139-140, 1996.

Svenningsson, I. B., H.-C. Hansson, A. Wiedensohler, J. A. Ogren, K. J. Noone, and A. Hallberg, Hygroscopic growth of aerosol particles in the Po Valley, *Tellus, 44B*, 556-569, 1992.

Svenningsson, B., H.-C. Hansson, A. Wiedensohler, K. Noone, J. Ogren, A. Hallberg, and R. Colville, Hygroscopic Growth of Aerosol Particles and its Influence of Nucleation Scavenging in Cloud: Experimental Results from Kleiner Feldberg, *J. Atmos. Chem., 19*, 129-152, 1994.

Tang, I. N., W. T. Wong, and H. R. Munkewitz, The Relative Importance of Atmospheric Sulfates and Nitrates in Visibility Reduction, *Atmos. Env., 15*, 2463-2471, 1981.

Tang, I. N., and H. R. Munkelwitz, Composition and Temperature Dependence of the Deliquescence Properties of Hygroscopic Aerosols, *Atmos. Env., 27A*, 467-473, 1993.

Tang, I. N., and H. R. Munkelwitz, Water activities, densities, and refractive indices of aqueous sulfates and sodium nitrate droplets of atmospheric importance, *J. Geophys. Res., 99*, 18801-18808, 1994.

Tang, I. N., Thermodynamic and optical properties of mixed-salt aerosols of atmospheric importance, *J. Geophys. Res., 102*, 1883-1893, 1997.

Taylor, J. R., *An Introduction to Error Analysis: The Study of Uncertainties in Physical Measurements*, University Science Books, CA, 1982.

Wallace, J. M. and P. V. Hobbs, *Atmospheric Science An Introductory Survey*, Academic Press, NY, 1977.

Weast, R. C.,*Handbook of Chemistry and Physics, 69th Edition,* CRC Press, Inc.,Boca Raton, FL, 1988.

Wiedensohler, A., D. Orsini, D. S. Covert, D. Coffmann, W. Cantrell, M. Havlicek, F. J. Brechtel, L. M. Russell, R. J. Weber, J. Gras, J. G. Hudson, and M. Litchy, Intercomparison Study of the Size-Dependent Counting Efficiency of 26 Condensation Particle Counters, *Aerosol Science and Tech.,* 27, 224-242, 1997.

Wiedensohler, A., An Approximation of the Bipolar Charge Distribution for Particles in the Submicron Size Range, *J. Aerosol. Sci.,* 19, 387-389, 1988.

Weingartner, E., H. Burtscher, and U. Baltensperger, Hygroscopic Properties of Carbon and Diesel Soot Particles, *Atmos. Env., 31*, 2311-2327, 1997.

Wilemski, G., Composition of the critical nucleus in multicomponent vapor nucleation, *J. Chem. Phys. 80*, 1370-1372, 1984.

Willows, R. S., and E. Hatschek, *Surface Tension and Surface Energy and Their Influence on Chemical Phenomena*, P. Blakiston's Son & Co., Philadephia, 1923.

Winkler, P., The growth of atmospheric aerosol particles as a function of the relative humidity. Part II: An improved concept of mixed nuclei, *Aer. Sci. Tech., 4*, 373-387, 1973.

Winkler, P. and C. Junge, The growth of atmospheric aerosol particles as a function of the relative humidity. Part I: Method and measurements at different locations, *J. Rech. Atmos.* (Memorial Henri Dessens), 617-638, 1972.

Young, K. C. and A. J. Warren, A Reexamination of the Derivation of the Equilibrium Supersaturation Curve for Soluble Particles,*J. Atmos. Sci., 49*, 1138-1143, 1992.

Zdanovskii, A. B., *Tr. Solyanoi Lab. Vses. Inst. Galurgii Akad. Nauk SSSR*, no. 6, 1936.

Zhang, X. Q., P. H. McMurry, S. V. Hering, and G. S. Casuccio, Mixing Character-

istics and Water Content of Submicron Aerosols Measured in Los Angeles and at the Grand Canyon, *Atmos. Env., 27A*, 1593-1607, 1993.